Electrokinetic Transport at Microscale: Particle Electromigration and Fluid Pumping in Lab-on-Chip Microsystems

Zur Erlangung des akademischen Grades eines
DOKTORS DER INGENIEURWISSENSCHAFTEN (Dr.-Ing.)

von der KIT-Fakultät für Maschinenbau des
Karlsruher Instituts für Technologie (KIT)
angenommene

DISSERTATION

von

M. Sc. Philipp G. Marthaler

Tag der mündlichen Prüfung: 24. April 2023

Hauptreferent: Prof. Dr.-Ing. Andreas G. Class
Korreferenten: Prof. Dr.-Ing. Bettina Frohnapfel,
Prof. Michael J. Miksis

Abstract

The application fields of lab-on-chip (LOC) devices range from chemical and microbiological research topics, like genomics, via environmental monitoring to clinical diagnostics. Current efforts in LOC development are addressing miniaturization, multiplexing, and interface optimization. An LOC design promising to serve these trends is presented in this work. The active-surface programmable LOC features a channel-free design, easing fabrication at small length scales and outclassing classical systems with regard to flexibility. This study investigates the feasibility of the presented design by addressing two of the most critical aspects, sample control and fluid transport performance.

Crucial for both of these aspects is the understanding of complex electrokinetic phenomena. Wall electrodes inside the device enable fluid pumping and flow control. Electrode distances are of similar magnitude as the size of the respective charge clouds, determined by the Debye length. Simplifying assumptions, like the thin-Debye-layer limit, do not hold. Samples and reactants are in fluid form and dispersed in the surrounding phase of the carrier fluid. The control of such fluid droplets inside the LOC system relies heavily on the predictability of their behavior in the presence of electric fields. Traditional models, such as the Taylor-Melcher model, do not capture electromigration observed in experimental studies.

In this study, electromigration of immiscible droplet samples in strong electrolytes is investigated by an asymptotic approach resolving the nonlinear Debye-layer electrokinetics. Quantitative predictions on migration speed and deformation of the drop are made. In accordance with experimental results, the occurrence of electromigration is confirmed. Remarkably, this holds even for droplets with zero net charge. The influence of electrolyte strength in such systems is found to be small while other modeling parameters, e.g. approximation of the geometry, are of major impact.

In the second part of this investigation, a feasibility analysis of the pumping mechanism is performed by numerical simulation. Specifically for this purpose, a non-interpolating spectral solver was constructed. We confirm sufficiently high transport speeds and the desired homogeneous flow field. Heat dissipation, which acts as a limiting factor for miniaturization, is estimated from the Ohmic charge fluxes within the carrier fluid. Further technical limitations, such as prototyping cost, clock frequency, and producible electrode distance, are discussed and an optimization algorithm is presented. Together with a systematic description of the design architecture, the basis for successive further developments and their numerical verification is established.

Zusammenfassung

Lab-on-Chip(LOC)-Systeme werden in vielen Bereichen, wie Chemie und Mikrobiologie, insbesondere Genomik, über Umweltmonitoring bis hin zur klinischen Diagnostik eingesetzt. Die Weiterentwicklung bestehender Systeme fokussiert sich auf Miniaturisierung, Multiplexing und der Optimierung von Schnittstellen. In dieser Arbeit wird ein LOC-Design vorgestellt, das verspricht, diesen Trends gerecht zu werden. Durch seine Programmierbarkeit und aktive Elektrodenoberfläche ohne Kanalstruktur ist es klassischen Systemen in der Anwendungsflexibilität und der Möglichkeit zur Miniaturisierung überlegen. Die vorliegende Studie untersucht die Machbarkeit des vorgestellten Systems in zwei seiner kritischsten Aspekte, die Kontrollierbarkeit chemischer Proben und Leistungsfähigkeit des Pumpmechanismus.
Beide genannten Aspekte sind komplexe elektrokinetische Phänomene. Wandelektroden in der Oberfläche des Chips ermöglichen das kontrollierte Pumpen von Flüssigkeiten. Dabei sind die Elektrodenabstände von gleicher Größenordnung wie die entstehenden Ionenwolken, deren geometrische Größe durch die Debye-Länge charakterisiert ist. Die häufig verwendete vereinfachende Annahme einer dünnen Debye-Schicht gilt in diesem Zusammenhang nicht. Darüber hinaus liegen Proben und Reagenzien in flüssiger Form vor und sind von einer Trägerflüssigkeit umgeben. Diese Flüssigkeitstropfen sollen auf der Chipoberfläche kontrolliert bewegt werden. Entscheidend dafür ist ein grundlegendes Verständnis über das Verhalten der Tropfen unter dem Einfluss elektrischer Felder. Traditionelle Modelle, wie das Taylor-Melcher-Modell, scheitern hier, da sie Elektromigrationseffekte nicht erklären können, die in Experimenten beobachtet wurden.
Die vorliegende Studie untersucht im ersten Teil Elektromigration nicht mischbarer tropfenförmiger Proben in starken elektrolytischen Lösungen mithilfe eines asymptotischen Ansatzes. Nichtlineare elektrokinetische Effekte in der Debye-Schicht werden betrachtet und quantitative Vorhersagen über Migrationsgeschwindigkeit und Deformation des Tropfens getroffen. Experimentell beobachtete Elektromigrationseffekte können so bestätigt werden. Überraschenderweise können auch bei elektrisch neutralen Tropfen Migrationseffekte auftreten. Der Einfluss der Stärke des Elektrolyts auf die genannten Ergebnisse ist vergleichsweise klein. Im Gegensatz dazu haben andere Annahmen, die beispielsweise die Modellierung der Tropfengeometrie betreffen, erheblichen Einfluss.
Im zweiten Teil wird eine Machbarkeitsstudie des Pumpmechanismus mittels numerischer Simulation vorgestellt. Ein auf spektralen Methoden basierender Lösungsalgorithmus wurde speziell für diesen Zweck entwickelt. Ausreichend hohe Transportgeschwindigkeiten und das gewünschte homogene Strömungsfeld können damit bestätigt werden. Ebenfalls wird die Wärmeproduktion durch Ohm'sche Ströme in der Trägerflüssigkeit berechnet. Sie gilt als limitierender Faktor für die Miniaturisierung des Systems. Weitere Limitierungen sind

durch Produktionskosten des Prototypen, Schaltfrequenz und kleinstmöglicher Elektrodenabstand gegeben. Ein Optimierungsalgorithmus für verschiedene Parameter wird im Rahmen dieser Arbeit vorgestellt. Dieser bildet zusammen mit einer systematischen Beschreibung der Systemarchitektur die Grundlage für schrittweise Weiterentwicklungen und deren numerische Verifizierung.

Acknowledgments

This thesis was elaborated while working as a research associate at the Institute for Thermal Energy Technology at KIT and as a Visiting Predoctoral Fellow at the Department for Engineering Science and Applied Mathematics (ESAM) at Northwestern University. The collaboration with ESAM was financially supported by the Karlsruhe House of Young Scientists.

Firstly, I would like to thank my advisor, Prof. Dr.-Ing. Andreas Class for guiding me through my years as a doctoral student. Beyond supporting this work with so many discussions and ideas, he taught me spectral and asymptotic methods and introduced me to the world of differential geometry. For her interest in the topic, I thank Prof. Dr.-Ing. Bettina Frohnapfel who took over the co-advisorship. For chairing my doctoral exam, I thank Prof. Dr.-Ing. Thomas Boehlke.

I am also extremely grateful to Prof. Michael Miksis who was not afraid of working on a model connecting electrokinetics to electrohydrodynamics, although there would have been reasons to be. Thank you for asking the right questions. Special thanks go to Prof. Petia Vlahovska for sharing her knowledge on electrohydrodynamics with me. I cannot count the Friday-afternoon discussions with Petia and Mike that regularly left me exhausted, confused, and yet a little wiser than before. I would like to express my gratitude to Jorge Yanez. His infectious enthusiasm for differential geometry motivated me to push forward and his feedback is invaluable to me, for it is always sound and honest.

I had the pleasure of working with my students, Daxiao Liu and Noah Lettner. Both contributed to my own understanding of numerical simulations and electro-diffusion. I would like to express my appreciation to Shenhui Ruan, Lorenz Weber, and Biao Lyu for building a great community of doctoral students at ITES, for the mutual emotional support, and the conversations on science and life. Also, thank you to April Zhi Zhou who integrated me in the ESAM community at Northwestern.

I am grateful to my parents for all their continuous support, encouragement, and interest in my work. Lastly, I thank Sara-Lena for being my rock. During the work on this thesis she allowed me to pretend that this was the most important thing in life; now she is my daily proof that there is something even more important.

"It's as if we collectively intuited, long before science gave us the language, that the universe bends toward entropy, and every act of creation on our part is an act of defiance in the face of that evolving disorder."

– Tucker (2021), *The Meaning in the Making*

Contents

Acknowledgments **v**

1 Introduction **1**
1.1 Definition of the topic . . . 1
1.2 Historical Background and applications . . . 5
1.2.1 Life sciences and technical microsystems . . . 5
1.2.2 Application of LOC systems in diagnostic medicine . . . 6
1.2.3 Trends in LOC development . . . 7
1.3 State of the art and aims of this study . . . 8
1.3.1 Competitive systems and our design . . . 8
1.3.2 Our design . . . 11
1.3.3 Landscape of two-phase EHD models . . . 14
1.3.4 Aim and Hypothesis . . . 15
1.4 Methodology: Asymptotics and spectral simulations . . . 16
1.4.1 Asymptotic analysis of the Debye layer . . . 16
1.4.2 The non-interpolating spectral method for the actuator simulation . 16
1.5 Outline of the thesis . . . 17

2 Electric effects in fluid mechanics **19**
2.1 Terminology . . . 19
2.2 Important electrohydrodynamic effects . . . 20
2.2.1 Fick's law of diffusion . . . 20
2.2.2 Stokes flow . . . 21
2.2.3 The relation of diffusion, mobility, and conductivity in fluid electrolytes . . . 21
2.2.4 Structure of the electric double layer: The Gouy-Chapman solution and the Debye-Hückel approximation . . . 23
2.2.5 Electrokinetics as boundary effects: The Smoluchowski slip condition 26
2.2.6 Linear transient electrokinetics: The Debye-Falkenhagen approximation . . . 27
2.2.7 Influence of a streaming potential: The electric Reynolds number . . . 29
2.2.8 Association and dissociation of salt . . . 30

3 Electrokinetic models **33**
3.1 The Taylor-Melcher model . . . 34
3.2 The Saville model . . . 37
3.3 The Schnitzer-Yariv model . . . 42
3.4 The Mori-Young model . . . 46
3.4.1 The weak electrolyte limit . . . 49
3.4.2 Re-constitution of the TM model for large-Pe flow . . . 50
3.4.3 Charge transport in the surface: Surface convection and conduction 51
3.4.4 Particle migration . . . 51
3.5 Other important studies . . . 52
3.6 Model comparison . . . 53

4 Strong-electrolyte fluid-fluid model **57**
4.1 Model . . . 57
4.1.1 Set-up . . . 57
4.1.2 Dimensionless form . . . 59
4.1.3 Properties of the liquid-liquid interface . . . 60
4.1.4 Remarks on parameter dimensions . . . 61
4.1.5 Strong electrolyte limit . . . 62
4.1.6 Thin-Debye-layer limit . . . 62
4.1.7 Geometry in tensor notation . . . 63
4.1.8 Geometrical expansions . . . 64
4.2 Debye cloud analysis . . . 64
4.2.1 Electric problem at order δ^{-2} . . . 66
4.2.2 Electric problem at order δ^{-1} . . . 68
4.2.3 Pressure at order δ^{-2} . . . 70
4.2.4 Pressure at order δ^{-1} . . . 70
4.2.5 Normal velocity at $O(1)$ . . . 72
4.2.6 Transverse Velocity at $O(1)$ . . . 72
4.2.7 Normal stress at $O(1)$ . . . 74
4.2.8 Shear stress at $O(1)$ . . . 75
4.2.9 Model summary . . . 77
4.2.10 Absence of outer electrochemical gradients . . . 78
4.2.11 The Taylor-Melcher model in the absence of a Galvani potential . . 82
4.3 Electromigration of a spherical drop . . . 82
4.4 Conclusion . . . 91

5 Electrokinetic DNS **95**
5.1 Problem setup . . . 96
5.1.1 Geometry . . . 96
5.1.2 Material properties . . . 96
5.1.3 Excitation . . . 99
5.1.4 Governing equations . . . 99
5.1.5 Dimensionless form . . . 100
5.1.6 Streamfunction formulation . . . 100

5.1.7 Initial conditions . . . 102
5.2 The Fourier-Chebyshev spectral method . . . 102
5.2.1 Collocation methods as a special form of weighted residual methods 102
5.2.2 The non-interpolating spectral approach . . . 103
5.2.3 Transformations and grid . . . 104
5.2.4 Spectral operators . . . 105
5.2.5 The Lanczos method for the implementation of boundary conditions 106
5.3 Construction of a solver in Python . . . 108
5.3.1 General comments . . . 108
5.3.2 Spectral module containing the basic operations . . . 108
5.3.3 Discretization of the PNP system . . . 110
5.3.4 The no-flux boundary conditions and influence matrix method . . . 112
5.3.5 Equation coupling with Gummel's iteration . . . 114
5.3.6 Solution of the streamfunction equation . . . 115
5.3.7 Validation . . . 119
5.4 Post-processing . . . 119
5.4.1 Dissipation . . . 119
5.4.2 Total dissipation and actuator efficiency . . . 120
5.4.3 Termination conditions for the time loop . . . 120
5.5 Startup behavior and frequency dependence . . . 121
5.6 Conclusion . . . 124

6 Active-surface lab-on-chip system 127
6.1 System architecture . . . 127
6.1.1 Explanation models . . . 127
6.1.2 Structure and functional behavior of the lab and the fluid processing unit . . . 128
6.2 Technical limitations . . . 131
6.3 Optimization . . . 136
6.4 Final remarks . . . 137

7 Conclusion 139
7.1 Generalizing remarks on the electrokinetic transport phenomena in an LOC system . . . 139
7.2 Development status and outlook . . . 140
7.2.1 Electrohydrodynamic models . . . 140
7.2.2 Actuator and LOC simulation . . . 141
7.2.3 Product design . . . 142
7.3 Final remarks . . . 143

A The Stokes equation in curvilinear coordinates 151
A.1 The Stokes equation in general curvilinear coordinates . . . 151
A.2 Normal and tangential directions . . . 152
A.3 Hydrodynamic and electric stress tensors . . . 153
A.4 Relevant orders of the momentum equation . . . 154

A.5 Equations for weakly non-orthogonal coordinates 154
A.6 Equations for spherical coordinates 155
A.7 Charge form 156
A.8 Integration of the Maxwell shear stress at $O(1)$ 157
A.9 Charge form before the asymptotic expansion 158
A.10 Equivalence of stress and charge form 160

B Strong vs. weak electrolyte limit **163**

C UML diagram of the spectral solver **167**

D Patent graphics **169**

CHAPTER 1

Introduction

1.1 Definition of the topic

Lab-on-chip devices Microfluidic systems are an intensively used tool in DNA research, molecular and evolutionary biology, cytology, and drug testing, just to mention the most important fields of application. Scientific progress in these fields and the technical innovations enabling it go hand in hand.

This work focuses on a proposed microfluidic system whose most significant feature is its chip surface without channels. We will refer to this programmable active-surface lab-on-chip (LOC) device as "our chip/design". The design details are described in the publications of the patent application Marthaler and Class (2022a, 2022b). In the chip surface, individually addressable n-tuples of electrodes are embedded. It is subsequently denoted as active surface.

LOC devices are microfluidic systems that can perform laboratory processes (traditionally carried out in a macroscopic lab) on a small device with integrated circuits. Typically measuring several millimeters to centimeters in size, these devices are popular for their ease of use, automation opportunities, fast response times, low cost, low energy consumption, and small sample volumes. As an effect, LOC devices are efficient, reliable and reduce human error, which is especially important for point-of-care diagnostics (Haji Mohammadi et al., 2021; Staicu et al., 2021; Vidic et al., 2019) and environmental monitoring (Dhar & Lee, 2018). The low cost of some LOC systems can also have an impact on the democratization of health care. One particularly important trend contributing to this democratization is the integration of microfluidic systems in smartphones (Chen et al., 2021; Hernández-Neuta et al., 2019; Wilson, Steele, & Adeli, 2022; Wood et al., 2019; Zhu et al., 2013).

The controlled handling of small-scale research objects, like cells or bacteria, is an essential advantage of such systems. Figure 1.1 illustrates the relationship between the length scales of technical systems and typically investigated biological and chemical ob-

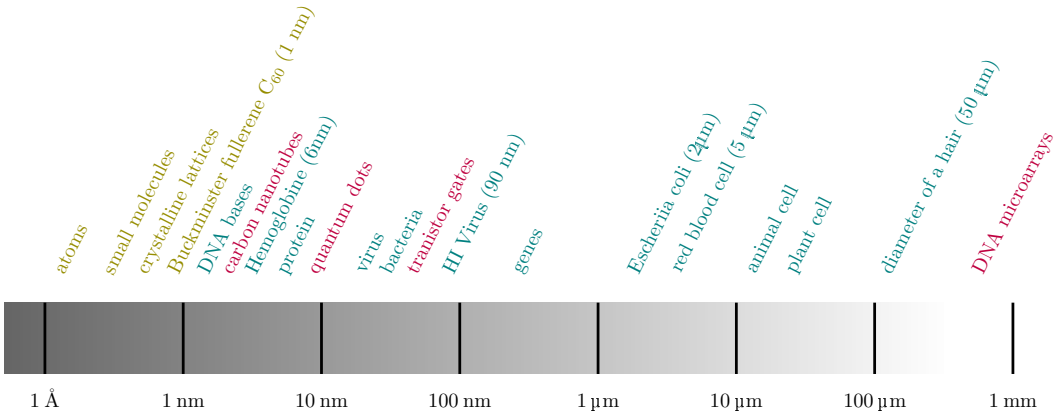

Figure 1.1: Scales of some important biological (teal), chemical (olive) and technical (purple) objects between 1 Å and 1 mm.

jects. Exploiting similar length scales, LOC systems are used in a number of important fields, such as DNA/RNA amplification and detection (Dhar & Lee, 2018; Keeble, Moser, Rodriguez-Manzano, & Georgiou, 2020), proteomics (Albala, 2001; Lazar, Gulakowski, & Lazar, 2020; Mouradian, 2002), cell biology (Fatanat Didar & Tabrizian, 2010; Gupta et al., 2010; Kovarik et al., 2012), and chemical research (Dittrich & Manz, 2006; Elvira, i Solvas, Wootton, & de Mello, 2013; Suryawanshi, Gumfekar, Bhanvase, Sonawane, & Pimplapure, 2018). The application field of single-cell-analysis is outstanding as the prerequisite for studying the mutation of cells and the development of cancer at cell level.

While most microfluidic systems rely on channel designs, the system central for this work exhibits a flat surface with embedded electrodes, which is covered by a carrier fluid. In small areas of the chip surface, a predefined flow field can be induced enabling transport, mixing, or separation of fluid probes inside the carrier fluid. This design has the potential to outclass classical channel-design systems with its flexibility, non-destructive sample handling, as well as its miniaturization and multiplexing opportunities. Multiplexing in this context means the parallel execution of multiple (analytical) processes. Miniaturization acts as an important step towards the handling of smaller objects than cells, such as complex molecules or proteins. Beneath other functions, proteins act as the means of communication between cells in biological organisms. The related field of research, proteomics, is dedicated to their understanding, the identification of biomarkers, and the development of new drugs.

Electrokinetics The benefits of the active-surface LOC system come with a number of technical challenges, which are particularly related to electric effects near the fluid-chip interface. The interplay between electrostatic and hydrodynamic effects is called electrokinetics. The complexity of the related phenomena originates from their multi-physical and

multi-scale nature. At microscale, the surface-to-volume ratio of the relevant control volumes becomes high. Thus, electric effects, often appearing as surface effects, are significantly more important than in macroscale problems. The majority of problems allows for the simplified treatment of these effects as boundary conditions, such as the Smoluchowski slip condition. In contrast, this work covers problems with a stronger coupling between electrostatic and hydrodynamic forces in the fluid volume. The dimensionless Debye length δ acts as a measure for how thin the area is where electrokinetic effects occur. For $\delta \ll 1$, electric effects are limited to a thin layer. In contrast, the electrokinetic problems discussed in this work have a dimensionless Debye length of order unity

$$\delta \sim O(1), \tag{1.1}$$

in common. For that reason, stronger nonlinearities occur, giving rise to phenomena that are not observed in the small-Debye-layer limit.

Figure 1.2 gives an overview on the most important electrokinetic phenomena in our LOC system. The actual chip (Fig. 1.2b), which we also refer to as Fluid Processing Unit (FPU), is the core element of the whole lab (Fig. 1.2a). Inside the chip, different phenomena occur that are crucial to sample transport and control. Three exmaples are presented in figures 1.2c-e. On the chip surface, carrier fluid is transported by electrokinetic forces (Fig. 1.2c). In the vicinity of the fluid-fluid interface between carrier fluid and sample, electrokinetic effects also occur (Fig. 1.2d) and are observed in form of shape changes, translational or rotational movement of the sample, i.e. electrodeformation, electromigration, and electrorotation. A third example is the additional drag of transported solid particles carrying a surface charge (Fig. 1.2e).

The electrokinetic transport of the carrier fluid (Fig. 1.2c) is induced by electrode arrays that are embedded in the wall. Although the largest electric effects occur near the electrodes, electric forces act in almost the whole volume of the fluid film. This can be explained by similar length scales of the electrode distance and the electric double layer which forms near the wall. As a result, the dimensionless Debye length δ is of $O(1)$. An understanding of the nonlinear physics is crucial for the optimization of the chip geometry, the electric excitation, and the choice of the carrier fluid. Additionally, heat dissipation by strong electric fluxes inside the fluid is critical for the chip and cooling design.

Within the carrier fluid, immiscible fluid probes can be transported (Fig. 1.2d). At the interface between the two fluid electrolyte phases, electric double layers form that affect electromigration and -deformation of the sample phase. Although these layers are small, i.e. $\delta \ll 1$, the mentioned phenomena cannot be explained without a detailed analysis of the Debye-layer electrokinetics.

Solid particles often carry a surface charge. As an effect, they do not follow the flow, but show an additional drag. The flow field around the particle is responsible for charge fluxes near the particle surface. Consequently, the charge distribution in the Debye layer is different from the equilibrium state. The composite electric field near the particle surface gives rise to an additional electric drag. Similarly to the two-phase problem, those drag

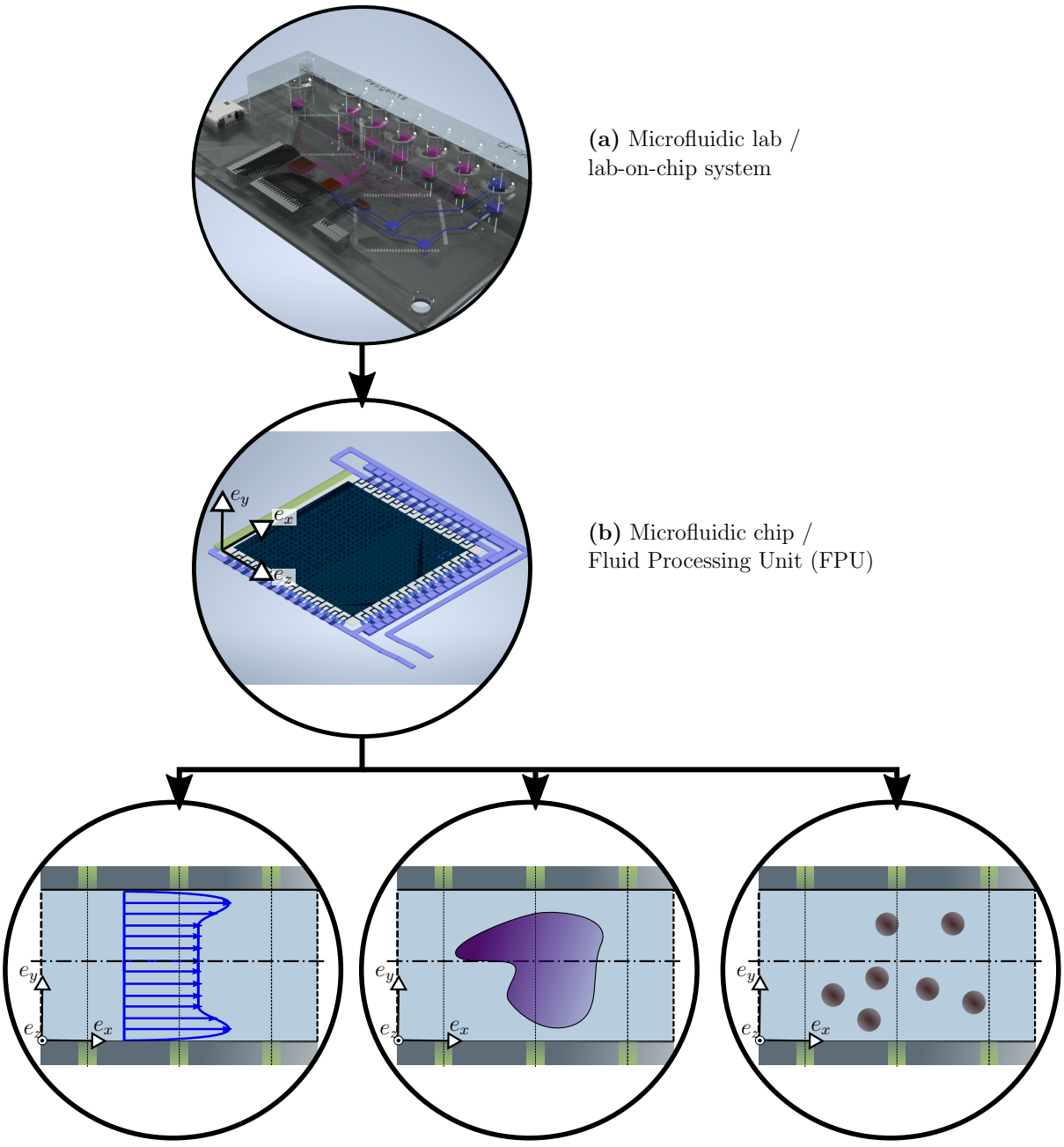

(a) Microfluidic lab / lab-on-chip system

(b) Microfluidic chip / Fluid Processing Unit (FPU)

(c) Carrier fluid pumping with traveling-wave electroosmosis

(d) Electrodeformation and electromigration of immiscible fluid samples

(e) Electric drag of solid particles by streaming potentials

Figure 1.2: Overview of electrokinetic phenomena in a lab-on-chip system that are discussed in this work.

effects can only be explained by a detailed analysis of the Debye layer as discussed in Marthaler and Class (2021a, 2021b, 2022c).

1.2 Historical background in life sciences and technical microsystems and their application in clinical diagnostics

1.2.1 Life sciences and technical microsystems

Milestones Life sciences are microscale. Milestones in this field since the 17th century include the discovery of the cell by Hooke, Allestry, and Martyn (1665), the synthesis of urea by Wöhler (1828) constituting the field of organic chemistry, and the breeding experiments by Mendel (1865) which were later connected to chromosomes as the hereditary material. In the first half of the 20th century important steps were made towards the understanding of the metabolism of living organisms (Krebs & Johnson, 1937; Lipmann, 1941) and the structure of DNA (Watson & Crick, 1953). Later, Sanger, Nicklen, and Coulson (1977) developed a gene sequencing technique and presented the first sequencing of an entire genome. In 1986, Mullis et al. developed the polymerase chain reaction technique for the amplification of DNA. Milestones in the 21st century include the publication of the complete human genome (Venter et al., 2001) and the first gene editing technique CRISPR (Jinek et al., 2012).

Connection to microfluidics As a result, many important branches developed, such as enzymology, virology, genetics, bacteriology, cytology, structural biology, synthetic biology, bioengineering, biomonitoring, genomics, pharmacology, and proteomics. The research objects of these fields range in their length scale between 10 µm for cells to 1 nm for proteins or DNA bases. Some important examples are displayed in Figure 1.1. Cells, bacteria, viruses, enzymes, and proteins, i.e. the subjects of the fields mentioned, can usually be found in a fluid environment. Microfluidic problems are different from macroscale fluid dynamics in crucial aspects, such as flow reversibility, surface tension, or the influence of electric forces. Mainly during the last century, a range of technical systems specifically adapted to these characteristics were developed.

Milestones in LOC systems The invention of the microscope made the early investigations of cells possible. Nevertheless, microscale science picked up in speed in the 20th century. The development of photo-lithography paved the way for the fabrication of electrical microsystems. Especially, integrated circuits and chips are produced with this method. The first LOC device was a miniaturized gas chromatograph designed by Terry, Jerman, and Angell (1979). The first microfluidic LOC was a high pressure liquid chromatograph developed by Manz, Graber, and Widmer (1990). Both of these devices were used for chemical analysis. The latter uses electroosmosis to transport the sample

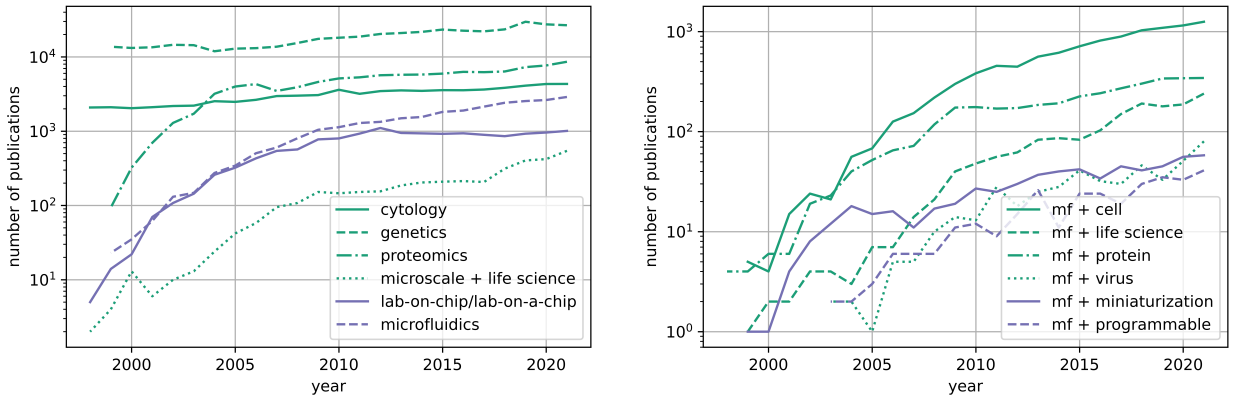

Figure 1.3: Publication statistics from Web of Science (`webofscience.com`) for different search terms. The term microfluidics is abbreviated with "mf".

inside the chip, capillary electrophoresis for separation and fluorescence detection. Applications for modern LOC devices analysing blood samples are the determination of gasses, electrolytes, and lactate. The detection of proteins or biomarkers is performed with immunoassays Hermsen, Roszek, van Drongelen, and Geertsma (2013).

Scientific relevance In a word, scientific progress in life sciences and innovation in technical microsystems go hand in hand. Without technical devices, the investigation of bio-chemical objects would not have been possible. At the same time, findings in life sciences drive technological progress. Figure 1.3 illustrates in two graphics the number of scientific publications for a selection of the fields mentioned. While a saturation point seems to be reached in some fields like cytology or LOC systems, combinations of these topics still show a growing research popularity. This is clearly not a formal proof of the importance of the field. Yet, is can act as an indicator for synergy effects between the technology and its application.

1.2.2 Application of LOC systems in diagnostic medicine

Market segmentation The medical sector is the main market for LOC systems (Hermsen et al., 2013). Point-of-care (POC) testing has several advantages to conventional laboratory testing, such as simplicity (the user does not need to be trained), low cost, speed (short turnaround time), and fabrication in large unit numbers (Sachdeva, Davis, & Saha, 2021). The market is segmented with respect to region, product type, or user type. The term *user type* defines the person performing the test and the circumstances under which the testing is done. POC testing can be performed by health-care professionals in laboratories, hospitals or the outpatient sector. However, equally important is POC testing by untrained individuals, either community-based or for at home testing. Important product types include glucose monitoring, cardiac markers, or testing for infectious diseases. Other examples are pregnancy tests or blood-gas testing (Sachdeva et al., 2021). Besides the application for POC testing, LOC systems can also be applied in agriculture, for food testing,

fertility, single cell analysis, or sequencing (Sachdeva et al., 2021). "Roche Diagnostics and Siemens Healthcare are tier I competitors that generate more than $5 Billion [in vitro diagnostics] revenues whereas companies such as Abbott, Danaher, Alere, Thermo Fisher, BioMérieux, Bio-Rad, Sysmex, Becton Dickinson, Bayer Healthcare, Werfen Group, Gen Probe generate $1–5 Billion revenues" (Sachdeva et al., 2021).

SARS-CoV-2 as a current example A prominent example illustrating the relevance of POC testing is the ongoing SARS-CoV-2 pandemic. As of August 2022, the SARS-CoV-2 was responsible for about 12 billion diagnosed cases of COVID-19 and 6.5 million total deaths (Center for Systems Science and Engineering (CSSE) at Johns Hopkins University (JHU), 2022). Large-scale testing is an essential part of monitoring and controlling the spread of the virus disease. Biomarkers are used to identify if the virus contained in a sample. In the case of SARS-CoV-2, genetic material in the form of DNA, RNA, or proteins, serves as biomarkers. These proteins can be found e.g. on the viral envelope. Another option are antibodies that are produced by the human body against the virus. The gold standard in clinical diagnostics are polymerase chain reaction (PCR) techniques using immunoassays. The process includes three main steps (Tymm, Zhou, Tadimety, Burklund, & Zhang, 2020):

- purification of the nucleic acids from the sample (by centrifugation or magnetic bead separation),
- amplification of relevant RNA sequences, and
- detection of the amplified RNA.

This time-expensive test needs to be performed by trained laboratory technicians using expensive equipment. Under these circumstances, LOC devices have several advantages. Automation of the clinical processes increase sensitivity, reproducibility and ease of use, while decreasing the necessary sample amount, the total-analytical time, and cost Tymm et al. (2020).

A programmable LOC device, as the one discussed in this work, can serve as bridging technology between manually performed testing, as described above, and the POC quick tests that everybody has been using for at-home testing during the last few years. Quick tests target antibodies making them less sensitive than the PCR testing described. With the presented design, automated PCR testing could be performed delivering a good trade-off between sensitivity, reproducibility and cost on one hand, and time-to-result on the other.

1.2.3 Trends in LOC development

The most important trends in the development of new LOC devices considers aspects like miniaturization, interfaces, and multiplexing (Hermsen et al., 2013). Miniaturization allows the reduction of sample volumes and can speed up the analytical processes, making the analysis more cost-effective. Another aspect of miniaturization is the targeting

of smaller objects, like cells. Single-cell analysis investigates metabolism and interactions of single cells expecting insights in e.g. cancer growth, drug development, or aging (Zenobi, 2013). We should note at this point that smaller length scales make traditional mechanical liquid pumping extremely inefficient as the resistance becomes large. Thus, flow excitation by electrokinetic methods is very popular in microfluidic devices. Electroosmotic pumping can be applied directly inside the device and makes liquid transport more controllable and effective.

Multiplexing allows for the simultaneous performance of different analytical processes on one single device. Traditionally, microfluidic systems are designed as single-purpose devices. Designs that are more flexible can reduce fabrication and development cost in research as well as investments in clinical or point-of-care situations. Even more crucial is that complex analytical processes are not possible without a design that can handle different samples and processes at the same time.

Interfaces between the microfluidic system and the outside world often are the source of contamination and thus of measurement errors. Optimization of the interface system to reduce technical issues is a large part of future LOC developments. Yet, the focus of this work and the presented design lies clearly on the multiplexing and miniaturization opportunities.

1.3 State of the art and aims of this study

1.3.1 Competitive systems and our design

Classification of electrokinetic actuators The core element of our design is the actuator as depicted in Figure 1.2c. Electrokinetic actuators working with arrangements of electrodes in a wall tangential to the desired flow direction have been discussed for the last few decades. Figure 1.4 gives an overview on a number of competitive actuator designs. These designs have in common that AC voltages are applied via a number of wall electrodes in order to produce a controlled flow. However, differences between these systems include their function (e.g. translational transport, rotational transport, mixing), the length scale, voltage, frequency, wall/channel geometry, and the materials used. We analyzed the data from six research articles and 13 patents that are summarized in the table, which belongs to Figure 1.4. In Figure 1.4, the actuators from these publications are arranged depending on their minimal length scale/electrode distance and their minimum voltage. The given length scale is used as a measure for how small the system can be built. Equivalently, the voltage defines what type of samples can be handled on the chip. The reason for that is that biological probes, especially cell membranes, can be damaged or destroyed by large electric fields. We note that some of these actuators (indicated in yellow) can only produce a flow in one direction (one-dimensional actuators) (Palmieri & Brianza, 2005; Schlautmann, Gardeniers, & Van den Berg, 2003; Tsuyoshi, Tsuyoshi, & Suguyama, 2009). As a result, it is not possible to simply integrate them into a two-dimensional chip surface.

When assessing actuator designs, we consider high pumping velocities and a homogeneous flow field as desirable. At the same time, the actuator architecture should be as simple as possible, featuring straightforward geometries and a small variety of materials. As an effect, downscaling possibilities are given. Eddies in the produced flow field are unwanted as they reduce the pumping velocity and can affect sample deformation.

Milestones in actuator design Three different design principles of electrokinetic actuators are compared in Figure 1.5. The first actuators that were intensively studied are designed with electrodes integrated into a flat wall (Loucaides et al., 2007; Ramos et al., 1999, 2005) (Figure 1.5a). The working principle is AC electroosmosis (ACEO), which includes but is not limited to traveling-wave electroosmosis (TWEO). AC voltages are applied via the wall electrodes attracting charges inside the fluid electrolyte. An electric double layer (EDL) is formed in direct vicinity to the wall. Superposition of those charge clouds with the electric field between the electrodes generates a Coulomb force acting on the fluid volume. We note that the EDL is sufficiently slim that the small-Debye-layer assumption holds. Numerical and experimental studies (e.g. Ramos et al. (2005)) showed that AC potentials in form of traveling waves are optimal for fluid pumping. Traveling waves provide a continuous reciprocal excitation with one preferential direction. One particularly important drawback, however, is the formation of eddies near the wall.

A variation of this idea was presented by Barz and Class (2007). Here an asymmetry is created by a multi-material surface (example in Figure 1.5a). Thus, a simpler AC voltage pattern can be applied to the electrodes. Those are arranged between dielectric substrate sections with different ζ-potentials. The combination of time-constant wall voltages at this dielectrics and time-varying voltages at the electrodes delivers an asymmetric electric excitation featuring one preferred direction. Obviously, sharp edges and a great number of surfaces with an angle to the intended flow direction produce a very inhomogeneous flow field. This class of actuators can only be used for the pumping of homogeneous liquids. Diffuse samples would be spread out and dissected, sensitive objects are possibly damaged.

In 2010, M. Z. Bazant et al. patented a similar actuator which mainly differed from the Ramos et al.-design by the geometry of the surface (Figure 1.5b). While in the Ramos-design all electrodes were at a leveled height, the more recent patent by M. Z. Bazant et al. (2010) showed stepped electrodes. As a result, between the electrodes, zones of controlled re-circulation are formed. Thus, the eddies affecting the main flow in the Ramos-design are confined in these zones where they are desired. Thus, the main flow stays nearly uniform. This setup however is more complex to manufacture, limiting miniaturization. Variations are depicted in the examples in Figure 1.5b.

A different class of actuators (not depicted in 1.5) exploits ACEO in combination with asymmetric geometries, as discussed by M. Z. Bazant and Squires (2004). The flow channels exhibit wall electrodes, just like in the designs discussed before. In this case however, the electrode surface and the wall form an angle. Thus one flow direction is preferred, even if only AC voltages are applied. Variations include rods with a triangular profile in

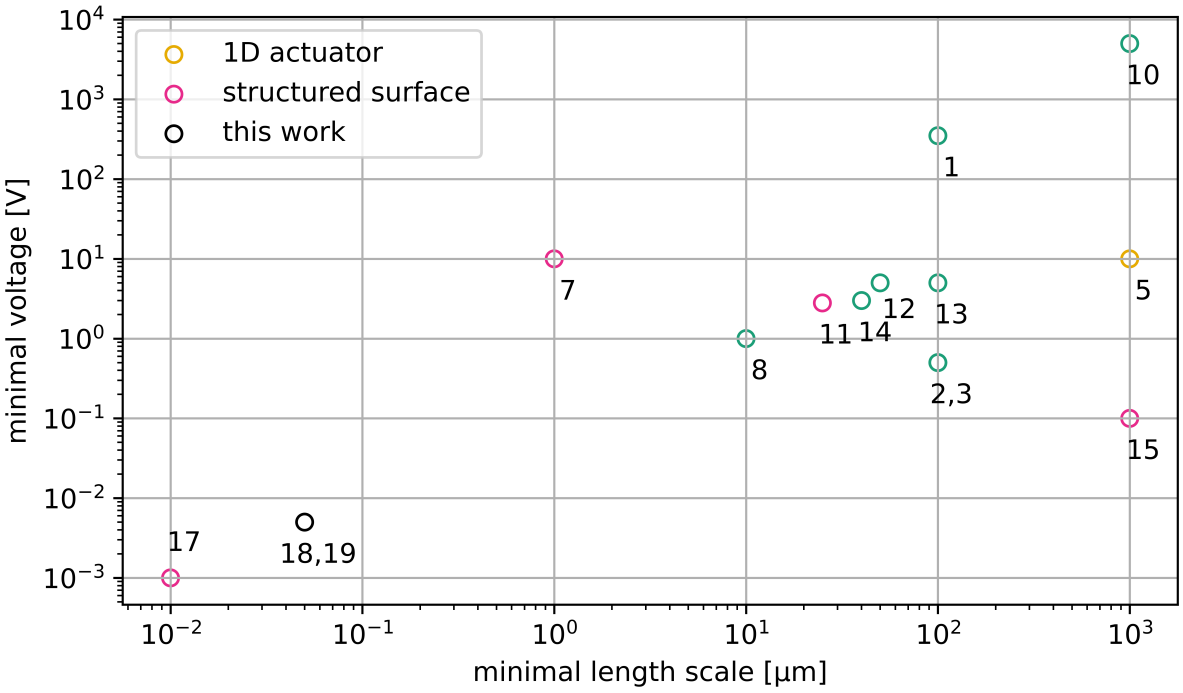

	publication	comments
1	Faigle (2020)	
2	Farzanehnia & Taheri (2019)	
3	Loucaides et al. (2007)	
4	Palmieri & Brianza (2005)	designed as 1D actuator
5	Tsuyoshi et al.)(2009)	designed as 1D actuator (not in diagram)
6	Schlautmann et al. (2003)	designed as 1D actuator (not in diagram)
7	Desai et al. (2001)	structured surface
8	Ledeboer (2009)	
9	Medoro et al. (2014)	
10	Sohn (2006)	
11	Huang et al. (2014)	stepped electrodes
12	Noh et al. (2012)	
13	Ramos et al. (1999)	
14	Ramos et al. (2005)	
15	Bazant et al. (2010)	stepped electrodes
16	Bazant & Prakash (2013)	
17	Barz & Class (2007)	multi-material surface
18	Marthaler & Class (2022a)	
19	Marthaler & Class (2022b)	

Figure 1.4: Product environment. 19 publications on similar actuators have been analyzed and arranged by the minimal voltage and electrode distance.

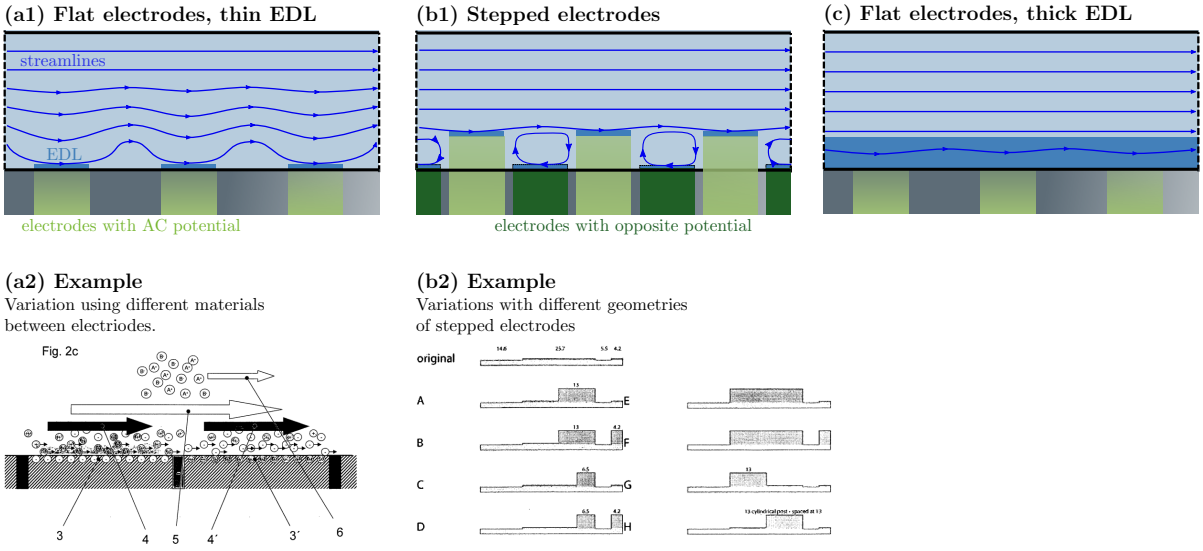

Figure 1.5: Comparison of actuator designs with examples. (a1) Design with flat electrodes and thin EDL as used by Ramos et al. (1999). (a2) An example with different substrate materials as suggested by Barz and Class (2007). (b1) Stepped electrode design also featuring thin EDLs. Recirculation zones are caged in the gaps between the electrodes. (b2) Design variations suggested by M. Z. Bazant and Squires (2004). (c) Design discussed in this study with thick EDLs.

the middle of a channel with flat walls. Although these systems are capable of pumping liquids, the formation of eddies cannot be avoided (Squires & Bazant, 2006).

Other publications discuss variations of the main designs discussed above and apply them e.g. to mixing (K.-R. Huang et al., 2014) or rotating flows (Ledeboer, 2009).

1.3.2 Our design

The thin-Debye-layer assumption vs. full electrokinetics Common to all the designs presented in section 1.3.1 is the thin-Debye-layer assumption $\delta \ll 1$. For a typical aqueous solution with millimolar charge concentrations the Debye layer thickness is $l_D^* \sim 10\,\mathrm{nm}$ and it becomes thicker for smaller concentrations. Predictions on the behavior of the competing actuators can only be made as long as the electrode distance is significantly larger than the Debye layer thickness. In these cases, the electric problem only influences the flow via a slip boundary condition. The flow field can be described as Stokes flow, which is simpler than full-electrokinetic flow.

In contrast, our actuator (1.5c) is designed to work in the full-electrokinetics regime $\delta \sim O(1)$ featuring the simple Ramos-architecture together with the homogeneous flow field of the Bazant-design. An important step towards this setup is the code presented in chapter 5. Using that code, predictions of the nonlinear full-electrokinetic behavior of electrolytic systems are possible. This new actuator design was published in the patent

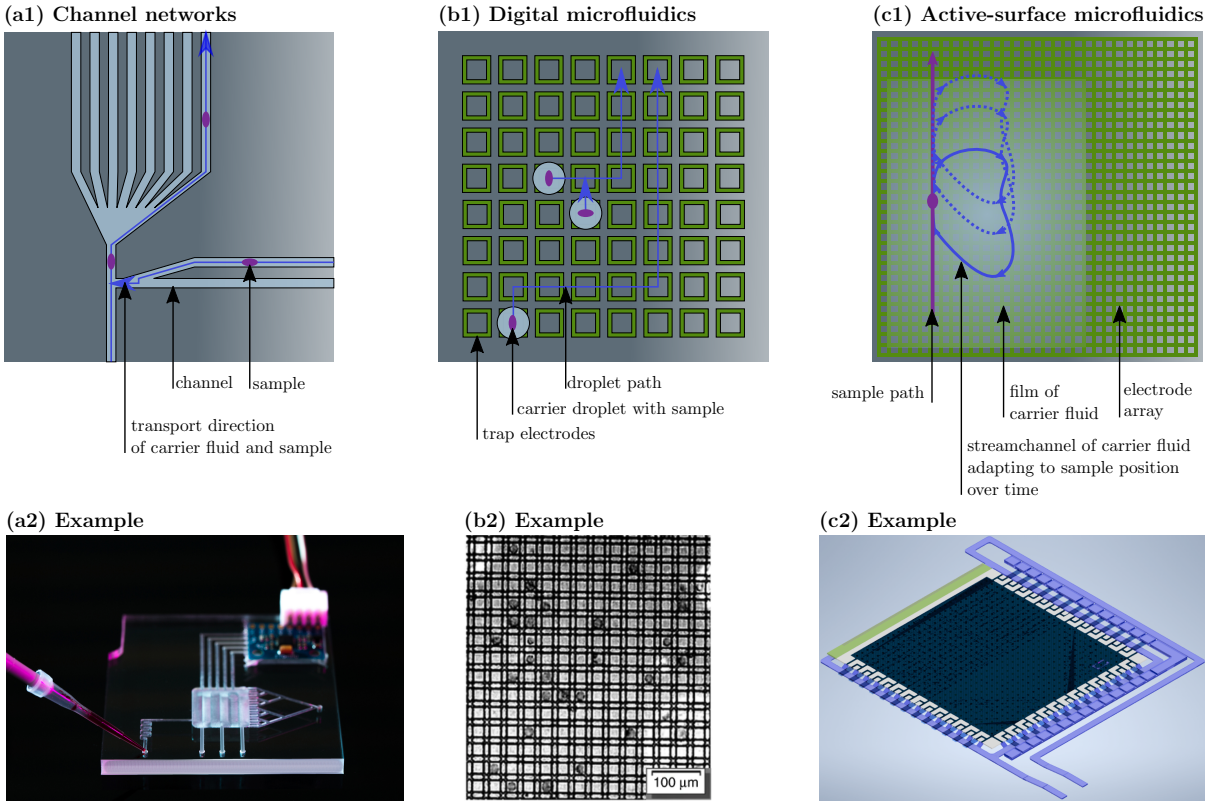

Figure 1.6: Comparison of two-dimensional array designs. Grey surface: substrate. Blue: carrier fluid / channels. Purple: Samples/sample paths. Green: electrodes.
(a1) Channel design, schematic representation. (a2) Example : iStock/luschen. (b1) Digital microfluidics, schematic representation. (b2) Example: Zhai et al. (2020), licensed for reuse and adaption (CC-BY `https://creativecommons.org/licenses/by/4.0/`). (c1) Active-surface microfluidics, schematic representation. (c2) Chip design discussed in this study, cp. Figure 1.7.

applications Marthaler and Class (2022a, 2022b) (publications 18 and 19 in Figure 1.4). Thus, the length scales can be of the order of the small layer thickness and electrode distances of several nanometers become possible. At the same time, lower voltages can be used, avoiding the destruction of biological samples by strong electric fields.

Remarks on two-dimensional arrays While the actuators discussed above enable one-directional fluid pumping, the functionality of LOC systems necessitates two-directional transport on the surface. Different design approaches are compared in Figure 1.6. Channel networks (Figure 1.6a) have predefined channel branches, junctions, and valves. Samples are transported in a carrier fluid along those channels. Pumping is performed with syringes or electrokinetic actuators. These systems are manufactured and optimized for a specific application with very limited variation options.

Two-dimensional arrays with caging electrodes are part of several designs published in

the last few decades. Designs featuring pulsed droplet transport between electrode cells are summarized using the term digital microfluidics (Figure 1.6b). Examples include the array for particle transportation and filtering by Desai et al. (2001) or the array design by Medoro et al. (2014) which consists of squared cage electrodes. In the latter array, fluid droplets are exchanged between the cages by pulsed transport. Although dielectrophoretic transport is possible, the applied working principle is electrowetting. It is not clear if in any of these two designs that a continuous sample transport is possible, which would be important to perform chromatographic analyses. Noh et al. (2012) published an active-matrix arrangement of thin-film transistors which works analogously to a TFT display. With that system, the number of control lines could be reduced, which is an important step towards system integration and minimization. A newer study exploring long-time drug testing via single-cell analysis with a digital-microfluids array was presented by Zhai et al. (2020).

A third class of two-dimensional arrangements can be seen as a combination of the two mentioned above (Figure 1.6c). The electrode array is completely covered by a film of carrier fluid. The carrier fluid is pumped in loops, i.e. closed flow paths to sustain continuity and avoid eddies. Samples can be transported by continuously adapting the respective carrier fluid loop as depicted in Figure 1.6c. Here, the blue line depicts the moving carrier fluid while the purple line illustrates the respective sample path. The patent by Barz and Class (2007) suggests a chess-board arrangement consisting of fields of different materials separated by electrodes and the fluid transport in the aforementioned loops. Our design (discussed in the next paragraph) and this setup can be summarized with the term active-surface microfluidics.

In our design, multiple actuators are connected to form a flat chip surface as illustrated in the 3D model 1.7. For that purpose, a set of synchronized actuators as the one in Figure D.3 form a pixel. All actuators inside one pixel are specified by the same flow direction. Several pixels are controlled by one adjacent control unit. The design with pixels and control units is displayed in the patent sketch D.6 and the CAD model 1.7. We denote the combination of the chip surface with the carrier fluid channel, data-connection, and fluid memory elements (FRAM) as a fluid processing unit (FPU). The FRAM is a set of small storage units for probes and reagents that can be accessed quickly. The TFT-matrix as presented by Noh et al. (2012) is applied in our design to connect the single control units.

With this section, we intend to put the chip design into the context of product design. While a feasibilty analysis for the actuator, discussed in section 1.3.2, is performed in this study, the three-dimensional flow is not verified and postponed to later investigations.

Aim of this study This study seeks to verify the presented actuator design by direct numerical simulation. When developing the product, it was unclear if high enough flow velocities could be reached and if the heat dissipation was low enough to be transported away by fan cooling. After verifying the functional principal, optimization of the actuator within the current technological limits is performed. Those limits include the minimum

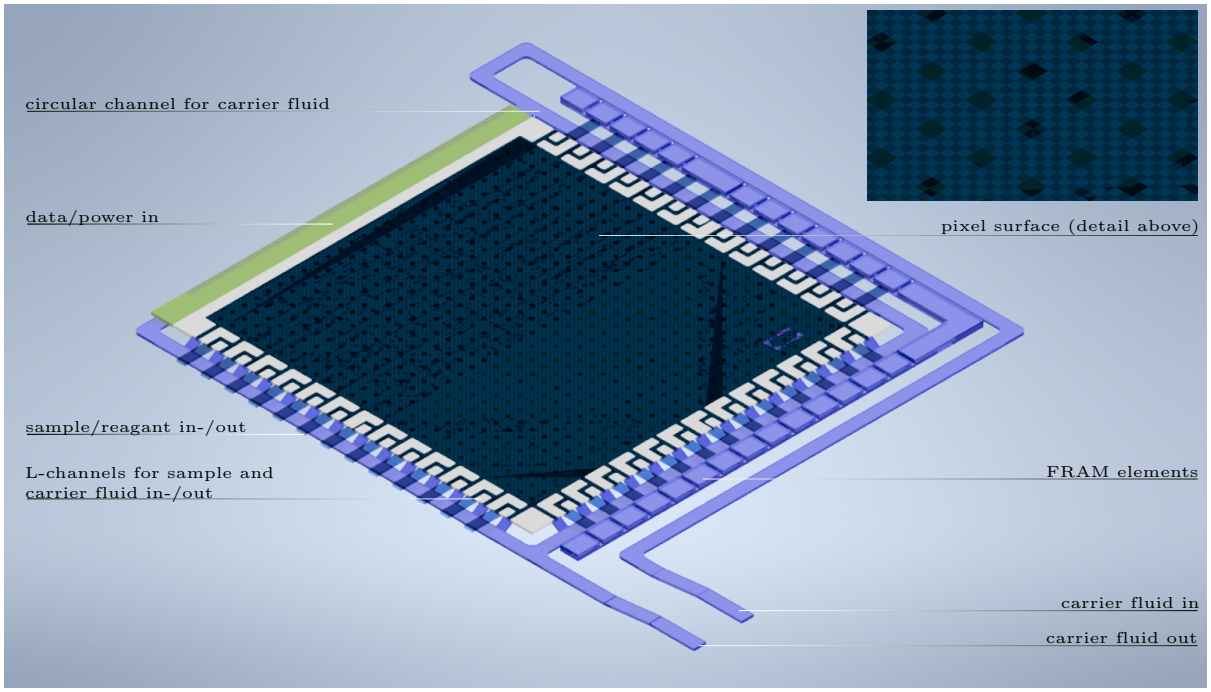

Figure 1.7: 3D model of the fluid processing unit (FPU) and detail view of the pixel surface. The second pixel surface which is arranged on top of the system is hidden. Thus, the lower surface, L-channels and FRAM are visible. Note that the black elements on the pixel surface are the control units as specified in Figure D.6.

electrode distance, maximum clock frequency, and price.

1.3.3 Landscape of two-phase EHD models

In addition to the feasibility study of the pumping mechanism, this work focuses on a second phenomenon – the behavior of an immiscible fluid drop under the influence of an electric field. Both phenomena are clearly coupled. For the sake of simplicity, we isolate them. Relevant terms for this toipic are electrolyte strength, electrodeformation, and electromigration. The strength of an electrolytic solution is determined by the percentage of salt that is dissociated. Sodium chloride dissociates nearly completely into its ions, such that its aqueous solution acts as a strong electrolyte. In contrast to that, water itself shows autodissociation into hydronium and hydroxyd ions. However, the ratio of this ion concentration with respect to the amount of water is very low, which is typical for a weak electrolyte. The term electrodeformation covers shape changes of fluid droplets under the influence of an electric field. A drop elongating in the field direction is called prolate. Contrarily, drops elongating in a field-normal direction are specified as oblate. Lastly, electromigration is defined as the movement of particles caused by an outer applied electric field.

Experiments The related experimental setup consists of a fluid particle suspended in a surrounding fluid, both exposed to an outer electric field. In experiments, electromigra-

tion was first discovered by Taylor (1966) and later also by Vizika and Saville (1992), but could not be explained by the models at that time. Electrodeformation could already be obeserved and explained by Taylor (1966). He derived a mathematical formulation that was able to predict if a spherical particle would take a prolate (long axis aligned with the electric field) or oblate (long axis perpendicular to the electric field) shape. However, in later experiments by Russel, Russel, Saville, and Schowalter (1991) a deformation behavior deviating from this condition was observed.

Models The current landscape of two EHD models addressing these phenomena is spanned by the publications of Mori and Young (2018); Schnitzer and Yariv (2015) and Ma, Booty, and Siegel (2022). These works have a detailed analysis of the Debye layer in common. In contrast to that, earlier approaches by Melcher and Taylor (1969) and Saville (1997) neglected the electrokinetics in the Debye layer near the interface. While the early publication by Melcher and Taylor (1969) defined the topic of electrohydrodynamics, Saville (1997) performed a dimensional analysis considering the dissociation and association of ions. In the last decade, the scientific discussion shifted towards the interface properties. It is still unclear if the electric properties of the fluid-fluid interface are correctly described by adsorption (Schnitzer & Yariv, 2015) or partition coefficients (Ma et al., 2022; Mori & Young, 2018), if there is charge permeability (Mori & Young, 2018; Schnitzer & Yariv, 2015), or transport of charges adhesive to the interface (Schnitzer & Yariv, 2015). Yet, Schnitzer and Yariv (2015) and Mori and Young (2018) predicted electromigration, and Ma et al. (2022) the deformation deviating from Taylor's condition.

Research gap and aim of this study It should be stressed that the mentioned modeling approaches are derived either for weak or strong electrolytes. Although these are two fundamentally different prerequisites, the underlying hypothesis is that a good model is valid beyond its assumptions. Yet, there has not been formal proof for that in electrohydrodynamic research. This work addresses the question of what influence electrolyte strength has on the model's predictions. To achieve this goal, the publication by Mori and Young (2018) is used as the main reference. They presented a weak-electrolyte model that was able to explain electromigration. In contrast, our study focuses on understanding electromigration in strong electrolytes. Although Schnitzer and Yariv (2015) predicted electromigration in a strong-electrolyte setting, their result is solely qualitative, lacking predictions on e.g. the migration velocity. By choosing a similar setup to both of the above studies, the purpose of this work is to outline under which conditions electromigration can be observed.

1.3.4 Aim and Hypothesis

In the section above, we have defined two individual aims for each, the actuator and the two-phase problem. Yet, the overarching goal of this work is to build a deeper understanding of the electrokinetic transport phenomena happening inside the LOC system. In

the next step, we want to extract the underlying principals of electrokinetic transport in order to achieve a more general understanding of this class of problems.

1.4 Methodology: Asymptotics and spectral simulations

The two research goals are tackled with suitable methods. The two-phase problem is examined by an asymptotic approach while the actuator is investigated by a numerical non-interpolating spectral method. This section delivers a short review on both methodologies with the used literature. A detailed discussion follows in the respective chapters 4 and 5.

1.4.1 Asymptotic analysis of the Debye layer

For investigations of the Debye-layer electrokinetics, an asymptotic approach is predestined. Here, we follow the foundational works by Hinch (1991) and Bender and Orszag (1999). The thin-Debye-layer limit in particular was investigated by a range of authors, such as Cox (1997); Dukhin, Derjaguin, and Matijevič (1974); Saville (1977); Schnitzer, Frankel, and Yariv (2012); Schnitzer and Yariv (2015, 2016); Yariv, Schnitzer, and Frankel (2011).

In accordance with these works, we rescale the interface-normal coordinate with the thickness of the small layer. As a result, the full resolution of the Debye-layer physics becomes possible. The inner Debye-layer problem and the outer bulk problem are solved independently and combined via asymptotic matching using Van Dyke's matching rule (Van Dyke, 1964).

As our problem consists of two phases, a Debye layer on each side of the fluid-fluid interface exists. They are coupled via interface boundary conditions. Each of the Debye-layer solutions is matched with the bulk of the suspending and drop phase respectively. Finally, we derive effective boundary conditions inheriting the complex Debye-layer physics. Together with the set of bulk equations, a macroscopic problem can be solved. The solution to the Stokes equation for the flow and the Laplace equation for the electric field is well-known (Leal, 2007; Taylor, 1966). The general solution can be adapted to the effective boundary conditions derived earlier to find the resulting flow field, surface deformation, and the migration velocity of the drop.

1.4.2 The non-interpolating spectral method for the actuator simulation

This study is a first approach to understand the discussed setup and to act as a benchmark for later approaches. The choice for a spectral method to simulate the electrohydrodynamic flow in the actuator was made for that reason. Near the electrode wall, strong gradients in the flow and electric field, as well as small eddies, are observed. In order

to capture these effects, a high-accuracy simulation is necessary. The smooth laminar flow results suggest that a simpler code could be used to speed up the simulation in later studies. As a by-product, a high-accuracy spectral module was developed. It is capable of solving a variety of simulation problems. One current example is the simulation of stratification phenomena in a lead-cooled fast reactor (Liu, Marthaler, Class, & Gu, 2023).

The spectral module uses a non-interpolating collocation method (Boyd, 2000) and was constructed based on the descriptions by Canuto (1988). Using that module, the differential equations are solved in spectral space and only transformed back to their physical equivalent when needed. In our two-dimensional experimental setting, Fourier modes were used for the periodic direction, and Chebyshev modes for the wall-normal direction. Essential references in this context are the books by Boyd (2000) and Peyret (2002). Canuto (2006, 2007) include important updates and corrections to Canuto's earlier book. The investigations by Srinivas and Fletcher (1992) and Thirumalai and Seshadri (2019) validate the accuracy of spectral collocation methods in the context of electrohydrodynamic problems. However, those are examples of the very limited amount of publications on the combination of spectral methods and EHD flow.

One crucial step during the solution of the differential equations in spectral space is the application of boundary conditions with the Lanczos method (Lanczos, 1964). The nonlinear no-flux boundary conditions at the wall were taken into account using an influence matrix method (Peyret, 2002). The iterative scheme to solve the electric problem for charge transport and electric potential, was adapted from semiconductor simulations. It is named Gummel's scheme or Gummel's iteration (Gummel, 1964). For the time-integration of the fourth-order differential equation governing the streamfunction, a composite backwards differentiation formula of second order (C-BDF2) was used. This approach has been developed for the investigation cardiac dynamics by Ying (2005) and Ying, Rose, and Henriquez (2008).

Those numerical schemes are combined to a spectral code capable of predicting the electrokinetic flow in the actuator and the produced heat dissipation. Together with an evolutionary algorithm, the actuator is optimized. The "differential_evolution" routine in the scipy library serves this purpose.

1.5 Outline of the thesis

In order to reach the aim specified in section 1.3 we first discuss terminology and the basic phenomena in chapter 2. An overview on EHD modeling approaches is given in chapter 3. Chapter 4 follows, where electromigration of a drop is investigated using a strong-electrolyte fluid-fluid model. In chapter 5, the second problem of electrokinetic transport, the electrokinetic actuator, is addressed. The results are used in chapter 6 to discuss product development, design limitations, and optimization of the actuator. The final chapter, 7, summarizes the conclusions on electrokinetic transport drawn before, and adds some generalizing remarks. Further steps in the chip development are outlined.

CHAPTER 2

Electric effects in fluid mechanics

Microscale fluid mechanics differs from macroscale physics by a range of effects, such as Stokesian motion, electrohydrodynamic, and capillary phenomena. The research in this field has evolved from understanding the fluid motion of low-Reynolds-number flow in the 18th century, to the investigation of the non-linear, multi-scale, and multi-physical behavior of electrolytic solutions in arbitrary geometries. The present chapter gives an overview on the terminology and the fundamental phenomena, with some historical remarks.

2.1 Terminology

It is indispensable to clarify some of the terms that will be used throughout this manuscript. In some cases they are not used consistently in the literature, especially since different research branches used different terms to describe similar phenomena. Table 2.1 summarizes the most important terminology. Here, we follow the definitions by Lyklema (1991).

The term electrohydrodynamics is used to describe hydrodynamics with additional electric force effects in electrolytes. Although the term includes 'hydro', the materials in this research field are general fluid electrolytes, i.e. fluids which contain dissolved charged particles/ions. Those include a large number of electrolytes, ranging from auto-dissociating liquids (e.g. water) containing very small amounts of ions, to liquid solutions of salt that can dissociate nearly completely (e.g sodium chloride). We describe the electrolytes depending on the percentage of dissociated ions relative to the original substance either as 'weak' or 'strong' electrolytes. The term 'leaky dielectrics', which is frequently used in the literature, is less tangible and refers to liquids that feature dielectric properties and contain dissolved ions.

In the following chapters, we will notice the existence of a large number of cases in which the coupling between electric and hydrodynamic effects can be assumed to be one-directional, i.e. electric effects influence the fluid behavior while the fluid flow has no effect on the electric field. This is referred to as electroosmosis. In contrast, electric potentials and currents originating from fluid motion are called streaming currents or streaming

field	
electrohydrodynamics (EHD)	hydrodynamics with electrical force effects
electrokinetics (EK)	EHD with strong bidirectional coupling of flow and electric field
phenomena	
electromigration/-phoresis	particle motion caused by an electric field
electroosmosis	liquid motion caused by an electric field
streaming current	electric current caused by fluid flow near charged walls
streaming potential	potential difference caused by fluid flow near charged walls
sedimentation potential	streaming potential due to sedimentation of a charged particle
diffusiophoresis	particle motion caused by a concentration gradient
diffusioosmosis	liquid motion caused by concentration gradient

Table 2.1: Terminology used throughout this manuscript for electrohydrodynamic phenomena (adapted from Lyklema (1991)).

potentials.

The transport of charged particles that are dissolved in the fluid can lead to local polarization of the fluid, and thus also affect the electric field. To emphasize the strong bidirectional coupling in some problems we will call them 'electrokinetic' or even 'full electrokinetic'.

2.2 Important electrohydrodynamic effects

This section briefly summarizes important basic electrokinetic problems. Examples are the definition of electromobility and conductivity, or creeping flow. After that, more advanced effects are discussed. They typically originate from combinations of the basic phenomena. One example is the formation of an electric double layer as a result of diffusive and electric forces.

2.2.1 Fick's law of diffusion

Particle motion is often driven by electric effects. Yet, concentration gradients also affect particles to move, independent of their charge. This can in general be described by a relation that was named after the German physician Adolf Fick (1829–1901). Fick's 1st law in a one-dimensional frame of reference,

$$j^*_{\text{diff}} = -D^* \frac{\partial c^*}{\partial x^*}, \tag{2.1}$$

relates the diffusive flux j^*_{diff} of a particle species with the local concentration c^* to the spatial concentration gradient multiplied by the diffusion coefficient D^*. The unit of the ion concentration is $[c^*] = \text{m}^{-3}$ and it can be transformed to the molar ion concentration n^* by multiplication with the Avogadro number $n^* = c^* \text{N}^*_\text{A}$. Throughout this manuscript, parameters with units are denoted with an asterisk superscript while all symbols without that superscript are dimensionless.

2.2.2 Stokes flow

Electrokinetic effects become important at small length scales. The related flow fields are ususally characterized by small Reynolds numbers. Sir George Gabriel Stokes (1819–1903) first discussed the behavior of viscous fluids in his publication *On the effect of the internal friction of fluids on the motion of pendulums* (Stokes, 1850). The simplest form of the Stokes equation reads

$$0 = -\nabla^* p^* + \eta^* {\nabla^*}^2 \vec{v}^*. \tag{2.2}$$

In this equation, p^* is the sum of static and osmotic pressures, η^* the dynamic viscosity and $\vec{v}^*$ the hydrodynamic velocity. We note that in the absence of electrochemical effects the pressure in the momentum equation only includes the static part. Following Stokes we can introduce the Reynolds number as relation between inertia and viscous forces $\text{Re} = \frac{\rho^* v^*_\text{ref} l^*_\text{ref}}{\eta^*}$ with the fluid density ρ^*, the reference velocity v^*_ref, reference length l^*_ref, and reference time $t^*_\text{ref} = \frac{l^*_\text{ref}}{v^*_\text{ref}}$. Thus, the momentum equation for incompressible Newtonian fluids in the absence of volume forces is

$$\text{Re}\left(\frac{\partial \vec{v}}{\partial t} + \vec{v} \cdot \nabla \vec{v}\right) = -\nabla p + \nabla^2 \vec{v}. \tag{2.3}$$

The material derivative on the left hand side can be neglected when the Reynolds number becomes small, which is the case for experimental settings where velocities or length scales are small, or the kinematic viscosity is large. Microfluidics is certainly the most important field of application in which low-Reynolds-number flow (alternatively "Stokes flow", "viscous flow" or "creeping flow") appears. Yet, the fabrication of highly viscous substances like certain polymers or silicon oils also relies on creeping flow.

2.2.3 The relation of diffusion, mobility, and conductivity in fluid electrolytes

In their works on Brownian motion, Albert Einstein (1879–1955) and Marian Smoluchowski (1872–1917) discussed the drag on translating particles that are subject to external forces. They defined the friction coefficient as the ratio of the applied force f^*_applied and the drift velocity v^*_drift of the particle

$$\eta^*_\text{fric} = \frac{f^*_\text{applied}}{v^*_\text{drift}}. \tag{2.4}$$

The resulting flux of concentration c^* is $j^*_{\text{applied}} = c^* v^*_{\text{drift}}$. In steady state, this flux is balanced by diffusion delivering the ordinary differential equation (ODE)

$$0 = -D^* \frac{\partial c^*}{\partial x^*} + c^* \frac{f^*_{\text{applied}}}{\eta^*_{\text{fric}}}. \tag{2.5}$$

The solution to the boundary value problem (BVP) with $c^*(x = 0) = c^*_0$ is

$$c^* = c^*_0 \exp\left(-\frac{w^*}{\eta^*_{\text{fric}} D^*}\right) \tag{2.6}$$

with the reversible work $w^*(x) = -\int f^*_{\text{applied}}(x)dx$ of the external force. Following Boltzmann's law, this relation has to be equal to $c^*_0 \exp\left(-\frac{w^*}{k^*_{\text{B}} T^*_{\text{a}}}\right)$. Thus, we get the diffusion coefficient

$$D^* = \frac{k^*_{\text{B}} T^*_{\text{a}}}{\eta^*_{\text{fric}}} = \eta^*_{\text{mob}} k^*_{\text{B}} T^*_{\text{a}}. \tag{2.7}$$

Note that the mobility coefficient η^*_{mob} is introduced as the inverse of the friction coefficient. The parameters k^*_{B} and T^*_{a} are the Boltzmann constant and the ambient temperature respectively. There are three special cases of this law that we are particularly interested in, the electric mobility of ions, the drag of an uncharged spherical particle, and the conductivity of an electrolytic solution, respectively.

By choosing the external force in the above one-dimensional example as the Coulomb force, we find the respective mobility coefficient called electric mobility μ^*. It is defined by the so-called Einstein-Smoluchowski relation

$$\mu^* = \frac{D^* \mathcal{Z} e^*_0}{k^*_{\text{B}} T^*_{\text{a}}} = \frac{D^*}{\phi^*_{\text{th}}} \tag{2.8}$$

of an electrically charged particle with the valence $\mathcal{Z}$. Here, e^*_0 describes the charge of a proton and we introduce the thermal potential as

$$\phi^*_{\text{th}} = \frac{k^*_{\text{B}} T^*_{\text{a}}}{\mathcal{Z} e^*_0} = \frac{\text{R}^* T^*_{\text{a}}}{\mathcal{Z} \text{Fa}^*}. \tag{2.9}$$

The alternative definition of the thermal potential includes the gas constant, which is defined as product of the Avogadro number and the Boltzmann constant $\text{R}^* = \text{N}^*_{\text{A}} k^*_{\text{B}}$ and the Faraday constant, which is the product of Avogadro number and the elementary charge $\text{Fa}^* = \text{N}^*_{\text{A}} e^*_0$.

Stokes' work includes the analysis of the drag exerted on a translating spherical particle with radius l^*_{ref} in a fluid with dynamic viscosity η^*. For low Reynolds numbers, the friction coefficient is $\eta^*_{\text{fric}} = 6\pi\eta^* l^*_{\text{ref}}$. Using relation 2.7, one can find the diffusion coefficient of a spherical particle

$$D^* = \frac{k^*_{\text{B}} T^*_{\text{a}}}{6\pi\eta^* l^*_{\text{ref}}}. \tag{2.10}$$

This equation is known as the Stokes-Einstein relation.

An important property of a fluid electrolyte is its conductivity. In EHD problems, the mobility of ions and varying concentrations lead to conductivities that change in space and time. In order to find the conductivity of an electrolytic solution we need the equivalent conductivities of each ion

$$\varsigma_i^* = e_0^* \mathcal{Z}_i c_i^* \mu_i^* \tag{2.11}$$

which has the unit $[\varsigma^*] = \mathrm{S\,m^{-1}} = (\Omega\,\mathrm{m})^{-1}$. In this work, we use the local electrolytic conductivity ς^* which results as the sum of the conductivities of the single ions

$$\varsigma^* = \sum_i \varsigma_i^* = e_0^* \sum_i \mathcal{Z}_i c_i^* \mu_i^*. \tag{2.12}$$

An important example in this context is a dilute electrolyte problem characterized by the dissociation equilibrium

$$\mathcal{S} \rightleftharpoons \mathcal{C}_+ + \mathcal{C}_-. \tag{2.13}$$

The equivalent local conductivity resulting from the concentration of the dissociated ions $\mathcal{C}_+$ and $\mathcal{C}_-$ is

$$\varsigma^* = e_0^* \left(\mathcal{Z}_+ c_+^* \mu_+^* + \mathcal{Z}_- c_-^* \mu_-^* \right). \tag{2.14}$$

where $\mathcal{Z}_\pm = 1$. Using the definition of the ion mobility in eq. 2.8, we find

$$\varsigma^* = \frac{e_0^{*2}}{k_\mathrm{B}^* T_\mathrm{a}^*} \left(\mathcal{Z}_+^2 c_+^* D_+^* + \mathcal{Z}_-^2 c_-^* D_-^* \right). \tag{2.15}$$

In cases where the molar conductivity is of interest this can be found by multiplication with the Avogadro number

$$\varsigma_\mathrm{mol}^* = \frac{e_0^{*2} \mathrm{N_A^*}}{k_\mathrm{B}^* T_\mathrm{a}^*} \left(\mathcal{Z}_+^2 c_+^* D_+^* + \mathcal{Z}_-^2 c_-^* D_-^* \right) = \frac{\mathrm{Fa}^{*2}}{\mathrm{R}^* T_\mathrm{a}^*} \left(\mathcal{Z}_+^2 c_+^* D_+^* + \mathcal{Z}_-^2 c_-^* D_-^* \right). \tag{2.16}$$

This relation was derived by Albert Einstein and Walther Nernst (1864–1941) and is thus called the Nernst-Einstein relation.

2.2.4 Structure of the electric double layer: The Gouy-Chapman solution and the Debye-Hückel approximation

The emergence of an electric double layer near a solid charged wall has been described independently by Gouy (1911) and Chapman (1913). We follow their investigation by considering a one-dimensional problem. The semi-infinite fluid domain is on one boundary limited by a solid wall with given ζ-potential $\zeta^* > 0$. The electric double layer results from an equilibrium between the electrophoretic and diffusive forces acting on the dissolved electric charges. The problem is fully described by the balance relation for the two ion species $c_\pm^*$ of a binary electrolyte

$$0 = \partial_x^* \left(-D^* \partial_x^* c_\pm^* \mp \mu^* c_\pm^* \partial_x^* \phi^* \right) \tag{2.17}$$

and the Poisson equation for the electric potential ϕ^*

$$\epsilon\epsilon_0^*\partial_{xx}^*\phi^* = -e_0^*\mathcal{Z}\left(c_+^* - c_-^*\right). \tag{2.18}$$

Here, ϵ and ϵ_0^* denote the relative and vacuum permittivity respectively. Without loss of generality, we assume the ion diffusivities D^*, ion mobilities μ^* and valences $\mathcal{Z}$ to be equal for both ion species. The respective boundary conditions at the wall read

$$\begin{aligned} 0 &= -D^*\partial_x^* c_\pm^* \mp \mu^* c_\pm^* \partial_x^*\phi^*\Big|_{x^*=0}, \\ \zeta^* + \phi_\infty^* &= \phi^*\Big|_{x^*=0}. \end{aligned} \tag{2.19}$$

The first is a no-flux condition representing the impermeability of the wall for ions. The potential at the wall is the ζ-potential of the wall superimposed with an outer applied far-field potential ϕ_∞^*. Far away from the wall another set of three relations holds

$$\begin{aligned} \lim_{x^*\to\infty} c_\pm^* &= c_\infty^*, \\ \lim_{x^*\to\infty} \phi^* &= \phi_\infty^*. \end{aligned} \tag{2.20}$$

Using the no-flux condition, we can integrate relation 2.17 with respect to x^* to find

$$0 = -D^*\partial_x^* c_\pm^* \mp \mu^* c_\pm^* \partial_x^*\phi^*. \tag{2.21}$$

This equation can be solved together with the far-field conditions. We obtain for the charge distributions

$$c_\pm^* = c_\infty^* \exp\left(\mp\frac{\mu^*}{D^*}\psi^*\right), \tag{2.22}$$

with the excess potential ψ^* that we define as

$$\psi^* := \phi^* - \phi_\infty^*. \tag{2.23}$$

Plugging this into the Poisson equation delivers

$$\frac{\epsilon\epsilon_0^*}{2e_0^*\mathcal{Z}}\partial_{xx}^*\psi^* = c_\infty^* \sinh\left(\frac{\mu^*}{D^*}\psi^*\right). \tag{2.24}$$

Multiplication with $\psi^{*\prime} = \partial_x^*\psi^*$ gives

$$\begin{aligned} \frac{\epsilon\epsilon_0^*}{2e_0^*\mathcal{Z}c_\infty^*}\left(\frac{1}{2}\psi^{*\prime 2}\right)' &= \psi^{*\prime}\sinh\left(\frac{\mu^*}{D^*}\psi^*\right) \\ \frac{\epsilon\epsilon_0^*}{2e_0^*\mathcal{Z}c_\infty^*}\int\left(\frac{1}{2}\psi^{*\prime 2}\right)' \mathrm{d}x^* &= \int \sinh\left(\frac{\mu^*}{D^*}\psi^*\right)\mathrm{d}\psi^* \\ \frac{\epsilon\epsilon_0^*\mu^*}{2e_0^*\mathcal{Z}c_\infty^*D^*}\frac{1}{2}\psi^{*\prime 2} &= \cosh\left(\frac{\mu^*}{D^*}\psi^*\right) + k. \end{aligned} \tag{2.25}$$

Far away from the wall, for large x^*, both ψ^* and $\psi^{*\prime}$ vanish. We thus find $k = -1$ and

$$\begin{aligned}\sqrt{\frac{\epsilon\epsilon_0^*\mu^*}{4e_0^*\mathcal{Z}c_\infty^*D^*}}\psi^{*\prime} &= \pm\sqrt{\cosh\left(\frac{\mu^*}{D^*}\psi^*\right)-1} = \pm\sqrt{2}\sqrt{\frac{1}{2}\left(\cosh\left(\frac{\mu^*}{D^*}\psi^*\right)-1\right)} \\ &= \pm\sqrt{2}\sinh\left(\frac{\mu^*}{D^*}\frac{\psi^*}{2}\right).\end{aligned} \tag{2.26}$$

As we assumed the potential $\zeta^* > 0$, the potential in the elecrtolyte decays, i.e. $\psi^{*\prime} < 0$. Multiplying both sides with $\sqrt{2}$, we find

$$\sqrt{\frac{\epsilon\epsilon_0^*\mu^*}{2e_0^*\mathcal{Z}c_\infty^*D^*}}\psi^{*\prime} = -2\sinh\left(\frac{\mu^*}{D^*}\frac{\psi^*}{2}\right). \tag{2.27}$$

Another separation step delivers

$$\begin{aligned}\int\left(-2\sinh\left(\frac{\mu^*}{D^*}\frac{\psi^*}{2}\right)\right)^{-1}\mathrm{d}\psi^* &= \left(\frac{\epsilon\epsilon_0^*\mu^*}{2e_0^*\mathcal{Z}c_\infty^*D^*}\right)^{-\frac{1}{2}}\int\mathrm{d}x^*, \\ -\frac{D^*}{\mu^*}\ln\tanh\left(\frac{\mu^*}{D^*}\frac{\psi^*}{4}\right) &= \left(\frac{\epsilon\epsilon_0^*\mu^*}{2e_0^*\mathcal{Z}c_\infty^*D^*}\right)^{-\frac{1}{2}}x^* + k \\ \tanh\left(\frac{\mu^*}{D^*}\frac{\psi^*}{4}\right) &= \tilde{k}\exp\left(-\left(\frac{\epsilon\epsilon_0^*D^*}{2e_0^*\mathcal{Z}c_\infty^*\mu^*}\right)^{-\frac{1}{2}}x^*\right).\end{aligned} \tag{2.28}$$

At the wall, for $x^* = 0$ the excess potential takes the value $\psi^* = \zeta^*$ which defines the integration constant.

$$\tanh\left(\frac{\mu^*}{D^*}\frac{\psi^*}{4}\right) = \tanh\left(\frac{\mu^*}{D^*}\frac{\zeta^*}{4}\right)\exp\left(-\left(\frac{\epsilon\epsilon_0^*D^*}{2e_0^*\mathcal{Z}c_\infty^*\mu^*}\right)^{-\frac{1}{2}}x^*\right). \tag{2.29}$$

We can solve this for the excess potential and find

$$\psi^* = 2\phi_{\mathrm{th}}^*\ln\frac{1+\tanh\left(\frac{1}{4}\frac{\zeta^*}{\phi_{\mathrm{th}}^*}\right)\exp\frac{-x^*}{l_{\mathrm{D}}^*}}{1-\tanh\left(\frac{1}{4}\frac{\zeta^*}{\phi_{\mathrm{th}}^*}\right)\exp\frac{-x^*}{l_{\mathrm{D}}^*}}, \tag{2.30}$$

where we have used the thermal potential as introduced in equation 2.8. We further define the Debye length as

$$l_{\mathrm{D}}^* = \sqrt{\frac{\epsilon\epsilon_0^*D^*}{2e_0^*\mathcal{Z}c_\infty^*\mu^*}} = \sqrt{\frac{\epsilon\epsilon_0^*\phi_{\mathrm{th}}^*}{2e_0^*\mathcal{Z}c_\infty^*}} \tag{2.31}$$

which acts as a scale for the thickness of the electric double layer that emerges near the wall. Yet, there is no sharp edge of this layer. Indeed, the length l_{D}^* is the length measured from the wall by which the potential has decayed by the factor of the Euler number e. This can be illustrated by expanding the so-called Gouy-Chapman solution 2.30 in a Taylor series for small ζ-potentials. The first coefficient of this series reads

$$\psi^* = \zeta^* e^{-\frac{x^*}{l_{\mathrm{D}}^*}} + O(\zeta^{*3}). \tag{2.32}$$

This last formulation is the so-called Debye-Hückel approximation for $\zeta^* \ll 1$.

2.2.5 Electrokinetics as boundary effects: The Smoluchowski slip condition

The Smoluchowski slip condition is a simplification often used in EHD problems. It replaces the complex electrokinetics inside the three-dimensional double layer by a boundary condition. A surface charge with a superimposed electric field give rise to strong shear stresses inside the double layer. Thus, it seems like the boundary is moving with a speed known as the Smoluchowski slip. The associated boundary condition is called Smoluchowski slip condition.

We derive this condition for a minimal two-dimensional example. For that purpose, we assume a fluid domain that is on one side at $x = 0$ limited by a stationary wall with a surface charge that is equivalent to a ζ-potential denoted by ζ^*. We assume the domain semi-infinite in x-direction so that all gradients disappear for $x \to \infty$. We further assume that a constant external electric field $\vec{E}^*$ is applied in the y-direction tangential to the wall. The fluid flow is assumed to be uniform in y-direction so that the tangential velocity $v_y(x)$ does not depend on the coordinate y. The fluid flow and the electric field are governed by the momentum equation in tangential direction and the Poisson equation respectively

$$\begin{aligned} 0 &= -\partial_y^* p^* + \eta^* \left(\partial_{xx}^* + \partial_{yy}^*\right) v_y^* - q^* \partial_y^* \phi^*, \\ 0 &= \epsilon_0^* \epsilon \left(\partial_{xx}^* + \partial_{yy}^*\right) \phi^* + q^*. \end{aligned} \tag{2.33}$$

Here, q^* denotes the charge density which is for the a binary electrolyte defined as $q^* = c_+^* - c_-^*$. As mentioned, our assumptions include the flow field to be constant in y-direction, i.e. $\partial_y^* v_y^* = \partial_y^* p^* = 0$. As the electric field is constant in this direction, the 2nd derivative of the potential also vanishes $\partial_{yy}^* \phi^* = 0$ and we call the constant first derivative $\partial_y^* \phi^* := -E_y^*$. The two equations simplify to

$$\begin{aligned} 0 &= \eta^* \partial_{xx}^* v_y^* + q^* E_y^*, \\ 0 &= \epsilon_0^* \epsilon \partial_{xx}^* \phi^* + q^*. \end{aligned} \tag{2.34}$$

Combining the two delivers an equation for the velocity field

$$0 = \eta^* \partial_{xx}^* v_y^* - \epsilon_0^* \epsilon \partial_{xx}^* \phi^* E_y^*. \tag{2.35}$$

Using the Gouy-Chapman solution of the double layer with the definition of the excess potential ψ^*, we find

$$v_y^* = \frac{\epsilon_0^* \epsilon}{\eta^*} \psi^* E_y^* + A x^* + B. \tag{2.36}$$

With the boundary conditions

$$\begin{aligned} \lim_{x \to 0} v_y^* = 0, \quad \lim_{x \to 0} \psi^* = \zeta, \\ \lim_{x \to \infty} \partial_x^* v_y^* = 0, \quad \lim_{x \to \infty} \psi^* = 0, \end{aligned} \tag{2.37}$$

we find the integration constants

$$A = 0, \quad B = -\frac{\epsilon_0^* \epsilon}{\eta^*} \zeta^* E_y^* \tag{2.38}$$

so that the solution for the tangential velocity is

$$v_y^* = \frac{\epsilon_0^* \epsilon}{\eta^*} \left(\psi^* - \zeta^*\right) E_y^*, \tag{2.39}$$

when sufficiently far from the wall it takes the constant value

$$v_{y,\text{slip}}^* = \lim_{x \to \infty} v_y^* = -\frac{\epsilon_0^* \epsilon}{\eta^*} \zeta^* E_y^*. \tag{2.40}$$

2.2.6 Linear transient electrokinetics: The Debye-Falkenhagen approximation

Another analytical approach to the electrodiffusive problem (in the absence of convection) can be found using the so-called Debye-Falkenhagen approximation (M. Z. Bazant, Thornton, & Ajdari, 2004; Checa, Millan-Solsona, & Gomila, 2019; Debye & Falkenhagen, 1928). In contrast to the solutions discussed in the section before, we now consider the transient one-dimensional problem

$$\begin{aligned} 0 &= \partial_t^* c_\pm^* + \partial_x^* \left(-D^* \partial_x^* c_\pm^* \mp \mu^* c_\pm^* \partial_x^* \phi^*\right), \\ 0 &= \epsilon \epsilon_0^* \partial_{xx}^* \phi^* + e_0^* \mathcal{Z} \left(c_+^* - c_-^*\right), \end{aligned} \tag{2.41}$$

with the boundary conditions at the wall and far away from it

$$\begin{aligned} -D^* \partial_x^* c_\pm^* \mp \mu^* c_\pm^* \partial_x^* \phi^* \Big|_{x^*=0} &= 0, \\ \phi^* \Big|_{x^*=0} &= \zeta^*, \\ \lim_{x^* \to \infty} c_\pm^* &= c_\infty^*, \\ \lim_{x^* \to \infty} \phi^* &= 0. \end{aligned} \tag{2.42}$$

We use the notation for charge density $q^* = c_+^* - c_-^*$ and concentration $c^* = c_+^* + c_-^*$, and rewrite the above set of equations as

$$\begin{aligned} 0 &= \partial_t^* q^* - D^* q^{*\prime\prime} - \mu^* c^{*\prime} \phi^{*\prime} - \mu^* c^* \phi^{*\prime\prime}, \\ 0 &= \partial_t^* c^* - D^* c^{*\prime\prime} - \mu^* q^{*\prime} \phi^{*\prime} - \mu^* q^* \phi^{*\prime\prime}, \\ 0 &= \frac{\epsilon \epsilon_0^*}{e_0^* \mathcal{Z}} \phi^{*\prime\prime} + q^*. \end{aligned} \tag{2.43}$$

In the two charge transport equations, we can rewrite the last term using the Poisson equation for the potential. The set then reads

$$\begin{aligned} 0 &= \partial_t^* q^* - D^* q^{*\prime\prime} - \mu^* c^{*\prime} \phi^{*\prime} + \frac{\mu^* e_0^* \mathcal{Z}}{\epsilon \epsilon_0^*} c^* q^*, \\ 0 &= \partial_t^* c^* - D^* c^{*\prime\prime} - \mu^* q^{*\prime} \phi^{*\prime} + \frac{\mu^* e_0^* \mathcal{Z}}{\epsilon \epsilon_0^*} q^{*2}, \\ 0 &= \frac{\epsilon \epsilon_0^*}{e_0^* \mathcal{Z}} \phi^{*\prime\prime} + q^*. \end{aligned} \tag{2.44}$$

We can linearize this problem assuming the potential at the wall to be small $\zeta^* \sim O(\varepsilon)$ with $\varepsilon \ll 1$. We find from the boundary conditions and the Poisson equation that $\phi^* \sim O(\varepsilon)$ and $q^* \sim O(\varepsilon)$, i.e. $q^*_{(0)} = 0$. The equation for the concentration delivers $c^*_{(0)} = c^*_\infty$ and $c^*_{(1)} = 0$. Thus, the set of leading order equations reads

$$\begin{aligned} 0 &= \partial_t^* q^*_{(1)} - D^* {q^*_{(1)}}'' + \frac{\mu^* e_0^* \mathcal{Z} c^*_\infty}{\epsilon \epsilon_0^*} q^*_{(1)}, \\ 0 &= \partial_t^* c^*_{(2)} - D^* {c^*_{(2)}}'' - \mu^* {q^*_{(1)}}' {\phi^*_{(1)}}' + \frac{\mu^* e_0^* \mathcal{Z}}{\epsilon \epsilon_0^*} {q^*_{(1)}}^2, \\ 0 &= \frac{\epsilon \epsilon_0^*}{e_0^* \mathcal{Z}} {\phi^*_{(1)}}'' + q^*_{(1)}. \end{aligned} \tag{2.45}$$

We can rewrite the first equation using the Debye length

$$\begin{aligned} \frac{1}{D^*} \partial_t^* q^*_{(1)} &= {q^*_{(1)}}'' - {l_{\mathrm{D}}^*}^{-2} q^*_{(1)}, \\ l_{\mathrm{D}}^* &= \sqrt{\frac{\epsilon \epsilon_0^* D^*}{e_0^* \mathcal{Z} c^*_\infty \mu^*}} = \sqrt{\frac{\epsilon \epsilon_0^* \phi^*_{\mathrm{th}}}{e_0^* \mathcal{Z} c^*_\infty}}. \end{aligned} \tag{2.46}$$

Note that in this case the Debye length differs by the factor $\sqrt{2}$ from the definition 2.31. Both definitions can be used equivalently. However, if the definition in 2.31 is used, the charge density and concentration are usually also defined with the factor $\frac{1}{2}$.
The set of linear equations is complemented by the boundary conditions

$$\begin{aligned} -D^* \partial_x^* q^*_{(1)} - \mu^* c^*_\infty \partial_x^* \phi^*_{(1)}\Big|_{x^*=0} &= 0, \\ -D^* \partial_x^* c^*_{(2)} - \mu^* \partial_x^* q^*_{(1)} \partial_x^* \phi^*_{(1)}\Big|_{x^*=0} &= 0, \\ \phi^*_{(1)}\Big|_{x^*=0} &= \zeta^*_{(1)}, \\ \lim_{x^* \to \infty} q^*_{(1)} &= 0, \\ \lim_{x^* \to \infty} c^*_{(2)} &= 0, \\ \lim_{x^* \to \infty} \phi^*_{(1)} &= 0. \end{aligned} \tag{2.47}$$

The equations for $\phi^*_{(1)}$ and $q^*_{(1)}$ are only coupled via the linear no-flux boundary condition and need to be solved together. After that, $c^*_{(2)}$ can be computed. Long-term and relaxation behavior of this problem was discussed by M. Z. Bazant et al. (2004). The approximation was first derived by Debye and Falkenhagen (1928). For the stationary case, the linearized problem will deliver the Debye-Hückel solution that was already discussed in the section before.

2.2.7 Influence of a streaming potential: The electric Reynolds number

The electric Reynolds number was originally introduced by Stuetzer (1962) together with the magnetic Reynolds number. In his scaling analysis, the Buckinham-Π theorem delivers four dimensionless parameters. These are the Mach- and Reynolds numbers as well as two numbers that characterize the EHD problem. The ratio of the EHD velocity $v_{\mathrm{EHD}} = \epsilon\epsilon_0^* E^{*2}$ and a characteristic flow velocity is important for streaming-potential phenomena. The electric effects in these problems occur as a result of an outer flow field that produces charge inbalances, e.g. in the electric double layer. In most EHD problems however, the EHD velocity can be used as characteristic velocity resulting in the parameter defined by Stuetzer (1962) to be unity. The second characteristic number he identified is the electric Reynolds number

$$\mathrm{Re}_{\mathrm{el}} = \frac{\epsilon\epsilon_0^* v_{\mathrm{ref}}^*}{e_0^* \mathcal{Z} c_{\mathrm{equ}}^* \mu l_{\mathrm{ref}}^*}, \tag{2.48}$$

which we can rewrite in terms of the Debye screening length

$$\mathrm{Re}_{\mathrm{el}} = \frac{{l_{\mathrm{D}}^*}^2 v_{\mathrm{ref}}^*}{D^* l_{\mathrm{ref}}^*} = \delta^2 \mathrm{Pe}. \tag{2.49}$$

We have here rewritten the electric Reynolds number in terms of two dimensionless numbers that are more commonly used today, the Péclet number and the dimensionless Debye length, defined as

$$\mathrm{Pe} = \frac{v_{\mathrm{ref}}^* l_{\mathrm{ref}}^*}{D^*} \qquad \text{and} \qquad \delta = \frac{l_{\mathrm{D}}^*}{l_{\mathrm{ref}}^*}. \tag{2.50}$$

The Péclet number is the ratio of diffuse and convective time scales, t_{D}^* and t_{v}^*, respectively. The term δ^2 is the ratio of charge relaxation and diffusive time scales and thus the electric Reynolds number the ratio of charge relaxation and convective time scales, t_{C}^* and t_{v}^*, respectively. In summary, these relations read

$$\begin{aligned} \mathrm{Pe} &= \frac{t_D^*}{t_v^*}, & \delta^2 &= \frac{t_C^*}{t_D^*}, & \mathrm{Re}_{\mathrm{el}} &= \frac{t_C^*}{t_v^*}, \\ \text{with} \quad t_D^* &= \frac{{l_{\mathrm{ref}}^*}^2}{D^*}, & t_v^* &= \frac{l_{\mathrm{ref}}^*}{v_{\mathrm{ref}}^*}, & t_C^* &= \frac{\epsilon\epsilon_0^*}{\varsigma^*}. \end{aligned} \tag{2.51}$$

In the absence of a given flow field, electric forces drive the flow. In that case, the convective time scale is defined with the EHD velocity

$$t_v^* = \frac{{l_{\mathrm{ref}}^*}^2 \eta^*}{\epsilon\epsilon_0^* {\phi_{\mathrm{th}}^*}^2}. \tag{2.52}$$

As this is the case in most problems, we mainly use the dimensionless Debye length and the Péclet number and compare with older results, e.g. by Melcher and Taylor (1969) by using the relations presented in this section.

2.2.8 Association and dissociation of salt

A large variety of dissociation mechanisms can appear in fluid materials. In general, these can be described as a neutrally charged molecule breaking up into a number of smaller molecules whose charges sum up to zero. Throughout this manuscript, we refer to the neutral species as "salt" and the respective charged species as "ions". The contrary reaction mechanism reconstituting the salt species from its ions is called association. The most simple example (e.g. sodium chloride) is described by the equilibrium

$$\mathcal{S} \rightleftharpoons \mathcal{C}_+ + \mathcal{C}_-, \tag{2.53}$$

where we denote the salt with $\mathcal{S}$ and the respective ions with $\mathcal{C}_\pm$.

In electrohydrodynamic problems, the redistribution of charges by convection or electromigration can for instance lead to a local decrease in the ion concentration. Effectively, by dissociation more ions are produced from the salt in that specific region. The accumulation of ions or redistribution of salt have similar effects. In order to describe these phenomena, we call the concentrations $c^*_{+,\mathrm{equ}}$, $c^*_{-,\mathrm{equ}}$, and s^*_{equ} when the reaction is in equilibrium. In equilibrium state, the relation

$$k^*_{\mathrm{d,equ}} s^*_{\mathrm{equ}} - k^*_{\mathrm{a,equ}} c^*_{+,\mathrm{equ}} c^*_{-,\mathrm{equ}} = 0 \tag{2.54}$$

holds, where $k^*_{\mathrm{d,equ}}$ and $k^*_{\mathrm{a,equ}}$ are the rate constants at equilibrium. The rate constants depend on the ions, salt and the respective solvent. The latter relation can be rewritten using the equilibrium constant $K^*_{\mathrm{equ}} = \frac{k^*_{\mathrm{d,equ}}}{k^*_{\mathrm{a,equ}}}$ and reads

$$K^*_{\mathrm{equ}} s^*_{\mathrm{equ}} - c^*_{+,\mathrm{equ}} c^*_{-,\mathrm{equ}} = 0. \tag{2.55}$$

Thus, the equilibrium constant is given by

$$K^*_{\mathrm{equ}} = \frac{c^*_{+,\mathrm{equ}} c^*_{-,\mathrm{equ}}}{s^*_{\mathrm{equ}}}. \tag{2.56}$$

In the above reaction 2.53, equal amounts of ions are produced by dissociation. We assume that all diluted ions have been produced from a salt added to the fluid (or alternatively by auto-dissociation of the fluid). Thus, the equlibrium concentrations are equal $c^*_{+,\mathrm{equ}} = c^*_{-,\mathrm{equ}} := c^*_{\mathrm{equ}}$ and we can rewrite the above equation as

$$K^*_{\mathrm{equ}} s^*_{\mathrm{equ}} - {c^*_{\mathrm{equ}}}^2 = 0 \quad \text{or} \quad K^*_{\mathrm{equ}} = \frac{{c^*_{\mathrm{equ}}}^2}{s^*_{\mathrm{equ}}}. \tag{2.57}$$

In the case of large equlibrium constant $K^*_{\mathrm{equ}} \gg 1$, the amount of ions relative to salt is high (strong electrolyte), contrarily if $K^*_{\mathrm{equ}} \ll 1$, we have a weak electrolyte. It is important to note that we will later introduce the dimensionless electrolyte strength

$$\alpha := \frac{c^*_{\mathrm{equ}}}{s^*_{\mathrm{equ}}}. \tag{2.58}$$

which is not identical with the equilibrium constant. However, it is obvious that for $K^*_{\mathrm{equ}} \gg 1$ also $\alpha \gg 1$ holds vice versa. We note that the units of both rate constants are not equal. Consider eq. 2.54 and that $\left[s^*_{\mathrm{equ}}\right] = \left[c^*_{\pm\mathrm{equ}}\right] = \mathrm{m}^{-3}$. For $\left[k^*_{\mathrm{d,equ}}\right] = \mathrm{s}^{-1}$ the unit of the association rate constant is $\left[k^*_{\mathrm{a,equ}}\right] = \mathrm{m}^3\mathrm{s}^{-1}$. As mentioned, we will only consider electrolytic solutions following the reaction 2.53. In general, reactions with more than two molecules on the product side are possible. Similarly, we conclude from eq. 2.57 the unit of the equilibrium constant $\left[K^*_{\mathrm{equ}}\right] = \mathrm{m}^{-3}$. Then, the unit of the rate constants and the equilibrium constant have to be adjusted accordingly.

After discussing the equilibrium state, we now focus on the processes when the reaction is not in equilibrium. For that purpose, the general ion and salt concentrations $c^*_{\pm}$, $s^*_{\pm}$ are used. Analogously, we denote the rate constants with k^*_{d} and k^*_{a} when the reaction is not necessarily in equilibrium. The production of ions is described by the reaction term

$$\mathcal{R}^*_c = k^*_{\mathrm{d}} s^* - k^*_{\mathrm{a}} c^*_+ c^*_- . \tag{2.59}$$

We find the production of salt equivalently

$$\mathcal{R}^*_s = -\left(k^*_{\mathrm{d}} s^* - k^*_{\mathrm{a}} c^*_+ c^*_-\right), \tag{2.60}$$

noting that for dissociation $\mathcal{R}^*_c > 0$ and $\mathcal{R}^*_s < 0$, while for association $\mathcal{R}^*_c < 0$ and $\mathcal{R}^*_s > 0$. The rate constants k^*_{d} and k^*_{a} do not only depend on ions, salt, and fluid as the respective equilibrium rate constants, but also on the concentrations. The stronger the mismatch between $c^*_{\pm}$ and c^*_{equ}, the faster the rate of change stabilizing the equilibrium state.

CHAPTER 3

An overview of fluid-fluid interface electrokinetic models

The phenomena discussed in chapter 2 are fundamental not only for the understanding of the interaction between charged solids and fluid electrolytes. They are also crucial for problems featuring two phases of fluid electrolytes. Such problems include drops, cells, or vesicles. In this work, the focus lies on problems with fluid droplets suspended in a second liquid phase. However, the findings can also be used for investigating biomechanical structures by adding the respective interface effects. Examples for such interface properties are electrical capacities, porosity, or inextensibility.

This chapter recaptures the development of fluid-fluid interface models mainly referring to the two Annual Reviews in Fluid Dynamics by Melcher and Taylor (1969), Saville (1997), and the JFM articles by Schnitzer and Yariv (2015) and Mori and Young (2018), as summarized in table 3.1. The work of Melcher and Taylor (1969) defined the field of electrohydrodynamics by setting up a closed set of equations. It is capable of explaining a large number of experimental problems from which some were assumed to be irreproducible effects or systematic errors until then. Saville (1997) later delivered a derivation of the Taylor-Melcher model from basic principles allowing for dissociation terms and multiple ion species. As the Saville model is derived for leaky dielectrics, delimiting it from strong electrolyte models, it is also referred to as the 'leaky dielectric model'. However, both their works lack a detailed analysis of the thin region near the interface in which electric charge can accumulate. Recent approaches by Schnitzer and Yariv (2015) and Ma et al. (2022) for strong electrolytes and Mori and Young (2018) for weak electrolytes address these effects. They can explain effects like particle migration, surface convection / conduction, and the resulting deformations. They build the framework for the model derived in chapter 4 which is used to investigate electromigration and the influence of electrolyte strength.

year	authors	abbr.	materials	electrokinetics
1969	Melcher and Taylor (1969)	TM	general fluids	no
1997	Saville (1997)	SA	'leaky dielectrics'	no
2015	Schnitzer and Yariv (2015)	SY	strong electrolytes	yes
2018	Mori and Young (2018)	MY	weak electrolytes	yes

Table 3.1: Overview of modeling approaches discussed in this chapter. The right column refers to if electrokinetic effects at the interface are modeled.

3.1 The Taylor Melcher model for droplet electrohydrodynamics

The field of electrohydrodynamics was defined by Melcher and Taylor (1969) in 1969. They suggested a closed set of equations for a problem with two immiscible liquid phases. Both liquids in the TM model are considered homogeneous, incompressible, and have constant conductivity and permittivity. Yet, conductivity, permittivity, and viscosity are not assumed to be identical in both liquids.

Melcher and Taylor (1969) do not deliver a definition for the charge density q^*. We note that later models account for the existence of different ion species whose charges sum up to a net charge q^*. Yet, in the TM model only this net charge is defined. The associated electric current is defined as the superposition of convective and electrophoretic charge transport

$$\vec{j}_q^* = \vec{j}_{q,\mathrm{conv}}^* + \vec{j}_{q,\mathrm{elph}}^* = \vec{v}^* q^* + \varsigma^* \vec{E}^*, \tag{3.1}$$

neglecting diffusive fluxes without discussion. Mori and Young (2018) were later able to clarify the legitimacy of this latent assumption. The relation $\vec{j}_{q,\mathrm{elph}}^* = \varsigma^* \vec{E}^*$ is also referred to as Ohm's law, relating conductivity ς^* and electric field $\vec{E}^*$ to the ion flux. The surface charge q_Γ^*, which is the charge attached to the interface Γ is defined in analogy to the charge density, as well as the regarding surface flux $\vec{j}_{q,\Gamma}^*$.

We further note that Melcher and Taylor (1969) derived their model using the electrical displacement field

$$\vec{D}^* = \epsilon_0^* \epsilon \vec{E}^* + \vec{P}^* \tag{3.2}$$

which is a function of the electric field $\vec{E}^*$ and the polarization density $\vec{P}^*$ which accounts for electric dipole moments in the electric material. It can be a material property of the dielectric or a response to an externally applied electric field.

The forces affecting fluid motion in this model are gravitation $\rho^* \vec{g}^*$ with the gravitational acceleration $\vec{g}$, as well as viscous and electric forces, expressed by the divergence of

Newton stress and Maxwell stress that are defined as

$$\begin{aligned} \xi^* &= -p^* I + \eta^* \left(\vec{\nabla}^* \vec{v}^* + \left(\vec{\nabla}^* \vec{v}^* \right)^\top \right) \\ \theta^* &= \epsilon_0^* \epsilon \left(-\frac{1}{2} \left(\vec{E}^* \cdot \vec{E}^* \right) I + \vec{E}^* \otimes \vec{E}^* \right) \end{aligned} \tag{3.3}$$

respectively using the unity matrix I and the tensor product $\otimes$ over two vector spaces.

The TM model is given by the governing equations

$$\begin{aligned} \vec{\nabla}^* \times \vec{E}^* &= 0 && \text{irrotational electric field,} \\ \vec{\nabla}^* \cdot \vec{D}^* &= q^* && \text{Poisson eq. for the potential,} \\ \partial_t^* q^* + \vec{\nabla}^* \cdot \vec{j}_q^* &= 0 && \text{conservation of charge density,} \\ \rho^* D_t^* \vec{v}^* &= \rho^* \vec{g}^* + \vec{\nabla}^* \cdot (\xi^* + \theta^*) && \text{conservation of momentum,} \\ \vec{\nabla}^* \cdot \vec{v}^* &= 0 && \text{incompressibility condition} \end{aligned} \tag{3.4}$$

together with the interface conditions that can be found by integration of the governing equations over the thin surface

$$\begin{aligned} \vec{n} \times [\![\vec{E}^*]\!] &= 0 && \text{continuity of the tangential el. field,} \\ \vec{n} \cdot [\![\vec{D}^*]\!] &= q_\Gamma^* && \text{surface charge,} \\ \vec{n} \cdot [\![\vec{j}_q^*]\!] + \vec{\nabla}_\parallel^* \cdot \vec{j}_{q,\Gamma}^* &= u_\perp^* [\![q^*]\!] - \partial_t^* q_\Gamma^* && \text{surface current,} \\ \vec{n} \cdot [\![\xi^* + \theta^*]\!] &= 0 && \text{absence of surface tension,} \\ \vec{n} \times [\![\vec{v}^*]\!] &= 0 && \text{continuity of the tangential velocity field,} \\ \vec{n} \cdot [\![\vec{v}^*]\!] &= 0 && \text{continuity of the normal velocity field.} \end{aligned} \tag{3.5}$$

We denote the interface velocities with $\vec{u}$ in contrast to the fluid velocity $\vec{v}$. The surface current condition above depends on the normal interface velocity $u_\perp$. We refer to tables I and II as given by Melcher and Taylor (1969).

Melcher and Taylor (1969) make a number of simplifying assumptions that we discuss in detail and summarize the governing equations thereafter. Polarization effects are neglected. As mentioned at the beginning of this section, the permittivity is assumed to be piece wise constant for each electrolyte. Due to

$$\vec{D}^* = \epsilon_0^* \epsilon \vec{E}^* \quad \text{and} \quad \vec{\nabla}^* \vec{D}^* = \epsilon_0^* \epsilon \vec{\nabla}^* \vec{E}^* \tag{3.6}$$

the use of the electric field is sufficient for further description of the problem. We note that eq. 3.4 states that the electric field is irrotational and therefore conservative. It is uniquely defined by the scalar electric potential ϕ^* with $\vec{E}^* = -\vec{\nabla}^* \phi^*$.

An analysis of the charge density distribution reveals further simplifications that can be applied to the electrical problem. The conservation law for the charge density q^* in eq. 3.4 can be combined with Gauss' law for constant permittivity

$$\epsilon_0^* \epsilon \vec{\nabla}^* \cdot \vec{E}^* = q^* \tag{3.7}$$

to yield

$$\left(\partial_t^* + \vec{v}^* \cdot \vec{\nabla}^*\right) q^* + \frac{\varsigma^*}{\epsilon_0^* \epsilon} q^* = 0. \tag{3.8}$$

From this relation, two conclusions can be drawn. The characteristic time scale for charge relaxation is $t_C^* = \frac{\epsilon_0^* \epsilon}{\varsigma^*}$. Along streamlines, perturbations of charge decay on this time scale. For open streamlines, i.e. originating at infinity with no outer source of charge, in a single fluid this relation delivers $q^* = 0$. However, in a two-phase setting, the interface Γ can act as a source of charge.

After examining the electrical problem we focus on how these simplifications affect the flow. For constant permittivity, the divergence of the Maxwell stress can be simplified to the Coulomb force

$$\vec{\nabla}^* \cdot \theta^* = \epsilon_0^* \epsilon \left(\vec{\nabla}^* \cdot \vec{E}^*\right) \vec{E}^* = q^* \vec{E}^*. \tag{3.9}$$

In the frequently used case of $q^* = 0$ this force vanishes. Then, the only way electric effects influence the flow is through the boundaries.

In summary, the above simplifications lead to the set of governing equations

$$\begin{aligned}
\vec{\nabla}^* \cdot \vec{E}^* &= 0 && \text{solenoidal electric field,} \\
\rho^* D_t^* \vec{v}^* &= \vec{\nabla}^* \cdot (\xi^* + \theta^*) && \text{conservation of momentum,} \\
\vec{\nabla}^* \cdot \vec{v}^* &= 0 && \text{incompressibility condition}
\end{aligned} \tag{3.10}$$

together with the boundary conditions

$$\begin{aligned}
\vec{n} \times [\![\vec{E}^*]\!] &= 0 && \text{continuity of the tangential el. field,} \\
\vec{n} \cdot [\![\epsilon \vec{E}^*]\!] &= q_\Gamma^* && \text{surface charge,} \\
\vec{n} \cdot [\![\vec{j}_q^*]\!] + \vec{\nabla}_\parallel^* \cdot \vec{j}_{q,\Gamma}^* &= -\partial_t^* q_\Gamma^* && \text{surface current,} \\
[\![\xi^* + \theta^*]\!] \cdot \vec{n} &= 0 && \text{absence of surface tension,} \\
\vec{n} \times [\![\vec{v}^*]\!] &= 0 && \text{continuity of the tangential velocity field,} \\
\vec{n} \cdot [\![\vec{v}^*]\!] &= 0 && \text{continuity of the normal velocity field.}
\end{aligned} \tag{3.11}$$

This model (Melcher & Taylor, 1969) is capable of explaining convection phenomena induced by an outer electric field. Different settings are used, such as experiments in a rectangular apparatus, or spherical droplets. The discontinuity in the outer applied electric field at the interface between the two phases (cp. eq. 3.11) leads to a discontinuity of the Maxwell stress and thus hydrodynamic shear stresses. The prediction of convection cells, as well as droplet deformations and flow instabilities, are possible with this model.

The electric Reynolds number was introduced as an estimate of the influence of fluid convection relative to the charge relaxation in the bulk

$$\mathrm{Re}_{\mathrm{el}} = \frac{\epsilon_0^* \epsilon v_{\mathrm{ref}}^*}{\varsigma^* l_{\mathrm{ref}}^*}. \tag{3.12}$$

For small electric Reynolds numbers $\mathrm{Re_e} \ll 1$, convection can be neglected, while it becomes particularly important for $\mathrm{Re_e} \sim O(1)$. Problems which are dominated by convection ($\mathrm{Re_e} \gg 1$) are not discussed in this context because electric effects play a minor role. The list of applications for this model is completed by stability problems in which excitating electric forces and damping vscous force are counterparts. A second dimensionless number, relating these two forces is the electric Hartmann number

$$\mathrm{Ha_{el}} = E^*_{\mathrm{ref}} \sqrt{\frac{\epsilon_0^{*2}\epsilon^2}{\eta^* \varsigma^*}}. \tag{3.13}$$

Despite its large range of capabilities, the model lacks a rigorous scaling analysis and thus an overview on the experimental parameters that limit the model validity. The two dimensionless numbers mentioned above have been derived for certain experimental settings. However, a scaling analysis of the whole model can predict what experimental settings lead to which phenomena a priori. For that reason, we will follow the derivation of a very similar model by Saville in the next section.

3.2 The Saville model

In his Annual Review from 1997, Saville considered the foundations of the TM model, delivering some insights into its limits. He confined his research area to poorly conducting liquids 'leaky dielectrics' under the influence of strong fields. Due to Saville, electrokinetics in contrast deals with the better conducting 'electrolytes' and relatively small field strengths. We note that these statements do not exactly agree with our definition terminology in sec. 2.2. Saville claims that the boundary between electrokinetics and leaky dielectric EHD is defined by conductivity and electric field strength. Yet, from today's point of view both of the fluid materials that he called 'leaky dielectrics' and 'electrolytes' are electrolytic solutions. The poor conductivity of 'leaky dielectrics' originates from the small amount of dissolved charges in the liquid, while 'electrolytes' contain a large amount of such charged particles. Therefore, throughout this manuscript we will refer to such materials as weak and strong electrolytes. As a result, electrolyte strength does not turn out to be a defining property of the respective field of research. In addition, the electric field strength is a more vague argument. It is not obvious at which field strength a line between the different fields can be drawn. In fact, the resulting physics significantly depends on more parameters beyond the field strength, e.g. dielectric constants, viscosities, or ion diffusivities. Therefore, we define the respective research fields depending on the existence of different physical effects. In particular, electrokinetics feature a two-way coupling between electric and flow problem.

Saville derives his model starting from a fully coupled system of equations. Unlike Melcher and Taylor, he starts from the dissociation equilibrium between a salt and the respective ions. Consequently, the charge density is a parameter uniquely defined by

$$q^* = \sum_i \mathcal{Z}_{+,i} c^*_{+,i} - \sum_j \mathcal{Z}_{-,j} c^*_{-,j}. \tag{3.14}$$

Without loss of generality, a binary symmetric electrolyte can be assumed, reducing the above relation to

$$q^* = c_+^* - c_-^*. \tag{3.15}$$

The respective ion fluxes take convection, electromigration, and diffusion into account

$$\vec{j}_\pm^* = \vec{j}_{\pm,\mathrm{conv}}^* + \vec{j}_{\pm,\mathrm{elph}}^* + \vec{j}_{\pm,\mathrm{diff}}^* = \vec{v}^* c_\pm^* \pm \mu_\pm^* c_\pm^* \vec{E}^* - D_\pm^* \vec{\nabla}^* c_\pm^*. \tag{3.16}$$

The salt flux $\vec{j}_s^*$ is composed similarly, yet it does not contain electromigration due to the electroneutrality, and reads

$$\vec{j}_s^* = \vec{j}_{s,\mathrm{conv}}^* + \vec{j}_{s,\mathrm{diff}}^* = \vec{v}^* s^* - D_\pm^* \vec{\nabla}^* s^*. \tag{3.17}$$

The divergence of those fluxes is balanced by the reaction terms $\mathcal{R}_\pm$ and $\mathcal{R}_s$ which are defined as introduced in sec. 2.2.8

$$\begin{aligned} \mathcal{R}_c^* &= k_\mathrm{d}^* s^* - k_\mathrm{a}^* c_+^* c_-^*, \\ \mathcal{R}_s^* &= -\left(k_\mathrm{d}^* s^* - k_\mathrm{a}^* c_+^* c_-^*\right). \end{aligned} \tag{3.18}$$

Now, a closed model can be set up with the governing equations

$$\begin{aligned} \vec{\nabla}^* \times \vec{E}^* &= \vec{0} && \text{irrotational electric field,} \\ \vec{\nabla}^* \cdot \left(\epsilon_0^* \epsilon \vec{E}^*\right) &= q^* && \text{Poisson eq. for the potential,} \\ \partial_t^* c_\pm^* + \vec{\nabla}^* \cdot \vec{j}_\pm^* &= \mathcal{R}_c^* && \text{conservation of each ion species,} \\ \partial_t^* s^* + \vec{\nabla}^* \cdot \vec{j}_s^* &= \mathcal{R}_s^* && \text{conservation of salt,} \\ \rho^* \partial_t^* \vec{v}^* + \vec{v}^* \cdot \vec{\nabla}^* \vec{v}^* &= \vec{\nabla}^* \cdot (\xi^* + \theta^*) && \text{conservation of momentum,} \\ \vec{\nabla}^* \cdot \vec{v}^* &= 0 && \text{incompressibility condition} \end{aligned} \tag{3.19}$$

with the boundary conditions

$$\begin{aligned} \vec{n} \times [\![\vec{E}^*]\!] &= \vec{0} && \text{continuity of the tangential el. field,} \\ \vec{n} \cdot [\![\epsilon_0^* \epsilon \vec{E}^*]\!] &= q_\Gamma^* && \text{surface charge,} \\ \vec{n} \cdot [\![\vec{j}_q^*]\!] + \vec{\nabla}_\parallel^* \cdot \vec{j}_{q,\Gamma}^* &= u_\perp^* [\![q^*]\!] - \partial_t^* q_\Gamma^* && \text{surface current,} \\ [\![\xi^* + \theta^*]\!] \cdot \vec{n} &= 0 && \text{absence of surface tension,} \\ \vec{n} \times [\![\vec{v}^*]\!] &= 0 && \text{continuity of the tangential velocity field,} \\ \vec{n} \cdot [\![\vec{v}^*]\!] &= 0 && \text{continuity of the normal velocity field.} \end{aligned} \tag{3.20}$$

In order to follow the dimensional analysis by Saville, we start with the reference values used to nondimensionalize the equations and the resulting dimensionless parameters as summarized in table 3.2. In dimensionless form, the momentum equation reads

$$\frac{t_\eta^*}{t_\mathrm{ref}^*} \partial_t \vec{v} + \mathrm{Re}\, \vec{v} \cdot \vec{\nabla} \vec{v} = \vec{\nabla} \cdot (\xi + \theta). \tag{3.21}$$

reference parameter	**symbol**	**unit**	**definition**	**estimate**	**comments**
length scale	l^*_{ref}	m	–	10^{-3}	
time scale	t^*_{ref}	s	–	–	
velocity scale	v^*_{ref}	$\mathrm{m\,s^{-1}}$	$\frac{\epsilon^*_0 \epsilon l^*_{\mathrm{ref}} {E^*_\infty}^2}{\mu}$	$0.35 \cdot 10^{-3}$	EHD velocity
surface velocity scale	v^*_Γ	$\mathrm{m\,s^{-1}}$	–	–	
pressure scale	p^*_{ref}	Pa	$\epsilon^*_0 \epsilon {E^*_\infty}^2$	0.35	
viscosity	η^*	Pa s	–	1	e.g. oil, glycerine
relative permittivity	ϵ	–	–	4	e.g. some oils
reference salt concentration	s^*_{ref}	$\mathrm{m^{-3}}$	–	10^{24}	$10^{-3}\,\mathrm{mol}\,l^{-1}$
reference ion concentration	c^*_{ref}	$\mathrm{m^{-3}}$	$\sqrt{K^*_{\mathrm{equ}} s^*_{\mathrm{ref}}}$	10^{20}	$10^{-7}\,\mathrm{mol}\,l^{-1}$
applied electric field	E^*_∞	$\mathrm{V\,m^{-1}}$	–	10^5	
parameter	**symbol**	**unit**	**definition**		
viscous relaxation time	t^*_η	s	$\frac{\rho^* {l^*_{\mathrm{ref}}}^2}{\eta^*}$	$1 \cdot 10^{-3}$	
electrical relaxation time	t^*_{C}	s	$\frac{\epsilon^*_0 \epsilon}{\varsigma^*}$	$35 \cdot 10^{-3}$	
characteristic diffusion time	t^*_{D}	s	$\frac{{l^*_{\mathrm{ref}}}^2}{D^*}$	10^6	
characteristic convection time	t^*_{v}	s	$\frac{l^*_{\mathrm{ref}}}{v^*_{\mathrm{ref}}}$	2.82	for $v^*_{\mathrm{ref}} = v^*_{\mathrm{EHD}}$
characteristic surface time	t^*_Γ	s	$\frac{l^*_{\mathrm{ref}}}{v^*_\Gamma}$	–	
thermal potential	ϕ^*_{th}	V	$\frac{k^*_{\mathrm{B}} T^*_{\mathrm{a}}}{\mathcal{Z} e^*_0}$	$25 \cdot 10^{-3}$	
dimensionless parameter	**symbol**	**unit**	**definition**		
Reynolds number	Re	–	$\frac{t^*_\eta}{t^*_{\mathrm{v}}}$	10^{-4}	for $v^*_{\mathrm{ref}} = v^*_{\mathrm{EHD}}$
Peclet number	Pe	–	$\frac{t^*_{\mathrm{D}}}{t^*_{\mathrm{v}}}$	10^5	for $v^*_{\mathrm{ref}} = v^*_{\mathrm{EHD}}$
Damköhler number	Da	–	$k^*_{d,\mathrm{equ}} t^*_{\mathrm{D}}$	10^5	
electrolyte strength	α	–	$\frac{c^*_{\mathrm{ref}}}{s^*_{\mathrm{ref}}}$	10^{-4}	
dimensionless field strength	β	–	$\frac{E^*_\infty l^*_{\mathrm{ref}}}{\phi^*_{\mathrm{th}}}$	10^3	
dimensionless length	Λ_{SA}	–	$\frac{\epsilon^*_0 \epsilon E^*_\infty}{l^*_{\mathrm{ref}} e^*_0 c^*_{\mathrm{ref}}}$	10^{-4}	

Table 3.2: Reference parameters, scales, and dimensionless numbers of the Saville model. The values were estimated for a material with $\epsilon = 4$, $\varsigma^* = 10^{-9}\,\mathrm{S\,m^{-1}}$, $\mu^* = 1\,\mathrm{Pa\,s}$ and an applied electric field with strength $E^*_\infty = 10^5\,\mathrm{V\,m^{-1}}$. The dissociation is set to $K^* = 10^{17}\,\mathrm{m^{-3}}$, $k^*_{\mathrm{a}} = 10^{-18}\,\mathrm{m^3\,s^{-1}}$, and $k^*_{\mathrm{a}} = 10^{-1}\,\mathrm{s^{-1}}$ and the reference concentration $c^*_{\mathrm{ref}} = 10^7 \mathrm{m^{-3}}$. The estimated values give an overview on the relative size of the parameters in the Saville model. Yet, they can vary significantly with different materials and field strengths. (Saville, 1997)

With the assumption $\mathrm{Re} \ll 1$, the convective term is neglected. Similarly, the charge transport equations are non-dimensionalized, and we get

$$\begin{aligned} \frac{t_\mathrm{D}^*}{t_\mathrm{ref}^*}\partial_t c_\pm + \vec{\nabla}\cdot\left(\mathrm{Pe}\,\vec{v}c_\pm \mp \beta\, c_\pm \vec{E} - \vec{\nabla}c_\pm\right) &= \mathrm{Da}\,\alpha^{-1}\left(k_\mathrm{d}s - k_\mathrm{a}c_+c_-\right), \\ \frac{t_\mathrm{D}^*}{t_\mathrm{ref}^*}\partial_t s + \vec{\nabla}\cdot\left(\mathrm{Pe}\,\vec{v}s - \vec{\nabla}s\right) &= -\mathrm{Da}\left(k_\mathrm{d}s - k_\mathrm{a}c_+c_-\right). \end{aligned} \tag{3.22}$$

Here, the rate constants were made dimensionless using the respective equilibrium values. Saville (1997) suggests considering the resultant equation for the charge density

$$\frac{t_\mathrm{D}^*}{t_\mathrm{ref}^*}\partial_t q + \vec{\nabla}\cdot\left(\mathrm{Pe}\,\vec{v}q + \beta\, c\vec{E} - \vec{\nabla}q\right) = 0, \tag{3.23}$$

with the dimensionless conductivity $c = c_+ + c_-$. Due to Saville (1997), the respective condition for the conductivity is given by $\mathrm{Da} \gg 1$ and eq. 3.22 and reads

$$k_\mathrm{d}s - k_\mathrm{a}c_+c_- = 0. \tag{3.24}$$

The electrical system is closed by the Poisson for the electric potential

$$\Lambda_\mathrm{SA}\vec{\nabla}\cdot\vec{E} = q \tag{3.25}$$

which yields for $\Lambda_\mathrm{SA} \ll 1$ charge neutrality $q = 0$. Together with eq. 3.23, we find a relation for the electric potential

$$\vec{\nabla}\cdot\left(c\vec{E}\right) = 0. \tag{3.26}$$

In most application cases Saville (1997) assumes ς to be a constant without formal proof. We will later discuss under which conditions this assumption is valid. In problems with surface conduction or close to charged walls, regions with charge amounts that are larger or smaller than the equilibrium value emerge. Thus, the conductivity in those regions is not equal to the conductivity in equilibrium.

In contrast to the bulk, the surface charge density is scaled as $q_\Gamma^* = \epsilon_0^*\epsilon E_\infty^* q_\Gamma$ and the surface velocity is scaled as $\vec{v}^* = v_\Gamma^*\vec{v}$, where v_Γ^* is a velocity inherent to the interface, e.g. the tangential surface speed. The dimensionless form of the surface current relation reads

$$\begin{aligned} \vec{n}\cdot[\![\vec{j}_q]\!] + \vec{\nabla}_\parallel\cdot\vec{j}_{q,\Gamma} &= \frac{t_\mathrm{C}^*}{t_\Gamma^*}u_\perp[\![q]\!] - \frac{t_\mathrm{C}^*}{t_\mathrm{ref}^*}\partial_t q_\Gamma, \\ \vec{j}_q &= \frac{t_\mathrm{C}^*}{t_\Gamma^*}\vec{v}q + c\vec{E} - \frac{1}{\beta}D_\pm\vec{\nabla}q, \\ \vec{j}_{q,\Gamma} &= \frac{t_\mathrm{C}^*}{t_\Gamma^*}\vec{v}q_\Gamma. \end{aligned} \tag{3.27}$$

We note here that surface fluxes due to electromigration and diffusion are neglected in this model. The diffusive flux from the bulk into the surface (or from surface to bulk),

can be neglected for strong applied fields $\beta \gg 1$.

We can summarize the Saville model with the discussed assumptions. The equations in dimensionless form read

$$\begin{aligned}
\vec{\nabla} \times \vec{E} &= \vec{0} && \text{irrotational electric field,} \\
\vec{\nabla} \cdot \left(c\vec{E} \right) &= 0 && \text{electric field,} \\
\frac{t^*_\eta}{t^*_{\text{ref}}} \partial_t \vec{v} + \text{Re}\, \vec{v} \cdot \vec{\nabla} \vec{v} &= \vec{\nabla} \cdot (\xi + \theta) && \text{conservation of momentum,} \\
\vec{\nabla} \cdot \vec{v} &= 0 && \text{incompressibility condition}
\end{aligned} \tag{3.28}$$

with the boundary conditions

$$\begin{aligned}
\vec{n} \times [\![\vec{E}]\!] &= \vec{0} && \text{continuity of the tangential el. field,} \\
\vec{n} \cdot [\![\epsilon \vec{E}]\!] &= q_\Gamma && \text{surface charge,} \\
\vec{n} \cdot [\![\frac{t^*_\text{C}}{t^*_\Gamma} \vec{v} q - c\vec{E}]\!] + \vec{\nabla}_\parallel \cdot \left(\frac{t^*_\text{C}}{t^*_\Gamma} \vec{v} q_\Gamma \right) &= \frac{t^*_\text{C}}{t^*_\Gamma} u_\perp [\![q]\!] && - \frac{t^*_\text{C}}{t^*_{\text{ref}}} \partial_t q_\Gamma \quad \text{surface current,} \\
[\![\xi + \theta]\!] \cdot \vec{n} &= 0 && \text{absence of surface tension,} \\
\vec{n} \times [\![\vec{v}]\!] &= 0 && \text{continuity of the tangential velocity field,} \\
\vec{n} \cdot [\![\vec{v}]\!] &= 0 && \text{continuity of the normal velocity field.}
\end{aligned} \tag{3.29}$$

Despite the simplifications made, the leaky dielectric model supports many experimental studies. The most important examples are the deformation and motion of drops, and their stability under external electric fields. Yet, its applications range beyond spherical geometries, e.g. in the breakup of jets.

In most applications, the above leaky dielectric model is used with the assumptions $\text{Re} \ll 1$ and constant c, which we already discussed. Yet, formal proof for the latter condition is still necessary. It is also questionable under which experimental conditions a different scaling for the charge density in the surface and bulk equations make sense. A similar ambiguity occurs for the velocity scale.

In some cases, the limit for $\Lambda_{\text{SA}} \to 0$ can be singular which is equivalent to the existence of a thin electric layer. An analysis of this limit might help to better understand the charge transport close to or through the interface. In particular, the transverse electric currents that are neglected by both, Saville (1997) and Mori and Young (2018), can be investigated.

3.3 Strong electrolytes by Schnitzer and Yariv

In contrast to the previous works by Mori and Young (2018) and Saville (1997), Schnitzer and Yariv (2015) derived a liquid-liquid electrohydrodynamic model for a stationary problem and strong electrolytic solutions from an intensive analysis of the interfacial electric layers. The Reynolds number is assumed to be a priori small. A list of other important scales is presented in tabel 3.3. The initial set of equations in dimensionless form reads

$$\begin{aligned} \delta^2\epsilon\nabla^2\phi + q &= 0 && \text{Poisson eq. for the potential,}\\ \vec{\nabla}\cdot\vec{j}_\pm &= 0 && \text{conservation of each ion species,}\\ \vec{\nabla}\cdot(\xi+\theta) &= 0 && \text{conservation of momentum,}\\ \vec{\nabla}\cdot\vec{v} &= 0 && \text{incompressibility condition.} \end{aligned} \tag{3.30}$$

The corresponding boundary conditions at the interface are

$$\begin{aligned} \vec{n}\cdot[\![\epsilon\vec{E}]\!] &= q_\Gamma && \text{surface charge,}\\ \varkappa_\pm c_\pm &= c_{\Gamma,\pm} && \text{ion adsorption (on each side),}\\ \vec{n}\cdot[\![\vec{j}_\pm]\!] + \vec{\nabla}_\parallel\cdot(2\delta\mathrm{Pe}\vec{v}q_\Gamma) &= 0 && \text{surface current,}\\ [\![\xi]\!]\cdot\vec{n} &= \theta_\Gamma && \text{absence of surface tension,}\\ \vec{n}\times[\![\vec{v}]\!] &= 0 && \text{continuity of the tangential velocity field,}\\ \vec{n}\cdot\vec{v} &= 0 && \text{impermeability.} \end{aligned} \tag{3.31}$$

In the above equations, the charge current is defined similarly to Saville, as

$$\vec{j}_\pm = \vec{j}_{\pm,\mathrm{conv}} + \vec{j}_{\pm,\mathrm{elph}} + \vec{j}_{\pm,\mathrm{diff}} = \mathrm{Pe}\,\vec{v}c_\pm \mp c_\pm\vec{\nabla}\phi - \vec{\nabla}c_\pm \tag{3.32}$$

and the parameter θ_Γ denotes the surface tension due to the surface charge $q_\Gamma = c_{+,\Gamma} - c_{-,\Gamma}$. It consists of two terms for the electric shear stress and the Marangoni effect respectively. We refer to Schnitzer and Yariv (2015) and Baygents and Saville (1990) for a more detailed discussion of these effects. The concentration of adsorped charges is linearly dependent on the adsorption coefficients $\varkappa_\pm$ which are not necessarily equal on both sides of the interface. In addition to the boundary conditions at the interface 3.31, when sufficiently far from the interface the condition for the electric field holds

$$\lim_{|\vec{x}|\to\infty} -\vec{\nabla}\phi = \beta\vec{x}_E, \tag{3.33}$$

where the vector $\vec{x}_E$ denotes the direction of the outer electric field and β the dimensionless field strength.

At this point, it is important to emphasize that there is no uniform definition of the Péclet number in the literature. The reader might notice the difference in the definitions by Schnitzer and Yariv (2015) and Saville (1997). Schnitzer and Yariv (2015) call the dimensionless number "drag coefficient" or intrinsic Péclet number. The reason for that

reference parameter	**symbol**	**unit**	**definition**	**estimate**	**comments**
length scale	l^*_{ref}	m	–	10^{-3}	
velocity scale	v^*_{ref}	$\mathrm{m\,s^{-1}}$	$\frac{\epsilon^*_0 \epsilon {\phi^*_{\mathrm{th}}}^2}{l^*_{\mathrm{ref}} \mu}$	$0.5 \cdot 10^{-6}$	EHD velocity
time scale	t^*_{ref}	s	$\frac{l^*_{\mathrm{ref}}}{v^*_{\mathrm{ref}}}$	$2 \cdot 10^3$	
pressure scale	p^*_{ref}	Pa	$\frac{\epsilon^*_0 \epsilon {\phi^*_{\mathrm{th}}}^2}{{l^*_{\mathrm{ref}}}^2}$	$0.5 \cdot 10^{-6}$	
reference ion concentration	c^*_{ref}	$\mathrm{m^{-3}}$	–	10^{24}	$10^{-3}\,\mathrm{mol}\,l^{-1}$
parameter	**symbol**	**unit**	**definition**		
thermal potential	ϕ^*_{th}	V	$\frac{k^*_{\mathrm{B}} T^*_{\mathrm{a}}}{\mathcal{Z} e^*_0}$	$25 \cdot 10^{-3}$	
applied electric field	E^*_∞	$\mathrm{V\,m^{-1}}$	–	10^3	
diffusion coefficients	$D^*_\pm$	$\mathrm{m^2\,s^{-1}}$	–	10^{-9}	
Debye length	l^*_{D}	m	$\sqrt{\frac{\epsilon^*_0 \epsilon \phi^*_{\mathrm{th}}}{\mathcal{Z} e^*_0 c^*_{\mathrm{equ}}}}$	$14 \cdot 10^{-9}$	
dimensionless parameter	**symbol**	**unit**	**definition**		
Reynolds number	Re	–	$\frac{\rho^* v^*_{\mathrm{ref}} l^*_{\mathrm{ref}}}{\eta^*}$	10^{-4}	for $v^*_{\mathrm{ref}} = v^*_{\mathrm{EHD}}$
Peclet number	Pe	–	$\frac{v^*_{\mathrm{ref}} l^*_{\mathrm{ref}}}{D^*_\pm}$	0.5	for $v^*_{\mathrm{ref}} = v^*_{\mathrm{EHD}}$
electrolyte strength	α	–	–	$\gg 1$	
dimensionless field strength	β	–	$\frac{E^*_\infty l^*_{\mathrm{ref}}}{\phi^*_{\mathrm{th}}}$	$4 \cdot 10^3$	
dimensionless Debye length	δ	–	$\frac{l^*_{\mathrm{D}}}{l^*_{\mathrm{ref}}}$	10^{-5}	

Table 3.3: Reference parameters, scales, and dimensionless numbers of the SY model. The estimated values give an overview of the relative size of the parameters in the SY model. Yet, they can vary significantly with different materials and field strengths. Schnitzer and Yariv (2015)

is the definition using the EHD velocity based on the thermal potential. Alternatively, the outer electric field could be used to define a similar EHD velocity as Saville (1997) does. Thus, in some contexts, the latter is denoted as Péclet number while the dimensionless number based on the thermal potential is also called drag coefficient.

We note that the interface conditions 3.31 do not allow the particle to migrate or to deform. The study is yet important for a number of reasons. In contrast to the models discussed before, it comprises a detailed analysis of the diffuse charge layers near the interface. For that purpose, an asymptotic approach for strong electric fields and thin Debye layers is applied

$$1 \ll \beta \ll \frac{1}{\delta}. \tag{3.34}$$

In the bulk, the electric potential is assumed to be of $O(\beta)$, leading to an $O(\beta^2)$ electric stress which is balanced by an equal hydrodynamic stress. Thus, velocities and pressure are assumed to be of $O(\beta^2)$. The mean charge is postulated to be of $O(1)$ while the charge density is of $O(\delta^2\beta)$ due to Poisson's equation.

For the analysis of the Debye layer, the coordinate normal to the surface x^1 is rescaled as

$$\vec{n} \cdot \vec{x} = \delta X \tag{3.35}$$

where X is the stretched coordinate. As the analysis is based on two small parameters δ and β^{-1}, the following expansions are introduced

$$\begin{aligned} C_\pm &= C_{\pm(0,0)} + \delta\beta C_{\pm(1,-1)} + \dots \\ \Phi &= \beta\Phi_{\pm(0,-1)} + \Phi_{\pm(0,0)} + \delta\beta\Phi_{\pm(1,-1)} + \dots \\ V^\parallel &= \beta^2 V^\parallel_{\pm(0,-2)} + \beta V^\parallel_{\pm(0,-1)} + \delta\beta V^\parallel_{\pm(1,-1)} + \dots \end{aligned} \tag{3.36}$$

Using the continuity condition together with the impermeability condition of the interface, the normal velocity is found to be $V^\perp \sim O(\delta\beta^2)$. Here, we used capital letters for the Debye-layer parameters while the bulk parameters are still denoted with small letters. The orders of a parameter are denoted with the index in brackets, with the first number referring to the Debye-layer thickness and the second one to the electric field.

Although we omit the details of the analysis, it must be noted that Schnitzer and Yariv (2015) were, in contrast to Baygents and Saville (1990), able to match inner and outer regions and derive a closed model. Therefore, this work is discussed here. Now, we jump directly to the discussion of the resulting model

$$\begin{aligned} \epsilon\nabla^2\phi &= 0 && \text{Laplacian of the potential,} \\ \vec{\nabla}\cdot\xi &= 0 && \text{Stokes flow,} \\ \vec{\nabla}\cdot\vec{v} &= 0 && \text{incompressibility condition.} \end{aligned} \tag{3.37}$$

Together with the resulting jump conditions

$$\begin{aligned}
\vec{n}\cdot[\![\epsilon\vec{\nabla}\phi]\!]_\gamma &= q_\gamma && \text{surface charge,}\\
[\![\phi]\!]_\gamma &= 0 && \text{continuity of the el. potential,}\\
\vec{n}\times[\![\vec{v}]\!]_\gamma &= 0 && \text{continuity of the tangential velocity field,}\\
\vec{n}\cdot\vec{v} &= 0 && \text{impermeability,}\\
[\![\xi^{\perp\perp}]\!]_\gamma &= [\![\frac{1}{2}\epsilon\left((\partial_\perp\phi)^2-\left(\partial_\parallel\phi\right)^2\right)]\!]_\gamma && \text{normal stress jump,}\\
[\![\xi^{\perp\parallel}]\!]_\gamma &= q_\gamma\vec{\nabla}_\parallel\phi && \text{shear stress jump.}
\end{aligned} \tag{3.38}$$

In contrast to the physical surface Γ, we introduce here the apparent surface γ which includes the detailed physics of the thin layers on both sides of the surface. To stress the difference between the two jump conditions, the effective boundary conditions are denoted by $[\![\ldots]\!]_\gamma$ The apparent surface charge

$$q_\gamma = [\![\epsilon\vec{\nabla}\phi]\!]_\gamma \tag{3.39}$$

results from the jump in the displacement field. Note that the relations 3.31 and 3.39 are not the same despite their similar structure. Both surface charges are related by

$$q_\gamma = q_\Gamma + \int_{-\infty}^{\infty} Q\,\mathrm{d}X, \tag{3.40}$$

where the latter term is the effective surface charge of the two Debye layers.

Another important but controversial result of the model is the conductivity ratio

$$\frac{\varsigma_{\text{in}}}{\varsigma_{\text{ex}}} = \frac{\eta_{\text{in}}}{\eta_{\text{ex}}}\sqrt{\frac{\varkappa_{+,\text{ex}}\varkappa_{-,\text{ex}}}{\varkappa_{+,\text{in}}\varkappa_{-,\text{in}}}} \tag{3.41}$$

of both phases that are denoted with $(..)_{\text{in}}$ for the internal drop phase and $(..)_{\text{ex}}$ for the external suspending phase. Alternatively, we can use the parameter ratios (the permittivity ratio is mentioned for completeness)

$$R := \frac{\varsigma_{\text{in}}}{\varsigma_{\text{ex}}}, \quad S := \frac{\epsilon_{\text{in}}}{\epsilon_{\text{ex}}}, \quad M := \frac{\eta_{\text{in}}}{\eta_{\text{ex}}}, \tag{3.42}$$

to get

$$R = M\sqrt{\frac{\varkappa_{+,\text{ex}}\varkappa_{-,\text{ex}}}{\varkappa_{+,\text{in}}\varkappa_{-,\text{in}}}}. \tag{3.43}$$

As already mentioned, the latter result is controversial as the bulk conductivities of both phases would depend on the interface properties. However, one would assume the conductivities to be independent material properties of the electrolytes, and thus also their ratio. This contradiction cannot be resolved by Schnitzer and Yariv (2015). Another point of criticism is the absence of Debye layer charge transport due to convection or

electromigration in the model, which appears in the model of Melcher and Taylor (1969) (cp. eq. 3.11) and Saville (1997) (cp. eq. 3.29). Despite this critique, Schnitzer and Yariv (2015) derive a closed model with a detailed analysis of the diffuse layers. It is capable of predicting droplet deformation, as e.g. calculated by Torza, Cox, Mason, and Taylor (1971). They also claim that their model includes droplet migration at higher orders without providing a detailed analysis.

In summary, the SY model is built from an asymptotic analysis, while the earlier models discussed in this manuscript (Melcher & Taylor, 1969; Saville, 1997) were built from an empirical point of view. The discrepancies regarding conductivity, droplet migration, surface convection and surface conduction are addressed by Mori and Young (2018), whose study is discussed in the following.

3.4 The connection between full electrokinetics and the EHD regime by Mori & Young

One recent study addressing fluid-fluid interface phenomena was performed by Mori and Young (2018). It addresses a number of research questions, the most important of which are:

- For weak electrolytic solutions, can a model be derived considering the thin-Debye-layer limit?
- Is the conductivity ratio really a surface property as concluded by Schnitzer and Yariv (2015)?
- Under which conditions can surface convection and surface conduction be observed?
- Under which conditions can particle migration be observed?

The model is set up in a similar way to Saville (1997). The governing equations are

$$\begin{aligned}
\delta^2\nabla^2\phi + q &= 0 && \text{Poisson's equation,}\\
\partial_t c_\pm + \vec{\nabla}\cdot\vec{j}_\pm &= \mathrm{Da}\,\alpha^{-1}\mathcal{R}_c && \text{conservation of each ion species,}\\
\partial_t s + \vec{\nabla}\cdot\vec{j}_s &= -\mathrm{Da}\mathcal{R}_c && \text{conservation of salt,}\\
\vec{\nabla}\cdot(\xi+\theta) &= 0 && \text{conservation of momentum,}\\
\vec{\nabla}\cdot\vec{v} &= 0 && \text{incompressibility condition.}
\end{aligned} \tag{3.44}$$

The corresponding boundary conditions at the interface are

$$\begin{aligned}
\vec{n}\cdot[\![\epsilon\vec{\nabla}\phi]\!] &= 0 && \text{absence of surface charge,}\\
\cdot[\![\phi]\!] &= 0 && \text{potential continuity,}\\
c_{\pm,\mathrm{in}} &= l_{\pm}c_{\pm,\mathrm{ex}} && \text{ion partition coefficients,}\\
s_{\mathrm{in}} &= l_s s_{\mathrm{ex}} && \text{salt partition coefficient,}\\
\vec{n}\cdot[\![\vec{j}_{\pm}]\!] &= 0 && \text{continuity of surface current,}\\
[\![\xi+\theta]\!]\cdot\vec{n} &= -\delta^{-2}\sigma_{\Gamma}\kappa\vec{n} && \text{surface tension,}\\
\vec{n}\times[\![\vec{v}]\!] &= 0 && \text{continuity of the tangential velocity field,}\\
\vec{n}\cdot[\![\vec{v}]\!] &= 0 && \text{impermeability.}
\end{aligned} \tag{3.45}$$

Here, the dimensionless reaction term, in analogy to relation, reads 3.22 defined as

$$\mathcal{R}_c = k_{\mathrm{d}}s - k_{\mathrm{a}}c_{+}c_{-}. \tag{3.46}$$

In contrast to the studies discussed above, this model contains the scalar surface-tension term σ_{Γ}. At the interface, the charge distributions are in general not continuous. This incontinuity is accounted for by the partition coefficients $l_{\pm}$. There are two important aspects to these parameters. The first one is their derivation from the electrochemical potential equilibria at the interface Γ

$$\begin{aligned}
w^*_{+,\mathrm{in}} + \mathrm{R}^*T^*_{\mathrm{a}}\ln c^*_{+\mathrm{in}} + \mathrm{Fa}^*\phi^*_{\mathrm{in}} &= w^*_{+,\mathrm{ex}} + \mathrm{R}^*T^*_{\mathrm{a}}\ln c^*_{+\mathrm{ex}} + \mathrm{Fa}^*\phi^*_{\mathrm{ex}}\\
w^*_{-,\mathrm{in}} + \mathrm{R}^*T^*_{\mathrm{a}}\ln c^*_{-\mathrm{in}} - \mathrm{Fa}^*\phi^*_{\mathrm{in}} &= w^*_{-,\mathrm{ex}} + \mathrm{R}^*T^*_{\mathrm{a}}\ln c^*_{-\mathrm{ex}} - \mathrm{Fa}^*\phi^*_{\mathrm{ex}}
\end{aligned} \tag{3.47}$$

where the energies $w^*_{\pm,\mathrm{in}}$ and $w^*_{\pm,\mathrm{ex}}$ reflect inner solvation energies of each species. Using the potential continuity condition 3.44, we find

$$\begin{aligned}
c^*_{\pm\mathrm{in}} &= l_{\pm}c^*_{\pm\mathrm{ex}},\\
l_{\pm} &= \exp\left(\frac{w^*_{\pm,\mathrm{ex}} - w^*_{\pm,\mathrm{in}}}{\mathrm{R}^*T^*_{\mathrm{a}}}\right).
\end{aligned} \tag{3.48}$$

The second aspect is the connection between the dissociation equilibrium and the partition coefficients. Due to relation 3.48, the partition coefficients depend on the solvation energy. One of our basic assumptions is that the electrolytes contain only completely dissolved ions. For details of the energy analysis we refer to Mori and Young (2018) (Appendix A). The result of this examination is

$$\frac{l_{+}l_{-}}{l_s} = \frac{K^*_{\mathrm{equ,in}}}{K^*_{\mathrm{equ,ex}}}. \tag{3.49}$$

Although not having discussed the analysis yet, we can note already that the ion distributions at the interface are not independent of the dissociation reaction. This is in contrast to the model by Schnitzer and Yariv (2015), who conclude the conductivity ratio to be a function on interface properties. The MY model can resolve this contradiction by deriving the partition coefficients from bulk properties, i.e. the equilibrium constants.

reference parameter	**symbol**	**unit**	**definition**	**estimate**	**comments**
length scale	l^*_{ref}	m	–	10^{-3}	
velocity scale	v^*_{ref}	$\mathrm{m\,s^{-1}}$	$\frac{\epsilon^*_0 \epsilon {\phi^*_{\mathrm{th}}}^2}{l^*_{\mathrm{ref}} \mu}$	$2 \cdot 10^{-11}$	in. EHD velocity
time scale	t^*_{ref}	s	$\frac{l^*_{\mathrm{ref}}}{v^*_{\mathrm{ref}}}$	$2 \cdot 10^{3}$	
pressure scale	p^*_{ref}	Pa	$\frac{\epsilon^*_0 \epsilon {\phi^*_{\mathrm{th}}}^2}{{l^*_{\mathrm{ref}}}^2}$	$0.5 \cdot 10^{-6}$	
relative permittivity	ϵ	–	–	4	e.g. some oils
conductivity	ς^*	$\mathrm{S\,m^{-1}}$	–	10^{-9}	down to 10^{-12}
viscosity	η^*	Pa s	–	1	e.g. oil, glycerine
reference ion concentration	c^*_{ref}	$\mathrm{m^{-3}}$	–	10^{20}	$10^{-7}\,\mathrm{mol}\,l^{-1}$
surface tension	σ^*_Γ	$\mathrm{N\,m^{-1}}$	–	10^{-3}	
parameter	**symbol**	**unit**	**definition**		
thermal potential	ϕ^*_{th}	V	$\frac{k^*_{\mathrm{B}} T^*_{\mathrm{a}}}{\mathcal{Z} e^*_0}$	$25 \cdot 10^{-3}$	
applied electric field	E^*_∞	$\mathrm{V\,m^{-1}}$	–	10^{3}	
diffusion coefficients	$D^*_\pm$	$\mathrm{m^2\,s^{-1}}$	–	10^{-12}	
Debye length	l^*_{D}	m	$\sqrt{\frac{\epsilon^*_0 \epsilon \phi^*_{\mathrm{th}}}{\mathcal{Z} e^*_0 c^*_{\mathrm{ref}}}}$	$1.8 \cdot 10^{-7}$	
reference surface tension	$\sigma^*_{\Gamma,\mathrm{ref}}$	$\mathrm{N\,m^{-1}}$	$c^*_{\mathrm{ref}} \mathrm{R}^* T^*_{\mathrm{a}} l^*_{\mathrm{ref}}$	$0.7 \cdot 10^{-3}$	
dimensionless parameter	**symbol**	**unit**	**definition**		
Reynolds number	Re	–	–	$\ll 1$	
Peclet number	Pe	–	$\frac{v^*_{\mathrm{ref}} l^*_{\mathrm{ref}}}{D^*_\pm}$	$2.7 \cdot 10^{-2}$	for $v^*_{\mathrm{ref}} = v^*_{\mathrm{EHD}}$
electrolyte strength	α	–	–	10^{-4}	
dimensionless field strength	β	–	$\frac{E^*_\infty l^*_{\mathrm{ref}}}{\phi^*_{\mathrm{th}}}$	$O(1)$	
dimensionless Debye length	δ	–	$\frac{l^*_{\mathrm{D}}}{l^*_{\mathrm{ref}}}$	$1.8 \cdot 10^{-4}$	

Table 3.4: Reference parameters, scales and dimensionless numbers of the MY model. The estimated values give an overview of the relative size of the parameters in the MY model. Yet, they can vary significantly with different materials and field strengths. Mori and Young (2018)

An overview on the important parameters is given in table 3.4. These parameters are similar to the ones used by Saville (1997) (cp. table 3.2). However, the definition of the velocity scale is different. Saville used the outer electric field to define an extrinsic EHD velocity, while Mori and Young (2018) use the intrinsic EHD velocity with a comparably small thermal potential. Although this definition is identical to the one by Schnitzer and Yariv (2015), the choice of a more viscous fluid with $\eta^* = 1$ Pa s leads to very small values for the reference velocity and the diffusion coefficients. This basic set of parameters is valid for a viscous fluid, such as oil or glycerin, with a comparably small amount of charges. It is varied by Mori and Young (2018) for a number of experimental settings in order to investigate the effects of surface conduction / convection and particle migration.

3.4.1 The weak electrolyte limit

The assumption of a weak electrolytic solution with $\alpha \ll 1$ is valid throughout all variations of the model. For $\alpha \to 0$, one can find from the ion conservation in 3.44 that the reaction term $\mathcal{R}_c = 0$. This leads to the convection-diffusion equation for the salt distribution

$$\partial_t s + \vec{\nabla} \cdot \vec{j}_s = 0. \tag{3.50}$$

For a setting with open streamlines far from the interface, the salt distribution is constant along the streamlines and thus takes the equilibrium value

$$s = \begin{cases} s_{\mathrm{ref,ex}} = 1, & \Omega_{\mathrm{ex}} \\ s_{\mathrm{ref,in}} = l_s, & \Omega_{\mathrm{in}} \end{cases}. \tag{3.51}$$

By taking the difference of both ion transport equations, we find the transport of charge density

$$\begin{aligned} \partial_t q + \vec{\nabla} \cdot \vec{j}_q &= 0, \\ \vec{j}_q &= \mathrm{Pe}\, \vec{v} q - c\vec{\nabla}\phi - \vec{\nabla} q. \end{aligned} \tag{3.52}$$

The condition $\mathcal{R}_c = 0$ delivers together with 3.46 an algebraic expression relating the concentrations of both charge species

$$c_+ c_- = \frac{k_{\mathrm{d}}}{k_{\mathrm{a}}} s. \tag{3.53}$$

Here, similarly to Saville (1997), it is assumed that the deviation of the rate constants from the corresponding equilibrium rate constants can be neglected,

$$\begin{aligned} k_{\mathrm{d}}^* &= k_{\mathrm{d,equ}}^*, \\ k_{\mathrm{a}}^* &= k_{\mathrm{a,equ}}^*. \end{aligned} \tag{3.54}$$

Together with eq. 3.49 we obtain

$$K := \frac{k_{\mathrm{d}}}{k_{\mathrm{a}}} = \begin{cases} 1 =: K_{\mathrm{ex}}, & \Omega_{\mathrm{ex}} \\ \frac{k_{\mathrm{d,equ,in}}}{k_{\mathrm{a,equ,in}}} = \frac{K_{\mathrm{equ,in}}^*}{K_{\mathrm{equ,ex}}^*} = \frac{l_+ l_-}{l_s} =: K_{\mathrm{in}}, & \Omega_{\mathrm{in}} \end{cases}. \tag{3.55}$$

The assumption that the reaction rate constants are constant in each region was also made earlier by Saville (1997). However, the derived model is not affected by this assumption as it does not comprise a Debye-layer analysis. The MY model however can only be derived with the strong assumption of constant reaction rates, as we will show now.

The discussed simplifications lead to a new set of three equations for the ion species and the salt concentration consisting of relations 3.51, 3.52, and 3.53. The relations 3.51 and 3.53 deliver

$$\begin{aligned} c_+ &= \frac{q}{2} + \frac{c}{2} \\ c_- &= -\frac{q}{2} + \frac{c}{2} \\ c &= \sqrt{q^2 + 4Ks} \\ q &= \sqrt{c^2 - 4Ks} \\ Ks &= \begin{cases} 1, & \Omega_{\text{ex}}, \\ l_+ l_-, & \Omega_{\text{in}} \end{cases}. \end{aligned} \tag{3.56}$$

Thus, if the charge density q can be computed from the transport eq. 3.52 with $c = \sqrt{q^2 + 4Ks}$, then all concentrations are known from the relations 3.56. Using this simplified model for $\alpha \ll 1$, three different experimental settings are discussed that we briefly summarize in the following.

3.4.2 Re-constitution of the TM model for large-Pe flow

The diffuse-layer analysis is performed in the small-Debye limit $\delta \to 0$. As the weak electrolyte limit $\alpha \to 0$ was applied before, the relation

$$\alpha \ll \delta \ll 1 \tag{3.57}$$

must hold. It is further assumed that the Péclet number and the dimensionless surface tension have the sizes

$$\text{Pe} \sim O\left(\delta^{-2}\right), \quad \sigma_\Gamma \sim O\left(\delta^2\right), \quad \text{and} \quad \beta \sim O(1). \tag{3.58}$$

and that the partition coefficients are equal $l_+ = l_-$. For the analysis of the Debye layer, a stretched coordinate $X = \delta^{-1}\vec{x} \cdot \vec{n}$ is introduced. The physical parameters are extended in orders of δ. The innner (Debye) region, and outer (bulk) region parameters follow the same expansion as the charge density

$$q = q_{(0)} + \delta q_{(1)} + \dots. \tag{3.59}$$

The asymptotic analysis delivers the set of bulk equations

$$\begin{aligned} \nabla^2 \phi &= 0 && \text{irrotational electric field,} \\ c &= \text{const.} && \text{bulk conductivity,} \\ \vec{\nabla} \cdot \xi &= 0 && \text{conservation of momentum,} \\ \vec{\nabla} \cdot \vec{v} &= 0 && \text{incompressibility condition,} \end{aligned} \tag{3.60}$$

and the boundary conditions, inheriting the detailed physics of the diffuse layers

$$\begin{aligned}
[\![\phi]\!] &= 0 && \text{continuity of the el. potential,}\\
\vec{n}\cdot[\![\epsilon\vec{E}]\!] &= q_\Gamma && \text{surface charge,}\\
\partial_t q_\Gamma + \kappa v_\perp q_\Gamma + \vec{\nabla}_\parallel\cdot\left(\vec{v}_\parallel q_\Gamma\right) &= [\![c\nabla_\perp\phi]\!] && \text{surface current,}\\
[\![\xi+\theta]\!]\cdot\vec{n} &= -\vec{n}\kappa\sigma_\Gamma && \text{surface tension,}\\
\vec{n}\times[\![\vec{v}]\!] &= 0 && \text{continuity of the tangential velocity field,}\\
\vec{n}\cdot[\![\vec{v}]\!] &= 0 && \text{continuity of the normal velocity field.}
\end{aligned} \tag{3.61}$$

This result is very close to the model originally suggested by Melcher and Taylor (1969). However, it was derived from a detailed diffuse-layer analysis and additionally considers surface tension. The aim of investigating the diffuse layers is e.g. the understanding of surface conduction effects. As mentioned above, the absence of charge separation due to $l_+ = l_-$, leads to a continuous charge distribution near the interface. We will refer to this composition as electric mono-layer (EML).

3.4.3 Charge transport in the surface: Surface convection and conduction

The surface current equation in the set of boundary conditions 3.61 describes the charge transport inside the diffuse layer. Although this equation cannot be solved analytically, an analysis of stagnation points can give more insight into the structure of the boundary layer. Mori and Young (2018) derived the condition

$$-\vec{\nabla}^*_\parallel\cdot\vec{v}^*_\parallel < t^*_C \tag{3.62}$$

under which such a layer exists. Here $t_c = \frac{\epsilon^*_0\epsilon}{\varsigma^*}$is the charge relaxation time or Maxwell-Wagner time scale.

For the investigation of surface conduction under stronger electric fields Mori and Young (2018) suggest a re-scaling of Péclet number, Debye length, and Damköhler number with the dimensionless el. field strength

$$\delta_E = \sqrt{\beta}\delta, \quad \mathrm{Pe}_E = \beta\mathrm{Pe}, \quad \mathrm{Da}_E = \beta^{-1}\mathrm{Da}. \tag{3.63}$$

This results in a a re-scaled version of the equations already obtained for surface convection and leads to a similar condition for the existence of surface conduction.

3.4.4 Particle migration

The assumption of strong convection (large Péclet number) and absence of charge separation (equal partition coefficients) leads to the model discussed in section 3.4.2 which is similar to the one proposed by Melcher and Taylor (1969). However, the effect of particles migrating under an applied outer electric field cannot be explained by that model.

A different experimental setup is necessary to observe this phenomenon. Therefore, Mori and Young (2018) consider

$$\mathrm{Pe} \sim O(1), \quad \sigma_\Gamma \sim O(\delta), \quad l_+ \neq l_-, \quad \text{and} \quad \beta \sim O(1). \tag{3.64}$$

They observe particle migration in their model which results from the existence of a Galvani potential

$$\phi_\mathrm{G} = [\![\phi]\!] = \frac{1}{2} \ln \frac{l_+}{l_-} \tag{3.65}$$

and predict a migration velocity depending on the mismatches between conductivities, viscosities, and permittivities between the two phases.

We include a correction of the migration velocity derived by Mori and Young (2018). The shear stress jump given in equation (5.95) with a sign mistake corrected reads (note that the notation of the original paper is used in this equation)

$$\begin{aligned}\left[\mu\left(\frac{\partial v_0^i}{\partial \xi} + g^{ij}\frac{\partial u_0}{\partial \eta^j}\right)\right] = &\left(\kappa_0\left(\epsilon_\mathrm{in}\phi_\mathrm{in}^\Delta + \epsilon_\mathrm{ex}\phi_\mathrm{ex}^\Delta\right) + \left(\frac{\epsilon_\mathrm{in}}{\sigma_\mathrm{in}} - \frac{\epsilon_\mathrm{ex}}{\sigma_\mathrm{ex}}\right) J_0\right) g^{ij}\frac{\partial \phi_0}{\partial \eta^j} \\ &-2\left(\frac{\epsilon_\mathrm{in}}{\sigma_\mathrm{in}}\phi_\mathrm{in}^\Delta + \frac{\epsilon_\mathrm{ex}}{\sigma_\mathrm{ex}}\phi_\mathrm{ex}^\Delta - I_J\right) g^{ij}\frac{\partial J_0}{\partial \eta^j}\end{aligned} \tag{3.66}$$

The correction of the sign mistake leads to the additional term marked in blue. It translates to the notation used in the following chapter as

$$[\![\xi^{\perp\parallel}]\!] = -\left(\kappa_0\left(\zeta - S\bar{\zeta}\right) + (S-R)\, j_{(0)}\right) g^{ij}\frac{\partial \phi_0}{\partial \eta^j} + 2\left(\zeta - \frac{S}{R}\bar{\zeta} - I_J\right) g^{ij}\frac{\partial j_{(0)}}{\partial \eta^j} \tag{3.67}$$

As a result, the migration velocity of the droplet now reads

$$V_\mathrm{mgr} = \frac{-2E_\infty}{(2+3M)(2+R)}\left(R(3-4M)\bar{\zeta} + (2+M-2R)\zeta\right) + f(I_J). \tag{3.68}$$

A strong-electrolyte model is presented in chapter 4 featuring similar assumptions and results. Thus, the corrected migration velocity is discussed in section 4.3. The critics discussed in chapter 4 of this work led to the corrigendum (Marthaler, Class, Mori, & Young, 2023) to the original paper by Mori and Young (2018).

3.5 Other important studies

We have discussed four seminal studies on fluid-fluid interface models in this section in order to give an overview on the most important developments in the field. However, this overview cannot claim completeness. Some of the important publications that have only been mentioned as a side note or not been mentioned at all are by Baygents and Saville (1990), Pascall and Squires (2011), and Ma et al. (2022). Especially the aforementioned publication derives a strong-electrolyte model with a detailed analysis of the inner layer. Other important aspects are the higher Péclet number (due to choosing a different time scale) and the impermeability of the interface to ions. Small deformations different from the ones proposed by Taylor (1966) could be observed possibly explaining some experimental observations.

3.6 Comparison of the models and a generalizing formulation

In the previous section, a variety of modeling approaches is discussed. Their differences are not limited to the assumptions, but also include notation and terminology. This section suggests a formulation that is general and can be reduced to the models discussed earlier. For that reason, we introduce a formulation of the governing equations for EHD problems in dimensionless form. The respective boundary conditions are not discussed here, as they are more specific to each problem. Without loss of generality, we assume a symmetric binary electrolyte solution. Thus, we find a transport equation for the salt concentration and the concentrations of the two ion species that are related by the dissociation equilibrium

$$\mathcal{S} \rightleftharpoons \mathcal{C}_+ + \mathcal{C}_-. \tag{3.69}$$

The equations governing the charge transport and the electric potential read

$$\begin{aligned} \partial_t^* s^* + \vec{\nabla}^* \cdot \left(\vec{v}^* s^* - D_s^* \vec{\nabla}^* s^* \right) &= - \left(k_\mathrm{d}^* s^* - k_\mathrm{a}^* c_+^* c_-^* \right), \\ \partial_t^* c_\pm^* + \vec{\nabla}^* \cdot \left(\vec{v}^* c_\pm^* - D_\pm^* \vec{\nabla}^* c_\pm^* \mp \mu^* c_\pm^* \vec{\nabla}^* \phi^* \right) &= k_\mathrm{d}^* s^* - k_\mathrm{a}^* c_+^* c_-^*, \\ \epsilon \epsilon_0^* {\nabla^*}^2 \phi^* &= -e_0^* \mathcal{Z} q^*. \end{aligned} \tag{3.70}$$

The flow is governed by the conservation equations of momentum and mass

$$\begin{aligned} 0 &= \rho^* \partial_t^* \vec{v}^* + \vec{\nabla}^* \cdot \left(\xi_\mathrm{conv}^* + \xi^* + \theta^* \right), \\ 0 &= \vec{\nabla}^* \cdot \vec{v}^*. \end{aligned} \tag{3.71}$$

In the momentum equation, the stress tensors ξ_conv^*, ξ^*, and θ^* (covective, viscous, electric stress) are rank-2 tensors representing flow convection, viscous stress, and electric stress. The two latter stress tensors are important for this work and read

$$\begin{aligned} \xi^* &= -p^* + \eta^* (\vec{\nabla}^* \vec{v}^*) + (\vec{\nabla}^* \vec{v}^*)^\top, \\ \theta^* &= \epsilon_0^* \epsilon \left(-\frac{1}{2} \vec{\nabla}^* \phi^* \cdot \vec{\nabla}^* \phi^* + \vec{\nabla}^* \phi^* \otimes \vec{\nabla}^* \phi^* \right). \end{aligned} \tag{3.72}$$

We use a number of general reference parameters l_ref^*, v_ref^*, c_equ^*, ϕ_ref, $k_\mathrm{d/a,equ}^*$, for length, time, velocity, concentration, and potential, and the reaction rates. The time is scaled as $t_\mathrm{ref}^* = l_\mathrm{ref}^* {v_\mathrm{ref}^*}^{-1}$, the pressure as $p_\mathrm{ref}^* = \eta^* v_\mathrm{ref}^* {l_\mathrm{ref}^*}^{-1}$ and the convective stress with $\rho^* {v_\mathrm{ref}^*}^2$. The dimensionless momentum equation reads

$$\mathrm{Re}\, \partial_t^* \vec{v} + \vec{\nabla} \cdot \left(\mathrm{Re}\, \xi_\mathrm{conv} + \xi + \mathrm{Ha} \beta^2\, \theta \right) = 0, \qquad \mathrm{Re} = \frac{\rho^* v_\mathrm{ref}^* l_\mathrm{ref}^*}{\eta^*}. \tag{3.73}$$

In the problems discussed in this work, the Reynolds number is small, usually because of the small length scale l_ref^*. Thus, the transient and convective term is neglected and the

set of governing equations reduces to

$$\begin{aligned}
\mathrm{Pe}_s \partial_t s + \vec{\nabla} \cdot \left(\mathrm{Pe}_\pm \, \vec{v} s - \vec{\nabla} s \right) &= -\frac{\mathrm{Da}}{\alpha} \left(k_\mathrm{d} s - k_\mathrm{a} c_+ c_- \right), \\
\mathrm{Pe}_\pm \partial_t c_\pm + \vec{\nabla} \cdot \left(\mathrm{Pe}_\pm \, \vec{v} c_\pm - \vec{\nabla} c_\pm \mp \beta c_\pm \vec{\nabla} \phi \right) &= \frac{\mathrm{Da}}{\alpha} \left(k_\mathrm{d} s - k_\mathrm{a} c_+ c_- \right), \\
\delta^2 \beta \, \nabla^2 \phi &= -q, \\
\vec{\nabla} \cdot \left(\xi + \mathrm{Ha} \beta^2 \, \theta \right) &= 0, \\
\vec{\nabla} \cdot \vec{v} &= 0.
\end{aligned} \tag{3.74}$$

The dimensionless parameters are

$$\begin{aligned}
&\text{Péclet numbers:} && \mathrm{Pe}_\pm &&= \frac{v^*_\mathrm{ref} l^*_\mathrm{ref}}{D^*_\pm}, && \mathrm{Pe}_s &&= \frac{v^*_\mathrm{ref} l^*_\mathrm{ref}}{D^*_s}, \\
&\text{Damköhler number:} && \mathrm{Da} &&= \frac{k^*_\mathrm{d,equ} v^*_\mathrm{ref}}{l^*_\mathrm{ref}}, \\
&\text{Hartmann number:} && \mathrm{Ha} &&= \frac{v^*_\mathrm{EHD}}{v^*_\mathrm{ref}}, && v^*_\mathrm{EHD} &&= \frac{\epsilon^*_0 \epsilon \phi^{*2}_\mathrm{th}}{l^*_\mathrm{ref} \eta^*}, \\
&\text{Electrolyte strength:} && \alpha &&= \frac{c^*_\mathrm{equ}}{s^*_\mathrm{equ}}, \\
&\text{Dimensionless Field strength:} && \beta &&= \frac{\phi^*_\mathrm{ref}}{\phi^*_\mathrm{th}}, && \phi^*_\mathrm{th} &&= \frac{k^*_\mathrm{B} T^*_\mathrm{a}}{\mathcal{Z} e^*_0}, \\
&\text{Dimensionless Debye length:} && \delta &&= \frac{l^*_\mathrm{D}}{l^*_\mathrm{ref}}, && l^*_\mathrm{D} &&= \sqrt{\frac{\epsilon \epsilon^*_0 \phi^*_\mathrm{th}}{e^*_0 \mathcal{Z} c^*_\infty}}.
\end{aligned} \tag{3.75}$$

The number of six free parameters can in most cases be reduced by assuming either a strong or weak electrolytic solution, i.e. $\alpha \to 0$ or $\alpha \to \infty$. As a result, the electrolyte strength α, the Damköhler number Da, and the Péclet number for the salt species Pe_s vanish from the system. In the following step a matched asymptotic solution can be derived assuming the dimensionless Debye thickness to be small $\delta \ll 1$. Further common assumptions are the choice of $v^*_\mathrm{ref} = v^*_\mathrm{EHD}$ and $\phi^*_\mathrm{ref} = \phi^*_\mathrm{th}$ leading to $\mathrm{Ha} = 1$ and $\beta = 1$ respectively. The remaining free parameters are the Péclet numbers for the two ion species $\mathrm{Pe}_\pm$. Assuming equal diffusion coefficients for both species, both Péclet numbers take the same value $\mathrm{Pe}_\pm = \mathrm{Pe}$.

A comparison between the models reviewed in this chapter is summarized in table 3.5. We note that electromigration phenomena could only be observed with the recent models capturing the Debye-layer electrokinetics. However, while Mori and Young (2018) derived quantitative predictions for weak electrolytes, Schnitzer and Yariv (2015) concluded the particle to migrate without quantitative results. This leads to two main questions:

- Can particle migration also be observed for strong electrolytes under moderate electric fields?
- If yes, what are the quantitative differences in the migration velocity for weak and strong electrolytic solutions?

authors	**important assumptions**	**observed phenomena**
Melcher and Taylor (1969)	weak electrolytes, no charge diffusion, no Debye-layer effects	(cellular) convection, particle rotation, shear-induced instabilities
Saville (1997)	weak electrolytes, moderate el. fields, no Debye-layer effects	drop stability, electrodeformation
Schnitzer and Yariv (2015)	strong electrolytes, strong el. fields, Debye-layer effects	electromigration (qual.)
Mori and Young (2018)	weak electrolytes moderate el. fields, Debye-layer effects	electromigration (quant.) electrodeformation
Mori and Young (2018)	weak electrolytes strong el. fields, Debye-layer effects	surface conduction

Table 3.5: Overview of modeling approaches discussed in this chapter. The right column refers to if electrokinetic effects at the interface are modeled.

These questions are addressed in the following chapter by deriving the missing model. Beyond the phenomenon of electromigration, general conclusions on the effect of electrolyte strength and electrokinetic transport are made.

CHAPTER 4

A strong-electrolyte fluid-fluid interface model

This chapter presents a two-phase model connecting Debye-layer electrokinetics to the macroscopic electrohydrodynamics. The main objective is to understand the influence of electrolyte strength on electromigration. An asymptotic analysis of the Debye layer delivers effective boundary conditions for the apparent interface. We note that those conditions depend not only on the outer applied electric field, but also on outer concentration gradients. Comparison to the weak-electrolyte model by Mori and Young (2018) reveals partly analogous results, but also differences due to distinct geometrical modeling of the surface.

4.1 Model

4.1.1 Set-up

The dilute electrolyte problem shall be characterized by the dissociation equilibrium

$$\mathcal{S} \rightleftharpoons \mathcal{C}_+ + \mathcal{C}_- \tag{4.1}$$

between the neutral salt and two charged ion species with equal valences $\mathcal{Z}$. We assume that this reaction is valid in both the domain of the suspending fluid Ω and the interior drop domain $\bar{\Omega}$ as depicted in Figure 4.1. In general, the diffusion coefficients of the ion species D_+^* and D_-^* are not equal[1]. Without loss of generality, we assume the diffusivities of both positive species to be equal, as well as the diffusivities of both negative species. The reaction equilibrium is described by the equilibrium constants K^* and $\bar{K}^*$ respectively. Both fluids with the electric permittivities ϵ, $\bar{\epsilon}$ and dynamic viscosities η^*, $\bar{\eta}^*$ are assumed to have equal densities ρ^*. The thermal voltage of the problem is defined by $\phi_{\mathrm{th}}^* = \frac{k_{\mathrm{B}}^* T_{\mathrm{a}}^*}{\mathcal{Z} e^*}$ where k_{B}^* is the Boltzmann constant and T_{a}^* the ambient temperature. The parameters mentioned in this paragraph are all assumed to be uniform in space and time.

[1] We will use the superscript $(..)^*$ for all parameters with dimensions while all parameters without an asterix are dimensionless.

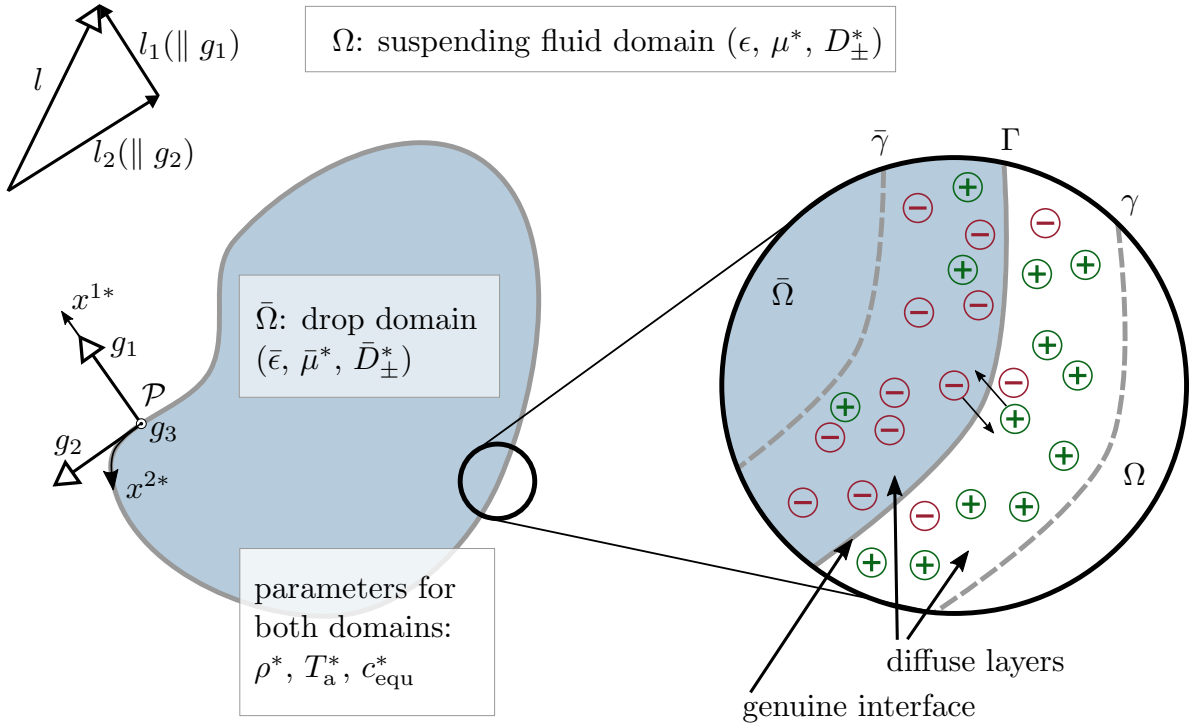

Figure 4.1: Schematic overview of physical parameters and geometry.

The conservation of the charge concentration $c^*_\pm$, the salt concentration s^* and displacement field $\epsilon^*_0\epsilon\nabla^*\phi^*$ are governed by the Nernst-Planck equations and the Poisson equation

$$\begin{aligned} \partial^*_t c^*_\pm + \left(\vec{\nabla}^* \cdot \vec{v}^*\right) c^*_\pm + \vec{\nabla}^* \cdot \vec{j}_\pm &= R^*, \\ \partial^*_t s^* + \left(\vec{\nabla}^* \cdot \vec{v}^*\right) s^* &= -R^*, \\ -\vec{\nabla}^* \cdot \left(\epsilon^*_0\epsilon\, \vec{\nabla}^*\phi^*\right) &= q^*. \end{aligned} \tag{4.2}$$

The reaction terms $R^* = k^*_\mathrm{d} s^* - k^*_\mathrm{a} c^*_+ c^*_-$ on the right hand side of the charge and salt equations contain the rates of dissociation k^*_d and association k^*_a. We further define the charge fluxes as

$$\vec{j}^*_\pm = D^*_\pm \left(-\vec{\nabla}^* c^*_\pm \mp c^*_\pm \vec{\nabla}^*\phi^*\right). \tag{4.3}$$

An equivalent description of the charges can be made by defining the two parameters

$$\begin{aligned} q^* &= \frac{1}{2}\left(c^*_+ - c^*_-\right), \\ c^* &= \frac{1}{2}\left(c^*_+ + c^*_-\right). \end{aligned} \tag{4.4}$$

Here, the charge density q^* accounts for the local net charge while the mean charge concentration c^* represents a measure for the local conductivity of the electrolyte. We will later refer to the the sum and difference of both charge fluxes (divided by two) that

we define as

$$\begin{aligned}\vec{j}_q^* &= -\vec{\nabla}^* \left(D_+^* c_+^* - D_-^* c_-^*\right) - \left(D_+^* c_+^* + D_-^* c_-^*\right) \vec{\nabla}^* \phi^*, \\ \vec{j}_c^* &= -\vec{\nabla}^* \left(D_+^* c_+^* + D_-^* c_-^*\right) - \left(D_+^* c_+^* - D_-^* c_-^*\right) \vec{\nabla}^* \phi^*.\end{aligned} \tag{4.5}$$

The system is complemented by the Stokes equations for viscous flow

$$\begin{aligned}\vec{\nabla}^* \cdot \sigma^* &= 0, \\ \vec{\nabla}^* \cdot \vec{v}^* &= 0.\end{aligned} \tag{4.6}$$

The total stress $\sigma^* = \xi^* + \theta^*$ is composed of hydrodynamic (Newton) and electric (Maxwell) stresses

$$\begin{aligned}\xi^* &= -p^* + \eta^* (\vec{\nabla}^* \vec{v}^*) + (\vec{\nabla}^* \vec{v}^*)^\top, \\ \theta^* &= \epsilon_0^* \epsilon \left(-\frac{1}{2} \vec{\nabla}^* \phi^* \cdot \vec{\nabla}^* \phi^* + \vec{\nabla}^* \phi^* \otimes \vec{\nabla}^* \phi^* \right),\end{aligned} \tag{4.7}$$

with the hydrostatic pressure p^*, the velocity field $\vec{v}^*$, and the electric potential ϕ^*. The equations for the drop domain $\bar{\Omega}$ are written in the analogous form.

4.1.2 Dimensionless form

When the chemical reaction 4.1 is at equilibrium, i.e. $R^* = 0$, the amounts of positive and negative ions are equal $c_{+,\mathrm{equ}}^* := c_{+,\mathrm{equ}}^* = c_{-,\mathrm{equ}}^*$. Together with the equilibrium constant $K^* = \frac{k_{\mathrm{d,equ}}^*}{k_{\mathrm{a,equ}}^*}$ we find

$$\begin{aligned}0 &= k_{\mathrm{d,equ}}^* s_{\mathrm{equ}}^* - k_{\mathrm{a,equ}}^* c_{\mathrm{equ}}^{*^2}, \\ 0 &= K^* s_{\mathrm{equ}}^* - c_{\mathrm{equ}}^{*^2}.\end{aligned} \tag{4.8}$$

We define the concentrations and reaction rates at equilibrium as references. As reference length, we use an intrinsic length of the drop, e.g. its radius. Together with the thermal voltage and a reference scale as scale for the electric potential, we can introduce the EHD velocity as reference velocity

$$v_{\mathrm{EHD}}^* = \frac{\epsilon_0^* \epsilon \phi_{\mathrm{th}}^{*2}}{l_{\mathrm{ref}}^* \eta^*}. \tag{4.9}$$

An overview of all reference scales is displayed in table 4.1. The governing equations in non-dimensional form are

$$\begin{aligned}\mathrm{Pe} \left(\partial_t c_\pm + \left(\vec{\nabla} \cdot \vec{v} \right) c_\pm \right) + \vec{\nabla} \cdot \vec{j}_\pm &= \frac{\mathrm{Da}}{\alpha} \left(k_\mathrm{d} s - k_\mathrm{a} c_+ c_- \right), \\ \mathrm{Pe} \left(\partial_t s + \left(\vec{\nabla} \cdot \vec{v} \right) s \right) &= -\mathrm{Da} \left(k_\mathrm{d} s - k_\mathrm{a} c_+ c_- \right), \\ -\delta^2 \nabla^2 \phi &= q. \\ \vec{\nabla} \cdot \sigma &= \vec{0}, \\ \vec{\nabla} \cdot \vec{v} &= 0.\end{aligned} \tag{4.10}$$

$$\phi^* = \phi^*_{\mathrm{th}}\phi = \frac{k^*_{\mathrm{B}}T^*_{\mathrm{a}}}{\mathcal{Z}e^*}\phi \qquad c^*_{\pm} = c^*_{\mathrm{equ}}c_{\pm} \qquad k^*_{\mathrm{d,a}} = k^*_{\mathrm{d,a,equ}}k_{\mathrm{d,a}}$$
$$D^*_{\pm} = \frac{1}{2}\left(D^*_{+} + D^*_{-}\right)D_{\pm} = D^*D_{\pm} \qquad \vec{v}^* = v^*_{\mathrm{EHD}}\vec{v}_{\mathrm{ref}} = \frac{\epsilon^*_0\epsilon\phi^{*2}_{\mathrm{th}}}{l^*_{\mathrm{ref}}\eta^*}\vec{v} \qquad t^* = \frac{l^*_{\mathrm{ref}}}{v^*_{\mathrm{EHD}}}t = t^*_{\mathrm{EHD}}t$$
$$p^* = \frac{\eta^* v^*_{\mathrm{EHD}}}{l^*_{\mathrm{ref}}}p \qquad l^{*2}_{\mathrm{D}} = \frac{\epsilon^*_0\epsilon\phi^*_{\mathrm{th}}}{2\mathcal{Z}e^*_0c^*_{\mathrm{equ}}}$$

Table 4.1: Parameter scaling

$$\mathrm{Pe} = \frac{l^*_{\mathrm{ref}}v^*_{\mathrm{EHD}}}{D^*} = \frac{\epsilon^*_0\epsilon\phi^{*2}_{\mathrm{th}}}{D^*\eta^*} \qquad \delta = \frac{l^*_{\mathrm{D}}}{l^*_{\mathrm{ref}}} \qquad \mathrm{Da} = t^*_{\mathrm{EHD}}k^*_{\mathrm{D,equ}}$$
$$\alpha = \frac{c^*_{\mathrm{equ}}}{s^*_{\mathrm{equ}}} \qquad S = \frac{\bar{\epsilon}}{\epsilon} \qquad M = \frac{\bar{\eta}^*}{\eta^*}$$

Table 4.2: Dimensionless numbers

The charge equations may be written in the alternative form for q and c

$$\begin{aligned}\mathrm{Pe}\left(\partial_t q + \left(\vec{\nabla}\cdot\vec{v}\right)q\right) + \vec{\nabla}\cdot\vec{j}_q &= 0,\\ \mathrm{Pe}\left(\partial_t c + \left(\vec{\nabla}\cdot\vec{v}\right)c\right) + \vec{\nabla}\cdot\vec{j}_c &= \frac{\mathrm{Da}}{\alpha}\left(k_{\mathrm{d}}s - k_{\mathrm{a}}c_+c_-\right).\end{aligned} \tag{4.11}$$

The charge fluxes used in the above equations for the two ion species, as well as charge density and mean charge concentration are

$$\begin{aligned}\vec{j}_{\pm} &= D_{\pm}\left(-\vec{\nabla}c_{\pm} \mp c_{\pm}\vec{\nabla}\phi\right),\\ \vec{j}_q &= -\vec{\nabla}\left(D_+c_+ - D_-c_-\right) - \left(D_+c_+ + D_-c_-\right)\vec{\nabla}\phi,\\ \vec{j}_c &= -\vec{\nabla}\left(D_+c_+ + D_-c_-\right) - \left(D_+c_+ - D_-c_-\right)\vec{\nabla}\phi.\end{aligned} \tag{4.12}$$

So far all of the equations in non-dimensionalized form can be used for both regions Ω and $\bar{\Omega}$ respectively. However, the Newton and Maxwell stresses

$$\begin{aligned}\xi &= -p + (\vec{\nabla}\vec{v}) + (\vec{\nabla}\vec{v})^{\top},\\ \theta &= -\frac{1}{2}\vec{\nabla}\phi\cdot\vec{\nabla}\phi + \vec{\nabla}\phi\otimes\vec{\nabla}\phi,\\ \bar{\xi} &= M\left(-\bar{p} + (\vec{\nabla}\vec{\bar{v}}) + (\vec{\nabla}\vec{\bar{v}})^{\top}\right),\\ \bar{\theta} &= S\left(-\frac{1}{2}\vec{\nabla}\bar{\phi}\cdot\vec{\nabla}\bar{\phi} + \vec{\nabla}\bar{\phi}\otimes\vec{\nabla}\bar{\phi}\right)\end{aligned} \tag{4.13}$$

differ by their viscosity and permittivity ratios $M = \frac{\bar{\eta}^*}{\eta^*}$ and $S = \frac{\bar{\epsilon}^*}{\epsilon^*}$

4.1.3 Properties of the liquid-liquid interface

The interface separating the two electrolytes exhibits both, hydromechanical and electrical properties. The ratio of charge concentrations on each side of the interface is defined by

the partition coefficients l_+, l_-, and l_S which result in the boundary condition

$$\begin{aligned} \bar{c}_{\pm,\Gamma} &= l_\pm c_{\pm,\Gamma}, \\ \bar{s}_\Gamma &= l_S s_\Gamma. \end{aligned} \tag{4.14}$$

In accordance with Mori and Young (2018), we define the partition coefficients using the equilibrium constants of the respective electrolyte solutions

$$\frac{l_+ l_-}{l_S} = \frac{K}{\bar{K}}. \tag{4.15}$$

Thus, the conductivities in both domains do not depend on interface properties, but on the dissociation equilibrium of each electrolyte. We further assume the interface to be permeable for ion fluxes and find the continuity of fluxes, potential and displacement field

$$\begin{aligned} \left(\vec{j}_{\pm,\Gamma} - \bar{\vec{j}}_{\pm,\Gamma}\right) \cdot \vec{n} &= 0, \\ \phi_\Gamma - \bar{\phi}_\Gamma &= 0, \\ \partial_1(\phi_\Gamma) - \partial_1(S\bar{\phi}_\Gamma) &= 0. \end{aligned} \tag{4.16}$$

A controversial discussion is ongoing addressing the question if the interface is permeable to ions and if so, under which conditions (Gschwend, Olaya, Peljo, & Girault, 2020; Mareček & Samec, 2017). For simplicity, we assume a permeable interface, noting that other studies, e.g. Ma et al. (2022), do not allow ions to pass through. The hydrodynamic properties consist of continuity of velocities and a stress jump which is

$$\begin{aligned} v_\Gamma^j - \bar{v}_\Gamma^j &= 0, \\ \sigma_\Gamma^{11} - \bar{\sigma}_\Gamma^{11} &= t_\Gamma\, \kappa, \\ \sigma_\Gamma^{1\alpha} - \bar{\sigma}_\Gamma^{1\alpha} &= 0 \end{aligned} \tag{4.17}$$

where κ is the curvature and t_Γ is the surface tension coefficient of the interface, which is assumed to be sufficiently large that the interface stays stable.

4.1.4 Remarks on parameter dimensions

A common approach in experimental settings is to use aqueous solutions with a millimolar concentration of sodium chloride. Under such conditions, the thermal voltage is ~ 25 mV and the diffuse layers at the interface typically have a thickness of about 10 nm. With particle sizes of at least 1 µm, rather 10 - 100 µm, the assumption of $\delta \ll 1$ holds. We further assume that the mean diffusion coefficient of both ion species is of the order $10^{-9}\frac{\mathrm{m}^2}{\mathrm{s}}$ which corresponds via the Stokes-Einstein Relation to an ion radius of 0.2 nm. In his derivation of the leaky dielectric model, Saville (1997) estimated the ion radius to be between 0.14 nm and 0.25 nm. The resulting time and velocity scales are 2 ms and $0.5\frac{\mathrm{mm}}{\mathrm{s}}$.

4.1.5 Strong electrolyte limit

This work focuses on strong electrolytes. We assume for the electrolyte strength that $\alpha^{-1} \ll \delta \ll 1$. Applying $\alpha \gg 1$ to the equations 4.10 and 4.11, we find

$$\begin{aligned} \mathrm{Pe}\left(\partial_t c_\pm + \left(\vec{\nabla}\cdot\vec{v}\right)c_\pm\right) + \vec{\nabla}\cdot\vec{j}_\pm = 0, \\ \mathrm{Pe}\left(\partial_t s + \left(\vec{\nabla}\cdot\vec{v}\right)s\right) = -\mathrm{Da}\left(k_\mathrm{d} s - k_\mathrm{a} c_+ c_-\right). \end{aligned} \tag{4.18}$$

Here, the salt conservation is decoupled from the ion equations. The electroneutral salt does not have any influence on the fluiddynamic behavior and will not be further considered in our analysis. However, with knowledge of the ion concentrations, the salt concentration can always be re-established from the last relation.

4.1.6 Thin-Debye-layer limit

The Debye layer is assumed to be thin, i.e. $\delta \ll 1$. It can be used as a small parameter, such that the expansion holds

$$f \sim f_{(0)} + \delta f_{(1)} + \dots. \tag{4.19}$$

At leading order, the set of equations for the bulk reads

$$\begin{aligned} \vec{\nabla}\cdot\vec{j}_q &= 0, \\ q_{(0)} &= 0. \\ \mathrm{Pe}\left(\partial_t c_{(0)} + \vec{v}_{(0)}\cdot\vec{\nabla}c_{(0)}\right) - \nabla^2 c_{(0)} &= 0, \\ \vec{\nabla}\cdot\sigma_{(0)} &= \vec{0}, \\ \vec{\nabla}\cdot\vec{v}_{(0)} &= 0. \end{aligned} \tag{4.20}$$

The first of the above equations reads in detail

$$0 = -D_\Delta \nabla^2 c_{(0)} - \vec{\nabla}\cdot\left(c_{(0)}\vec{\nabla}\phi\right) \tag{4.21}$$

with the two combined diffusion coefficients

$$\begin{aligned} D = D_+ + D_- &= \frac{D_+^* + D_-^*}{D_+^* + D_-^*} = 1, \\ D_\Delta := D_+ - D_- &= \frac{D_+^* - D_-^*}{D_+^* + D_-^*} \end{aligned} \tag{4.22}$$

and for the $\bar{\Omega}$ domain

$$0 = -\bar{D}_\Delta \nabla^2 c_{(0)} - \bar{D}\vec{\nabla}\cdot\left(c_{(0)}\vec{\nabla}\phi\right) \tag{4.23}$$

with the two combined diffusion coefficients

$$\begin{aligned} \bar{D} = \bar{D}_+ + \bar{D}_- &= \frac{\bar{D}_+^* + \bar{D}_-^*}{\bar{D}_+^* + \bar{D}_-^*}, \\ \bar{D}_\Delta := \bar{D}_+ - \bar{D}_- &= \frac{\bar{D}_+^* - \bar{D}_-^*}{\bar{D}_+^* + \bar{D}_-^*}. \end{aligned} \tag{4.24}$$

The vanishing divergence of the flux $\vec{j}_{q(0)}$ allows for gradients in the ion concentration. This holds either locally or as a result of inhomogeneous boundary conditions, e.g. if the domain is located between two reservoirs of constant concentration, but in the absence of ion exchange (when a membrane separates the domains). The bulk equations for the strong electrolyte reduce to those of the weak electrolyte for uniform ion concentrations $c_{(0)} = 1$ or for equal diffusion coefficients, i.e $D_\Delta = 0$. For the weak electrolyte limit, compare Mori and Young (2018) or appendix B.

4.1.7 Geometry in tensor notation

The present discussion of the conservation equations in the vicinity of an interface follows Aris (1989), which we refer to for more details in the tensorial notation. We assume that at each point $\mathcal{P}$ of the interface the contravariant coordinate x^1 is perpendicular to the surface (cp. 4.1). Thus, the base vector g^1 is at all positions normal to the tangential base vectors g^α [2]. The resulting contravariant metric g^{ij} has the special properties $g^{11} = 1$ and $g^{1\alpha} = 0$. We further define the volume element $\sqrt{g} = \sqrt{\det g_{ij}} = \sqrt{\det g^{ij}}^{-1}$. We use Ricci's lemma[3] to find

$$\begin{aligned} 0 = g^{11}_{,j} = \partial_j g^{11} + 2\Gamma^1_{jl} g^{1l} = 2\Gamma^1_{1j} \quad &\Rightarrow \quad \Gamma^1_{1j} = 0, \\ 0 = g^{1\alpha}_{,1} = \partial_1 g^{1\alpha} + \Gamma^1_{1l} g^{\alpha l} + \Gamma^\alpha_{1l} g^{1l} = \Gamma^\alpha_{11} \quad &\Rightarrow \quad \Gamma^\alpha_{11} = 0. \end{aligned} \tag{4.25}$$

Here, Γ^i_{jk} represents the Christoffel symbols of the second kind. We also define the curvature of a surface defined by constant x^1 as

$$\kappa := \frac{1}{\sqrt{g}} \partial_1 \sqrt{g}. \tag{4.26}$$

Taking the volume element into account, the equations for strong electrolytes read in contravariant form

$$\begin{aligned} \mathrm{Pe}\left(\partial_t\left(\sqrt{g}c_\pm\right) + \partial_j\left(\sqrt{g}v^j c_\pm\right)\right) + \partial_j\left(\sqrt{g}j^j_\pm\right) &= 0, \\ \delta^2 \partial_j\left(\sqrt{g}\partial_i\phi\right) &= -\sqrt{g}q. \\ \sigma^{ij}_{,j} &= 0, \\ \partial_j\left(\sqrt{g}v^j\right) &= 0 \end{aligned} \tag{4.27}$$

and for the $\bar{\Omega}$-domain

$$\begin{aligned} \mathrm{Pe}\left(\partial_t\left(\sqrt{g}\bar{c}_\pm\right) + \partial_j\left(\sqrt{g}\bar{v}^j \bar{c}_\pm\right)\right) + \partial_j\left(\sqrt{g}\bar{j}^j_\pm\right) &= 0, \\ S\,\delta^2 \partial_j\left(\sqrt{g}g^{ij}\partial_i\bar{\phi}\right) &= -\sqrt{g}\bar{q}. \\ \bar{\sigma}^{ij}_{,j} &= 0, \\ \partial_j\left(\sqrt{g}\bar{v}^j\right) &= 0. \end{aligned} \tag{4.28}$$

Details on the derivation of the momentum equation in curvilinear coordinates are shifted to appendix A.

[2] We refer to the tangential directions with Greek indices, e.g., $\alpha \in \{2, 3\}$ and use latin indices to include all directions $i \in \{1, 2, 3\}$.

[3] Ricci's lemma says that the covariant and contravariant metrics are both constant with respect to covariant differentiation. Here, we use the contravariant metric to derive simplifications for the Christoffel symbols.

4.1.8 Geometrical expansions

We expand the geometrical parameters into a power series of the small parameter δ. Alternatively to a power series, we can use a Taylor series expansion which is convergent in close vicinity to the surface of interest for $x^1 = 0$. The following expansions hold

$$\begin{aligned} g_{ij} &= g_{ij(0)}\left(x^\alpha\right) + \delta X g_{ij(1)}\left(x^\alpha\right) + O(\delta^2), \\ g^{ij} &= g^{ij}_{(0)}\left(x^\alpha\right) + \delta X g^{ij}_{(1)}\left(x^\alpha\right) + O(\delta^2), \\ \sqrt{g} &= \sqrt{g}_{(0)}\left(x^\alpha\right) + \delta X \sqrt{g}_{(1)}\left(x^\alpha\right) + O(\delta^2), \\ \kappa &= \kappa_{(0)}\left(x^\alpha\right) + \delta X \kappa_{(1)}\left(x^\alpha\right) + O(\delta^2), \\ \Gamma^i_{jk} &= \Gamma^i_{jk(0)}\left(x^\alpha\right) + \delta X \Gamma^i_{jk(1)}\left(x^\alpha\right) + O(\delta^2). \end{aligned} \tag{4.29}$$

We note that the surface metrics $g_{\alpha\beta(0)}$ and $g_{\alpha\beta(1)}$ are the first and second fundamental forms of the surface. The leading-order curvature term $\kappa_{(0)}$ is the sum of the principal curvatures of the surface, i.e. two times the mean curvature and can be expressed using the expansion of the volume element or the fundamental forms of the surface

$$\kappa_{(0)} = \frac{\sqrt{g}_{(1)}}{\sqrt{g}_{(0)}} = g_{\alpha\beta(1)} g^{\alpha\beta}_{(0)}. \tag{4.30}$$

The first-order curvature

$$\kappa_{(1)} = 2\frac{\sqrt{g}_{(2)}}{\sqrt{g}_{(0)}} - \kappa^2_{(0)} \tag{4.31}$$

can also be expressed using the volume element. This term vanishes for problems with only weakly non-orthogonal coordinates, e.g. spherical coordinates.

4.2 Debye cloud analysis

We derived the outer solution of our problem in section 4.1.6. Thus, we focus in this chapter on the inner regions of the diffuse layers. The normal coordinate is stretched by the layer thickness, resulting in the stretched coordinate X which is given by

$$x^1 = \delta X. \tag{4.32}$$

We expand the inner parameters (denoted in capital letters) in powers of δ

$$\begin{aligned} \Phi &= \Phi_{(0)} + \delta\Phi_{(1)} + \dots \\ C_\pm &= C_{\pm(0)} + \delta C_{\pm(1)} + \dots \\ Q &= Q(0) + \delta Q_{(1)} + \dots \\ C &= C_{(0)} + \delta C_{(1)} + \dots \\ V^1 &= \delta V^1_{(1)} + \dots \\ V^\alpha &= V^\alpha_{(0)} + \dots \\ P &= \delta^{-2} P_{(-2)} + \delta^{-1} P_{(-1)} + P_{(0)} + \dots \end{aligned} \tag{4.33}$$

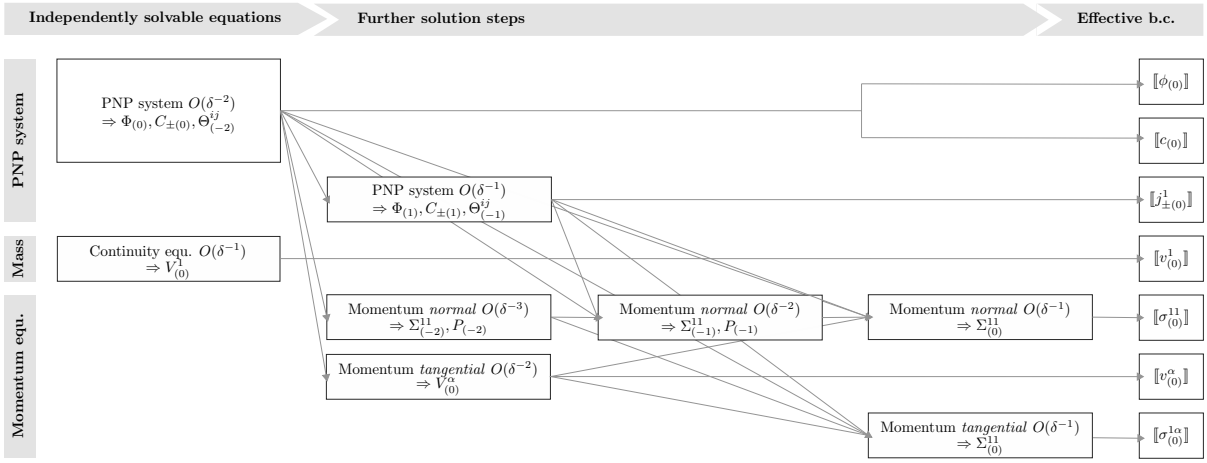

Figure 4.2: Solution scheme of the Debye-layer problem leading to the effective boundary conditions for the macroscopic problem.

As a result, the stresses and charge fluxes are expanded in the orders

$$\begin{aligned}
\Sigma^{11} &= \delta^{-2}\Sigma^{11}_{(-2)} + \delta^{-1}\Sigma^{11}_{(-1)} + \Sigma^{11}_{(0)} + \dots, \\
\Sigma^{1\alpha} &= \delta^{-1}\Sigma^{1\alpha}_{(-1)} + \Sigma^{1\alpha}_{(0)} + \dots, \\
\Sigma^{\alpha\beta} &= \delta^{-2}\Sigma^{\alpha\beta}_{(-2)} + \delta^{-1}\Sigma^{\alpha\beta}_{(-1)} + \Sigma^{\alpha\beta}_{(0)} + \dots, \\
J^1_\pm &= \delta^{-1}J^1_{\pm(-1)} + J^1_{\pm(0)} + \dots, \\
J^\alpha_\pm &= J^\alpha_{\pm(0)} + \dots .
\end{aligned} \tag{4.34}$$

We also assume the surface tension t_Γ to be of $O(\delta^{-1})$ so that the following expansion holds

$$t_\Gamma = \delta^{-1}t_{\Gamma(-1)} + t_{\Gamma(0)} + \dots . \tag{4.35}$$

We will later see that a large surface tension is necessary to balance the electric stresses at the interface and to avoid the particle from collapsing.

The asymptotic solution procedure is displayed in Figure 4.2. We start with the electric Poisson-Nernst Planck problem which decouples and can be solved independently of the hydrodynamic problem. The leading order of the continuity equation can also be solved independently. The momentum equation is split up in its normal and tangential directions. Their derivation can be found in appendix A. Three orders of the normal momentum equation and two orders of the tangential momentum equation are solved to deliver the effective boundary conditions for the flow field. Note, that we use the two notations $\Box_\gamma - \bar{\Box}_\gamma = [\![\Box]\!]$ for the effective jump conditions.

The apparent boundary γ appears as a jump condition for the macroscopic problem at $\lim_{x^1\to 0}$ and as the far-field boundary for the Debye-cloud analysis. Thus, we denote the integration constants with the subscript $\Box_\gamma$. In reality, the transition between both domains is smooth which is accounted for by the asymptotic scheme.

4.2.1 Electric problem at order δ^{-2}

The leading-order electric problem can be described as a two-phase Gouy-Chapman problem (cp. section 2.2.4). The solution for two-phase problem presented here has been discussed by other authors before, i.e. by Ma et al. (2022). Although starting from different equations, the solution for the weak-electrolyte problem derived by Mori and Young (2018) is identical.

As the leading order electric fluxes are of size $O(\delta^{-1})$, we need to solve two orders of the electric problem. The charge conservation 4.27 of $O(\delta^{-2})$ reads

$$0 = \partial_X J^1_{\pm(-1)}. \tag{4.36}$$

From our assumption 4.19 we know that the respective fluxes $j^i_{\pm(-1)}$ in the outer domain vanish. Thus, the far-field condition

$$\lim_{X\to\infty} J^1_{\pm(-1)} = 0 \tag{4.37}$$

holds and we can integrate equation 4.36 with respect to X and obtain

$$0 = J^1_{\pm(-1)} = -C'_{\pm(0)} - C_{\pm(0)}\Phi'_{(0)}. \tag{4.38}$$

In order to solve this equation, we need a far-field boundary condition for the inner electric potential which reads

$$\lim_{X\to\infty} \Phi_{(0)}(X, x^\alpha) = \lim_{x^1\to 0} \phi_{(0)}(x^1, x^\alpha) = \phi_\gamma(x^\alpha). \tag{4.39}$$

It is a common approach to define the excess potential Ψ as the electric potential that is observed in the Debye layer in addition to the outer potential as

$$\Psi(X, x^\alpha) := \Phi_{(0)} - \phi_\gamma(x^\alpha). \tag{4.40}$$

We can now integrate equation 4.38 and obtain for the charge distributions

$$\begin{aligned} C_{\pm(0)} &= c_\gamma e^{\mp\Psi}, \\ Q_{(0)} &= -c_\gamma \sinh\Psi, \\ C_{(0)} &= c_\gamma \cosh\Psi. \end{aligned} \tag{4.41}$$

The integration constants read

$$\lim_{X\to\infty} C_{\pm(0)}(X, x^\alpha) = \lim_{x^1\to 0} c_{\pm(0)}(x^1, x^\alpha) = c_\gamma(x^\alpha). \tag{4.42}$$

At leading order, the Poisson equation in 4.27 reads

$$\Psi'' + Q_{(0)} = 0. \tag{4.43}$$

Plugging in the result for the charge density 4.41 yields

$$\Psi'' - c_\gamma \sinh\Psi = 0. \tag{4.44}$$

From relations 4.39 and 4.40 we obtain that $\lim_{X\to\infty} \Psi = 0$ and thus $\lim_{X\to\infty} \Psi' = 0$. We can integrate equation 4.44 to find

$$\Psi' = -2\sqrt{c_\gamma}\sinh\frac{\Psi}{2}. \tag{4.45}$$

The above result is adapted to the aforementioned boundary condition $\lim_{X\to\infty} \Psi' = 0$. A second integration with respect to X delivers the solution for the excess potential

$$\Psi = 2\ln\frac{1+\tanh\frac{\zeta}{4}e^{-\sqrt{c_\gamma}X}}{1-\tanh\frac{\zeta}{4}e^{-\sqrt{c_\gamma}X}}. \tag{4.46}$$

Here, we define the value of the excess potential at the interface according to $\Psi(X = 0) =: \zeta$. The ζ-potential is yet to be defined. Analogously, we find for the $\bar{\Omega}$-domain the results

$$\begin{aligned} \bar{C}_{\pm(0)} &= \bar{c}_\gamma e^{\mp\bar{\Psi}}, \\ \bar{\Psi}' &= 2\sqrt{c_\gamma/S}\sinh\frac{\bar{\Psi}}{2}, \\ \bar{\Psi} &= 2\ln\frac{1+\tanh\frac{\bar{\zeta}}{4}e^{\sqrt{\bar{c}_\gamma/S}X}}{1-\tanh\frac{\bar{\zeta}}{4}e^{\sqrt{\bar{c}_\gamma/S}X}}. \end{aligned} \tag{4.47}$$

To emphasize the similarities between the solutions for both domains we introduce the following abbreviations

$$\begin{aligned} \Psi' = 2B\sinh\frac{\Psi}{2} = \frac{4ABe^{BX}}{1-A^2e^{2BX}}, \quad \bar{\Psi}' = 2\bar{B}\sinh\frac{\bar{\Psi}}{2} = \frac{4\bar{A}\bar{B}e^{\bar{B}X}}{1-\bar{A}^2e^{2\bar{B}X}}, \\ \Psi = 2\ln\frac{1+Ae^{BX}}{1-Ae^{BX}}, \quad \bar{\Psi} = 2\ln\frac{1+\bar{A}e^{\bar{B}X}}{1-\bar{A}e^{\bar{B}X}}, \\ A := \tanh\frac{\zeta}{4} \quad \bar{A} := \tanh\frac{\bar{\zeta}}{4}, \\ B := -\sqrt{c_\gamma} \quad \bar{B} := \sqrt{\bar{c}_\gamma/S}. \end{aligned} \tag{4.48}$$

Using the ratios of charges at the interface 4.14 and the results in equations 4.41 and 4.47, we find the jump condition for the charges

$$\bar{c}_\gamma = \sqrt{l_+l_-}c_\gamma \quad \Rightarrow \quad R := \sqrt{l_+l_-}. \tag{4.49}$$

At this point, we also find the relation for the conductivity ratio R. We will later need the tangential derivatives of the charge

$$\partial_\alpha\bar{c}_\gamma = \sqrt{l_+l_-}\partial_\alpha c_\gamma \tag{4.50}$$

and especially the derivative of $\ln c_\gamma$ which is constant throughtout the inner regions, i.e. in the vicinity of the apparent interface

$$\partial_\alpha \ln\bar{c}_\gamma = \partial_\alpha \ln c_\gamma. \tag{4.51}$$

We note that in the weak electrolyte model c_γ is independent of x^α, and thus Ψ only depends on the normal coordinate X. We further find from the potential continuity in 4.16 a relation between the jump of ζ-potentials and the potentials at γ and $\bar{\gamma}$

$$\begin{aligned} \zeta - \phi_\gamma - \bar{\zeta} + \bar{\phi}_\gamma &= 0, \\ -\left(\phi_\gamma - \bar{\phi}_\gamma\right) &= \zeta - \bar{\zeta}. \end{aligned} \tag{4.52}$$

Here, the integration constant[4] $\bar{\phi}_\gamma$ is defined as

$$\lim_{X\to\infty} \bar{\Phi}_{(0)}(X, x^\alpha) = \lim_{x^1\to 0} \bar{\phi}_{(0)}(x^1, x^\alpha) = \bar{\phi}_\gamma(x^\alpha). \tag{4.53}$$

The boundary condition for the displacement field in 4.16 finally delivers the ζ-potentials

$$\zeta = \ln \frac{1+\sqrt{Sl_+}}{1+\sqrt{Sl_-}} \qquad \text{and} \qquad \bar{\zeta} = \ln \frac{1+(\sqrt{Sl_+})^{-1}}{1+(\sqrt{Sl_-})^{-1}} \tag{4.54}$$

which yields the potential jump

$$\phi_{\mathrm{G}} := \phi_\gamma - \bar{\phi}_\gamma = \frac{1}{2}\ln\frac{l_-}{l_+} \qquad \text{and} \qquad \zeta - \bar{\zeta} = -\frac{1}{2}\ln\frac{l_-}{l_+}. \tag{4.55}$$

In accordance with other authors (Ma et al., 2022; Mori & Young, 2018), We refer to the jump condition for the electric potential also as the Galvani potential ϕ_{G}.

4.2.2 Electric problem at order δ^{-1}

The δ^{-1}-order electric problem consists of two equations for the charges and one for the electric potential

$$\begin{aligned} 0 &= \partial_X J^1_{\pm(0)} + \kappa_{(0)} J^1_{\pm(-1)}, \\ 0 &= \Phi''_{(1)} + \kappa\, \Phi'_{(0)} + Q_{(1)}. \end{aligned} \tag{4.56}$$

We know from equation 4.38 that the $O\left(\delta^{-1}\right)$ flux vanishes and obtain

$$\begin{aligned} 0 &= \partial_X J^1_{\pm(0)}, \\ 0 &= \Phi''_{(1)} + \kappa\, \Phi'_{(0)} + Q_{(1)}. \end{aligned} \tag{4.57}$$

We use the boundary condition for the charge fluxes

$$\lim_{X\to\infty} J^1_{\pm(0)} = j^1_{\pm\gamma(0)} = \mp c_\gamma \phi'_\gamma \tag{4.58}$$

to integrate the first equation of 4.57 and obtain

$$j^1_{\pm\gamma(0)} = J^1_{\pm(0)} = -C'_{\pm(1)} \mp C_{\pm(1)}\Phi'_{(0)} \mp C_{\pm(0)}\Phi'_{(1)}. \tag{4.59}$$

[4]Note that we will from now on introduce integration constants of the forms $\square_\gamma$ and $\bar{\square}_\gamma$ without explicitly introducing their definition with the limits $\lim_{X\to\infty}$ and $\lim_{x^1\to\infty}$.

Together with the flux continuity condition 4.16, we find an effective boundary condition for the flux continuity between the two bulk domains

$$j^1_{\pm\gamma(0)} = \bar{j}^1_{\pm\gamma(0)}. \tag{4.60}$$

The homogeneous solution to the differential equation 4.59 is

$$C_{(1)\mathrm{h}} = \mp k_\pm e^{\mp\Psi}. \tag{4.61}$$

Variation of constants delivers for the particular solution with $k = k(X)$

$$\begin{aligned} j^1_{\pm\gamma(0)} &= \pm k'_\pm e^{\mp\Psi} - \cancel{k_\pm \Psi' e^{\mp\Psi}} + \cancel{k_\pm \Psi' e^{\mp\Psi}} \mp c_\gamma \Phi'_{(1)} e^{\mp\Psi}, \\ k'_\pm &= \Phi'_{(1)} \pm j^1_{\pm\gamma(0)} e^{\pm\Psi} = c_\gamma \left(\Phi'_{(1)} - \phi'_\gamma e^{\pm\Psi}\right). \end{aligned} \tag{4.62}$$

Introducing the parameters

$$\begin{aligned} E_\pm &:= \int e^{\pm\Psi} \mathrm{d}X = X + 4B^{-1}\left(1 \mp A e^{BX}\right)^{-1} - 4B^{-1}\left(1 \mp A\right)^{-1}, \\ \bar{E}_\pm &:= \int e^{\pm\bar{\Psi}} \mathrm{d}X = X + 4\bar{B}^{-1}\left(1 \mp \bar{A} e^{\bar{B}X}\right)^{-1} - 4\bar{B}^{-1}\left(1 \mp \bar{A}\right)^{-1}. \end{aligned} \tag{4.63}$$

Thus, the solutions for both phases read

$$\begin{aligned} C_{(1)} &= \mp c_\gamma k_\pm e^{\mp\Psi}, \qquad & k_\pm &= \Phi_{(1)} \pm \frac{j^1_{\pm\gamma(0)}}{c_\gamma} E_\pm + K_\pm, \\ \bar{C}_{(1)} &= \mp \bar{c}_\gamma \bar{k}_\pm e^{\mp\bar{\Psi}}, \qquad & \bar{k}_\pm &= \bar{\Phi}_{(1)} \pm \frac{\bar{j}^1_{\pm\gamma(0)}}{\bar{c}_\gamma} \bar{E}_\pm + \bar{K}_\pm. \end{aligned} \tag{4.64}$$

The interface condition 4.14 delivers

$$\bar{C}_{\pm(1)} = l_\pm C_{\pm(1)} \quad \Rightarrow \quad \bar{K}_\pm = K_\pm. \tag{4.65}$$

Without loss of generality, we assume that the $O(\delta)$ potential and charges vanish in the bulk regions, i.e.

$$\lim_{X\to\pm\infty} C_{\pm(1)},\, \bar{C}_{\pm(1)} = 0, \qquad \text{and} \qquad \lim_{X\to\pm\infty} \Phi_{(1)},\, \bar{\Phi}_{(1)} = 0. \tag{4.66}$$

We find the solution for the charge distributions (analogously for the drop phase $\bar{\Omega}$)

$$\begin{aligned} C_{\pm(1)} &= \mp c_\gamma \left(\Phi_{(1)} \pm \frac{j^1_{\pm\gamma(0)}}{c_\gamma} E_\pm\right) e^{\mp\Psi}, \\ Q_{(1)} &= -c_\gamma \Phi_{(1)} \cosh\Psi + \frac{1}{2}\left(j^1_{-\gamma} E_- e^{\Psi} + j^1_{+\gamma} E_+ e^{-\Psi}\right). \end{aligned} \tag{4.67}$$

Thus, the equations for the potential read

$$\begin{aligned} \Phi''_{(1)} - c_\gamma \Phi_{(1)} \cosh\Psi &= -\kappa\, \Psi' - \frac{1}{2}\left(j^1_{-\gamma} E_- e^{\Psi} + j^1_{+\gamma} E_+ e^{-\Psi}\right), \\ \bar{\Phi}''_{(1)} - \frac{\bar{c}_\gamma}{S} \bar{\Phi}_{(1)} \cosh\bar{\Psi} &= -\kappa\, \bar{\Psi}' - \frac{1}{2S}\left(\bar{j}^1_{-\gamma} \bar{E}_- e^{\bar{\Psi}} + \bar{j}^1_{+\gamma} \bar{E}_+ e^{-\bar{\Psi}}\right). \end{aligned} \tag{4.68}$$

The equations for the δ^1-potential are complemented by interface conditions which result from 4.16

$$\begin{aligned} \Phi_{(1),\Gamma} - \bar{\Phi}_{(1),\Gamma} &= 0, \\ \Phi'_{(1),\Gamma} - S\bar{\Phi}'_{(1),\Gamma} &= 0. \end{aligned} \tag{4.69}$$

At this point, we cannot solve equations 4.68 and 4.69 analytically. However, a solution for the problem with absent outer electrochemical gradients is discussed in section 4.2.10.

4.2.3 Pressure at order δ^{-2}

The leading order momentum equation A.25 that we derived in the appendix A reads

$$0 = {\Sigma^{11}_{(-2)}}' = {\Xi^{11}_{(-2)}}' + {\Theta^{11}_{(-2)}}'. \tag{4.70}$$

We use $\Xi^{11}_{(-2)} = -P_{(-2)}$ and $\Theta^{11}_{(-2)} = \frac{1}{2}{\Phi'_{(0)}}^2$ from table A.1 to find an expression for the pressure that we can solve together with the boundary condition

$$\begin{aligned} \lim_{X\to\infty} P_{(-2)} &= 0, \\ \lim_{X\to-\infty} \bar{P}_{(-2)} &= \bar{p}_{\gamma(-2)}, \end{aligned} \tag{4.71}$$

to find (we proceed in the $\bar{\Omega}$ domain analogously)

$$\begin{aligned} P_{(-2)} &= \frac{1}{2}{\Phi'_{(0)}}^2 = \frac{1}{2}\left(\Psi'\right)^2, \\ \bar{P}_{(-2)} &= \frac{1}{2}\frac{S}{M}\left(\bar{\Psi}'\right)^2 + \bar{p}_{\gamma(-2)}. \end{aligned} \tag{4.72}$$

As a result, the total stresses $\Sigma^{11}_{(-2)}$ and $\bar{\Sigma}^{11}_{(-2)}$ vanish at leading order. In order to compute the outer stress jump we use the interface condition

$$\Sigma^{11}_{(-2)}(X=0) - \bar{\Sigma}^{11}_{(-2)}(X=0) = 0, \tag{4.73}$$

which delivers $\bar{p}_{\gamma(-2)} = 0$ and

$$\bar{P}_{(-2)} = \frac{1}{2}\frac{S}{M}\left(\bar{\Psi}'\right)^2. \tag{4.74}$$

4.2.4 Pressure at order δ^{-1}

The $O\left(\delta^{-2}\right)$-momentum equation A.25 that we derived in appendix A reads

$$0 = {\Sigma^{11}_{(-1)}}' + \kappa_{(0)}\left(\Sigma^{11}_{(-2)} - \Sigma^{\bullet}_{(-2)}\right). \tag{4.75}$$

From the previous section 4.2.3 we know that the total stress $\Sigma^{11}_{(-2)} = 0$ throughout the inner layers. Thus, this relation simplifies to

$$0 = {\Sigma^{11}_{(-1)}}' - \kappa_{(0)}\,\Sigma^{\bullet}_{(-2)}. \tag{4.76}$$

We find from table A.1 that

$$\begin{aligned}
\Xi^{11}_{(-1)} &= -P_{(-1)},\\
\Theta^{11}_{(-1)} &= \Phi'_{(0)}\Phi'_{(1)} = \Psi'\Phi'_{(1)},\\
\Xi^{\bullet}_{(-2)} &= -P_{(-2)} = -\frac{1}{2}\left(\Psi'\right)^2,\\
\Theta^{\bullet}_{(-2)} &= -\frac{1}{2}{\Phi'_{(0)}}^2 = -\frac{1}{2}\left(\Psi'\right)^2,\\
\Sigma^{\bullet}_{(-2)} &= \Xi^{\bullet}_{(-2)} + \Theta^{\bullet}_{(-2)} = -\left(\Psi'\right)^2.
\end{aligned} \tag{4.77}$$

We substitute the above stresses into equation 4.76 to get an expression for the δ^{-1}-pressure

$$0 = \left(-P_{(-1)} + \Psi'\Phi'_{(1)}\right)' + \kappa_{(0)}\left(\Psi'\right)^2. \tag{4.78}$$

We assume that the pressure in the suspending-fluid bulk domain at $O\left(\delta^{-1}\right)$ to vanish with the respective pressure in the drop domain $\bar{p}_{\gamma(-1)}$ to be determined

$$\begin{aligned}
\lim_{X\to\infty} P_{(-1)} &= 0,\\
\lim_{X\to-\infty} P_{(-1)} &= \bar{p}_{\gamma(-1)}.
\end{aligned} \tag{4.79}$$

Integrating equation 4.78 together with the matching condition 4.79 delivers

$$\begin{aligned}
P_{(-1)} &= \Psi'\Phi'_{(1)} + \kappa_{(0)}\left(-I_\Psi\right),\\
-I_\Psi &:= \int_\infty^X \left(\Psi'\right)^2 \mathrm{d}\,\tilde{X}.
\end{aligned} \tag{4.80}$$

We have here defined the integral I_Ψ such that it is always positive. The resulting solution for the pressure is

$$\begin{aligned}
P_{(-1)} &= \Psi'\Phi'_{(1)} - \kappa_{(0)} I_\Psi,\\
I_\Psi &:= \int_X^\infty \left(\Psi'\right)^2 \mathrm{d}\,\tilde{X}.
\end{aligned} \tag{4.81}$$

Equivalently, the $\bar{\Omega}$ problem delivers

$$\begin{aligned}
\bar{P}_{(-1)} &= \frac{S}{M}\left(\bar{\Phi}'_{(0)}\bar{\Phi}'_{(1)} + \kappa_{(0)}\bar{I}_\Psi\right) + \bar{p}_{\gamma(-1)},\\
-\bar{I}_\Psi &:= \int_{-\infty}^X \left(\bar{\Psi}'\right)^2 \mathrm{d}\tilde{X}.
\end{aligned} \tag{4.82}$$

We can plug the results for the pressure back into the total stress and find

$$\begin{aligned}
\Sigma^{11}_{(-1)} &= -P_{(-1)} + \Psi'\Phi'_{(1)} = \kappa_{(0)} I_\Psi,\\
\bar{\Sigma}^{11}_{(-1)} &= -\bar{P}_{(-1)} + \bar{\Psi}'\bar{\Phi}'_{(1)} = -\frac{S}{M}\kappa_{(0)}\bar{I}_\Psi - p_{\gamma(-1)}.
\end{aligned} \tag{4.83}$$

Substituting this into the condition for the stress condition 4.17 at the interface Γ to find

$$\begin{aligned}
\kappa_{(0)} t_{\Gamma(-1)} &= \Sigma^{11}_{(-1)}(X=0) - \bar{\Sigma}^{11}_{(-1)}(X=0)\\
\kappa_{(0)} t_{\Gamma(-1)} &= \kappa_{(0)}\left[I_\Psi + \frac{S}{M}\bar{I}_\Psi\right]_{X=0} + \bar{p}_{\gamma(-1)}.
\end{aligned} \tag{4.84}$$

We define the electric and effective surface tension coefficients as

$$\begin{aligned} t_{\Gamma,\mathrm{el}(-1)} &= \left[I_\Psi + \frac{S}{M} \bar{I}_\Psi \right]_{X=0}, \\ t_{\Gamma,\mathrm{eff}(-1)} &= t_{\Gamma(-1)} - t_{\Gamma,\mathrm{el}(-1)}. \end{aligned} \tag{4.85}$$

We note that the surface tension of the interface needs to be larger than the electric surface tension for the drop not to collapse. With vanishing effective surface tension the pressure in the drop region also vanishes $\bar{p}_{\gamma(-1)} = 0$.

4.2.5 Normal velocity at $O(1)$

The normal velocity can be found from the continuity equation which at $O\left(\delta^{-1}\right)$ simply reads

$$V_{(0)}^{1\,\prime} = 0. \tag{4.86}$$

Integration with respect to X delivers

$$V_{(0)}^1 = v_{\gamma(0)}^1 \quad \text{and} \quad \bar{V}_{(0)}^1 = \bar{v}_{\gamma(0)}^1, \tag{4.87}$$

where

$$v_{\gamma(0)}^1 = \lim_{X\to\infty} V_{(0)}^1 \quad \text{and} \quad \bar{v}_{\gamma(0)}^1 = \lim_{X\to-\infty} V_{(0)}^1. \tag{4.88}$$

The velocity continuity condition 4.17 delivers

$$v_{\gamma(0)}^1 - \bar{v}_{\gamma(0)}^1 = 0, \tag{4.89}$$

an effective condition for the normal velocity.

4.2.6 Transverse Velocity at $O(1)$

We start with the shear tangential momentum equation at order δ^{-2} in equation A.26

$$0 = \Sigma_{(-1)}^{1\alpha\,\prime} + g_{(0)}^{\alpha\beta} \partial_\beta \Sigma_{(-2)}^{\bullet}. \tag{4.90}$$

With the stresses

$$\begin{aligned} \Xi_{(-1)}^{1\alpha} &= V_{(0)}^{\alpha\,\prime} \\ \Theta_{(-1)}^{1\alpha} &= g^{\alpha\beta} \Psi' \partial_\beta \Phi_{(0)} \\ \Xi_{(-2)}^{\bullet} &= -P_{(-2)} = -\frac{1}{2} \left(\bar{\Psi}' \right)^2, \\ \Theta_{(-2)}^{\bullet} &= -\frac{1}{2} \Phi_{(0)}'^{\,2} = -\frac{1}{2} \left(\bar{\Psi}' \right)^2, \end{aligned} \tag{4.91}$$

we get

$$\begin{aligned} 0 &= V_{(0)}^{\alpha\,\prime\prime} + g^{\alpha\beta} \Psi'' \partial_\beta \Phi_{(0)} + g^{\alpha\beta} \Psi' \partial_\beta \Psi' - g^{\alpha\beta} \partial_\beta \left(\bar{\Psi}' \right)^2, \\ 0 &= V_{(0)}^{\alpha\,\prime\prime} + g^{\alpha\beta} \Psi'' \partial_\beta \Phi_{(0)} - g^{\alpha\beta} \Psi' \partial_\beta \Psi', \\ V_{(0)}^{\alpha\,\prime\prime} &= g^{\alpha\beta} \left(\Psi' \partial_\beta \Psi' - \Psi'' \partial_\beta \Psi - \Psi'' \partial_\beta \phi_\gamma \right). \end{aligned} \tag{4.92}$$

We integrate the expression using the matching condition

$$\lim_{X\to\infty} V_{(0)}^{\alpha\,\prime} = 0 \tag{4.93}$$

and obtain using integration by parts in the next step

$$\begin{aligned} V_{(0)}^{\alpha\,\prime} &= g^{\alpha\beta}\left(\int \Psi'\partial_\beta\Psi'\mathrm{d}X - \int \Psi''\partial_\beta\Psi\mathrm{d}X - \int \Psi''\partial_\beta\phi_\gamma\mathrm{d}X\right), \\ V_{(0)}^{\alpha\,\prime} &= g^{\alpha\beta}\left(2\int \Psi'\partial_\beta\Psi'\mathrm{d}X - \Psi'\partial_\beta\Psi - \Psi'\partial_\beta\phi_\gamma\right). \end{aligned} \tag{4.94}$$

We use the result for the excess potential

$$\Psi = 2\ln\frac{1+Ae^{BX}}{1-Ae^{BX}} \tag{4.95}$$

with the two parameters that we have defined earlier

$$A = \tanh\frac{\zeta}{4} \qquad \text{and} \qquad B = -\sqrt{c_\gamma} \tag{4.96}$$

to solve the first integral

$$\begin{aligned} I_{v1}^{\beta} := 2\int \Psi'\partial_\beta\Psi'\mathrm{d}X &= 8\frac{\partial B}{\partial c_\gamma}\left(\partial_\alpha c_\gamma\right)\left(-1+\frac{1-A^2e^{2BX}+2BXA^2e^{2BX}}{1-A^2e^{2BX}}\right) \\ &= 8\frac{\partial B}{\partial c_\gamma}\left(\partial_\alpha c_\gamma\right)\left(-1+\frac{1-a+2BXa}{1-A^2e^{2BX}}\right) \end{aligned} \tag{4.97}$$

with

$$a = A^2e^{2BX}. \tag{4.98}$$

We integrate this result a second time together with the velocity matching

$$\lim_{X\to\infty} V_{(0)}^{\alpha} = v_\gamma^\alpha \tag{4.99}$$

and find

$$V_{(0)}^{\alpha} = g^{\alpha\beta}\left(I_{v2}^{\beta} + I_{v3}^{\beta} - \Psi\partial_\alpha\phi_\gamma\right) + v_\gamma. \tag{4.100}$$

The two integrals are

$$\begin{aligned} I_{v2}^{\beta} &:= \int I_{v1}^{\beta}\mathrm{d}X = \frac{2BaX}{1-a}\,\partial_\beta\ln c_\gamma \\ I_{v3}^{\beta} &:= \int \Psi'\partial_\beta\Psi\mathrm{d}X = \left(2\ln\left(1-a\right) - 4BX\left(1-\left(1-a\right)^{-1}\right)\right)\,\partial_\beta\ln c_\gamma. \end{aligned} \tag{4.101}$$

As we find an analogous result for the $\bar{\Omega}$ domain we can use the velocity continuity at the interface to obtain the velocity jump

$$v_\gamma - \bar{v}_\gamma = g_{(0)}^{\alpha\beta}\left(\zeta - \frac{S}{M}\bar{\zeta}\right)\partial_\beta\phi_\gamma + g_{(0)}^{\alpha\beta}\left(2\ln\left(1-A^2\right) - 2\frac{S}{M}\ln\left(1-\bar{A}^2\right)\right)\,\partial_\beta\ln c_\gamma. \tag{4.102}$$

Here, the gradient operator $g_{(0)}^{\alpha\beta}\partial_\beta$ takes the surface metric $g_{(0)}^{\alpha\beta}$ into account.

4.2.7 Normal stress at $O(1)$

The momentum equation of $O\left(\delta^{-1}\right)$ delivers the $O(1)$ normal stress. The respective equation (derived in appendix A) reads (cp. A.25)

$$0 = {\Sigma^{11}_{(0)}}' + \kappa_{(0)}\left(\Sigma^{11}_{(-1)} - \Sigma^{\bullet}_{(-1)}\right) + \frac{1}{\sqrt{g}_{(0)}}\partial_\alpha\left(\sqrt{g}_{(0)}\Sigma^{1\alpha}_{(-1)}\right). \tag{4.103}$$

According to table A.1 the relevant stresses are

$$\begin{aligned}
\Xi^{11}_{(-1)} &= -P_{(-1)} = \Xi^{\bullet}_{(-1)},\\
\Theta^{11}_{(-1)} &= \Phi'_{(0)}\Phi'_{(1)} = -\Theta^{\bullet}_{(-1)},\\
\Xi^{1\alpha}_{(-1)} &= {V^{\alpha}_{(0)}}',\\
\Theta^{1\alpha}_{(-1)} &= g^{\alpha\beta}_{(0)}\Phi'_{(0)}\partial_\beta\Phi_{(0)}.
\end{aligned} \tag{4.104}$$

We find that $\Xi^{11}_{(-1)} - \Xi^{\bullet}_{(-1)} = 0$ and $\Theta^{11}_{(-1)} - \Theta^{\bullet}_{(-1)} = 2\Theta^{11}_{(-1)}$ so that equation 4.103 reads

$$0 = {\Sigma^{11}_{(0)}}' + 2\kappa_{(0)}\Theta^{11}_{(-1)} + \frac{1}{\sqrt{g}_{(0)}}\partial_\alpha\left(\sqrt{g}_{(0)}\Sigma^{1\alpha}_{(-1)}\right). \tag{4.105}$$

From equation 4.90 we know that

$${\Sigma^{1\alpha}_{(-1)}}' = -g^{\alpha\beta}_{(0)}\partial_\beta\Sigma^{\bullet}_{(-2)}. \tag{4.106}$$

We find from table A.1 or equations 4.92 that $\Sigma^{\bullet}_{(-2)} = -{\Psi'}^2$. Thus, we can integrate equation 4.106 and obtain

$$\Sigma^{1\alpha}_{(-1)} = -g^{\alpha\beta}_{(0)}\partial_\beta I_\Psi. \tag{4.107}$$

Note that the integration limits are chosen such that $I_\Psi > 0$, as discussed in section 4.2.4 (cp. equations 4.81 and 4.82). We can now rewrite equation 4.105 to find

$$0 = {\Sigma^{11}_{(0)}}' + 2\kappa_{(0)}\Psi'\Phi'_{(1)} - \frac{1}{\sqrt{g}_{(0)}}\partial_\alpha\left(\sqrt{g}_{(0)}g^{\alpha\beta}_{(0)}\partial_\beta I_\Psi\right). \tag{4.108}$$

We introduce the Laplacian $\nabla^2_\parallel$ for the tangential plane as

$$\nabla^2_\parallel(..) := \frac{1}{\sqrt{g}_{(0)}}\partial_\alpha\left(\sqrt{g}_{(0)}g^{\alpha\beta}_{(0)}\partial_\beta(..)\right), \tag{4.109}$$

i.e. $\nabla^2 = \nabla^2_\parallel + \frac{\partial^2}{(\partial x^1)^2}$. That notation allows us to rewrite equation 4.108 as

$${\Sigma^{11}_{(0)}}' = -2\kappa_{(0)}\Psi'\Phi'_{(1)} + \nabla^2_\parallel I_\Psi. \tag{4.110}$$

Integration with respect to the normal coordinate delivers

$$\begin{aligned}
\Sigma^{11}_{(0)} &= -2\kappa_{(0)}\left(-I_\Phi\right) + \nabla^2_\parallel\left(-I_{\Psi\Psi}\right) + \sigma^{11}_{\gamma(0)},\\
-I_{\Psi\Psi} &:= \int_\infty^X I_\Psi \,\mathrm{d}\tilde{X},\\
-I_\Phi &:= \int_\infty^X \Psi'\Phi'_{(1)} \,\mathrm{d}\tilde{X}.
\end{aligned} \tag{4.111}$$

We can again exchange the integration limits to obtain

$$\begin{aligned}\Sigma^{11}_{(0)} &= 2\kappa_{(0)} I_\Phi - \nabla^2_\parallel I_{\Psi\Psi} + \sigma^{11}_{\gamma(0)},\\ I_{\Psi\Psi} &:= \int_X^\infty I_\Psi \,\mathrm{d}\tilde{X},\\ I_\Phi &:= \int_X^\infty \Psi' \Phi'_{(1)} \,\mathrm{d}\tilde{X}.\end{aligned} \tag{4.112}$$

For the $\bar{\Omega}$ domain, we find equivalently

$$\begin{aligned}\bar{\Sigma}^{11}_{(0)} &= -2\kappa_{(0)} I_{\bar{\Phi}} + \nabla^2_\parallel \bar{I}_{\Psi\Psi} + \bar{\sigma}^{11}_{\gamma(0)},\\ \bar{I}_{\Psi\Psi} &= S\int_{-\infty}^X \bar{I}_\Psi \,\mathrm{d}\tilde{X},\\ \bar{I}_\Phi &= S\int_{-\infty}^X \bar{\Psi}' \bar{\Phi}'_{(1)} \,\mathrm{d}\tilde{X}.\end{aligned} \tag{4.113}$$

Finally, we adapt this solution to the surface stress condition 4.17 which reads at $O(1)$

$$\begin{aligned}\kappa_{(0)} t_{\Gamma(0)} &= \Sigma^{11}_{(0)}(X=0) - \bar{\Sigma}^{11}_{(0)}(X=0),\\ \kappa_{(0)} t_{\Gamma(0)} &= 2\kappa_{(0)} \left[I_\Phi + \bar{I}_\Phi\right]_{X=0} - \nabla^2_\parallel \left[I_{\Psi\Psi} + \bar{I}_{\Psi\Psi}\right]_{X=0} + \sigma^{11}_{\gamma(0)} - \bar{\sigma}^{11}_{\gamma(0)}.\end{aligned} \tag{4.114}$$

Note that for the chosen metric $\kappa_{(1)} = 0$. As a result, we obtain the normal stress jump

$$\begin{aligned}\sigma^{11}_{\gamma(0)} - \bar{\sigma}^{11}_{\gamma(0)} &= \kappa_{(0)} t_{\mathrm{eff}(0)} + \nabla^2_\parallel \left[I_{\Psi\Psi} + \bar{I}_{\Psi\Psi}\right]_{X=0},\\ t_{\mathrm{el}(0))} &= 2\left[I_\Phi + I_{\bar{\Phi}}\right]_{X=0},\\ t_{\mathrm{eff}(0))} &= t_{\Gamma(0)} - t_{\mathrm{el}(0)}.\end{aligned} \tag{4.115}$$

where we named $t_{\mathrm{el}(0))}$ and $t_{\mathrm{eff}(0))}$ the electric and effective surface stresses respectively.

4.2.8 Shear stress at $O(1)$

We consider the shear tangential momentum equation of order δ^{-1} in equation A.26

$$0 = {\Sigma^{1\alpha}_{(0)}}' + g^{\alpha\alpha}_{(0)} \partial_\alpha \Sigma^\bullet_{(-1)} + X g^{\alpha\beta}_{(1)} \partial_\beta \Sigma^\bullet_{(-2)} + \left(\kappa_{(0)} + k^\alpha_{\alpha(0)}\right) \Sigma^{1\alpha}_{(-1)}. \tag{4.116}$$

The Newton and Maxwell stresses from table A.1 together with the solutions for the two leading orders of the pressure 4.72 and 4.80, are

$$\begin{aligned}\Xi^\bullet_{(-2)} &= -P_{(-2)} = -\frac{1}{2}{\Psi'}^2,\\ \Theta^\bullet_{(-2)} &= -\frac{1}{2}{\Psi'}^2,\\ \Xi^\bullet_{(-1)} &= -P_{(-1)} = -\Psi' \Phi'_{(1)} + \kappa_{(0)} I_\Psi,\\ \Theta^\bullet_{(-1)} &= -\Psi' \Phi'_{(0)}.\end{aligned} \tag{4.117}$$

We thus find the normal stresses

$$\begin{aligned}\Sigma^{\bullet}_{(-2)} &= -\Psi'^2,\\ \Sigma^{\bullet}_{(-1)} &= -2\Psi'\Phi'_{(1)} + \kappa_{(0)} I_\Psi.\end{aligned} \tag{4.118}$$

Additionally, we need the shear stress as defined by relation 4.107. We can now rewrite equation 4.116 and obtain

$$\begin{aligned}0 &= \Sigma^{1\alpha\,\prime}_{(0)} + g^{\alpha\alpha}_{(0)}\partial_\alpha\left(-2\Psi'\Phi'_{(1)} + \cancel{\kappa_{(0)} I_\Psi}\right) - X g^{\alpha\beta}_{(1)}\partial_\beta\Psi'^2 - \left(\cancel{\kappa_{(0)}} + k^\alpha_{\alpha(0)}\right) g^{\alpha\alpha}_{(0)}\partial_\alpha I_\Psi,\\ 0 &= \Sigma^{1\alpha\,\prime}_{(0)} - g^{\alpha\alpha}_{(0)}\partial_\alpha\left(2\Psi'\Phi'_{(1)} + k^\alpha_{\alpha(0)} I_\Psi\right) - X g^{\alpha\beta}_{(1)}\partial_\beta\Psi'^2,\end{aligned} \tag{4.119}$$

which we can solve for the shear stress

$$\Sigma^{1\alpha\,\prime}_{(0)} = g^{\alpha\alpha}_{(0)}\partial_\alpha\left(2\Psi'\Phi'_{(1)} + k^\alpha_{\alpha(0)} I_\Psi\right) + X g^{\alpha\beta}_{(1)}\partial_\beta\Psi'^2. \tag{4.120}$$

Integration with respect to the normal coordinate delivers

$$\begin{aligned}\Sigma^{1\alpha}_{(0)} &= g^{\alpha\alpha}_{(0)}\partial_\alpha\left(2\left(-I_\Phi\right) + k^\alpha_{\alpha(0)}\left(-I_{\Psi\Psi}\right)\right) + g^{\alpha\beta}_{(1)}\partial_\beta\left(-I_{X\Psi}\right) + \sigma^{1\alpha}_{\gamma(0)},\\ -I_{\Psi\Psi} &:= \int_\infty^X I_\Psi \,\mathrm{d}\tilde{X},\\ -I_\Phi &:= \int_\infty^X \Psi'\Phi'_{(1)} \,\mathrm{d}\tilde{X},\\ -I_{X\Psi} &:= \int_\infty^X X\Psi'^2 \,\mathrm{d}\tilde{X},\end{aligned} \tag{4.121}$$

with the integrals defined in such a way that they are positive. Inverting the direction of integration yields

$$\begin{aligned}\Sigma^{1\alpha}_{(0)} &= -g^{\alpha\alpha}_{(0)}\partial_\alpha\left(2I_\Phi + k^\alpha_{\alpha(0)} I_{\Psi\Psi}\right) - g^{\alpha\beta}_{(1)}\partial_\beta I_{X\Psi} + \sigma^{1\alpha}_{\gamma(0)},\\ I_{\Psi\Psi} &:= \int_X^\infty I_\Psi \,\mathrm{d}\tilde{X},\\ I_\Phi &:= \int_X^\infty \Psi'\Phi'_{(1)} \,\mathrm{d}\tilde{X},\\ I_{X\Psi} &:= \int_X^\infty X\Psi'^2 \,\mathrm{d}\tilde{X}.\end{aligned} \tag{4.122}$$

For the $\bar{\Omega}$ domain the equivalent equation to 4.119 reads

$$\begin{aligned}0 &= \bar{\Sigma}^{1\alpha\,\prime}_{(0)} + S g^{\alpha\alpha}_{(0)}\partial_\alpha\left(-2\bar{\Psi}'\bar{\Phi}'_{(1)} - \cancel{\kappa_{(0)}\bar{I}_\Psi}\right) - SX g^{\alpha\beta}_{(1)}\partial_\beta\bar{\Psi}'^2 - S\left(\cancel{\kappa_{(0)}} + k^\alpha_{\alpha(0)}\right) g^{\alpha\alpha}_{(0)}\partial_\alpha\bar{I}_\Psi,\\ 0 &= \bar{\Sigma}^{1\alpha\,\prime}_{(0)} - S g^{\alpha\alpha}_{(0)}\partial_\alpha\left(2\bar{\Psi}'\bar{\Phi}'_{(1)} + k^\alpha_{\alpha(0)}\bar{I}_\Psi\right) - SX g^{\alpha\beta}_{(1)}\partial_\beta\bar{\Psi}'^2.\end{aligned} \tag{4.123}$$

Integration delivers

$$\begin{aligned}
\bar{\Sigma}^{1\alpha'}_{(0)} &= g^{\alpha\alpha}_{(0)}\partial_\alpha\left(2\bar{I}_\Phi + k^\alpha_{\alpha(0)}\bar{I}_{\Psi\Psi}\right) + g^{\alpha\beta}_{(1)}\partial_\beta\bar{I}_{X\Psi} + \bar{\sigma}^{1\alpha}_{\gamma(0)},\\
\bar{I}_{\Psi\Psi} &:= S\int_{-\infty}^{X} I_\Psi \,\mathrm{d}\tilde{X},\\
\bar{I}_\Phi &:= S\int_{-\infty}^{X} \Psi'\Phi'_{(1)} \,\mathrm{d}\tilde{X},\\
\bar{I}_{X\Psi} &:= S\int_{-\infty}^{X} X\Psi'^2 \,\mathrm{d}\tilde{X}.
\end{aligned} \tag{4.124}$$

We use the shear stress continuity 4.17 at $O(1)$ to identify

$$\begin{aligned}
0 &= \Sigma^{1\alpha}_{(0)}(X=0) - \bar{\Sigma}^{1\alpha}_{(0)}(X=0),\\
\sigma^{1\alpha}_{\gamma(0)} - \bar{\sigma}^{1\alpha}_{\gamma(0)} &= g^{\alpha\alpha}_{(0)}\partial_\alpha\left(2\left[I_\Phi + \bar{I}_\Phi\right]_{X=0} + k^\alpha_{\alpha(0)}\left[I_{\Psi\Psi} + \bar{I}_{\Psi\Psi}\right]_{X=0}\right) + g^{\alpha\beta}_{(1)}\partial_\beta\left[I_{X\Psi} + \bar{I}_{X\Psi}\right]_{X=0},
\end{aligned} \tag{4.125}$$

which is the effective jump in the shear stress.

4.2.9 Model summary

The analysis of the Debye layer allows us to write an EHD model with effective boundary conditions. The bulk equations for the suspending fluid have been derived in equations 4.20 through 4.24 and read

$$\begin{aligned}
0 &= \mathrm{Pe}\left(\partial_t c_{(0)} + \vec{v}_{(0)}\cdot\vec{\nabla}c_{(0)}\right) - \nabla^2 c_{(0)},\\
0 &= \vec{\nabla}\cdot\vec{\vec{j}}_{q(0)}\\
&= -D_\Delta\nabla^2 c_{(0)} - \vec{\nabla}\cdot\left(c_{(0)}\vec{\nabla}\phi_{(0)}\right),\\
\vec{0} &= \vec{\nabla}\cdot\sigma_{(0)},\\
0 &= \vec{\nabla}\cdot\vec{v}_{(0)}.
\end{aligned} \tag{4.126}$$

Equivalently, the drop-domain equations read

$$\begin{aligned}
0 &= \mathrm{Pe}\left(\partial_t \bar{c}_{(0)} + \vec{v}_{(0)}\cdot\vec{\nabla}\bar{c}_{(0)}\right) - \nabla^2\bar{c}_{(0)},\\
0 &= \vec{\nabla}\cdot\vec{\vec{j}}_{q(0)}\\
&= -\bar{D}_\Delta\nabla^2\bar{c}_{(0)} - \vec{\nabla}\cdot\left(\bar{c}_{(0)}\vec{\nabla}\bar{\phi}_{(0)}\right),\\
\vec{0} &= \vec{\nabla}\cdot\bar{\sigma}_{(0)},\\
0 &= \vec{\nabla}\cdot\vec{\bar{v}}_{(0)}.
\end{aligned} \tag{4.127}$$

Note that the charge density in both domains vanishes $q_{(0)} = \bar{q}_{(0)} = 0$. The coupling between the domains is established by the conditions derived in the Debye cloud analysis. In summary, equations 4.49, 4.55, 4.60, 4.89, 4.102, 4.115, and 4.125 read

$$
\begin{aligned}
\bar{c}_{\gamma(0)} &= \sqrt{l_+ l_-}\, c_{\gamma(0)}, \\
\phi_{\gamma(0)} - \bar{\phi}_{\gamma(0)} &= \frac{1}{2} \ln \frac{l_-}{l_+}, \\
j^1_{\pm\gamma(0)} - \bar{j}^1_{\pm\gamma(0)} &= 0, \\
v^1_{\gamma(0)} - \bar{v}^1_{\gamma(0)} &= 0, \\
v^\alpha_{\gamma(0)} - \bar{v}^\alpha_{\gamma(0)} &= \left(\zeta - \frac{S}{M} \bar{\zeta} \right) \partial_\beta \phi_{\gamma(0)} + \left(2 \ln \left(1 - A^2 \right) - 2 \frac{S}{M} \ln \left(1 - \bar{A}^2 \right) \right) \partial_\beta \ln c_{\gamma(0)}, \\
\sigma^{11}_{\gamma(0)} - \bar{\sigma}^{11}_{\gamma(0)} &= \kappa_{(0)} t_{\mathrm{eff}(0)} + \nabla^2_{\parallel} \left[I_{\Psi\Psi} + \bar{I}_{\Psi\Psi} \right]_{X=0}, \\
\sigma^{1\alpha}_{\gamma(0)} - \bar{\sigma}^{1\alpha}_{\gamma(0)} &= g^{\alpha\alpha}_{(0)} \partial_\alpha \left(2 \left[I_\Phi + \bar{I}_\Phi \right]_{X=0} + k^\alpha_{\alpha(0)} \left[I_{\Psi\Psi} + \bar{I}_{\Psi\Psi} \right]_{X=0} \right) \\
&\quad + g^{\alpha\beta}_{(1)} \partial_\beta \left[I_{X\Psi} + \bar{I}_{X\Psi} \right]_{X=0}.
\end{aligned}
\tag{4.128}
$$

4.2.10 Absence of outer electrochemical gradients

In a number of experimental settings, the flux-diffusion equation $0 = \vec{\nabla} \cdot \vec{j}_{q(0)}$ simply delivers a condition for constant mean charge/conductivity $\vec{\nabla} c_{(0)} = 0$. In particular, this is the case if the diffusion coefficients of both ion species are equal $D_+ = D_-$, and thus $D_\Delta = 0$. We also find constant $c_{(0)} = 0$ in the case of a homogeneous far-field boundary condition for $c_{(0)} = 0$ (no outer charge gradient applied) and the absence of a Debye-layer charging mechanism. Debye-layer charging is discussed e.g. by Ma et al. (2022) but absent in our model due to the flux-continuity condition 4.16.

If either $D_+ = D_-$, or $\lim_{x^1 \to \infty} \vec{\nabla} c_{(0)} = 0$ holds, the bulk conductivity is constant. In that case we can assume that the value of $c_{(0)}$ approaches the equilibrium concentration far away from the interface $\lim_{x^1 \to \infty} c_{(0)} = 1$ and effectively in the whole suspending fluid $c_{(0)} = c_{\gamma(0)} = 1$ (besides the Debye layer). In the drop fluid, we find from the jump condition at the interface γ that $\bar{c}_{(0)} = \bar{c}_{\gamma(0)} = \sqrt{l_+ l_-}$. The governing equations for the suspending fluid bulk simplify to

$$
\begin{aligned}
0 &= \nabla^2 \phi_{(0)} \\
\vec{0} &= \vec{\nabla} \cdot \xi_{(0)}, \\
0 &= \vec{\nabla} \cdot \vec{v}_{(0)}.
\end{aligned}
\tag{4.129}
$$

The bulk physics in the drop domain is governed by an equivalent set of equations

$$
\begin{aligned}
0 &= \nabla^2 \bar{\phi}_{(0)} \\
\vec{0} &= \vec{\nabla} \cdot \bar{\xi}_{(0)}, \\
0 &= \vec{\nabla} \cdot \vec{\bar{v}}_{(0)}.
\end{aligned}
\tag{4.130}
$$

The effective jump conditions 4.128 now read

$$\begin{aligned}
\phi_{\gamma(0)} - \bar{\phi}_{\gamma(0)} &= \frac{1}{2} \ln \frac{l_-}{l_+}, \\
j^1_{\pm\gamma(0)} - \bar{j}^1_{\pm\gamma(0)} &= 0, \\
v^1_{\gamma(0)} - \bar{v}^1_{\gamma(0)} &= 0, \\
v^\alpha_{\gamma(0)} - \bar{v}^\alpha_{\gamma(0)} &= \left(\zeta - \frac{S}{M} \bar{\zeta} \right) \partial_\beta \phi_{\gamma(0)}, \\
\sigma^{11}_{\gamma(0)} - \bar{\sigma}^{11}_{\gamma(0)} &= \kappa_{(0)} t_{\mathrm{eff}(0)}, \\
\sigma^{1\alpha}_{\gamma(0)} - \bar{\sigma}^{1\alpha}_{\gamma(0)} &= 2 g^{\alpha\alpha}_{(0)} \partial_\alpha \left[I_\Phi + \bar{I}_\Phi \right]_{X=0}.
\end{aligned} \tag{4.131}$$

Tangential variations of the excess potential are only due to variations of the conductivity

$$\Psi \left(X, x^\alpha \right) = \Psi \left(X, c_{\gamma(0)} \left(x^\alpha \right) \right). \tag{4.132}$$

With $c_{\gamma(0)} = \text{const.}$, the derivatives $\partial_\alpha \Psi$ as well as the tangential derivatives of the integrals I_Ψ, $I_{\Psi\Psi}$, $I_{X\Psi}$ vanish. The equations 4.68 for the potential correction $\Phi_{(1)}$ now read

$$\begin{aligned}
\Phi''_{(1)} - B^2 \Phi_{(1)} \cosh \Psi &= -\kappa_{(0)} \, \Psi' + \frac{1}{2} j^1_{\gamma(0)} \left(E_- e^{\Psi} + E_+ e^{-\Psi} \right), \\
\bar{\Phi}''_{(1)} - \bar{B}^2 \bar{\Phi}_{(1)} \cosh \bar{\Psi} &= -\kappa_{(0)} \, \bar{\Psi}' + \frac{1}{2S} j^1_{\gamma(0)} \left(\bar{E}_- e^{\bar{\Psi}} + \bar{E}_+ e^{-\bar{\Psi}} \right).
\end{aligned} \tag{4.133}$$

The charge fluxes at the interface γ have equal absolute values and opposite directions

$$\begin{aligned}
j^1_{\gamma(0)} &:= j^1_{+\gamma(0)} = -j^1_{-\gamma(0)} = -c_{\gamma(0)} \partial_1 \phi_{(0)}, \\
\bar{j}^1_{\gamma(0)} &:= \bar{j}^1_{+\gamma(0)} = -\bar{j}^1_{-\gamma(0)} = -\bar{c}_{\gamma(0)} \partial_1 \bar{\phi}_{(0)}.
\end{aligned} \tag{4.134}$$

We note that the solution of the first equation in 4.133 takes the form

$$\Phi_{(1)} = -\kappa_{(0)} \Phi_{(1)\kappa} - j^1_{\gamma(0)} \Phi_{(1)j}, \tag{4.135}$$

where the particular solutions $\Phi_{(1)\kappa}$ and $\Phi_{(1)j}$ are defined by (analogously for the drop domain $\bar{\Omega}$)

$$\begin{aligned}
\Phi''_{(1)\kappa} - B^2 \Phi_{(1)\kappa} \cosh \Psi &= \Psi', \\
\bar{\Phi}''_{(1)\kappa} - \bar{B}^2 \bar{\Phi}_{(1)\kappa} \cosh \bar{\Psi} &= \bar{\Psi}', \\
\Phi''_{(1)j} - B^2 \Phi_{(1)j} \cosh \Psi &= -\frac{1}{2} \left(E_- e^{\Psi} + E_+ e^{-\Psi} \right), \\
\bar{\Phi}''_{(1)j} - \bar{B}^2 \bar{\Phi}_{(1)j} \cosh \bar{\Psi} &= -\frac{1}{2S} \left(\bar{E}_- e^{\bar{\Psi}} + \bar{E}_+ e^{-\bar{\Psi}} \right).
\end{aligned} \tag{4.136}$$

The boundary conditions 4.69 hold for both parameters

$$\begin{aligned}
\Phi_{(1)\chi,\Gamma} - \bar{\Phi}_{(1)\chi,\Gamma} &= 0, \\
\Phi'_{(1)\chi,\Gamma} - S \bar{\Phi}'_{(1)\chi,\Gamma} &= 0, \qquad \chi \in \{\kappa, j\}.
\end{aligned} \tag{4.137}$$

The homogeneous solution to both problems reads

$$\begin{aligned}\Phi_{(1)h} &= K_1\frac{e^{BX}}{1-A^2e^{2BX}} + K_2\frac{1-A^4e^{4BX}+4A^2BXe^{2BX}}{2e^{BX}\left(A^2e^{2BX}-1\right)},\\ \bar{\Phi}_{(1)h} &= \bar{K}_1\frac{e^{\bar{B}X}}{1-\bar{A}^2e^{2\bar{B}X}} + \bar{K}_2\frac{1-\bar{A}^4e^{4\bar{B}X}+4\bar{A}^2\bar{B}Xe^{2\bar{B}X}}{2e^{\bar{B}X}\left(\bar{A}^2e^{2\bar{B}X}-1\right)}.\end{aligned} \tag{4.138}$$

The second term in both solutions grows exponentially for large X. Thus, we find that the constants $K_2 = \bar{K}_2 = 0$. A finite particular solution to the κ-equation is

$$\Phi_{(1)\kappa,\mathrm{p}} = \frac{A}{B}e^{BX}\frac{1-2BX+A^2e^{2BX}}{B^2\left(-1+A^2e^{2BX}\right)}, \quad \bar{\Phi}_{(1)\kappa,\mathrm{p}} = \frac{\bar{A}}{\bar{B}}e^{\bar{B}X}\frac{1-2\bar{B}X+\bar{A}^2e^{2\bar{B}X}}{\bar{B}^2\left(-1+\bar{A}^2e^{2\bar{B}X}\right)}. \tag{4.139}$$

A particular solution to the j-equation reads

$$\begin{aligned}\Phi_{(1)j,\mathrm{p}} &= \frac{-4A^2+(1-A^2)BX-A^2\left(4+8BX\right)e^{BX}+\left(4A^2+A^4BX-A^2BX\right)e^{2BX}}{B^3\left(1-A^2\right)\left(1-A^2e^{2BX}\right)},\\ \bar{\Phi}_{(1)j,\mathrm{p}} &= \frac{-4\bar{A}^2+(1-\bar{A}^2)\bar{B}X-\bar{A}^2\left(4+8\bar{B}X\right)e^{\bar{B}X}+\left(4\bar{A}^2+\bar{A}^4\bar{B}X-\bar{A}^2\bar{B}X\right)e^{2\bar{B}X}}{S\bar{B}^3\left(1-\bar{A}^2\right)\left(1-\bar{A}^2e^{2\bar{B}X}\right)}.\end{aligned} \tag{4.140}$$

We define the solution

$$\begin{aligned}\Phi_{(1)j} &= \Phi_{(1)j,\mathrm{p}} + K_1\frac{e^{BX}}{1-A^2e^{2BX}},\\ \bar{\Phi}_{(1)j} &= \bar{\Phi}_{(1)j,\mathrm{p}} + \bar{K}_1\frac{e^{\bar{B}X}}{1-\bar{A}^2e^{2\bar{B}X}}\end{aligned} \tag{4.141}$$

where the constants K_1 and K_2 are found by adaption to the interface conditions

$$\begin{aligned}\Phi_{(1)j,\Gamma} - \bar{\Phi}_{(1)j,\Gamma} &= 0,\\ \Phi'_{(1)j,\Gamma} - S\bar{\Phi}'_{(1)j,\Gamma} &= 0.\end{aligned} \tag{4.142}$$

The behavior of these solutions away from the interface Γ is

$$\begin{aligned}\lim_{X\to\infty}\Phi'_{(1)j} &= \frac{1}{B^2} = c_\gamma^{-1},\\ \lim_{X\to\infty}\bar{\Phi}'_{(1)j} &= \frac{1}{S\bar{B}^2} = \bar{c}_\gamma^{-1}.\end{aligned} \tag{4.143}$$

The only parameter which depends on the tangential coordinates x^α in this solution is

$j^1_{\gamma(0)}$. Using $j^1_{\gamma(0)} = \bar{j}^1_{\gamma(0)}$ and $c_\gamma = 1$, $\bar{c}_\gamma = R$ we can now formulate the integral

$$\begin{aligned}
&\left[I_\Phi + \bar{I}_\Phi\right]_{X=0} \\
&= S\int_{-\infty}^{0} \bar{\Psi}'\left(-\kappa_{(0)}\bar{\Phi}'_{(1)\kappa} - j^1_{\gamma(0)}\bar{\Phi}'_{(1)j}\right)\mathrm{d}X + \int_0^\infty \Psi'\left(-\kappa_{(0)}\Phi'_{(1)\kappa} - j^1_{\gamma(0)}\Phi'_{(1)j}\right)\mathrm{d}X, \\
&= S\int_{-\infty}^{0} \bar{\Psi}'\left(-\kappa_{(0)}\bar{\Phi}'_{(1)\kappa} - j^1_{\gamma(0)}\left(\bar{\Phi}'_{(1)j} - R + R\right)\right)\mathrm{d}X \\
&\qquad\qquad + \int_0^\infty \Psi'\left(-\kappa_{(0)}\Phi'_{(1)\kappa} - j^1_{\gamma(0)}\left(\Phi'_{(1)j} - 1 + 1\right)\right)\mathrm{d}X, \\
&= j^1_{\gamma(0)}\left(\zeta - \frac{S}{R}\bar{\zeta}\right) - \kappa_{(0)}\left(I_\kappa + S\bar{I}_\kappa\right) - j^1_{\gamma(0)}\left(I_j + \frac{S}{R}\bar{I}_j\right),
\end{aligned} \tag{4.144}$$

where we have denoted the two integrals (which depend solely on the normal coordinate) as

$$\begin{aligned}
I_\kappa(X) &= \int_0^\infty \Psi'\Phi'_{(1)\kappa}\mathrm{d}X, & \bar{I}_\kappa(X) &= \int_{-\infty}^0 \bar{\Psi}'\bar{\Phi}'_{(1)\kappa}\mathrm{d}X, \\
I_j(X) &= \int_0^\infty \Psi'\left(\Phi'_{(1)j} - 1\right)\mathrm{d}X, & \bar{I}_j(X) &= \int_{-\infty}^0 \bar{\Psi}'\left(\bar{\Phi}'_{(1)j} - 1\right)\mathrm{d}X.
\end{aligned} \tag{4.145}$$

The tangential derivative of the integral 4.144 reads

$$\begin{aligned}
\partial_\alpha\left[I_\Phi + \bar{I}_\Phi\right]_{X=0} &= \left(\partial_\alpha j^1_{\gamma(0)}\right)\left(\zeta - \frac{S}{R}\bar{\zeta} - \mathcal{I}_j\right), \\
\mathcal{I}_j &:= I_j + \frac{S}{R}\bar{I}_j
\end{aligned} \tag{4.146}$$

As a result, we expect particle migration due to the jump in shear stresses which is proportional to $\partial_{1\alpha}\phi_{(0)}$ (compare equations 4.134 and 4.146). The details are discussed in section 4.3. The set of effective jump conditions 4.131 now reads

$$\begin{aligned}
\phi_{\gamma(0)} - \bar{\phi}_{\gamma(0)} &= \frac{1}{2}\ln\frac{l_-}{l_+}, \\
j^1_{\gamma(0)} - \bar{j}^1_{\gamma(0)} &= 0, \\
v^1_{\gamma(0)} - \bar{v}^1_{\gamma(0)} &= 0, \\
v^\alpha_{\gamma(0)} - \bar{v}^\alpha_{\gamma(0)} &= \left(\zeta - \frac{S}{M}\bar{\zeta}\right)\partial_\beta\phi_{\gamma(0)}, \\
\sigma^{11}_{\gamma(0)} - \bar{\sigma}^{11}_{\gamma(0)} &= \kappa_{(0)}t_{\Gamma(0)} - 2\kappa_{(0)}\left(\zeta - \frac{S}{R}\bar{\zeta} - \mathcal{I}_j\right)j^1_{\gamma(0)} + 2\kappa^2_{(0)}\left(I_\kappa + S\bar{I}_\kappa\right), \\
\sigma^{1\alpha}_{\gamma(0)} - \bar{\sigma}^{1\alpha}_{\gamma(0)} &= 2g^{\alpha\alpha}_{(0)}\left(\partial_\alpha j^1_{\gamma(0)}\right)\left(\zeta - \frac{S}{R}\bar{\zeta} - \mathcal{I}_j\right).
\end{aligned} \tag{4.147}$$

We here note that the conditions $j^1_{\pm\gamma(0)} - \bar{j}^1_{\pm\gamma(0)} = 0$ reduce to only one condition due to $c_{\gamma(0)} = \text{const.}$ (cp. equation 4.134).

4.2.11 The Taylor-Melcher model in the absence of a Galvani potential

In the case of equal partition coefficients $l_+ = l_-$, the Galvani potential vanishes. As a result, the apparent boundary conditions 4.147 reduce to

$$\begin{aligned} \phi_{\gamma(0)} - \bar{\phi}_{\gamma(0)} &= 0, \\ j^1_{\pm\gamma(0)} - \bar{j}^1_{\pm\gamma(0)} &= 0, \\ v^1_{\gamma(0)} - \bar{v}^1_{\gamma(0)} &= 0, \\ v^\alpha_{\gamma(0)} - \bar{v}^\alpha_{\gamma(0)} &= 0, \\ \sigma^{11}_{\gamma(0)} - \bar{\sigma}^{11}_{\gamma(0)} &= \kappa_{(0)} t_{\Gamma(0)}, \\ \sigma^{1\alpha}_{\gamma(0)} - \bar{\sigma}^{1\alpha}_{\gamma(0)} &= 0. \end{aligned} \tag{4.148}$$

Using the second condition, we find that

$$R\bar{\phi}'_\gamma = \phi'_\gamma. \tag{4.149}$$

The apparent surface charge can then be calculated from the Gauss interface condition

$$q_\gamma = S\bar{\phi}'_\gamma - \phi'_\gamma = \left(\frac{S}{R} - 1\right)\phi'_\gamma. \tag{4.150}$$

Thus, we re-establish the TM model for small Péclet numbers as discussed by Melcher and Taylor (1969) and Mori and Young (2018)[5]. In the special case discussed here, surface convection is absent due to the choice of $\mathrm{Pe} \ll 1$. In the cited publications, the Péclet number is of $O(\delta^{-2})$ giving rise to charge transport inside the Debye layer region.

4.3 Electromigration of a spherical drop

We now investigate the macroscale problem of a spherical droplet under the influence of an electric field. The droplet radius is assumed to be $l^*_{\mathrm{ref}} = 1$. The outer electric field of non-dimensional magnitude E_∞ is aligned with the z-coordinate of the Cartesian reference frame. The latter consists of a set of base vectors $\{\vec{e}_x, \vec{e}_y, \vec{e}_z\}$. A second base $\{\vec{g}_r, \vec{g}_\vartheta, \vec{g}_\varphi\}$ belongs to the spherical coordinates r (radial), ϑ (polar angle) and φ (azimuthal angle). The solution to the Laplace equation governing the electric potential

$$\nabla^2\phi = 0, \quad \nabla^2\bar{\phi} = 0, \quad [\![\phi]\!] = \phi_\gamma - \bar{\phi}_\gamma = \phi_{\mathrm{G}} \tag{4.151}$$

[5]Note that this work is based on the original publication by Mori and Young (2018) and that critics discussed in this work led to the corrigendum (Marthaler et al., 2023).

where according to Taylor (1966)

$$\begin{aligned} \phi &= -E_\infty \cos\vartheta \left(r + r^{-2} \frac{1-R}{2+R} \right); \qquad r \geq 1, \\ \bar{\phi} &= -E_\infty \cos\vartheta \, \frac{3}{2+R} r + \phi_\mathrm{G}; \qquad\quad r < 1. \end{aligned} \tag{4.152}$$

Here, we use the abbreviation for the Galvani potential as defined in relation 4.55

$$\phi_\mathrm{G} = \frac{1}{2} \ln \frac{l_-}{l_+}. \tag{4.153}$$

Due to the axisymmetry, the flow problem can be expressed in terms of the streamfunction ψ[6] that we define as (for the drop domain respectively)

$$v_r = \frac{1}{r^2 \sin\vartheta} \partial_\vartheta \psi, \quad v_\vartheta = \frac{-1}{r \sin\vartheta} \partial_r \psi. \tag{4.154}$$

The solution to the resulting biharmonic equation

$$\nabla^4 \psi = 0, \quad \nabla^4 \bar{\psi} = 0 \tag{4.155}$$

is according to Leal (2007)

$$\begin{aligned} \psi &= \sum_{n=1}^{2} \left(\mathcal{C}_n r^{2-n} + \mathcal{D}_n r^{-n} \right) Q_n \left(\cos\vartheta \right), \\ \bar{\psi} &= \sum_{n=1}^{2} \left(\mathcal{A}_n r^{n+3} + \mathcal{B}_n r^{n+1} \right) Q_n \left(\cos\vartheta \right), \\ Q_1(\cos\vartheta) &= 1 - \cos^2\vartheta, \\ Q_2(\cos\vartheta) &= \cos\vartheta \left(1 - \cos^2\vartheta \right), \end{aligned} \tag{4.156}$$

with the eight constants $\mathcal{A}_n$, $\mathcal{B}_n$, $\mathcal{C}_n$, $\mathcal{D}_n$ still to be identified. The pressure can be found via the momentum equation

$$\begin{aligned} \partial_r p &= \partial_r \left(\frac{1}{r^2} \partial_r \left(r^2 v_r \right) \right) + \frac{1}{r^2 \sin\vartheta} \partial_\vartheta \left(\sin\vartheta \partial_\theta \, v_r \right) - \frac{2}{r^2 \sin\vartheta} \partial_\vartheta \left(\sin\vartheta \, v_\vartheta \right), \\ M^{-1} \, \partial_r \bar{p} &= \partial_r \left(\frac{1}{r^2} \partial_r \left(r^2 \bar{v}_r \right) \right) + \frac{1}{r^2 \sin\vartheta} \partial_\vartheta \left(\sin\vartheta \partial_\theta \, \bar{v}_r \right) - \frac{2}{r^2 \sin\vartheta} \partial_\vartheta \left(\sin\vartheta \, \bar{v}_\vartheta \right), \end{aligned} \tag{4.157}$$

and reads

$$\begin{aligned} p &= \mathcal{C}_2 r^{-3} + 2\mathcal{C}_1 r^{-2} \cos\vartheta + 3\mathcal{C}_2 r^{-3} \cos 2\vartheta, \\ \bar{p} &= M \left(\frac{7}{2} \mathcal{A}_2 r^2 + 20 \mathcal{A}_1 \cos\vartheta + \frac{21}{2} \mathcal{A}_2 r^2 \cos 2\vartheta \right), \end{aligned} \tag{4.158}$$

[6]Note, that there are multiple uses for the letter ψ in this manuscript. In chapter 3 it is used for the excess potential, while in chpaters 4 and 5 it represents the streamfunction. The capital letter Ψ is used for the Debye-layer excess potential in this chapter and for the spectral modes of the streamfunction in chapter 5.

The Newton stresses can then be computed as

$$\begin{aligned}
\sigma_{rr} &= -p + 2\partial_r v_r, \\
\bar{\sigma}_{rr} &= -\bar{p} + 2M\partial_r \bar{v}_r, \\
\sigma_{r\vartheta} &= r\partial_r\left(\frac{1}{r}v_\vartheta\right) + \frac{1}{r}\partial_\vartheta v_r, \\
\bar{\sigma}_{r\vartheta} &= M\left(r\partial_r\left(\frac{1}{r}\bar{v}_\vartheta\right) + \frac{1}{r}\partial_\vartheta \bar{v}_r\right).
\end{aligned} \tag{4.159}$$

The electric stresses read

$$\begin{aligned}
\theta_{rr} &= \frac{1}{2}\left(\left(\partial_r\phi\right)^2 - \frac{1}{r^2}\left(\partial_\vartheta\phi\right)^2\right), \\
\bar{\theta}_{rr} &= \frac{S}{2}\left(\left(\partial_r\bar{\phi}\right)^2 - \frac{1}{r^2}\left(\partial_\vartheta\bar{\phi}\right)^2\right), \\
\theta_{r\vartheta} &= \frac{1}{r^2}\left(\partial_\vartheta\phi\right)\left(\partial_r\phi\right), \\
\bar{\theta}_{r\vartheta} &= \frac{S}{r^2}\left(\partial_\vartheta\bar{\phi}\right)\left(\partial_r\bar{\phi}\right).
\end{aligned} \tag{4.160}$$

We compute the jumps by plugging in the solution for the potential and streamfunction from equations 4.152 and 4.156. We find for the normal velocity

$$\begin{aligned}
v_r(r=1) =& 2\left(\mathcal{C}_1 + \mathcal{D}_1\right)\cos\vartheta + \frac{1}{2}\left(\mathcal{C}_2 + \mathcal{D}_2\right)\left(1 + 3\cos 2\vartheta\right), \\
\bar{v}_r(r=1) =& 2\left(\mathcal{A}_1 + \mathcal{B}_1\right)\cos\vartheta + \frac{1}{2}\left(\mathcal{A}_2 + \mathcal{B}_2\right)\left(1 + 3\cos 2\vartheta\right), \\
0 = \llbracket v_r \rrbracket =& -2\left(\mathcal{A}_1 + \mathcal{B}_1 - \mathcal{C}_1 - \mathcal{D}_1\right)\cos\vartheta \\
& - \frac{1}{2}\left(\mathcal{A}_2 + \mathcal{B}_2 - \mathcal{C}_2 - \mathcal{D}_2\right)\left(1 + 3\cos 2\vartheta\right).
\end{aligned} \tag{4.161}$$

We assume that the droplet migrates in z-direction with the velocity v_{mgr}, thus $v_r(r = 1) = \bar{v}_r(r = 1) = v_{\mathrm{mgr}}\cos\vartheta$. We conclude that

$$\begin{aligned}
v_{\mathrm{mgr}} &= 2\left(\mathcal{A}_1 + \mathcal{B}_1\right) = 2\left(\mathcal{C}_1 + \mathcal{D}_1\right), \\
0 &= \mathcal{A}_2 + \mathcal{B}_2 = \mathcal{C}_2 + \mathcal{D}_2.
\end{aligned} \tag{4.162}$$

For the tangential velocity, we find

$$\begin{aligned}
v_\vartheta(r=1) =& \left(-\mathcal{C}_1 + \mathcal{D}_1\right)\sin\vartheta + 2\mathcal{D}_2\sin\vartheta\cos\vartheta, \\
\bar{v}_\vartheta(r=1) =& \left(-4\mathcal{A}_1 - 2\mathcal{B}_1\right)\sin\vartheta + \left(-5\mathcal{A}_2 - 3\mathcal{B}_2\right)\sin\vartheta\cos\vartheta, \\
\llbracket v_\vartheta \rrbracket =& \left(-\mathcal{C}_1 + \mathcal{D}_1 + 4\mathcal{A}_1 + 2\mathcal{B}_1\right)\sin\vartheta \\
& + \left(2\mathcal{D}_2 + 5\mathcal{A}_2 + 3\mathcal{B}_2\right)\sin\vartheta\cos\vartheta.
\end{aligned} \tag{4.163}$$

We know that $\llbracket v_\vartheta \rrbracket$ is proportional to $\sin\vartheta$ and thus conclude

$$\begin{aligned}
\frac{1}{\sin\vartheta}\llbracket v_\vartheta \rrbracket =& -\mathcal{C}_1 + \mathcal{D}_1 + 4\mathcal{A}_1 + 2\mathcal{B}_1, \\
0 =& 2\mathcal{D}_2 + 5\mathcal{A}_2 + 3\mathcal{B}_2.
\end{aligned} \tag{4.164}$$

The jump in the tangential velocity reads in spherical coordinates (cp. equations 4.131)

$$[\![v_\vartheta]\!] = \left(\zeta - \frac{S}{M}\bar{\zeta}\right)\partial_\vartheta \phi_{\gamma(0)} = \left(\zeta - \frac{S}{M}\bar{\zeta}\right)\frac{3E_\infty}{2+R}\sin\vartheta. \tag{4.165}$$

We find for the normal stress that

$$\begin{aligned}
\xi_{rr}(r=1) =& (-6\mathcal{C}_1 - 12\mathcal{D}_1)\cos\vartheta + (-3\mathcal{C}_2 - 4\mathcal{D}_2)\left(1+3\cos 2\vartheta\right), \\
\bar{\xi}_{rr}(r=1) =& M\left((-12\mathcal{A}_1)\cos\vartheta + \left(-\frac{1}{2}M\mathcal{A}_2 + M\mathcal{B}_2\right)\left(1+3\cos 2\vartheta\right)\right) \\
[\![\xi_{rr}]\!] =& (-6\mathcal{C}_1 - 12\mathcal{D}_1 + 12M\mathcal{A}_1)\cos\vartheta \\
&+ \left(-3\mathcal{C}_2 - 4\mathcal{D}_2 + \frac{1}{2}M\mathcal{A}_2 - M\mathcal{B}_2\right)\left(1+3\cos 2\vartheta\right).
\end{aligned} \tag{4.166}$$

We can use the trigonometric relation $1 + 3\cos 2\vartheta = 2\left(3\cos^2\vartheta - 1\right)$ to rewrite the last line of the above jump condition

$$\begin{aligned}
[\![\xi_{rr}]\!] =& (-6\mathcal{C}_1 - 12\mathcal{D}_1 + 12M\mathcal{A}_1)\cos\vartheta \\
&+ \left(-3\mathcal{C}_2 - 4\mathcal{D}_2 + \frac{1}{2}M\mathcal{A}_2 - M\mathcal{B}_2\right)2\left(3\cos^2\vartheta - 1\right) \\
=& (-6\mathcal{C}_1 - 12\mathcal{D}_1 + 12M\mathcal{A}_1)\cos\vartheta \\
&+ (-18\mathcal{C}_2 - 24\mathcal{D}_2 + 3M\mathcal{A}_2 - 6M\mathcal{B}_2)\cos^2\vartheta \\
&+ (6\mathcal{C}_2 + 8\mathcal{D}_2 - M\mathcal{A}_2 + 2M\mathcal{B}_2).
\end{aligned} \tag{4.167}$$

We note that $[\![\xi_{rr}]\!] = [\![\sigma_{rr}]\!] - [\![\theta_{rr}]\!]$. We know $[\![\sigma_{rr}]\!]$ from the effective conditions 4.131. The electric stress jump is

$$\begin{aligned}
[\![\theta_{rr}]\!] &= \frac{1}{2}\left(\frac{3E_\infty}{2+R}\right)^2\left(R^2\cos^2\vartheta - \sin^2\vartheta - S\cos 2\vartheta\right) \\
&= \frac{1}{2}\left(\frac{3E_\infty}{2+R}\right)^2\left(R^2\cos^2\vartheta - \left(1-\cos^2\vartheta\right) - S\left(2\cos^2\vartheta - 1\right)\right) \\
&= \frac{1}{2}\left(\frac{3E_\infty}{2+R}\right)^2\left(\cos^2\vartheta\left(R^2 + 1 - 2S\right) + S - 1\right).
\end{aligned} \tag{4.168}$$

The total stress jump from 4.147 produces

$$[\![\sigma_{rr}]\!] = \kappa_{(0)} t_{\Gamma(0)} - 2\kappa_{(0)}\left(\zeta - \frac{S}{R}\bar{\zeta} - \mathcal{I}_j\right) j^1_{\gamma(0)} + 2\kappa^2_{(0)}\left(I_\kappa + S\bar{I}_\kappa\right). \tag{4.169}$$

The flux $j^1_{\gamma(0)}$ in the above expression is proportional to $\cos\vartheta$. Thus, we can split the expression up into two parts

$$\begin{aligned}
[\![\sigma_{rr}]\!] &=: [\![\sigma_{rr}]\!]_1 + [\![\sigma_{rr}]\!]_2\cos\vartheta, \\
[\![\sigma_{rr}]\!]_1 &= \kappa_{(0)} t_{\Gamma(0)} + 2\kappa^2_{(0)}\left(I_\kappa + S\bar{I}_\kappa\right), \\
[\![\sigma_{rr}]\!]_2 &= -2\kappa_{(0)}\frac{j^1_{\gamma(0)}}{\cos\vartheta}\left(\zeta - \frac{S}{R}\bar{\zeta} - \mathcal{I}_j\right).
\end{aligned} \tag{4.170}$$

We can now identify three equations

$$\begin{aligned}
-6\mathcal{C}_1 - 12\mathcal{D}_1 + 12M\mathcal{A}_1 = [\![\sigma_{rr}]\!]_2 &= -2\kappa_{(0)}\frac{j^1_{\gamma(0)}}{\cos\vartheta}\left(\zeta - \frac{S}{R}\bar{\zeta} - \mathcal{I}_j\right),\\
-18\mathcal{C}_2 - 24\mathcal{D}_2 + 3M\mathcal{A}_2 - 6M\mathcal{B}_2 &= -\frac{1}{2}\left(\frac{3E_\infty}{2+R}\right)^2\left(R^2+1-2S\right),\\
6\mathcal{C}_2 + 8\mathcal{D}_2 - M\mathcal{A}_2 + 2M\mathcal{B}_2 &= [\![\sigma_{rr}]\!]_1 - \frac{1}{2}\left(\frac{3E_\infty}{2+R}\right)^2(S-1).
\end{aligned} \tag{4.171}$$

The last equation determines the pressure difference between the inner and outer phases. It cannot be used to solve the flow problem as we have not specified the magnitude of the surface tension $t_{\Gamma(0)}$. However, it must be sufficiently large to avoid the drop from collapsing. The shear stresses and their jump at the interface are

$$\begin{aligned}
\xi_{r\vartheta}(r=1) &= -6\mathcal{D}_1\sin\vartheta + (-6\mathcal{C}_2 - 16\mathcal{D}_2)\sin\vartheta\cos\vartheta,\\
\bar{\xi}_{r\vartheta}(r=1) &= -6M\mathcal{A}_1\sin\vartheta + (-16M\mathcal{A}_2 - 6M\mathcal{B}_2)\sin\vartheta\cos\vartheta,\\
[\![\xi_{r\vartheta}]\!] &= (-6\mathcal{D}_1 + 6M\mathcal{A}_1)\sin\vartheta + (-6\mathcal{C}_2 - 16\mathcal{D}_2 + 16M\mathcal{A}_2 + 6M\mathcal{B}_2)\sin\vartheta\cos\vartheta.
\end{aligned} \tag{4.172}$$

The total stress from the effective jump conditions reads in spherical coordinates

$$[\![\sigma_{r\vartheta}]\!] = 2\partial_\vartheta\left[I_\Phi + \bar{I}_\Phi\right]_{X=0} = 2\left(\partial_\vartheta j^1_{\gamma(0)}\right)\left(\zeta - \frac{S}{R}\bar{\zeta} - \mathcal{I}_j\right), \tag{4.173}$$

which is proportional to $\sin\vartheta$. The electric stress at the interface reads

$$\begin{aligned}
\theta_{r\vartheta}(r=1) &= -R\left(\frac{3E_\infty}{2+R}\right)^2\sin\vartheta\cos\vartheta,\\
\bar{\theta}_{r\vartheta}(r=1) &= -S\left(\frac{3E_\infty}{2+R}\right)^2\sin\vartheta\cos\vartheta,\\
[\![\theta_{r\vartheta}]\!] &= (S-R)\left(\frac{3E_\infty}{2+R}\right)^2\sin\vartheta\cos\vartheta.
\end{aligned} \tag{4.174}$$

Plugging the above expressions into the jump condition for the total stress $[\![\xi_{r\vartheta}]\!] = [\![\sigma_{r\vartheta}]\!] - [\![\theta_{r\vartheta}]\!]$ delivers two equations for the constants

$$\begin{aligned}
-6\mathcal{D}_1 + 6M\mathcal{A}_1 &= 2\frac{\partial_\vartheta j^1_{\gamma(0)}}{\sin\vartheta}\left(\zeta - \frac{S}{R}\bar{\zeta} - \mathcal{I}_j\right),\\
-6\mathcal{C}_2 - 16\mathcal{D}_2 + 16M\mathcal{A}_2 + 6M\mathcal{B}_2 &= -(S-R)\left(\frac{3E_\infty}{2+R}\right)^2.
\end{aligned} \tag{4.175}$$

We know that the flux through the interface and its derivatives are

$$\begin{aligned}
j^1_{\gamma(0)} &= -\partial_r\phi = -R\,\partial_r\bar{\phi} = \frac{3RE_\infty}{2+R}\cos\vartheta,\\
\partial_r j^1_{\gamma(0)} &= \frac{2(R-1)}{R}\frac{3E_\infty}{2+R}\cos\vartheta,\\
\partial_\vartheta j^1_{\gamma(0)} &= -\frac{3RE_\infty}{2+R}\sin\vartheta.
\end{aligned} \tag{4.176}$$

We introduce the abbreviation $\mathcal{I}_j := I_j + S\bar{I}_j$ to find the following system of eight equations from the above relations 4.162, 4.164, 4.171, and 4.176. The equations for the constants with index 1 read

$$\begin{aligned}
\mathcal{A}_1 + \mathcal{B}_1 - \mathcal{C}_1 - \mathcal{D}_1 &= 0,\\
-\mathcal{C}_1 + \mathcal{D}_1 + 4\mathcal{A}_1 + 2\mathcal{B}_1 &= \left(\zeta - \frac{S}{M}\bar{\zeta}\right)\frac{3E_\infty}{2+R},\\
-6\mathcal{C}_1 - 12\mathcal{D}_1 + 12M\mathcal{A}_1 &= -2\kappa_{(0)}\frac{3RE_\infty}{2+R}\left(\zeta - \frac{S}{R}\bar{\zeta} - \mathcal{I}_j\right),\\
-6\mathcal{D}_1 + 6M\mathcal{A}_1 &= -2\frac{3RE_\infty}{2+R}\left(\zeta - \frac{S}{R}\bar{\zeta} - \mathcal{I}_j\right).
\end{aligned} \tag{4.177}$$

The equations for the four remaining constants with index 2 are the same as defined by Taylor (1966) and read

$$\begin{aligned}
\mathcal{A}_2 + \mathcal{B}_2 = \mathcal{C}_2 + \mathcal{D}_2 &= 0,\\
2\mathcal{D}_2 + 5\mathcal{A}_2 + 3\mathcal{B}_2 &= 0,\\
-18\mathcal{C}_2 - 24\mathcal{D}_2 + 3M\mathcal{A}_2 - 6M\mathcal{B}_2 &= -\frac{1}{2}\left(\frac{3E_\infty}{2+R}\right)^2\left(R^2 + 1 - 2S\right),\\
-6\mathcal{C}_2 - 16\mathcal{D}_2 + 16M\mathcal{A}_2 + 6M\mathcal{B}_2 &= -\left(S - R\right)\left(\frac{3E_\infty}{2+R}\right)^2.
\end{aligned} \tag{4.178}$$

We note that these are five equations from which one is used to identify the drop deformation and the remaining four to obtain the four unknown constants. We use the first three equations to find

$$\mathcal{A}_2 = -\mathcal{B}_2 = \mathcal{C}_2 = -\mathcal{D}_2. \tag{4.179}$$

Plugging this into the last equation (shear stress balance) of the set 4.178, we find

$$\mathcal{A}_2 = \left(\frac{3E_\infty}{2+R}\right)^2 \frac{R-S}{10(1+M)}, \tag{4.180}$$

and thus find the same constants $(..)_2$ as Taylor (1966). The set of equations 4.177 delivers solutions for the constants with index "1". The resulting flow field is depicted in figures 4.3 and 4.4. We note that the qualitative flow field is very similar to the experiments shown by Taylor (1966).

Choosing the curvature $\kappa_{(0)} = 2$, we find a formulation for the migration velocity of the drop

$$v_{\mathrm{mgr}} = 2\left(\mathcal{A}_1 + \mathcal{B}_1\right) = \frac{2E_\infty}{(2+3M)(2+R)}\left((2R+3M)\,\zeta - 5S\bar{\zeta} - 2R\mathcal{I}_j\right). \tag{4.181}$$

We note, that for small Galvani potentials the integral term in the above formulation is of size $\mathcal{I}_j \sim O(\phi_{\mathrm{G}}^2)$. The ζ-potentials in equation 4.54 can be rewritten using the definition of the Galvani potential 4.54. We replace the partition coefficient l_+ by ϕ_{G} and expand the ζ-potentials in orders of ϕ_{G}. Thus, we obtain

$$\zeta = -\frac{\sqrt{Sl_-}}{1+\sqrt{Sl_-}}\phi_{\mathrm{G}} + O(\phi_{\mathrm{G}}^2), \qquad \bar{\zeta} = \frac{1}{1+\sqrt{Sl_-}}\phi_{\mathrm{G}} + O(\phi_{\mathrm{G}}^2). \tag{4.182}$$

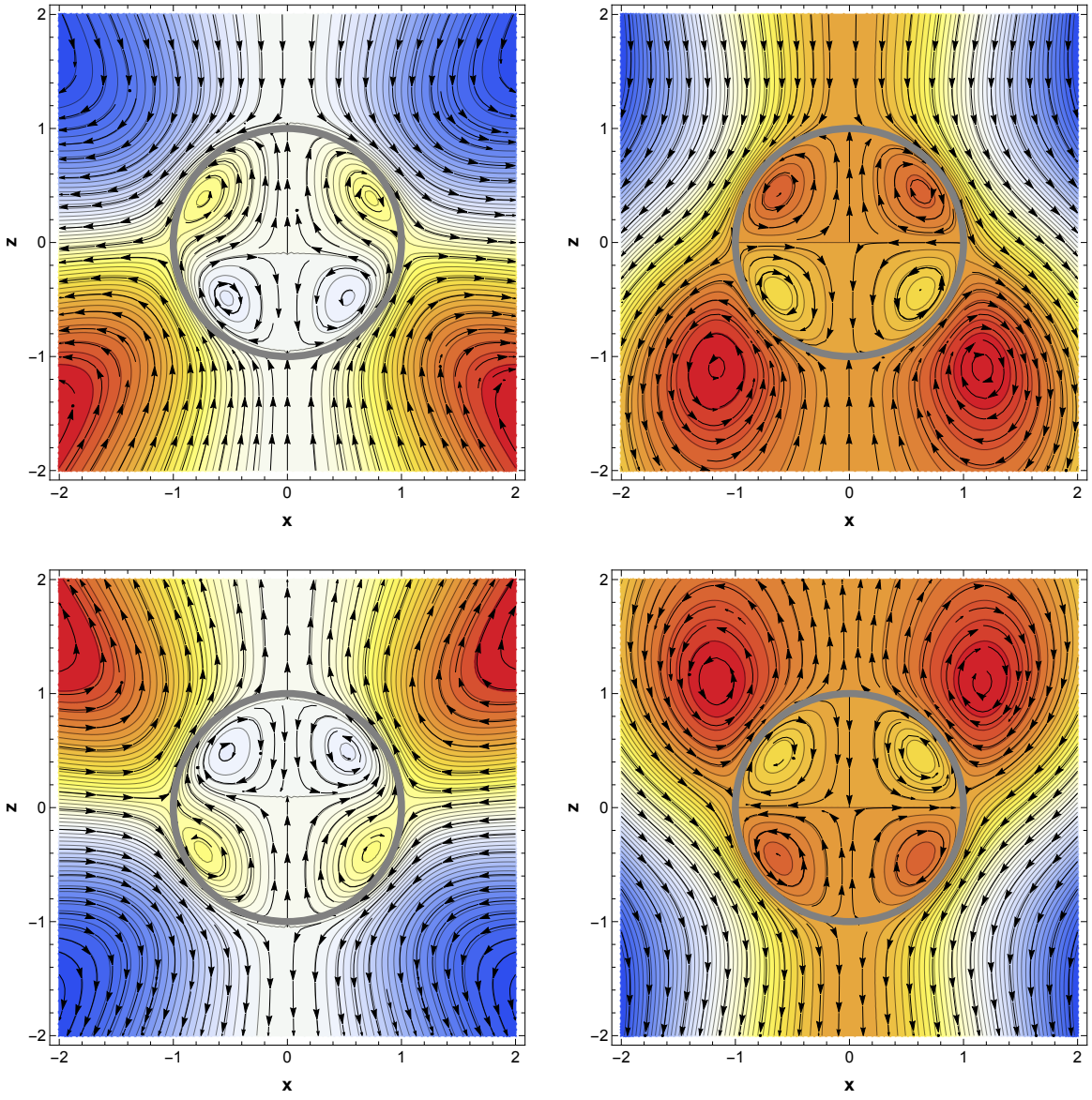

Figure 4.3: Flow field past a migrating drop with $l_+ = 1.01$, $l_- = l_+^{-1}$. The direction of flow is depicted by arrows and the value of the streamfunction by the coloring. Left column: inertial reference frame. Right column: reference frame moving with the drop. Upper row: $S = 2$. Lower row: $S = 0.5$.

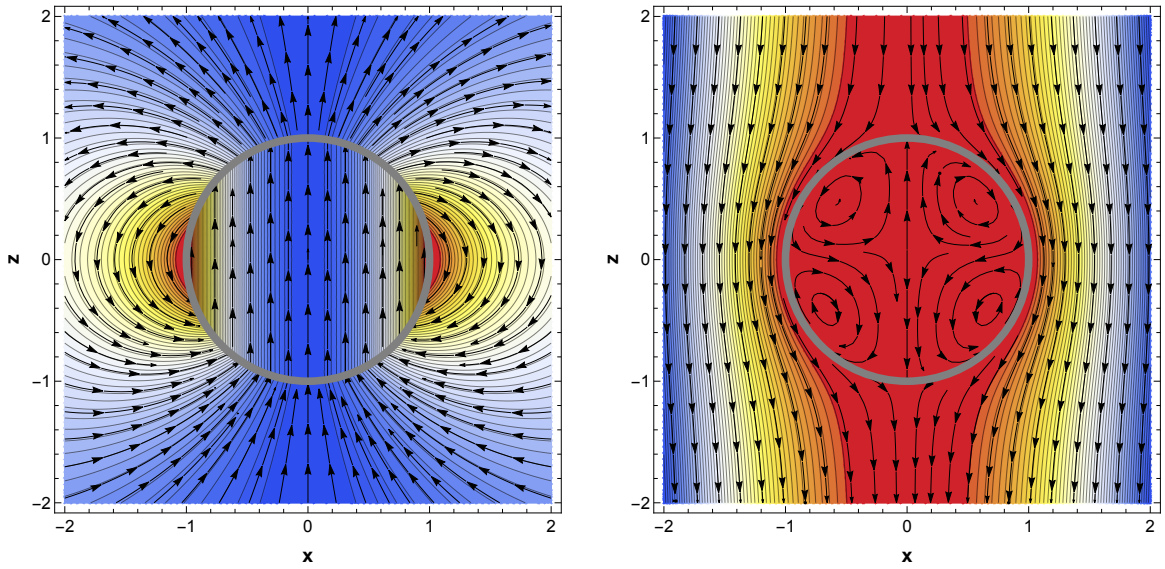

Figure 4.4: Flow field past a migrating drop with $l_+ = 1.01$, $l_- = l_+^{-1}$, and $S = 1$. The direction of flow is depicted by arrows and the value of the streamfunction by the coloring. Left: inertial reference frame. Right: reference frame moving with the drop.

The migration velocity then reads

$$v_{\mathrm{mgr}} = -2E_\infty \phi_{\mathrm{G}} \frac{(2R+3M)\sqrt{Sl_-}+5S}{(2+3M)(2+R)(1+\sqrt{Sl_-})} + O(\phi_{\mathrm{G}}^2). \tag{4.183}$$

The migration velocity depends on the material parameters S, M, $l_\pm$ as illustrated by Figure 4.5. We note that the strongest influence originates from the partition coefficients and the resulting Galvani potential. The sign of the Galvani potential defines the migration direction of the drop with respect to the electric field. The mismatch of viscosities and dielectric constants only influences the absolute value of the migration velocity, but not its direction.

Figure 4.5 is only valid under the simplifying assumption $\mathcal{I}_j \ll 1$. We assume this to be valid for small ϕ_{G}, i.e. $\frac{l_-}{l_+} \sim 1$. The exact solution of v_{mgr} was computed by numerically solving the integral $\mathcal{I}_j$ with Mathematica, as depicted by the circles in Figure 4.6.

As Mori and Young (2018)[7] derived a migration velocity for the weak-electrolyte limit we can compare the two results. We here refer to the original migration velocity from the cited paper and the velocity given in equation 3.68 of this work where a sign mistake is corrected. Figure 4.7 illustrates the difference between the two models.

The difference between the corrected result and our result for strong electrolytes originates from assumptions on the geometry of the Debye layer. The κ_0-term in relation 3.68

[7]Note that this work is based on the original publication by Mori and Young (2018) and that critics discussed in this work led to the corrigendum (Marthaler et al., 2023).

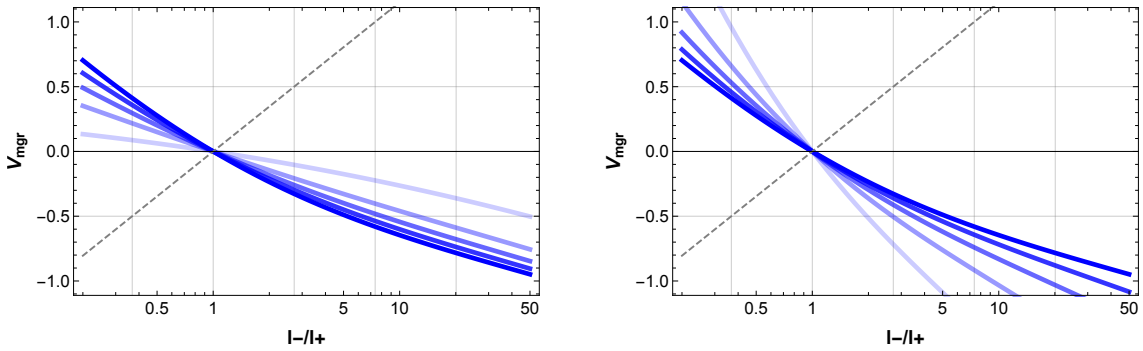

Figure 4.5: Migration velocity of the drop (blue). Left: Variation of $S \in \{0.1, 0.6, 1.1, 1.6, 2.1\}$ from light to dark blue values. Right: Variation of $M \in \{0.1, 0.6, 1.1, 1.6, 2.1\}$ from light to dark blue values. The value if the integral $\mathcal{I}_j$ is assumed to be small. The Galvani potential is depicted by the dashed curve.

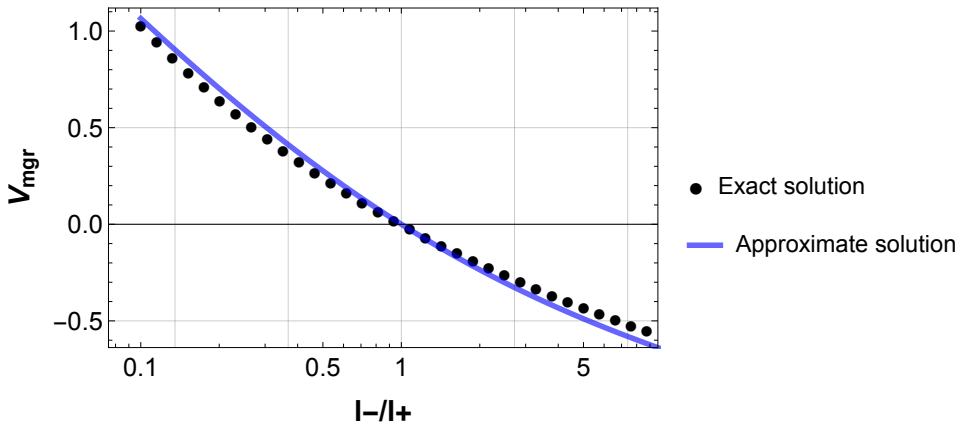

Figure 4.6: Comparison between the migration velocity for $\mathcal{I}_j = 0$ (blue curve) and the real migration velocity evaluated at single values for $\frac{l_-}{l_+}$.

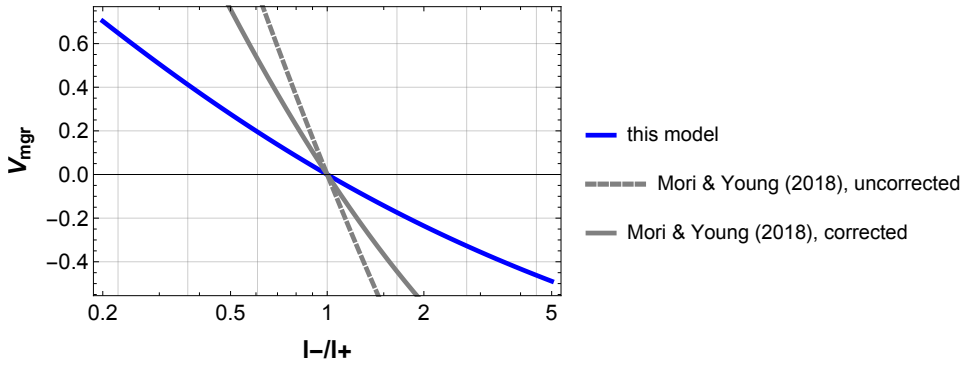

Figure 4.7: Comparison between the migration velocity evaluated for the presented model (blue curve) and the model by Mori and Young (2018) (gray curves, dashed: original publication, straight line: sign mistake corrected). The parameters are chosen as $M = 2.1$, $E_\infty = 1$, $S = 2.1$, $l_+ = 1$, and l_- varies.

does not appear in our model. The influence of this term is non-negligible as illustrated by the difference between the two models (solid gray and blue curves). The origin of this term can be explained by the different geometrical approaches used in both models to derive the curvilinear conservation equations for the Debye-layer problem. When transforming these equations to the respective equations for the inner layer, Mori and Young (2018)[8] fixed the coordinate system to the one on the surface. In contrast, we performed a series expansion of the metric allowing for higher-order terms to appear (cp. appendix A). These extra terms result distinguish between both models.

Apart from this modeling difference of the geometry, the difference between the strong and weak electrolyte model lies in the parameter $\mathcal{I}_j$. The model by Mori and Young (2018) includes a similar term. It is important to emphasize that these terms are not identical as they result from different sets of equations for the $O(\delta^{-1})$ electric problem. However, these differences are of the order $O(\phi_G^2)$ and have a significantly smaller impact on the result than the geometrical modeling discussed before.

4.4 Conclusion

We have derived a strong-electrolyte model for droplet migration. Therefore, a large Péclet number $\mathrm{Pe} \sim O(\delta^{-2})$ and large dimensionless surface tension $t_\Gamma \sim O(\delta^{-1})$ were considered. The electrokinetics of the thin Debye layer were calculated and effective boundary conditions derived. The partition coefficients are in general distinct, resulting in a Galvani potential. The genuine interface was assumed to be permeable to ions, and so is the apparent interface.

Figure 4.8 illustrates how the presented study compares to existing electrokinetic ap-

[8]Note that this work is based on the original publication by Mori and Young (2018) and that critics discussed in this work led to the corrigendum (Marthaler et al., 2023).

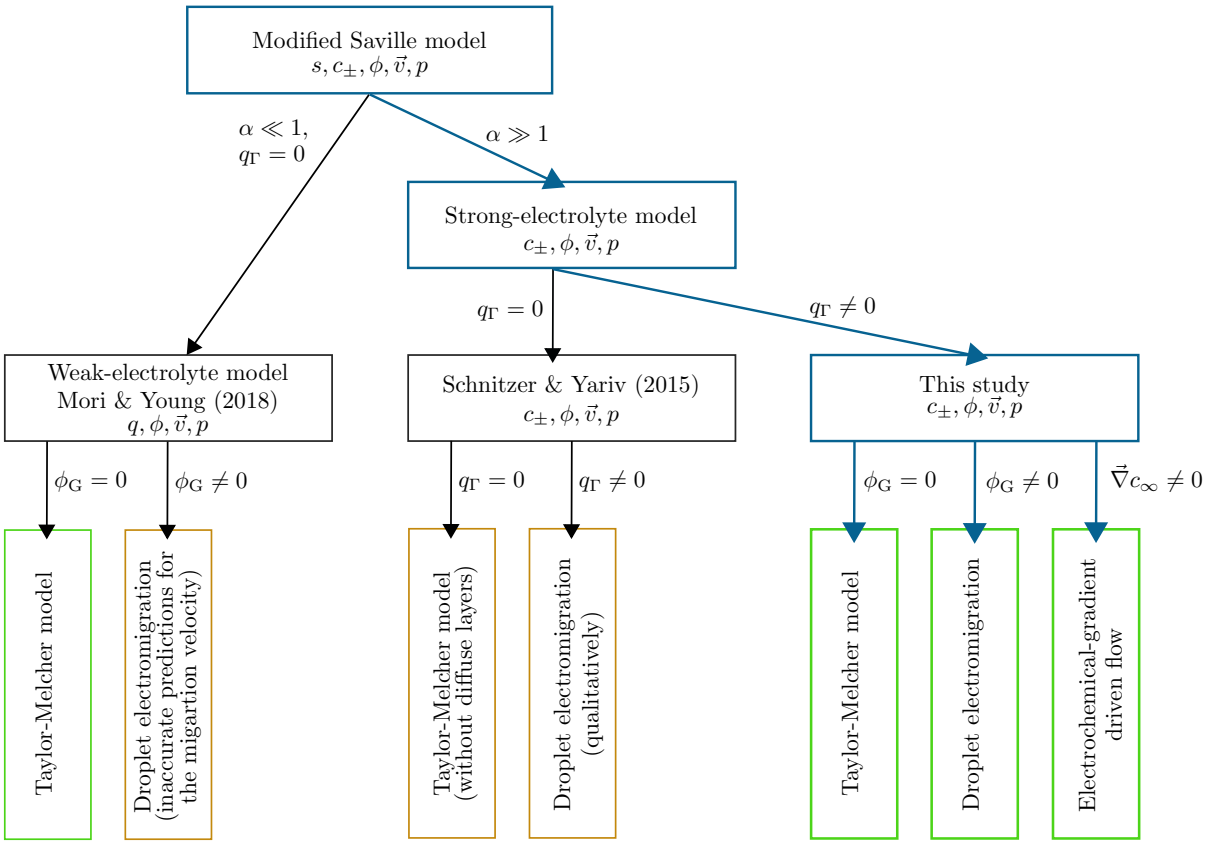

Figure 4.8: Model hierarchy and phenomenas captured by different electrokinetic approaches. Blue: Approach followed in this study. Green: Phenomena captured. Yellow: Phenomena qualitatively or inaccurately captured.

proaches by Mori and Young (2018)[9] and Schnitzer and Yariv (2015). The set of equations with reaction terms that we started our analysis with was called *Modified Saville model* by Mori and Young (2018). All approaches claim to capture droplet electromigration and can that they can be reduced to the TM model. However, Schnitzer and Yariv (2015) can also reduce the results to the TM model in the absence of diffuse layers. A coexistence of diffuse Debye clouds near the interface and the TM model – which can not be excluded in general – is not possible in their model approach. Additionally, they fail to make quantitative predictions on the migration velocity. They also could not explain the relation between conductivity ration and adsorption coefficients resulting from their model. Mori and Young (2018) deliver an explanation how interface properties and conductivities relate and derive a weak-electrolyte model that can be reduced to the TM model sustaining Debye clouds. The predictions on the migration velocity however are inaccurate. In contrast, the presented study derives a strong-electrolyte model and explains how its connection to the weak-electrolyte model. Better predictions on droplet electromigration can be drawn. Additionally, flow phenomena driven by electrochemical gradients can be explained with this model. We note that this phenomenon only occurs in systems with $D_+ \neq D_-$ and $\lim_{x^1 \to \infty} c_{(0)}$ as discussed in section 4.2.10.

The resulting model depends on gradients of an outer electric field, as well as charge gradients. The latter play a role in diffusio-osmotic problems with charge sources (e.g. the interface or with reservoirs far from the interface). However, the discussion of such problems is shifted to another work. Neglecting diffusio-osmotic effects, we investigated the influence of an outer electric field, observing both, electrodeformation and electromigration.

The electrodeformation agrees with the findings by Taylor (1966) and Mori and Young (2018). Deviating results for the electrodeformation can be found for larger Péclet numbers. This was discussed e.g. by Ma et al. (2022) who also performed a detailed Debye-layer analysis.

Electromigration could not be observed with earlier models (Melcher & Taylor, 1969; Saville, 1997) lacking an analysis of the Debye layer. However, in the weak electrolyte limit, with equivalent assumptions on δ, Pe, and t_Γ, Mori and Young (2018) also investigated the electromigration of a drop with non-equal partition coefficients. The qualitative results seem identical. Schnitzer and Yariv (2015) also predicted particle migration for the strong electrolyte limit, yet lacking a quantitative prediction, e.g. on the migration velocity.

Quantitatively, a comparison with Mori and Young (2018) helps to understand differences between the weak and strong electrolyte regimes. For small Galvani potentials, the predicted migration velocities agree. However, for larger Galvani potentials resulting from a stronger mismatch between the two partition coefficients, the predicted migration velocities are different. We note that many equations of the inner layer are identical in

[9]Note that this work is based on the original publication by Mori and Young (2018) and that critics discussed in this work led to the corrigendum (Marthaler et al., 2023).

both models, yet the electrical problem at $O(\delta^{-1})$ is not, resulting in the differences. This is discussed in more detail in appendix B. As a result of this work the original publication by Mori and Young (2018) was corrected (Marthaler et al., 2023).

For equal partition coefficients $l_+ = l_-$, both the weak electrolyte model and the strong electrolyte model presented in this work, reduce to the TM model. Surface convection does only appear at higher Péclet numbers that allow for the redistribution of charges inside the Debye region.

We here discussed particle transport under the influence of an outer electric field. Electromigration does only appear due to a mismatch between the two partition coefficients. From 4.131, we can conclude that

$$0 = \phi'_{\gamma(0)} - R\bar{\phi}'_{\gamma(0)} \tag{4.184}$$

while the surface charge is defined as

$$q_\gamma = S\bar{\phi}'_{\gamma(0)} - \phi'_{\gamma(0)} = \phi'_{\gamma(0)} \left(\frac{S}{R} - 1 \right). \tag{4.185}$$

In the absence of net surface charge, for $R = S$, the particle does still migrate in both regimes. The exchange of charges between inner and outer phase leads to a positive charge density on one side and a negative charge density on the other side of the interface. In the case of zero net charge, both ion clouds sum up to zero. However, the described charge dislocation effect together with the curved interface is sufficient for electromigration to arise.

CHAPTER 5

A feasibility study of the electrokinetic actuator by DNS with a Fourier-Chebyshev spectral code

In a wide range of electrohydrodynamic problems full-electrokinetic effects only appear within thin diffuse layers (as discussed in chapters 3 and 4). When exploiting asymptotic methods, those can be investigated analytically. Yet, when the underlying assumption $\delta \ll 1$ breaks down, an analytical treatment is not feasible.

This chapter focuses on experimental settings that are characterized by full-electrokinetic effects in the bulk and not only in a thin layer near the interface or solid surface. For that reason, we assume the Debye length to be of the order of the reference length

$$\delta = \frac{l_{\mathrm{D}}^*}{l_{\mathrm{ref}}^*} \sim O(1). \tag{5.1}$$

Although the Debye length l_{D}^* usually is relatively small, e.g. for a millimolar aqueous solution of sodium chloride $l_{\mathrm{D}}^* \approx 10\,\mathrm{nm}$, there still exist a range of problems in which the above assumption is valid. The Debye length is proportional to ${c_{\mathrm{equ}}^*}^{-1/2}$ and becomes large for relatively small ion concentrations. At the same time, the reference length of many experimental settings is beyond the milli- or micrometer scale of the droplet/cell problems discussed before. There are a range of biological objects like DNA, viruses, and proteins that are on the sub-micrometer length scale. The latest fabrication methods also allow manufacturing structures on similar length scales. In accordance with Moore's law, today transistor gate lengths can be fabricated that are in the order of 50 nm in size.

The focus of this chapter lies on the understanding of a microscale flow actuator whose operating point is in the full-electrokinetic regime, i.e. $\delta \sim O(1)$. The main function of this technical element is the controlled excitation of fluid flow in a small channel by electrohydrodynamic effects.

Although there exist many previous studies which treat similar applications operating in the small-Debye-length regime, the understanding of full-electrokinetic behavior

is still limited. A direct numerical simulation can help to understand electrokinetic flow excitation. In order to reach this goal, a spectral code is developed. For a rectangular two-dimensional domain, Fourier-collocation and Chebyshev-tau methods are combined. Pumping velocity and heat generation are computed.

5.1 Problem setup

5.1.1 Geometry

We assume the two-dimensional problem as depicted in Figure 5.1 with a fluid film between two substrate plates. Inside the substrate, electrodes are arranged in a regular pattern so that a traveling wave potential can be imposed on the boundaries. The electrode arrangement in the top and bottom plates is symmetrical to the central plane of the fluid layer. The computational domain only covers the lower half of the fluid film with symmetry conditions imposed on the central plane, i.e. the upper boundary. The rectangular domain has the height h^* and a single spatial period has the length l^*_{per}. The electrodes are arranged in an equidistant pattern and the electrode distance is used as reference length l^*_{ref}. We introduce the cartesian coordinates x^* for the longitudinal direction and y^* for the normal direction with respect to the lower wall. The respective orthonormal base $\{e_x,\, e_y,\, e_z\}$ is located in the origin $\mathcal{O}$ in the lower left corner of the domain. Although a three-phase/three-electrode actuator is depicted in Figure 5.1, any number of electrodes larger than three is possible. While a smoother signal can be produced with more electrodes, an actuator with a smaller number of electrodes is easier to design and takes less space. As the electrode distance is the limiting parameter in micro-fabrication, three-phase actuators can take smaller sizes than the respective elements with four or more electrodes. As actuators are supposed to be lined up in series, periodicity in the x^*-direction is assumed.

5.1.2 Material properties

We further assume that the fluid is an aqueous, binary, and symmetric electrolyte. Thus, the kinematic viscosity η^*, density ρ^*, permittivity ϵ, and heat capacity c_p^* of water is used. The electrolyte is assumed to be strong with $\alpha \gg 1$. We refer to the equilibrium concentration c^*_{equ} of a millimolar solution of sodium chloride with valence $\mathcal{Z}$ and diffusion coefficients $D^*_{\pm}$. The equilibrium conductivity is computed from the given diffusion coefficients, viscosity, and the equilibrium concentration. Yet, the conductivity is not uniform in the whole domain as ions are supposed to accumulate at the walls, thus resulting in a locally higher conductivity. The basic set of parameters is given in table 5.1.

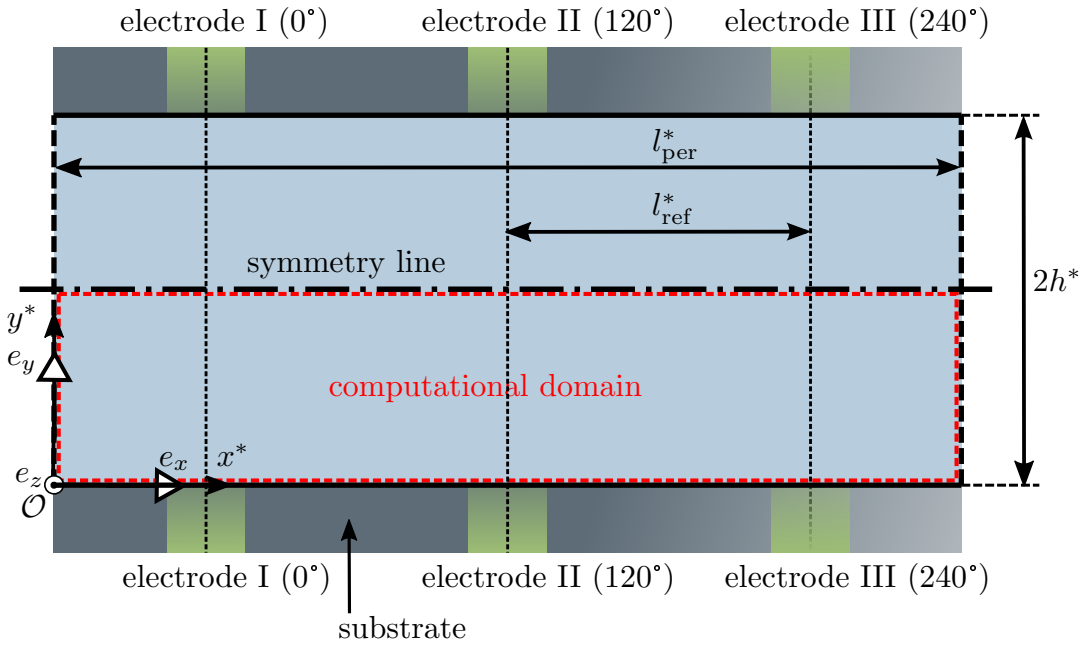

Figure 5.1: Schematic overview on the two-dimensional microfluidic actuator consisting of a fluid film between two plates of substrate. Individually controllable electrodes are arranged inside the substrate in a regular repeating pattern. Exemplatory, a three-phase actuator is depicted here. Higher numbers n of electrodes with a phase shift of $\frac{360°}{n}$ are possible.

fluid property	**symbol**	**unit**	**definition**	**value**	**comments**
density	ρ^*	$\mathrm{kg\,m^{-3}}$	–	10^3	
dynamic viscosity	η^*	$\mathrm{Pa\,s}$	–	10^{-3}	
relative permittivity	ϵ	–	–	80	
heat capacity	c_p^*	$\mathrm{J\,kg^{-1}\,K^{-1}}$	–	$4.2 \cdot 10^3$	
reference ion concentration	c_{equ}^*	$\mathrm{m^{-3}}$	–	10^{22}	$10^{-5}\,\mathrm{mol}\,l^{-1}$
diffusion coefficients	D^*	$\mathrm{m^2\,s^{-1}}$	–	10^{-9}	
valences	$\mathcal{Z}$	–	–	1	
reference parameter	**symbol**	**unit**	**definition**	**value**	**comments**
length scale/electrode dist.	l_{ref}^*	m	–	$150 \cdot 10^{-9}$	
time scale	t_{ref}^*	s	ν^{*-1}	$0.5 \cdot 10^{-3}$	$\nu^* = 2\,\mathrm{kHz}$
velocity scale	v_{ref}^*	$\mathrm{m\,s^{-1}}$	$l_{\mathrm{ref}}^* \nu^*$	$0.075 \cdot 10^{-3}$	
pressure scale	p_{ref}^*	Pa	$\eta^* \nu^*$	0.5	
intrinsic el. frequency	ν_{el}^*	Hz	$\frac{c_{\mathrm{equ}}^* k_{\mathrm{B}}^* T_{\mathrm{a}}^*}{\eta^*}$	$0.4 \cdot 10^6$	
Debye length	l_{D}^*	m	$\sqrt{\frac{\epsilon_0^* \epsilon \phi_{\mathrm{th}}^*}{\mathcal{Z} e_0^* c_{\mathrm{equ}}^*}}$	$88 \cdot 10^{-9}$	
dimensionless parameter	**symbol**	**unit**	**definition**	**value**	**comments**
Schmidt number	Sc	–	$\frac{\eta^*}{\rho^* D^*}$	10^3	
Reynolds number	Re	–	$\frac{\rho^* {l_{\mathrm{ref}}^*}^2 \nu^*}{\eta^*}$	10^{-5}	
Peclet number	Pe	–	$\frac{{l_{\mathrm{ref}}^*}^2 \nu^*}{D^*}$	0.05	
Hartmann number	Ha	–	$\frac{\nu_{\mathrm{el}}^*}{\nu_{\mathrm{ref}}^*}$	31	
dimensionless Debye length	δ	–	$\frac{l_{\mathrm{D}}^*}{l_{\mathrm{ref}}^*}$	0.6	$\sim O(1)$

Table 5.1: Material properties, reference parameters, and dimensionless numbers of the problem.

5.1.3 Excitation

On the lower boundary we assume the electric potential to be given a traveling wave as ζ-potential

$$\zeta^* = \zeta^*_{\text{amp}} \sin\left(2\pi\left(\frac{x^*}{l^*_{\text{per}}} - \nu^* t^*\right)\right) \tag{5.2}$$

where ζ^*_{amp} is the amplitude and ν^* the frequency. The phase shift is assumed to be zero. Note, there are cases where the excitation on the lower and upper electrodes are not synchronized, either unintentionally or intentionally, e.g. for driving a mixing mechanism.

5.1.4 Governing equations

The PDEs governing this problem are very similar to those discussed in chapters 3 and 4, i.e. the Poisson-Nernst-Planck (PNP) system coupled with the Stokes equations for low-Reynolds-number flow. However, there are two essential differences to the systems discussed so far, the geometry and the boundary conditions.

As discussed in section 5.1.1, the geometry of the actuator problem is rectangular. Thus, a number of simplifications apply to the equations. In particular, the stress-divergence form of the electric term in the Maxwell equation can be replaced by the Coulomb force as product of charge density and electric field

$$\vec{\nabla}^* \cdot \theta^* = -q^* \vec{\nabla}^* \phi^*. \tag{5.3}$$

Additionally, all curvature terms vanish in the rectangular geometry, i.e. $\kappa = 0$. We can thus write the governing equations as

$$\begin{aligned} \rho^* \partial_t^* \vec{v}^* &= -\vec{\nabla}^* p^* + \eta^* \nabla^{*2} \vec{v}^* - q^* \vec{\nabla}^* \phi^* \\ 0 &= \vec{\nabla}^* \cdot \vec{v}^* \\ \partial_t^* c_\pm^* &= -\vec{\nabla}^* \cdot \left(\vec{v}^* c_\pm^* - D^* \vec{\nabla}^* c_\pm^* \mp \mu^* c_\pm^* \vec{\nabla}^* \phi^*\right) \\ 0 &= \nabla^{*2} \phi^* + q^* \end{aligned} \tag{5.4}$$

assuming equal diffusivities D^* and mobilities μ^* for the ions. Due to the low Reynolds number, flow convection is neglected. Yet, we keep the transient term in order to track effects that may become relevant at high excitation frequencies. At the lower boundary for $y^* = 0$, we assume that the electric potential is equal to the ζ-potential given by relation 5.2. The wall is further assumed to be impermeable to the fluid and electrical currents, and friction is sufficiently high that the no-slip condition holds

$$\begin{aligned} \vec{v}^* &= \vec{0}, \\ \phi^* &= \zeta^*, \\ -D^* \partial_y^* c_\pm^* \mp \mu^* c_\pm^* \partial_y^* \phi^* &= 0. \end{aligned} \tag{5.5}$$

At the upper boundary for $y^* = h^*$, we assume the symmetry conditions

$$\begin{aligned} \partial_y^* v_x^* &= 0, \\ v_y^* &= 0, \\ \partial_y^* \phi^* &= 0, \\ \partial_y^* c_\pm^* &= 0. \end{aligned} \tag{5.6}$$

5.1.5 Dimensionless form

Employing the scaling presented in table 5.1, the set of equations 5.4 can be converted to a dimensionless form, and then reads

$$\begin{aligned} \mathrm{Re}\, \partial_t \vec{v} &= -\vec{\nabla} p + \nabla^2 \vec{v} - \mathrm{Ha}\, q \vec{\nabla} \phi, \\ 0 &= \vec{\nabla} \cdot \vec{v}, \\ \mathrm{Pe}\, \partial_t c_\pm^* &= -\vec{\nabla} \cdot \left(\mathrm{Pe}\, \vec{v} c_\pm - \vec{\nabla} c_\pm \mp c_\pm \vec{\nabla} \phi \right), \\ 0 &= \delta^2 \nabla^2 \phi + q. \end{aligned} \tag{5.7}$$

Analogously, we find from equations 5.5 the dimensionless boundary conditions at the wall $y = 0$

$$\begin{aligned} \vec{v} &= \vec{0}, \\ \phi &= \zeta, \\ \partial_y c_\pm \mp c_\pm \partial_y \phi &= 0, \end{aligned} \tag{5.8}$$

and from equations 5.6 at the mid-channel position $y = h = \frac{h^*}{l_{\mathrm{ref}}^*}$

$$\begin{aligned} \partial_y v_x &= 0, \\ v_y &= 0, \\ \partial_y \phi &= 0, \\ \partial_y c_\pm &= 0. \end{aligned} \tag{5.9}$$

The excitation function 5.2 which is used as wall-boundary condition for the potential reads in dimensionless form

$$\zeta = \zeta_{\mathrm{amp}} \sin\left(2\pi \left(\frac{x}{3} - t \right) \right). \tag{5.10}$$

We note that the electrode distance is used as reference length l_{ref}^*. Thus, for a three-phase actuator, the actuator length in x-direction is $l_{\mathrm{per}} = \frac{l_{\mathrm{per}}^*}{l_{\mathrm{ref}}^*} = 3$. The excitation amplitude $\zeta_{\mathrm{amp}} = \frac{\zeta_{\mathrm{amp}}^*}{\phi_{\mathrm{th}}^*}$ is scaled with the thermal potential.

5.1.6 Streamfunction formulation

Incompressible fluid flow is solenoidal, i.e. divergence-free (compare relation 5.7). According to the Poincaré lemma (Lee, 2018), on the whole domain a vector potential of $\vec{v}$

exists that is continuous and differentiable. As the problem is two-dimensional, this vector potential is a scalar. We introduce the streamfunction ψ in accordance with Batchelor (2010) and Lamb (1975), defined as

$$\vec{\nabla} \times \vec{\psi} = \vec{\nabla} \times \begin{pmatrix} 0 \\ 0 \\ \psi \end{pmatrix} = \begin{pmatrix} \partial_y \psi \\ -\partial_x \psi \\ 0 \end{pmatrix} = \begin{pmatrix} v_x \\ v_y \\ 0 \end{pmatrix} = \vec{v}. \tag{5.11}$$

We note some important properties of the streamfunction

$$\begin{aligned} \vec{\nabla} \cdot \left(\vec{\nabla} \times \vec{\psi} \right) = \vec{\nabla} \cdot \vec{v} = 0 \\ \vec{\nabla} \times \vec{v} = -\nabla^2 \psi. \end{aligned} \tag{5.12}$$

Applying the rotation to the momentum equation in 5.7 and using the properties 5.12 we find

$$\mathrm{Re}\, \partial_t \nabla^2 \psi = \nabla^4 \psi + \mathrm{Ha}\, \vec{\nabla} \times \left(q \vec{\nabla} \phi \right). \tag{5.13}$$

The pressure term vanishes from the equation due to the fact that the rotation of the gradient of a scalar is zero. However, the rotation of the Coulomb force term $\vec{\nabla} \times \left(q \vec{\nabla} \phi \right)$ does not vanish in general, while the same term without the charge density does $\vec{\nabla} \times \left(\vec{\nabla} \phi \right) = \vec{0}$.

The volume flow rate between two streamlines is constant. Additionally, there is no flow across a streamline. The volume flow rate between two streamlines ψ_1 and ψ_2 can be computed as $\psi_2 - \psi_1$. For that reason, the wall represents the zero-streamline where $\psi = 0$. Choosing a different value for this streamline changes the values of all other streamlines by a constant value. Volume flow and velocities stay unchanged.

Introducing the streamfunction, the set of equations 5.7 reads

$$\begin{aligned} \mathrm{Re}\, \partial_t \nabla^2 \psi &= \nabla^4 \psi + \mathrm{Ha}\, \vec{\nabla} \times \left(q \vec{\nabla} \phi \right) \\ \mathrm{Pe}\, \partial_t c_\pm &= -\vec{\nabla} \cdot \left(\mathrm{Pe}\, \vec{v} c_\pm - \vec{\nabla} c_\pm \mp c_\pm \vec{\nabla} \phi \right), \\ 0 &= \delta^2 \nabla^2 \phi + q. \end{aligned} \tag{5.14}$$

The biharmonic operator is a differential operator of fourth order and for the two-dimensional case defined as $\nabla^4 = \nabla^2 \nabla^2 = \partial_{xxxx} + \partial_{yyyy} + 2\, \partial_{xxyy}$. The mass conservation equation is used in the definition of the streamfunction and is thus not necessary in order to solve the problem. The wall boundary conditions now read

$$\begin{aligned} \psi &= 0, \\ \partial_y \psi &= 0, \\ \phi &= \zeta, \\ \partial_y c_\pm \mp c_\pm \partial_y \phi &= 0. \end{aligned} \tag{5.15}$$

Analogously, the mid-channel boundary conditions are adapted to the streamfunction formulation and read

$$\begin{aligned} \psi &= \psi_{\mathrm{tfr}}, \\ \partial_{yy}\psi &= 0, \\ \partial_y \phi &= 0, \\ \partial_y c_\pm &= 0, \end{aligned} \tag{5.16}$$

with the total flow rate $\psi_{\mathrm{tfr}} = \psi(y = h) - \psi(y = 0)$ not yet defined. In some cases the flow rate is given, e.g. when a pump with a known flow rate is mounted to the channel. However, in our case the flow rate is a parameter of interest and thus has to be computed. To reach this goal, one equation of the form

$$\mathrm{Re}\, \partial_t \vec{v} = -\vec{\nabla} p + \nabla^2 \vec{v} - \mathrm{Ha}\, q \vec{\nabla} \phi \tag{5.17}$$

has to be solved. As this solution is to be computed in spectral space, only one mode (a one-dimensional equation) needs to be computed using a given mean pressure gradient. This will be discussed in detail in section 5.3.6.

5.1.7 Initial conditions

When turning on the actuator / the actuator electrodes, dilute charges in the electrolyte travel towards the wall forming charge clouds. The Gouy-Chapman solution discussed in section 2.2.4 describes the resulting static charge distribution. Thus, we use the Gouy-Chapman solution as initial condition. The simulation time starts when the traveling wave starts moving.

5.2 The Fourier-Chebyshev spectral method

5.2.1 Collocation methods as a special form of weighted residual methods

The numerical approximation methods used in this chapter are a special form of collocation methods which are a special form of the weighted residual methods. Initial boundary value problems (IBVPs) often cannot be solved analytically. If this is the case, numerical methods like the weighted residual methods (WRM) or the Ritz method can be used to find an approximate solution.

Here, we apply on the weighted residual methods. For a general boundary value problem

$$\begin{aligned} A(u) &= b \qquad \text{in the domain } \Omega, \\ B(u) &= u_\Gamma \qquad \text{at the boundary } \Gamma \end{aligned} \tag{5.18}$$

where $u(x)$ is the parameter of interest, the spatial variable $x \in \Omega$ and A is a general

differential operator. The WRM utilizes the so-called trial solution

$$\begin{aligned} u_n &= U_0(x) + \sum_{i=1}^{N} U_n \varphi_n(x), \\ \text{with} \quad & B(U_0) = u_\Gamma, \quad B(\varphi_n) = 0 \quad \text{at the boundary,} \end{aligned} \tag{5.19}$$

where U_0, U_n are the unknown coefficients and $\varphi(x)$ is a set of known functions, usually referred to as trial functions. The residual error is obtained as

$$A(u_n) - b. \tag{5.20}$$

We remarked above that the WRM is used in cases where an analytical solution cannot be found. Thus, we cannot demand the residual 5.20 to globally vanish. However, in some cases an approximate solution can be found demanding the weighted residual to vanish

$$\int_\Omega w(x) \left(A(u_n) - b\right) \, \mathrm{d}x. \tag{5.21}$$

Different types of WRM utilize different weight functions, particularly sets of linearly independent functions $\{\lambda_i(x)\}_{i=1,\dots,N}$. One example of a WRM is the Galerkin method which uses the trial functions $\lambda_i = \varphi_i$.

Particularly important for this work are collocation methods demanding the residual at selected points x_i to vanish. Thus, the Dirac delta distribution for each of these collocation points $\lambda_i = \delta(x - x_i)$ are used as weights. In contrast to finite difference or finite volume methods which are more common in fluid mechanics, collocation methods stand out with their high accuracy. Already with a small number of grid points, e.g. which we also refer to as collocation points ~ 32, the numerical error can be in the order of machine precision. This is illustrated by a validation example in the next section.

Typical trial functions for collocation methods are orthogonal systems of polynomials. Fourier and Chebyshev polynomials are most commonly used on periodic or bounded domains respectively. Other examples for orthogonal systems of polynomials include Legendre polynomials, which are also used on bounded domains, as well as Laguerre polynomials for semi-infinite domains (Canuto, 1988). In this work, a combined spectral approach of a Fourier method for the periodic direction of the problem and a Chebyshev method for the bounded direction is utilized.

5.2.2 The non-interpolating spectral approach

The structure of the computational domain depicted in Figure 5.1 suggests the use of periodic Fourier modes in combination with Chebyshev modes for the finite direction. In the context of spectral methods, we will follow the terminology of Boyd (2000). With spectral methods, the solution of an equation can be computed in the spectral space, using the simpler spectral differentiation operators. At the same time, transformations between

physical parameters and their spectral modes are necessary. This is the approach used in this work which we will refer to as "non-interpolating" in accordance with Boyd (2000). Alternatively, "pseudospectral" or "interpolating" methods work without the necessity of such transformations, calculating derivatives in the physical space. For most applications, the simplicity and higher efficiency of pseudospectral methods outweigh the just slightly higher accuracy of the non-interpolating class of methods. However, the Gibb's phenomenon usually appears when using pseudospectral methods that necessitates the use of filters. In order to maintain the high accuracy of spectral methods, the actuator problem described above was solved with a non-interpolating method.

We introduce the rules of transformation, differentiation, and convolution for the combined Fourier-Chebyshev method following the descriptions in Peyret (2002). Thereafter, we apply those tools to the set of governing equations to find their spectral equivalent form. The equations are solved in spectral space and not transformed back, except for two cases. Those are, convolutions which can be computed faster in physical than spectral space, and additionally at time instances when we are interested in the physical values. Reducing this number, for example to only one point in time at which the result became stationary, can drastically speed up the respective computation.

This section delivers a detailed description of the algorithm. The crucial elements are the time integration method for the 4th-order flow problem, the coupling of charge transport and potential equations with Gummel's iteration, and the handling of the nonlinear charge boundary condition with the influence matrix method. Prior to discussing these techniques, we focus on the grid, the spectral equivalent form of the set of governing equations, and the Lanczos method (Lanczos, 1964) for the boundary conditions.

5.2.3 Transformations and grid

The solutions for each parameter $a \in \{\psi, c_\pm, \phi\}$ are sought in the form of a truncated Fourier series

$$a_i = \sum_{k=\frac{N_x}{2}}^{\frac{N_x}{2}-1} A_k \exp\left(\underline{\mathrm{i}} k x_i\right) = \mathcal{T}_\mathrm{F}^{-1}\left\{a_i\right\} \tag{5.22}$$

in the periodic x-direction, and in the form of a Chebyshev series

$$a_j = \sum_{l=0}^{N_y-1} A_l T_l(y_j) = \mathcal{T}_\mathrm{C}^{-1}\left\{a_j\right\} \tag{5.23}$$

in the y-direction. The shown 1D-transformations between physical space (small parameters) and spectral space (capital parameters) are denoted by $\mathcal{T}_\mathrm{F}$ and $\mathcal{T}_\mathrm{C}$, their 2D-combination is

$$A_{kl} = \mathcal{T}\left\{a_{ij}\right\} = \mathcal{T}_\mathrm{F}\left\{\mathcal{T}_\mathrm{C}\left\{a_{ij}\right\}\right\} = \mathcal{T}_\mathrm{C}\left\{\mathcal{T}_\mathrm{F}\left\{a_{ij}\right\}\right\}, \tag{5.24}$$

with $a_{ij} = a(x_i, y_j)$. In the code, both transformations are performed based on the FFT to reach acceptable performance. The application of the FFT for Chebyshev polynomials

requires minor pre- and post-processing which is implemented following Canuto (1988). The mesh in the periodic direction is aequidistant with N_x grid points, while in the wall-normal direction, we use the mesh

$$y_j = \frac{h}{2}\left(y_{\mathrm{GL},j} + 1\right) \tag{5.25}$$

which is adapted from the Gauss-Lobatto points

$$y_{\mathrm{GL},j} = \cos\frac{\pi j}{N_y - 1} \tag{5.26}$$

by stretching. Thus, the wall-normal grid with N_y grid points covers the interval $[0, h]$, while the interval of the x-direction is $[0, 3]$.

5.2.4 Spectral operators

Differentiation In order to solve the equations in spectral space, we need differential and convolution operators. While the differentiation of Fourier modes is the multiplication with $\underline{\mathrm{i}}k$, the regarding operator for Chebyshev modes is more derived from the recursion formula as discussed e.g. by Canuto (1988) and Peyret (2002). We denote the operators for differentiation of Fourier modes and Chebyshev modes with $\mathcal{D}_\mathrm{F}$ and $\mathcal{D}_\mathrm{C}$. Their definitions can be found, e.g. in Canuto (1988). The differentiation of Fourier modes is performed by multiplication of each mode with the imaginary unit and the respective wavenumber

$$\mathcal{D}_{F,km} = \begin{cases} \underline{\mathrm{i}}m, & k = m, \\ 0, & k \neq m \end{cases}. \tag{5.27}$$

The Chebyshev differentiation operator is defined by the recursion formula that can be given on p.68 in Canuto (1988). For the second order derivative, an analogous formula is given on p.69. The resulting differentiation matrix is a band matrix whose lower half is zero, as well as the main diagonal and every second of the upper diagonals. For $N_y = 5$, the derivation matrix is given by

$$\mathcal{D}_\mathrm{C} = \begin{pmatrix} 0 & 1 & 0 & 3 & 0 \\ 0 & 0 & 4 & 0 & 8 \\ 0 & 0 & 0 & 6 & 0 \\ 0 & 0 & 0 & 0 & 8 \\ 0 & 0 & 0 & 0 & 0 \end{pmatrix}. \tag{5.28}$$

Higher derivative operators can be obtained as a matrix product of these basic operators, e.g. for the Fourier operator (and analogously for the Chebyshev operator)

$$\mathcal{D}_\mathrm{F}^n = \underbrace{\mathcal{D}_\mathrm{F}\mathcal{D}_\mathrm{F}\ldots\mathcal{D}_\mathrm{F}}_{n \text{ times}}. \tag{5.29}$$

They can be combined to the spectral gradient operator in dimensionless form $\vec{\nabla\!\!\!/}$ defined as

$$\vec{\nabla\!\!\!/} A_{kl} = \left(\mathcal{D}_\mathrm{F} A_{kl}, A_{kl}\mathcal{D}_\mathrm{C}^\top\right)^\top \tag{5.30}$$

and the spectral Laplacian $\nabla\!\!\!/^2$ which is defined as

$$\nabla\!\!\!/^2 A_{kl} = \mathcal{D}_{\mathrm{F}}^2 A_{kl} + A_{kl} \mathcal{D}_{\mathrm{C}}^{2\top}. \tag{5.31}$$

The Fourier differential operators are applied as left-hand-side multiplications and the Chebyshev operators as right-handed multiplications. The reason for that is the structure of the arrays where the information for the x-direction is stored in the columns and the information for the y-direction in the rows. The operators include the matrix products $\mathcal{D}_{\mathrm{F}}^2 = \mathcal{D}_{\mathrm{F}}\mathcal{D}_{\mathrm{F}}$ and $\mathcal{D}_{\mathrm{C}}^{2\top} = \left(\mathcal{D}_{\mathrm{C}}\mathcal{D}_{\mathrm{C}}\right)^{\top}$.

Spectral convolution The nonlinear terms in the PDEs include products of parameters. In spectral space, these terms are calculated as convolutions. The convolution, denoted by $*$, is performed using three FFT-based transformations

$$A_{kl} * B_{kl} = \mathcal{T}\left\{\mathcal{T}^{-1}\left\{A_{kl}\right\} \odot \mathcal{T}^{-1}\left\{B_{kl}\right\}\right\}, \tag{5.32}$$

which is remarkably faster than the convolution procedure in spectral space[1] (logarithmic complexity versus quadratic complexity). Additionally, the back-transformation followed by a multiplication is very intuitive and does not necessitate the Cauchy product of two series. The Hadamard operator $\odot$ in relation 5.32 denotes the element-wise multiplication of two matrices with a matrix of same shape as result.

5.2.5 The Lanczos method for the implementation of boundary conditions

We transform the governing equations to spectral space and bring them in the form of the Helmholtz equation

$$\nabla\!\!\!/^2 A_{kl} - \lambda A_{kl} = B_{kl}. \tag{5.33}$$

where λ denotes a scalar operator. Alternatively, the Helmholtz operator $\mathcal{H}$ is used in the short form of the above equation

$$\begin{aligned} \mathcal{H}\, A_{kl} &= B_{kl}, \\ \mathcal{H} &= \nabla\!\!\!/^2 - \lambda\mathcal{I}. \end{aligned} \tag{5.34}$$

The right-hand-side B_{ij} includes all constant and nonlinear terms of the equations. As equation 5.33 is a second order differential equation, we need two boundary conditions in wall-normal direction to solve the problem. For that reason, the last two rows of the Helmholtz operator $\mathcal{H}$ and the right-hand-side B_{ij} are replaced by the boundary conditions in accordance to the Lanzcos scheme (Lanczos, 1964).

[1] The convolution algorithm in spectral space can be found in Canuto (1988), Canuto (2006), and Peyret (2002)

Linear boundary conditions The Robin boundary condition at the lower boundary $y = -1$ and the upper boundary $y = 1$ of a one-dimensional problem on the domain $[-1, 1]$

$$\begin{aligned} m_{0,-1}\, a(-1) + m_{1,-1}\, a'(-1) &= d_{-1} \\ m_{0,+1}\, a(1) + m_{1,+1}\, a'(1) &= d_{+1} \end{aligned} \tag{5.35}$$

with the scalar prefactors $m_{0,\pm1}$ and $m_{1,\pm1}$ can be transferred to the spectral space

$$\begin{aligned} \sum_{l=0}^{N_y-1} (-1)^l \left(m_{0,-1} - m_{1,-1}\, l^2\right) A_l &= d_{-1} \\ \sum_{l=0}^{N_y-1} \left(m_{0,+1} + m_{1,+1}\, l^2\right) A_l &= d_{+1}. \end{aligned} \tag{5.36}$$

For a one-dimensional problem discretized with 5 grid points, equation 5.34 reads

$$\begin{pmatrix} \mathcal{H}_{00} & \mathcal{H}_{01} & \mathcal{H}_{02} & \mathcal{H}_{03} & \mathcal{H}_{04} \\ \mathcal{H}_{10} & \mathcal{H}_{11} & \mathcal{H}_{12} & \mathcal{H}_{13} & \mathcal{H}_{14} \\ \mathcal{H}_{20} & \mathcal{H}_{21} & \mathcal{H}_{22} & \mathcal{H}_{23} & \mathcal{H}_{24} \\ 0 & 0 & 0 & -\lambda & 0 \\ 0 & 0 & 0 & 0 & -\lambda \end{pmatrix} \begin{pmatrix} A_0 \\ A_1 \\ A_2 \\ A_3 \\ A_4 \end{pmatrix} = \begin{pmatrix} B_0 \\ B_1 \\ B_2 \\ B_3 \\ B_4 \end{pmatrix}. \tag{5.37}$$

For instance, one Dirichlet boundary condition and one Neumann boundary condition, i.e. $m_{1,-1}, m_{0,+1} = 0$ and $m_{0,-1}, m_{1,+1} = 1$ can be applied following relation 5.36, so that we find

$$\begin{pmatrix} \mathcal{H}_{00} & \mathcal{H}_{01} & \mathcal{H}_{02} & \mathcal{H}_{03} & \mathcal{H}_{04} \\ \mathcal{H}_{10} & \mathcal{H}_{11} & \mathcal{H}_{12} & \mathcal{H}_{13} & \mathcal{H}_{14} \\ \mathcal{H}_{20} & \mathcal{H}_{21} & \mathcal{H}_{22} & \mathcal{H}_{23} & \mathcal{H}_{24} \\ 1 & 1 & 1 & 1 & 1 \\ 0 & -1 & 4 & -9 & 16 \end{pmatrix} \begin{pmatrix} A_0 \\ A_1 \\ A_2 \\ A_3 \\ A_4 \end{pmatrix} = \begin{pmatrix} B_0 \\ B_1 \\ B_2 \\ d_{-1} \\ d_{+1} \end{pmatrix}. \tag{5.38}$$

We denote the matrix operators which are adapted to the boundary conditions with a bar, so that we find for a two-dimensional problem

$$\bar{\mathcal{H}}\, A_{kl} = \bar{B}_{kl}. \tag{5.39}$$

This problem can be solved by computing the inverse of the matrix $\bar{\mathcal{H}}$ to find

$$A_{kl} = \bar{\mathcal{H}}^{-1} \bar{B}_{kl}. \tag{5.40}$$

In many cases, the matrix $\bar{\mathcal{H}}$ and thus also $\bar{\mathcal{H}}^{-1}$ stays constant for all time steps. It is then efficient to compute the inverse as a pre-processing step and to only compute the matrix product $\bar{\mathcal{H}}^{-1} \bar{B}_{kl}$ at each time step.

We will use the operators

$$\mathrm{bc}_- \{A_{kl}\} = D_{-,k} \quad \text{and} \quad \mathrm{bc}_+ \{A_{kl}\} = D_{+,k} \tag{5.41}$$

to describe that the spectral expression A_{kl} is to be evaluated at the lower and higher boundary respectively. If A_{kl} does not take the form 5.35, a more sophisticated solution procedure needs to be applied, as discussed in section 5.3.4.

5.3 Construction of a solver in Python

5.3.1 General comments

The solution of the system 5.14, 5.15, and 5.16 with the Fourier-Chebyshev spectral method introduced in section 5.2 is challenging for a number of reasons. The electric problem does not converge with traditional iteration methods, like Jacobi, Gauss-Seidel, relaxation or gradient methods. From the field of computational semiconductor research, an iteration method designed by Gummel (1964) was adapted to solve this problem. In solids, double layers are observed that can be described in a very similar way to the electric double layers in fluid electrolytes. The nonlinear boundary conditions (5.15) at the wall are accounted for with the influence matrix method, as discussed by Peyret (2002). Time-integration of the fourth-order PDE in 5.14 is not possible with the traditional methods suggested in the seminal summaries on spectral methods by Boyd (2000); Canuto (1988); Peyret (2002). Yet, a solution technique originally suggested by Ying (2005) and Ying et al. (2008) for the modeling of cardiac dynamics was successfully used to solve this equation. This method is called two-stage composite backward differentiation formula of second order and is abbreviated with C-BDF2.

The combined solution algorithm is illustrated in Figure 5.2. A detailed discussion of its important parts is delivered in the following sections. In order to give more insight into the implementation, a UML diagram is attached in the appendix. The time is discretized as

$$t^n = n\,\Delta t \quad \text{with} \quad n = 0, 1, 2, \ldots N_t - 1. \tag{5.42}$$

For the discretization of the physical space, a combination of equidistant points x_i and Gauss-Lobatto points y_j is used. As discussed in section 5.2.3, the respective spectral modes are denoted by k and l. At time t^n we have for a general parameter

$$\begin{aligned} a_{ij}^n &= \mathcal{T}^{-1}\left\{A_{kl}^n\right\} \qquad \text{physical parameter,} \\ A_{kl}^n &= \mathcal{T}\left\{a_{ij}^n\right\} \qquad \text{spectral parameter.} \end{aligned} \tag{5.43}$$

In case of an iterative scheme like Gummel's iteration, one more superscript can appear, indicating the iteration step m.

5.3.2 Spectral module containing the basic operations

The basic operations of the Fourier-Chebyshev spectral method are implemented in a self-designed spectral module which is illustrated by the UML diagram 5.3. These are mainly the operations discussed in section 5.2.

The basic Fourier- and Chebyshev spectral methods work best on their "natural" grids, the equidistant grid on $x \in [0, 2\pi]$ and the Gauss-Lobatto points on $y \in [-1, 1]$. Besides the meshing operations, all differentiation and transformation operations need a pre-processing step for domains that are different from those natural grid sizes, which is

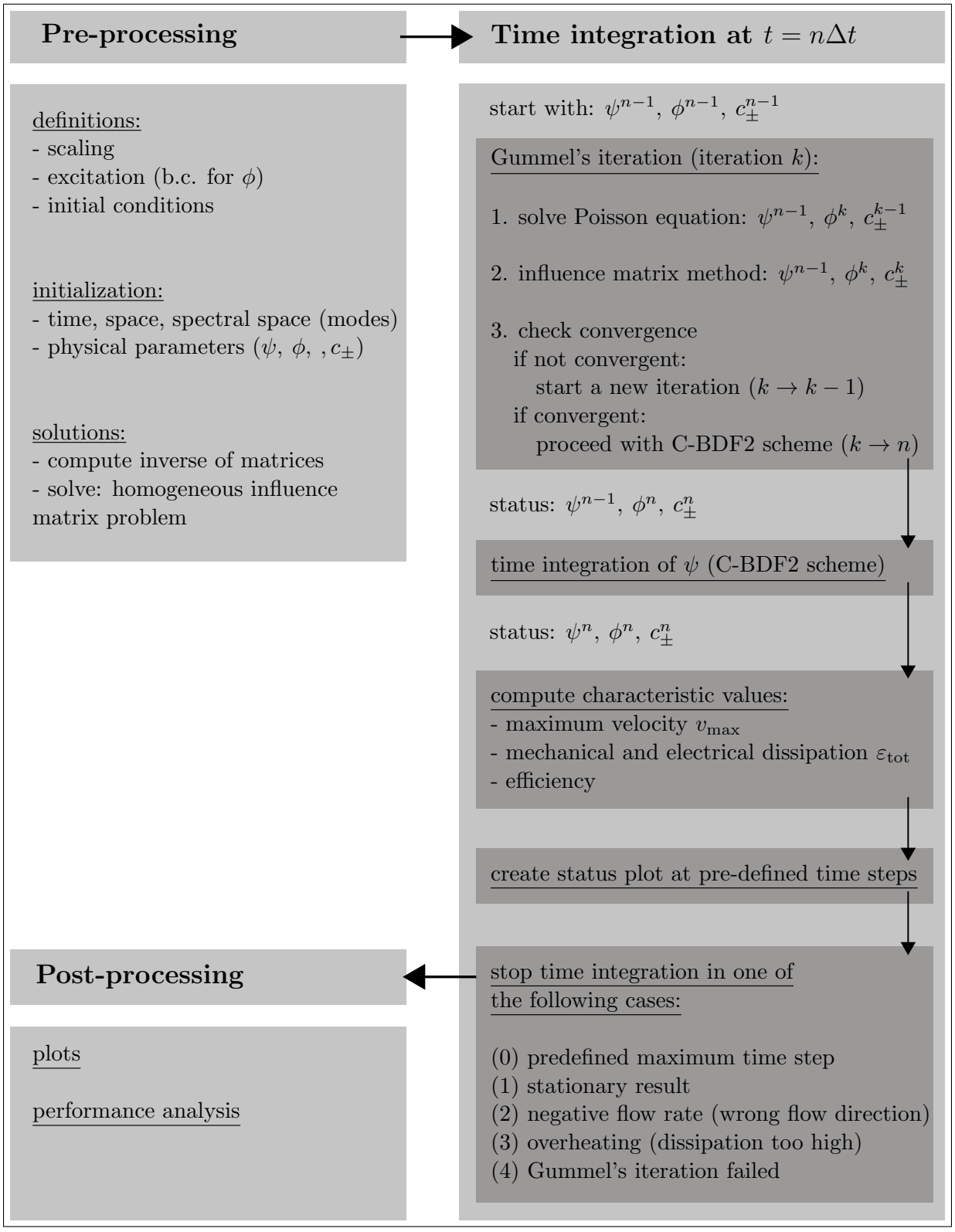

Figure 5.2: Python solver for the EHD-flow actuator. The time integration is split into the solution of the electric problem (using Gummel's iteration and the influence matrix method) and the flow problem using the C-BDF2 scheme. All other steps of the algorithm are pre- and post-processing

implemented in the module.

The transformations between spectral and physical space are the most expensive parts of a spectral solver. In order to reduce the runtime complexity, a fast Fourier transformation (FFT) is used instead of the discrete Fourier transformation (DFT). These methods have a runtime complexity of $\mathcal{O}_{DFT}(n^2)$ and $\mathcal{O}_{FFT}(n \log n)$. For the simulations, typically a grid size of $N_x = 32$ and $N_y = 40$ points was used. In that case, the FFT-based algorithm is by 2 orders faster that the DFT. For more collocation points, the advantage of the FFT becomes even larger.

The transformation of Chebyshev modes can also be performed using the FFT. Therefore, the necessary pre- and post-processing routines as described by Canuto (1988) were used. The additional cost of these extra-computations is outweighed by the faster FFT.

5.3.3 Discretization of the PNP system

As illustrated in the algorithm overview 5.2, the Poisson-Nernst-Planck (PNP) system is solved separately from the flow equation. For that reason we focus on the charge transport and Poisson equation 5.14. We introduce the spatial discretization at the collocation points as discussed in section 5.2.3. In the Helmholtz form (cp. relations 5.33, 5.34), the PNP system reads

$$\begin{aligned} \mathrm{Pe}\, \partial_t c_{\pm,ij} - \nabla^2 c_{\pm,ij} &= \mathrm{nl}_{\pm,ij}, \\ \delta^2 \nabla^2 \phi_{ij} + q_{ij} &= 0, \end{aligned} \tag{5.44}$$

where we have summarized the nonlinear terms (the convective and electrophoretic fluxes) as

$$\begin{aligned} \mathrm{nl}_{\pm} &= -\vec{\nabla} \cdot \left(\mathrm{Pe}\, \vec{v}_{ij} \odot c_{\pm,ij} \mp c_{\pm,ij} \odot \vec{\nabla} \phi_{ij} \right) \\ &= -\mathrm{Pe}\, \vec{v}_{ij} \cdot \vec{\nabla} c_{\pm,ij} \pm \vec{\nabla} \cdot \left(c_{\pm,ij} \odot \vec{\nabla} \phi_{ij} \right). \end{aligned} \tag{5.45}$$

The $\odot$-operator denotes element-wise products (compare the convolution procedure 5.32). In the case of a multiplication between a scalar and a vector, the element-wise multiplication is applied between the scalar and each vector-element. By applying the transformation 5.43, we obtain the equivalent equations in spectral space

$$\begin{aligned} \mathrm{Pe}\, \partial_t C_{\pm,kl} - \nabla\!\!\!/^2 C_{\pm,kl} &= \mathrm{NL}_{kl}, \\ \delta^2 \nabla\!\!\!/^2 \Phi_{kl} + Q_{kl} &= 0. \end{aligned} \tag{5.46}$$

The product operators transform to convolutions in spectral space and we get

$$\mathrm{NL}_{\pm} = \vec{\nabla\!\!\!/} \cdot \left(-\mathrm{Pe}\, \vec{V}_{kl} * C_{\pm,kl} \pm C_{\pm,kl} * \left(\vec{\nabla\!\!\!/} \Phi_{kl} \right) \right). \tag{5.47}$$

Introducing the time discretization 5.42 the system 5.46 reads

$$\begin{aligned} \left(\frac{\mathrm{Pe}}{\Delta t} - \nabla\!\!\!/^2 \right) \Delta C^n_{\pm,kl} &= \nabla\!\!\!/^2 C^{n-1}_{\pm,kl} + \mathrm{NL}^n_{\pm,kl}, \\ \delta^2 \nabla\!\!\!/^2 \Phi^n_{kl} + Q^n_{kl} &= 0. \end{aligned} \tag{5.48}$$

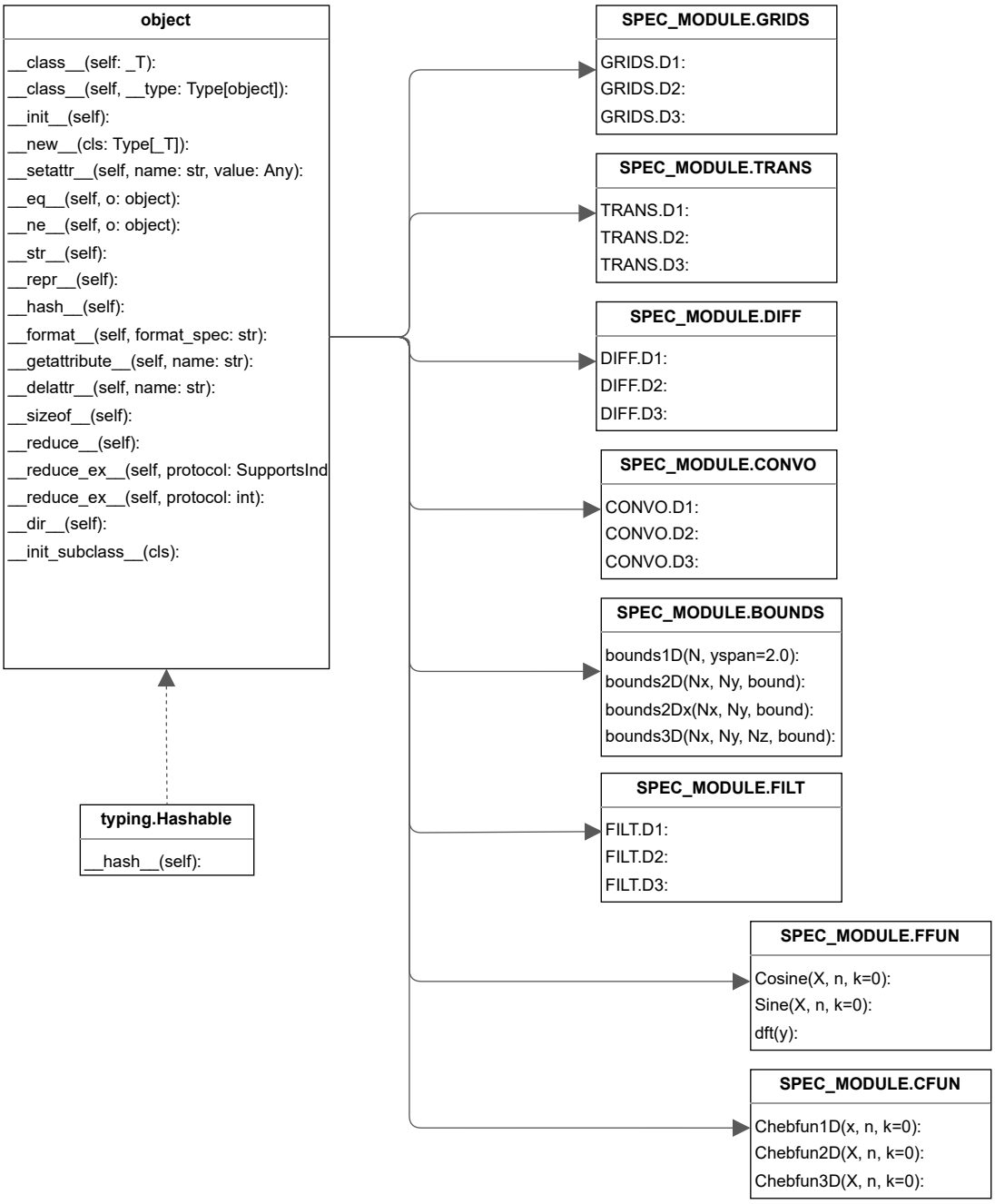

Figure 5.3: UML diagram of the spectral module, containing classes for meshing (grids), transformations between physical and spectral space, differentiation in spectral space, convolutions, boundary conditions, and filters. Additionally, classes delivering the Fourier and Chebyshev functions can be found in this module. The sub-classes named "D1", "D2", "D3" conatin the respective methods for one- two- and three-dimensional problems. Different combinations of Fourier("F")- and Chebyshev("C")-methods are possible. In 1D: F,C; in 2D: FF, FC, CC; in 3D: FFF, FFC, FCC, CCC.

We have here applied an Euler-backwards scheme with a constant time step using the formulation

$$C^n_{\pm,kl} = C^{n-1}_{\pm,kl} + \Delta C^n_{\pm,kl} \quad \text{with} \quad C^n_{\pm} = C_{\pm,kl}\left(n\Delta t\right). \tag{5.49}$$

As the system 5.48 is fully coupled, its solution necessitates an iterative procedure. This approach is discussed in section 5.3.5 after introducing the influence matrix method for the handling of the nonlinear boundary conditions. For each iteration step m, the system 5.48 can be written as

$$\begin{aligned} \mathcal{H}_C \Delta C^{n,m}_{\pm,kl} &= \nabla\!\!\!/^2 C^{n-1}_{\pm,kl} + \mathrm{NL}^{n,m-1}_{\pm,kl}, \\ \delta^2 \nabla\!\!\!/^2 \Phi^{n,m}_{kl} + Q^{n,m}_{kl} &= 0, \end{aligned} \tag{5.50}$$

where we have introduced the Helmholtz matrix $\mathcal{H}_C = \frac{\mathrm{Pe}}{\Delta t} - \nabla\!\!\!/^2$. We note that the charge transport equations are solved first and their solution is utilized for the computation of the electric potential.

5.3.4 The no-flux boundary conditions and influence matrix method

The system 5.50 cannot be solved without the boundary conditions 5.15 and 5.16. The latter two wall conditions of 5.15 for $c_\pm$ and ϕ read in spectral form

$$\begin{aligned} \mathcal{T}_{\mathrm{F}}\left\{\zeta_i\right\} &= \mathrm{bc}_-\left\{\Phi_{kl}\right\}, \\ 0 &= \mathrm{bc}_-\left\{-C_{\pm,kl}\mathcal{D}^\top_{\mathrm{C}} \mp C_{\pm,kl} * \left(\Phi_{kl}\mathcal{D}^\top_{\mathrm{C}}\right)\right\}, \end{aligned} \tag{5.51}$$

where we have used the boundary condition operator defined in 5.41. The symmetry conditions at the upper boundary are

$$\begin{aligned} 0 &= \mathrm{bc}_+\left\{\Phi_{kl}\mathcal{D}^\top_{\mathrm{C}}\right\}, \\ 0 &= \mathrm{bc}_+\left\{C_{\pm,kl}\mathcal{D}^\top_{\mathrm{C}}\right\}. \end{aligned} \tag{5.52}$$

We note that the no-flux condition in 5.51 does not have the linear form of the Robin boundary condition 5.35, but is nonlinear. For that reason, the Lanczos technique presented in section 5.2.5 fails. The solution of the system 5.50 together with the boundary conditions 5.51, 5.52 is found using the influence matrix method as suggested by Peyret (2002).

The influence matrix method is based on the assumption that the solution of the problem can be composed as linear superposition. For that purpose, N_x time-independent solutions of the homogeneous problem are computed before the time integration and one time-dependent solution with homogeneous boundary conditions is computed at each time-step. The $N_x + 1$ solutions are superposed to fulfill the nonlinear condition.

Homogeneous problem with inhomogeneous b.c. The respective homogeneous problem which belongs to 5.50 reads

$$\mathcal{H}_C \Delta C_{\pm,kl} = \mathcal{N}, \tag{5.53}$$

where $\mathcal{N} \in \mathbb{C}^{N_x \times N_y}$ denotes the zero matrix. This equation is not dependent on the time t^n and can thus be solved in the pre-processing step before starting the time integration. For a nonlinear boundary with N_x boundary points, the problem 5.53 is solved N_x times. In each of the solutions denoted by $\Delta\mathring{C}^r_{\pm,kl}$ all values at the boundary vanish besides at the r-th boundary point. The systems to solve are

$$\begin{aligned} \overline{\mathcal{H}_C}\Delta\mathring{C}^r_{\pm,kl} &= \overline{\mathcal{N}}, && \text{with} \quad r = 0, 1, \ldots, N_x - 1, \\ \mathrm{bc}_- \left\{\Delta\mathring{C}^r_{\pm,kl}\right\} &= \mathcal{T}_\mathrm{F}\left\{\delta^r_i\right\}, && \text{with} \quad \delta^r_i = \begin{cases} 0, & r \neq i, \\ 1, & r = i, \end{cases} \\ \mathrm{bc}_+ \left\{\Delta\mathring{C}^r_{\pm,kl}\mathcal{D}^\top_\mathrm{C}\right\} &= 0. \end{aligned} \tag{5.54}$$

Here, the operators $\overline{\mathcal{H}_C}$ and $\overline{\mathcal{N}}$ include the linear boundary conditions specified in 5.54 following the Lanczos method presented in section 5.2.5. As an alternative to setting one boundary value to unity, one mode per solution can also be set to unity. The respective condition is

$$\mathrm{bc}_- \left\{\Delta\mathring{C}^r_{\pm,kl}\right\} = \delta^r_k. \tag{5.55}$$

As long as the resulting solutions are linearly independent, any set of boundary values can be used. In some cases, using 5.55 instead of 5.54 is cheaper due to the Fourier transformation used in the latter.

Inhomogeneous problem with homogeneous b.c. In order to take the nonlinear terms of 5.50 into account, the nonlinear problem with homogeneous boundary conditions

$$\begin{aligned} \overline{\mathcal{H}_C}\Delta\tilde{C}^{n,m}_{\pm,kl} &= \overline{\nabla^2\tilde{C}^{n-1}_{\pm,kl} - \tilde{\mathrm{NL}}^{n,m-1}_{\pm,kl}} \\ \mathrm{bc}_- \left\{\Delta\mathring{C}^r_{\pm,kl}\right\} &= 0 \\ \mathrm{bc}_+ \left\{\Delta\mathring{C}^r_{\pm,kl}\mathcal{D}^\top_\mathrm{C}\right\} &= 0 \end{aligned} \tag{5.56}$$

is solved at each time step n and each iteration step m. We denote the solution to this problem with $\Delta\tilde{C}^{n,m}_{\pm,kl}$. Again, the overline represents the implementation of the linear boundary conditions stated in 5.56 with the Lanczos method.

Superposition Finally, we assume that the solution to the nonlinear problem can be represented as linear superposition of the form

$$\begin{aligned} C^{n,m}_{\pm,kl} &= C^{n-1}_{\pm,kl} + \Delta C^{n,m}_{\pm,kl} \\ \Delta C^{n,m}_{\pm,kl} &= \Delta\tilde{C}^{n,m}_{\pm,kl} + \lambda^{n,m,r}_\pm \Delta\mathring{C}^r_\pm \end{aligned} \tag{5.57}$$

with the unknown parameters $\lambda^{n,m,r}_\pm$. We drop the index m as the computation has to be performed at each iteration step. Also, we drop k and l to obtain the values at each time step

$$\begin{aligned} C^n_\pm &= C^{n-1}_\pm + \Delta C^n_\pm \\ &= C^{n-1}_\pm + \Delta\tilde{C}^n_\pm + \lambda^{n,r}_\pm \Delta\mathring{C}^r_\pm. \end{aligned} \tag{5.58}$$

We can now plug this result into the no-flux condition 5.51 to obtain

$$0 = \mathrm{bc}_- \left\{ - \left(C_\pm^{n-1} + \Delta\tilde{C}_\pm^n + \lambda_\pm^{n,r} \Delta\mathring{C}_\pm^r \right) \mathcal{D}_\mathrm{C}^\top \mp \left(C_\pm^{n-1} + \Delta\tilde{C}_\pm^n + \lambda_\pm^{n,r} \Delta\mathring{C}_\pm^r \right) * \left(\Phi^n \mathcal{D}_\mathrm{C}^\top \right) \right\}. \tag{5.59}$$

The only unknown in this equation is $\lambda_\pm^{n,r} \in \mathbb{C}^{N_x}$ which can be computed from the matrix equation

$$\mathcal{A}^n \left(\Delta\mathring{C}_\pm^r, \Phi^n \right) \lambda_\pm^{n,r} = \mathcal{B}^n \left(C_\pm^{n-1}, \Delta\tilde{C}_\pm^n, \Phi^n \right), \tag{5.60}$$

where $\mathcal{A}^n \in \mathbb{C}^{N_x \times N_x}$ is a regular matrix and $\mathcal{B}^n \in \mathbb{C}^{N_x}$ a vector. As $\mathcal{A}^n$ not only depends on the time-independent $\Delta\mathring{C}_\pm^r$, but also on ϕ^n, it has to be set up and inverted at each time step.

Concluding remarks The influence matrix method is based on the assumption that a linear decomposition of the solution is possible. Thus, it is expected to fail for strongly nonlinear problems. Although this reduces the range of possible conditions under which the Python code is applicable, practical use has proven that the code successfully delivers results for most of the relevant experimental settings.

5.3.5 Equation coupling with Gummel's iteration

As mentioned in section 5.3.3, the equations 5.50 are coupled and strongly nonlinear. The developed code takes this into account by using an iterative procedure. The procedure is adapted from a technique first published by Gummel (1964). However, it was developed for the numerical computation of electric double layers in semiconductors. For known charge concentrations, fluid double layers are mainly characterized by their thickness and the outer applied potential. Double layers in semiconductors additionally depend on quasi-Fermi potentials of holes and electrons, as well as ionized impurity scattering. Thus, their fluid equivalent appears to be more simple, assuming that convective charge transport does not have too strong an influence on the system.

Algorithm Although we have already derived the Poisson equation in spectral form, it is helpful to start with the physical formulation at time step n and iteration step m

$$0 = \delta^2 \nabla^2 \phi^{n,m} + q^{n,m}. \tag{5.61}$$

We use the decomposition introduced in section 5.3.4,

$$\begin{aligned} \phi_{ij}^{n,m} &= \phi_{ij}^{n,m-1} + \Delta^m \phi_{ij}^{n,m}, \\ c_{\pm,ij}^{n,m} &= c_{\pm,ij}^{n,m-1} + \Delta^m c_{\pm,ij}^{n,m}, \end{aligned} \tag{5.62}$$

with the operator Δ^m denoting the difference to the previous iteration step, in contrast to $\Delta = \Delta^n$, which is used to denote the difference to the previous time step $n-1$. We further assume the validity of the Gouy-Chapman solution (cp. section 2.2.4)

$$c_{\pm,ij}^{n,m} = \exp\left(\mp \phi_{ij}^{n,m} \right). \tag{5.63}$$

Plugging this into the Poisson equation 5.61, we obtain

$$0 = \delta^2\nabla^2\left(\phi_{ij}^{n,m-1} + \Delta^m\phi_{ij}^{n,m}\right) + \exp\left(-\phi_{ij}^{n,m-1} - \Delta^m\phi_{ij}^{n,m}\right) - \exp\left(\phi_{ij}^{n,m-1} + \Delta^m\phi_{ij}^{n,m}\right). \tag{5.64}$$

Assuming that the change of the electric potential per iteration step $\Delta^m\phi_{ij}^{n,m}$ is small, the series representation of the Euler function can be used to obtain

$$0 = \delta^2\nabla^2\left(\phi_{ij}^{n,m-1} + \Delta^m\phi_{ij}^{n,m}\right) + \exp\left(-\phi_{ij}^{n,m-1}\right)\left(1 - \Delta^m\phi_{ij}^{n,m}\right) - \exp\left(\phi_{ij}^{n,m-1}\right)\left(1 + \Delta^m\phi_{ij}^{n,m}\right) \tag{5.65}$$

which can also be written in terms of the charge density $q_{ij}^{n,m-1}$ and dimensionless conductivity $c_{ij}^{n,m-1}$ at the previous iteration step

$$0 = \delta^2\nabla^2\left(\phi_{ij}^{n,m-1} + \Delta^m\phi_{ij}^{n,m}\right) + q_{ij}^{n,m-1} - \left(\Delta^m\phi_{ij}^{n,m}\right)c_{ij}^{n,m-1}, \tag{5.66}$$

which can be rewritten as

$$\left(\Delta^m\phi_{ij}^{n,m}\right)c_{ij}^{n,m-1} - {l_\mathrm{D}^*}^2\nabla^2\left(\Delta^m\phi_{ij}^{n,m}\right) = q_{ij}^{n,m-1} + \delta^2\nabla^2\left(\phi_{ij}^{n,m-1}\right). \tag{5.67}$$

Finally, we transform this equation to spectral space. The system to solve then reads

$$\begin{aligned} \overline{\mathcal{H}_\Phi}\Delta^m\Phi_{kl}^{n,m} &= \overline{Q_{kl}^{n,m-1} + \delta^2\nabla^2\left(\Phi_{kl}^{n,m-1}\right)}, \\ \mathrm{bc}_-\left\{\Phi_{kl}^n\right\} &= \mathcal{T}_\mathrm{F}\left\{\zeta_i\right\} \\ \mathrm{bc}_+\left\{\Phi_{kl}^n\mathcal{D}_\mathrm{F}^\top\right\} &= 0 \end{aligned} \tag{5.68}$$

with the system matrix $\mathcal{H}_\Phi = C_{kl}^{n,m-1} - \delta^2\nabla^2$ and the linear boundary conditions.

Integration into the code When computing the solution at the time step n, the Poisson equation is solved first, delivering the potential for the first iteration step $\Phi_{kl}^{n,m}$. Afterwards, the charge transport equations are solved using the influence matrix method presented in section 5.3.4. The loop is interrupted if the change variables $\Delta^m\Phi_{kl}^{n,m}$ and $\Delta^m C_{\pm,kl}^{n,m}$ are smaller than a certain threshold value, which we denote with ϖ_Gummel. In the practical use of the code, values $\varpi_\mathrm{Gummel} \in [10^{-8}, 10^{-5}]$ are an acceptable trade-off between speed and accuracy.

5.3.6 Solution of the streamfunction equation

The solution to the flow problem is obtained after having solved the PNP problem. Both problems are coupled via the Coulomb-force term in the streamfunction equation and the convective term in the charge-transport equations. The set of equations for the streamfunction 5.14, 5.15, 5.16 reads in spectral form

$$\begin{aligned} \mathrm{Re}\,\partial_t\nabla^2\Psi_{kl} &= \nabla^4\Psi - \vec{\nabla}\times\vec{F}_{kl}, \\ \mathrm{bc}_-\left\{\Psi_{kl}\right\} &= 0, \\ \mathrm{bc}_-\left\{\Psi_{kl}\mathcal{D}_\mathrm{C}^\top\right\} &= 0, \\ \mathrm{bc}_+\left\{\Psi_{kl}\right\} &= \mathcal{T}_\mathrm{F}\left\{\psi_\mathrm{tfr}\right\}, \\ \mathrm{bc}_+\left\{\Psi_{kl}{\mathcal{D}_\mathrm{C}^{(2)}}^\top\right\} &= 0, \end{aligned} \tag{5.69}$$

where the spectral Coulomb force is abbreviated as $\vec{F}_{kl} = -\mathrm{Ha}\, Q_{kl} * \vec{\nabla}\!\!\!/ \Phi_{kl}$. As the upper boundary is assumed impermeable, the total flow rate ψ_{tfr} is not a function of x_i, but a constant. Thus, the transformed vector $\mathcal{T}_{\mathrm{F}}\{\psi_{\mathrm{tfr}}\}$, only has one entry, the constant mode. In order to determine this mode, the solution of one more equation is necessary, as specified in the next paragraph. After that, we discuss the time-integration scheme that is used to solve the spectral PDE in 5.69.

Determination of the non-zero flow rate The actuator in Figure 5.1 is not a closed system. For that reason, the rate of flow entering the system can vary over time. As the problem is periodic, the amount of in- and outflow are identical. In fact, one of the goals of this study is to determine how much flow can be transported by the actuator. The total flow rate ψ_{tfr} is used to describe the amount of flow and has the unit $[\psi^*_{\mathrm{tfr}}] = \frac{\mathrm{m}^2}{\mathrm{s}}$. In order to obtain the volume flow, multiplication with the constant channel depth $l^*_{z,\mathrm{ref}}$ is necessary.

The parameter ψ_{tfr} can be determined from the zeroth mode of the x-velocity only, as suggested by Peyret (2002). Thus, we consider the x-direction of equation 5.17 in spectral form

$$\mathrm{Re}\, \partial_t V_{x,kl} = -\mathcal{D}_{\mathrm{F}} P_{kl} + \nabla\!\!\!/^2 V_{x,kl} + F_{x,kl}. \tag{5.70}$$

All modes $k \neq 0$ are periodic in x-direction and do thus not contribute to the flow rate. For that reason we can focus on the equation for $k = 0$

$$\mathrm{Re}\, \partial_t V_{x,0l} = \nabla\!\!\!/^2 V_{x,0l} + F_{x,0l}, \tag{5.71}$$

where we have plugged in the assumption $\mathcal{D}_{\mathrm{F}} P_{0l} = 0$, i.e. that no outer pressure gradient is applied. By introducing the time discretization with the Euler implicit scheme, the Helmholtz-type equation

$$\left(\frac{\mathrm{Re}}{\Delta t} - \nabla\!\!\!/^2\right) \Delta V^n_{x,0l} = \nabla\!\!\!/^2 V^{n-1}_{x,0l} + F^n_{x,0l}, \tag{5.72}$$

is obtained. The respective linear boundary conditions are the no-slip condition at the lower boundary and the symmetry condition at the upper boundary

$$\begin{aligned} \mathrm{bc}_- \left\{V^n_{x,0l}\right\} &= 0, \\ \mathrm{bc}_+ \left\{\mathcal{D}_{\mathrm{C}} V^n_{x,0l}\right\} &= 0. \end{aligned} \tag{5.73}$$

Finally, we compute the total flow rate in accordance with Peyret (2002) as

$$\psi_{\mathrm{tfr}} = \frac{h}{2} \int_{-1}^{1} V^n_{x,0l}\, \mathrm{d}y = -\frac{h}{2} \sum_{\substack{l=0 \\ l\,\mathrm{even}}}^{N_y-1} \frac{2}{l^2-1} V^n_{x,0l}. \tag{5.74}$$

As a result, the system 5.69 and the time integration can be performed.

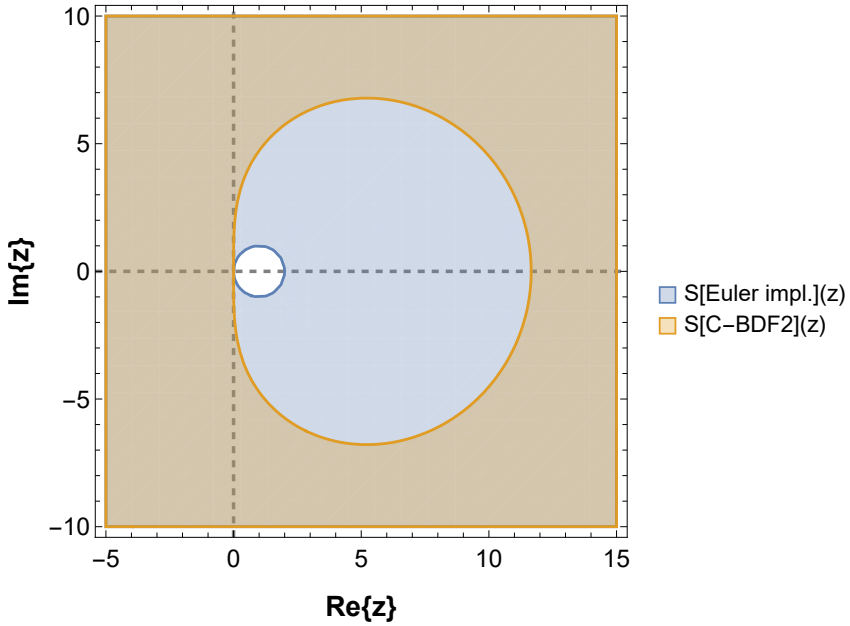

Figure 5.4: Stability region of the C-BDF2 scheme (orange; used for the streamfunction eq.) in comparison to the stability region of the Euler implicit scheme (blue; used for the charge transport equations). For $\mathrm{Re}(z) \leq 0$, both methods are stable.

The C-BDF2 scheme The streamfunction equation 5.72 is of fourth order and does not take the Helmholtz form 5.33 due to the the temporal-spatial operator $\partial_t \nabla^2$ and the biharmonic operator.

The stability of explicit time-integration schemes is limited by the smallest distance between two grid points. Due to the Gauss-Lobatto distribution, very small distances can appear near the boundaries of the discretized domain. As an example, we choose the domain height $h = 1$ and the amount of grid points $N_y = 32$ into the grid-point distribution 5.25. Then the distance between the boundary point and the first inner point is $\Delta x_{\mathrm{min},32} = 2.5 \cdot 10^{-3}$. For 64 grid points, this distance reduces to $\Delta x_{\mathrm{min},64} = 6 \cdot 10^{-4}$. In explicit schemes, the maximum size of the time step Δt_{max} is limited by the relation (LeVeque, 2007)

$$\Delta t_{\mathrm{max}} \leq \frac{\Delta x_{\mathrm{min}}^2}{2}, \tag{5.75}$$

delivering $\Delta t_{\mathrm{max},32} = 3.3 \cdot 10^{-6}$ and $\Delta t_{\mathrm{max},64} = 1.9 \cdot 10^{-7}$ respectively. Thus, explicit schemes are very expensive. However, Canuto (1988) and Peyret (2002) suggest, in some cases, the application of Adams-Bashforth methods. Yet, these methods are unstable in our case.

For that reason, an implicit method which is both stable and easy to implement is necessary. For the modeling of cardiac dynamics, a second-order one-step two-stage composite backward differentiation formula (C-BDF2) has been developed (Ying, 2005; Ying et al., 2008):

C-BDF2 scheme (Ying, 2005)
The differential equation for a general parameter $a(t)$ and a general right hand side $b(a)$

$$\partial_t a(t) = b\,(a(t)) \tag{5.76}$$

We assume that the approximation of a at the discretized time t^{n-1} is known and denoted by a^{n-1}. The method is aiming for the computation of a^n using the auxiliary variable $\hat{a}^n$. The two-stage scheme is given by

$$\begin{aligned} \hat{a}^n - \varrho\,\Delta t\, b(\hat{a}^n) &= a^{n-1}, \\ a^n - \varrho\,\Delta t\, b(a^n) &= \frac{1-\varrho}{\varrho}\hat{a}^n + \frac{2\varrho-1}{\varrho}a^{n-1}. \end{aligned} \tag{5.77}$$

The stability function of the method

$$\mathcal{S}(z) = \frac{1+(1-2\varrho)\,z}{(1-\varrho z)^2}, \quad \text{for} z \in \mathbb{C}, \tag{5.78}$$

is bounded to the left-half complex plane when choosing the characteristic constant $\varrho = 1 - \frac{\sqrt{2}}{2}$ (compare Figure 5.4). In that case, the scheme is A- and L-stable.

This method was successfully used for the solution of the problem 5.72. The scheme 5.77 is adapted to the streamfunction equation and delivers

$$\begin{aligned} \mathcal{H}_\Psi \Delta\hat{\Psi}^n_{kl} &= \nabla\!\!\!/^4 \Psi^{n-1}_{kl} - \vec{\nabla\!\!\!/} \times \vec{F}^n_{kl}, \\ \hat{\Psi}^n &= \Psi^{n-1}_{kl} + \Delta\hat{\Psi}^n_{kl}, \\ \hat{\hat{\Psi}}^n_{kl} &= \frac{1-\varrho}{\varrho}\hat{\Psi}^n + \frac{2\varrho-1}{\varrho}\Psi^{n-1}_{kl}, \\ \mathcal{H}_\Psi \Delta\hat{\hat{\Psi}}^n_{kl} &= \nabla\!\!\!/^4 \hat{\hat{\Psi}}_{kl} - \vec{\nabla\!\!\!/} \times \vec{F}^n_{kl}, \\ \Psi^n &= \hat{\hat{\Psi}}^n_{kl} + \Delta\hat{\hat{\Psi}}^n_{kl}. \end{aligned} \tag{5.79}$$

We note that the matrix

$$\mathcal{H}_\Psi = \frac{\mathrm{Re}}{\varrho\Delta t}\nabla\!\!\!/^2 - \nabla\!\!\!/^4 \tag{5.80}$$

is independent of the time as long as the time step size is constant (which is used in this code). Therefore, the matrix can be inverted in the pre-processing step before starting the time integration. Thus, only matrix products have to be evaluated during the time integration.

Concluding remarks The streamfunction is computed after solving the electric problem. Thus, both numerical solutions are loosely coupled. Yet, a more expensive approach with a stronger coupling using an iteration loop within a time step, did not show significantly better convergence or accuracy characteristics. The velocity field can directly be

obtained from the streamfunction by differentiation in the post-processing step, which is discussed in the next section.

5.3.7 Validation

A part of the methods in the spectral module presented in this work was validated by simulating Rayleigh-Bérnard convection (Liu et al., 2023) showing maximum relative errors of the size 10^{-10}. Validation of the flow field was performed with an example flow excited by a given volume force giving errors of similar size.

5.4 Post-processing

After performing the time-integration, a post-processing routine is performed. In this section of the code, the velocity field, local conductivity, and dissipation values are computed. While the velocity can simply be obtained by differentiation of the streamfunction, the computation of the dissipation is more complex. With the flow field and dissipation, an estimate for the efficiency of the system is derived. We finally discuss the termination conditions for the time loop.

5.4.1 Dissipation

Viscous dissipation The heat generated by internal friction due to shear stresses in the fluid depends on the velocity field and the viscosity. At the position defined by x_i and y_j the local dissipation rate is given by

$$\begin{aligned} \varepsilon_{\eta,ij}^{n,*} &= \eta^* \left(\partial_x^* v_{x,ij}^{n,*} + \partial_x^* v_{y,ij}^{n,*} + \partial_y^* v_{x,ij}^{n,*} + \partial_y^* v_{y,ij}^{n,*} \right), \\ \left[\varepsilon_{\eta,ij}^{n,*} \right] &= 1 \text{ W m}^{-3}. \end{aligned} \tag{5.81}$$

However, cooling systems for semiconductors are characterized by their relative cooling power per area. For that reason, we also compute a global relative dissipation rate by integration over the domain

$$\begin{aligned} \bar{\varepsilon}_{\eta}^{n,*} &= \frac{1}{l_{\text{per}}^*} \sum_{i=0}^{N_x-1} \sum_{j=0}^{N_y-1} \varepsilon_{\eta,ij}^{n,*} (\Delta x)_i^* (\Delta y)_j^*, \\ \left[\bar{\varepsilon}_{\eta}^{n,*} \right] &= 1 \text{ W m}^{-2}. \end{aligned} \tag{5.82}$$

Electrical dissipation In EHD sytems, electrical dissipation is observed in addition to viscous dissipation. It originates from electric ion fluxes relative to the resistive fluid environment. We define the electro-diffusive flux as a combination of diffusive and electrophoretic flux

$$\begin{aligned} \vec{j}_{\pm\text{eldi}}^* &= \vec{j}_{\pm\text{diff}}^* + \vec{j}_{\pm\text{elph}}^* \\ &= -D^* \vec{\nabla}^* c_{\pm}^* \mp \mu^* c_{\pm}^* \vec{\nabla}^* \phi^*. \end{aligned} \tag{5.83}$$

The convective flux is assumed to not contribute to the dissipation. It originates from the transport of the ions together with the fluid. Thus, there is no relative motion between

fluid and ions causing dissipation. Analogously to the viscous dissipation, a local electric dissipation rate is defined by

$$\begin{aligned} \varepsilon_{\varsigma,ij}^{n,*} &= \left(\varsigma_{ij}^{n,*}\right)^{-1} \left(\left\| \vec{j}_{\pm\text{eldi}}^{n,*} \right\|_2 \right)^2 \\ \left[\varepsilon_{\varsigma,ij}^{n,*}\right] &= 1\,\mathrm{W\,m^{-3}}, \end{aligned} \tag{5.84}$$

where $\|\dots\|_2$ denotes the L_2-norm. We find the relative dissipation rate with regard to the area as

$$\begin{aligned} \bar{\varepsilon}_{\varsigma}^{n,*} &= \frac{1}{l_{\text{per}}^*} \sum_{i=0}^{N_x-1} \sum_{j=0}^{N_y-1} \varepsilon_{\varsigma,ij}^{n,*} (\Delta x)_i^* (\Delta y)_j^*, \\ \left[\bar{\varepsilon}_{\varsigma}^{n,*}\right] &= 1\,\mathrm{W\,m^{-2}}. \end{aligned} \tag{5.85}$$

Note that the local conductivity ς_{ij}^* is not a constant but a function of the charge distributions $c_{\pm,ij}^{n,*}$ as defined by relation 2.15.

5.4.2 Total dissipation and actuator efficiency

The actuator will deliver different flow profiles depending on its geometry, excitation, and the amount of dissolved charges. In section 6.3, the optimization will be discussed in detail. In order to assess the quality of a particular actuator setup, we compute an estimate for its efficiency

$$e^{n,*} = \frac{\hat{v}_{x,h}^{n,*}}{\bar{\varepsilon}_{\text{tot}}^{n,*}} \quad \text{with} \quad [e^{n,*}] = 1 \frac{\mathrm{m\,s^{-1}}}{\mathrm{W\,m^{-2}}} \tag{5.86}$$

using the maximum x-velocity in the middle of the channel

$$\hat{v}_{x,h}^* = \max\left(v_{x,i0}^*\right). \tag{5.87}$$

Note that the definition of the Gauss-Lobatto points 5.26 assigns the largest value of the normal direction to the index 0, such that $y_0 = h$. The total dissipation rate is defined as the sum of electrical and viscous dissipation at the time step n

$$\bar{\varepsilon}_{\text{tot}}^{n,*} = \bar{\varepsilon}_{\eta}^{n,*} + \bar{\varepsilon}_{\varsigma}^{n,*}. \tag{5.88}$$

Further parameters can be introduced, e.g. assessing the velocity profile. For the transport of charges or diffuse probes within the system, a box profile is optimal to avoid "blurring" of the sample. Similarly, a box profile for the potential is also desirable. Thus, in the middle region of the channel no strong electric fields normal to the walls appear, causing a secondary flow field. We will denote the deviation of the real parameter shapes to the optimal box profiles with $e_v^{n,*}$ and $e_\phi^{n,*}$.

5.4.3 Termination conditions for the time loop

The time integration is performed until one of the following break conditions is fulfilled.

- Stationarity: The maximum x-velocity in the middle of the channel and the total dissipation rate are monitored throughout the calculation. If they change less than a defined value ϖ_{stat}, the calculation is aborted.
- Negative flow rate: If the mid-channel velocity $\hat{v}_{x,h}$ becomes negative the calculation is aborted, too.
- High dissipation: There is a maximum of dissipated heat that can be transported away from the actuator by the cooling system $\bar{\varepsilon}^*_{\text{cooling}}$. The calculation is aborted at the time step n if $\bar{\varepsilon}^{n,*}_{\text{tot}} > \bar{\varepsilon}^*_{\text{cooling}}$.
- Gummel's iteration fails: In some cases the iteration method which is used to solve the PNP problem fails. In case convergence is not reached after a defined maximum number of iteration steps, the computation is aborted.

5.5 Startup behavior and frequency dependence

The actuator behavior features some effects. Figure 5.5 presents the startup behavior. At $t = 0$, the electrodes are turned on, and the respective charge clouds are formed. For $t > 0$, the sinus-shaped ζ-potential starts traveling along the wall. Charge and potential directly at the wall, at $y = 0$, follow simultaneously. However, after some time, the charge clouds develop to fading stripes enclosing an angle with the wall. After stationarity is reached, this angle stays constant in time. We note that the angle is dependent of the Péclet number. The accumulation of charge near the wall results in a higher conductivity represented by the parameter c. Heat dissipation is linearly dependent on the Ohmic fluxes, as well as the fluid resistivity which is the reciprocal to the conductivity. We expect high fluxes near the wall, yet mainly between the charge clouds, in regions with lower conductivity.

A Coulomb force proportional to both, the electric field and the charge density, acts on the fluid, resulting in the depicted flow field. Strong gradients in charge and potential act near the wall. Effectively, vortices can be observed. These vortices are the determining elements of the early flow field. Later on, when a laminar flow has developed, they are of minor importance, yet still distinguishable. Carrier fluid transport shows the desired uniform behavior with vortices of acceptable size near the wall.

The transport velocity and dissipated heat depend on the excitation frequency, as illustrated by Figure 5.6. For an excitation potential $\zeta^*_{\text{amp}} = 25\,\text{mV}$, different actuator geometries were investigated. The depicted frequency spectra were identified by several numerical experiments. For smaller electrode distances, higher frequencies are needed to observe the desired flow pattern.

The investigations reveal that, contingent on the geometry of choice, an optimal frequency exists where the transport velocity reaches its maximum. For higher frequencies,

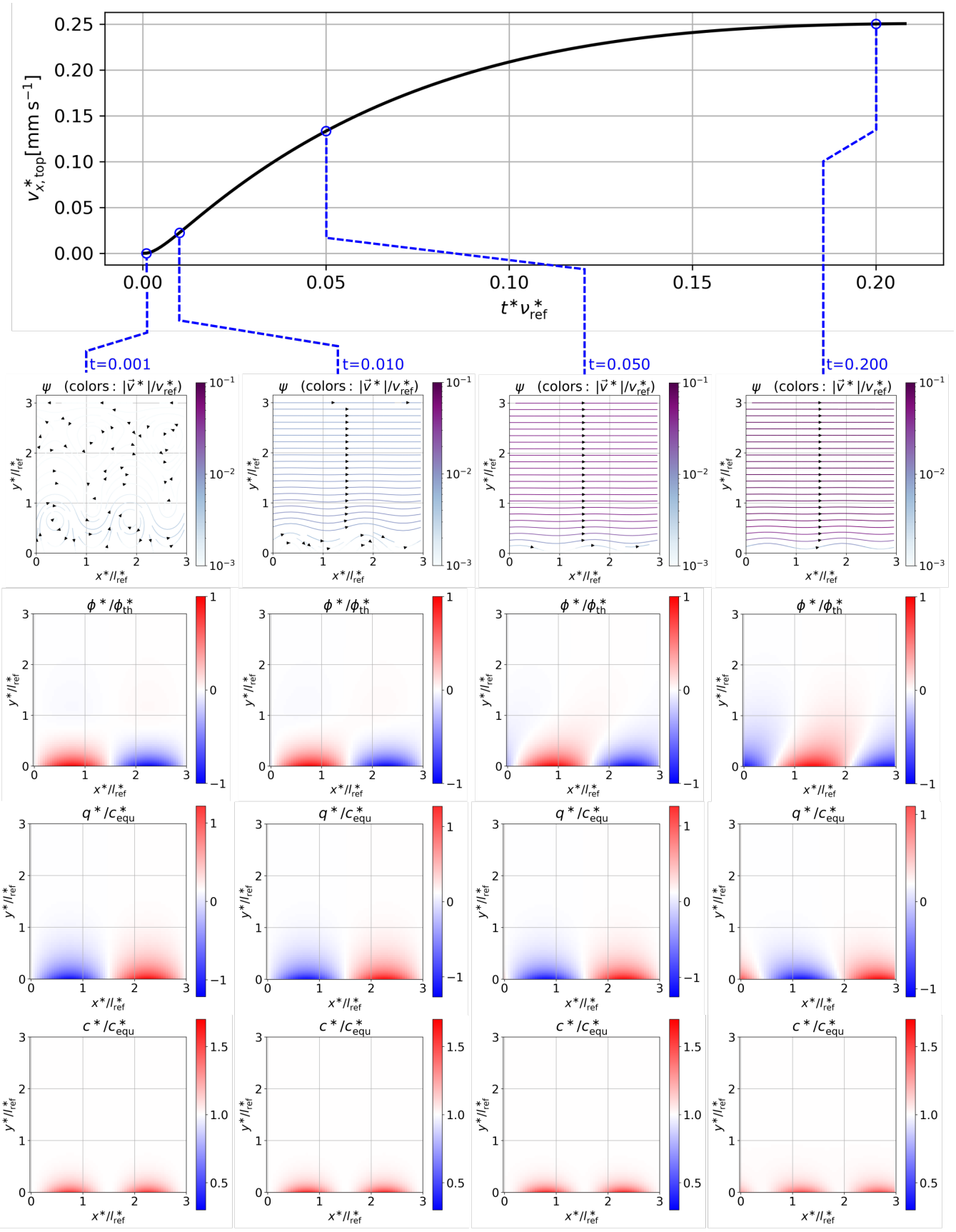

Figure 5.5: Start-up behavior for $\nu^*_{\mathrm{ref}} = 10\,\mathrm{kHz}$, $\zeta^*_{\mathrm{amp}} = \phi^*_{\mathrm{th}} = 25\,\mathrm{mV}$, $l^*_{\mathrm{ref}} = 300\,\mathrm{nm}$, $h^* = 900\mathrm{nm}$, $c^*_{\mathrm{equ}} = 0.01\mathrm{mmoll^{-1}}$. The corresponding reference velocity is $v^*_{\mathrm{ref}} = 3\mathrm{mms^{-1}}$.

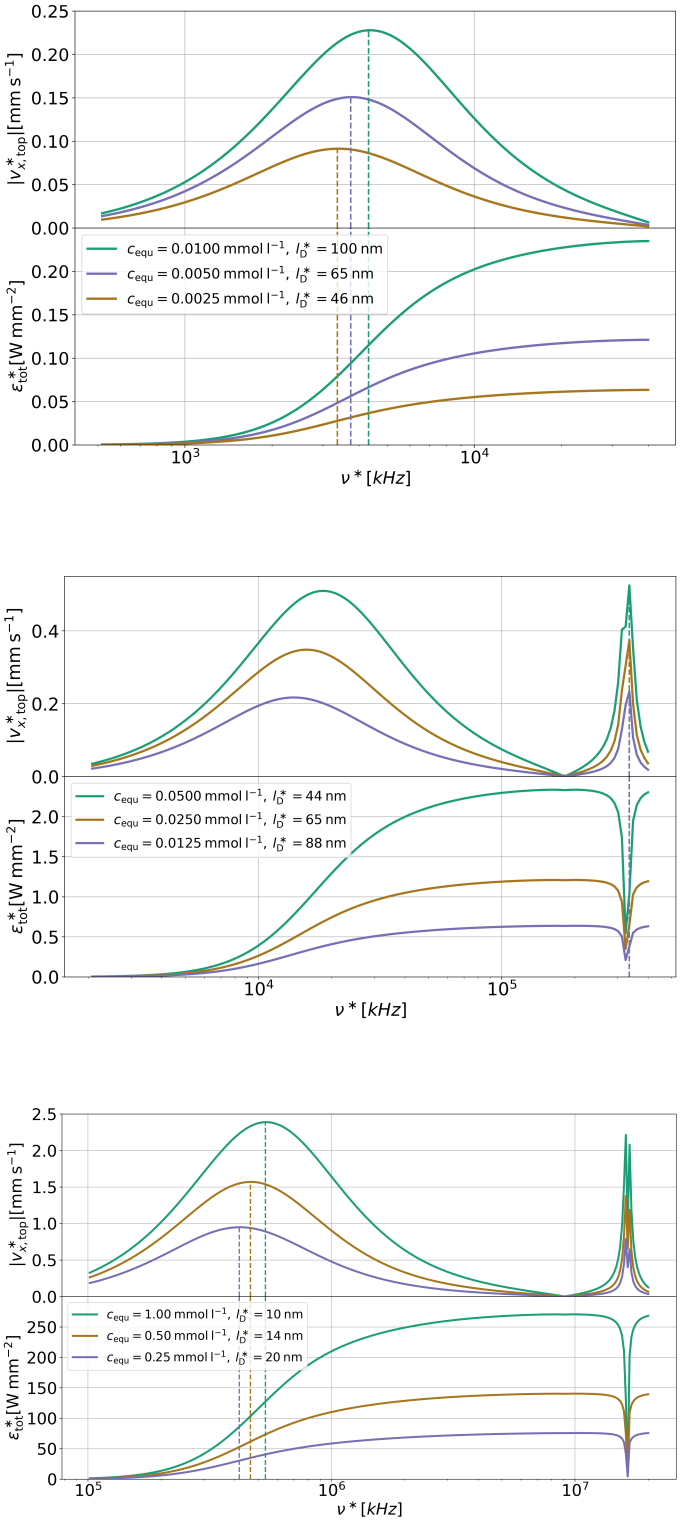

Figure 5.6: Frequency dependence of the velocity at the symmetry plane and dissipated energy. Parameters:
(Top) $l^*_{\mathrm{ref}} = 300$ nm, $h^* = 900$ nm, $\zeta^*_{\mathrm{amp}} = \phi^*_{\mathrm{th}} = 25$ mV.
(Mid) $l^*_{\mathrm{ref}} = 150$ nm, $h^* = 400$ nm, $\zeta^*_{\mathrm{amp}} = \phi^*_{\mathrm{th}} = 25$ mV.
(Bottom) $l^*_{\mathrm{ref}} = 30$ nm, $h^* = 75$ nm, $\zeta^*_{\mathrm{amp}} = \phi^*_{\mathrm{th}} = 25$ mV.

the velocity decreases and eventually becomes negative (transport in negative x-direction). In the second and third diagram, this effect is shown as a second peak in the velocity curve. Note that the diagrams show the absolute value of the velocity. For a quantitative interpretation, the second peak needs to be handled with care. The curves were determined by a quasi-stationary increase of the frequency during one simulation. The limited width of the peak combined with strong gradients and a lower scanning frequency result in the nonphysical behavior shown. Yet, the first peak is of higher relevance in the application due to its higher transport velocity and lower frequency sensitivity.

Heat dissipation increases when more electrical energy is supplied in form of higher frequencies, as illustrated by Figure 5.6. Compared to dissipation by Ohmic fluxes, mechanical dissipation is nearly negligible. With increasing frequency, the amount of energy transformed to heat within the fluid reaches a saturation level. In this region however, the actuator is inefficient, transforming the input energy mainly to heat, and not into carrier fluid transport. However, in the case of flow reversal, dissipation shows a similar peak as the transport velocity.

Finally, four frequency regions are identified:

I High efficiency: Low dissipated energy prevails. However, transport velocities are also low.

II High transport: Desired frequency range of operation.

III Bad efficiency: Decreasing transport velocity and high dissipation. Energy supply is mainly transformed to heat.

IV Flow reversal: Opposite transport direction, transport speed is lower and control more sensitive.

Even more significant is the influence of the actuator geometry on transport speed and losses. The electrode distance is decreased from top to bottom in Figure 5.6. Transport speeds increase accordingly. However, higher losses are observed in smaller geometries. Especially the increase of dissipation from $l^*_{\mathrm{ref}} = 150\,\mathrm{nm}$ to $l^*_{\mathrm{ref}} = 30\,\mathrm{nm}$ is astonishingly large.

5.6 Conclusion

The results presented in the section above help to understand the working principle of the actuator. Clearly, an optimal frequency range for different geometrical settings can be identified (II: high transport). The influence of electrode distances on the amount of losses is relatively strong compared to the influence on transport speed.

We note that, by choosing a design with electrode distances similar to the size of the double layer, wall-adjacent vortices are relatively small. Thus, a controllable, uniform

flow field is built up. With respect to the landscape of actuation mechanisms, our design features a simple and thus relatively cheap geometry, together with an easy to control homogeneous carrier fluid transport.

Miniaturization, however, is limited by the dissipated heat. Sufficient cooling must be provided to avoid overheating of the machine elements and damage of probes. A number of design limitations are discussed in the next chapter, together with an detailed explanation of the system's architecture and functional structure.

We note, that obtaining the presented results was relatively expensive. It serves the purpose of verifying the actuator's working principle. Surprisingly, no complex flow structures were observed that justify the use of a highly-accurate spectral simulation. For further investigations, a faster code is to be constructed. Finite-difference or finite-volume approaches in velocity-pressure formulation can be extended to the third spatial dimension with much less effort than is the case for the presented code. Also, optimization procedures would be much less expensive.

We could build up an understanding, not only of the driving mechanism, but also of full-electrokinetic transport in general. To the authors knowledge, there are no other publications investigating Ohmic dissipation in microchannels. As mentioned in the introduction, miniaturization is an important trend in LOC development. One important finding of our study is the strong nonlinear increase of heat losses in smaller channels. This is critical to structures and samples, and is recommended to be considered in further studies.

CHAPTER 6

Product design of an active-surface lab-on-chip

This chapter gives an overview of the functional structure of the LOC system with the microfluidic actuator of chapter 5 as a key component. Methods of model-based systems engineering are utilized to illustrate architecture and functions. Limitations of the product design are discussed. Within these limitations, actuator optimization is performed and recommendations for different use cases are made.

6.1 System architecture

In order to understand the design limitations of the system, a detailed discussion of its functional structure is necessary. We start by introducing some important explanation models in product design, i.e. Product Generation Development and Model-Based Systems Engineering. These models provide the framework and vocubulary which is needed for a systematic discussion of our design.

6.1.1 Explanation models

Product generation development (PGE) as a description method Over the past centuries, a range of approaches have been developed in order to describe product development and innovation processes. Important examples focus on the products' success on the market (Schumpeter, 1913), development by "abstraction and subsequent concretization" (Ehrlenspiel, 2009), categories of construction projects (Feldhusen, 2013), categories of innovation (Henderson & Clark, 1990), or user requirements in form of the Kano model (Kano, Seraku, Takahashi, & Tsuji, 1984).

For the structured discussion of our product, we use an explanation model called Product Generation Development (PGD) by Albers et al. (2018). Its key argument is that the development of a new product (generation) is "both specific carryover as well as significant new development of partial systems" (Albers et al., 2018). The carryover is performed from so-called reference products. Reference products, as well as the new generation, can be defined as systems with a system boundary and several levels of subsystems (Albers et

al., 2019). We will refer to these system parts and their structural interrelations as system architecture. Each subsystem is not only characterized by its structural properties, but also by its behavior. We denote the behavior of a (sub-)system, which can be either desired or accepted, as function (Albers et al., 2011; Albers & Wintergerst, 2014).

Model-based systems engineering (MBSE) In addition to this general explanation approach, model-based systems engineering represents a powerful tool for understanding the system architecture and functionality of complex products (Albers & Zingel, 2013; Dori, 2016). In this work, we use the open-source MBSE-software Capella (Eclipse Foundation, n.d.). Figure 6.2 depicts the architecture of the lab station and Figure 6.3 its functional structure. The architecture breaks down the physical components into two levels of subsystems. The functional structure illustrates the exchange of matter (reagents, carrier fluid), energy (in our system in the form of electrical energy), and information.

6.1.2 Structure and functional behavior of the lab and the fluid processing unit

System structure The system structure of the lab is illustrated by the CAD model 6.1 in combination with the Capella model 6.2. The reader is also referred to the publication Marthaler and Class (2022b) and the patent sketch D.8. All parts that contain fluids are located on the top, such as fluid in- and outlets, reservoirs, add-on elements, and the FPU. Electric elements are integrated in the printed circuit board (PCB) on the bottom of the structure. Black cables (Figure 6.1) connect the electric elements with the pumps, FPU and add-on elements. The air cooling system for the FPU is not displayed. The user interacts with the lab by inputting sample, reagents, and carrier fluid and controlling the processes with software. Analysis results are also directly sent to the connected computer.

Functional behavior The main function of the lab system is the transformation of chemical information into digital information. Here, the term "chemical information" aggregates a wide range of structural knowledge about the sample, e.g., the qualitative or quantitative composition of samples, or DNA information. In Figure 6.3, this main function is illustrated by one path: Sample input by the technician, transport in the fluid circuit into the FPU, performance of the identification algorithm (mixing, transport to add-on elements), reactions with reagents, detection, e.g. with charge spectrometer, data transmission via electric circuit to the software, and analysis of the results by the technician. The performance of the identification algorithm is the key part and strongly dependent on the type of sample and information to be extracted. We note that the FPU does allow for a wider range of such algorithms than most other LOC systems with predefined channels. We will discuss its technical properties in the next subsection 6.1.2.

The main function, as discussed above, can only be performed with the support of auxiliary or side functions. These are reagant transport, carrier fluid transport, cleansing

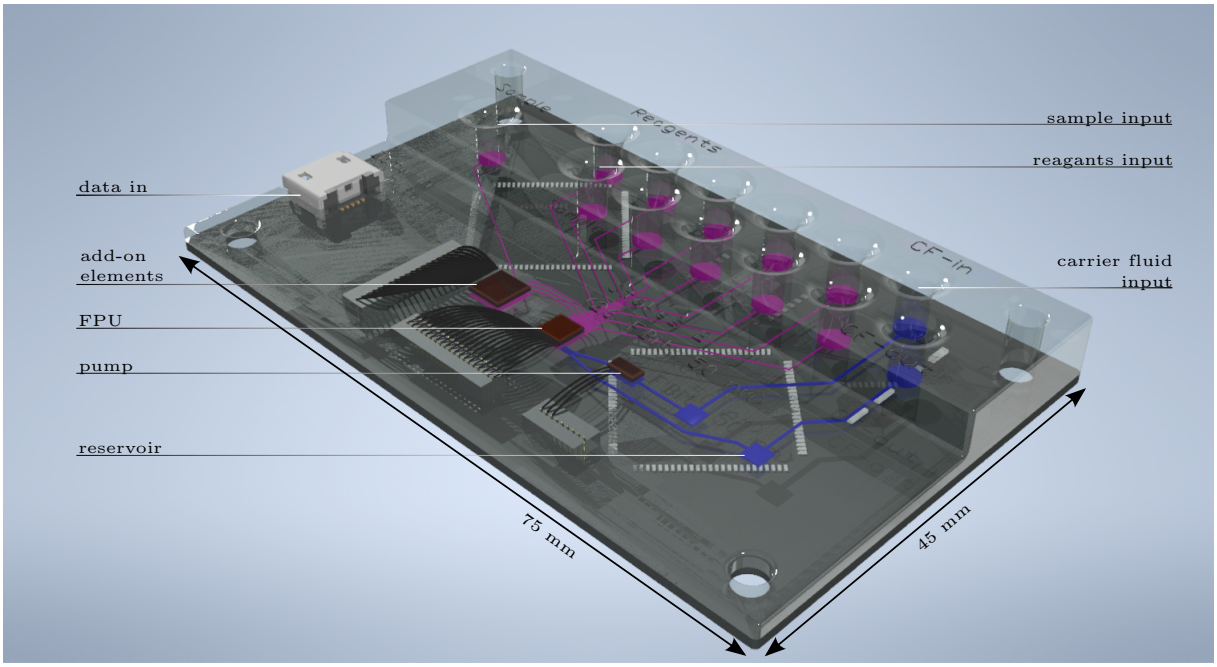

Figure 6.1: 3D model of the lab system with the FPU as central element. The carrier fluid is depicted in blue while the sample and reagant fluids are depicted in purple. The electric circuit is integrated in the PCB bottom plate, while the fluid circuit is in the transparent PDMS block on the top. The black cables connect the fluid control elements (FPU, pumps, add-on systems) with the electric circuit on the bottom.

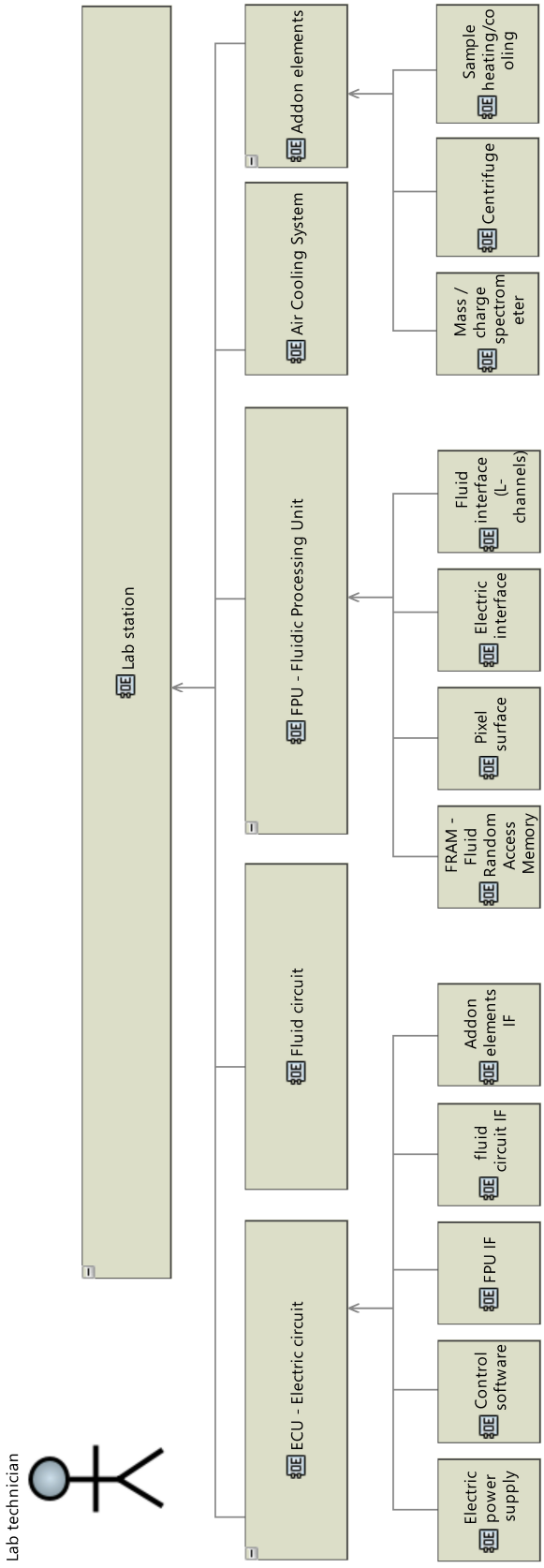

Figure 6.2: Overview of the system architecture illustrating two levels of subsystems and actors. The diagram was created using the open-source MBSE software Capella.

of fluid channels, provide electrical power to the components, cooling of the FPU, and sample/reagant heating by chemical reactions. Similarly, these functions can be broken down into energy/mass/information exchange between the lab components as illustrated by Figure 6.3.

The fluid processing unit (FPU) The fluid processing unit is the core part of the lab. The smallest unit is the actuator, typically consisting of three electrodes that provide a three-phase voltage pattern. In order to allow for two- or three-way transport on an active surface, different actuator types have been developed, compare figures D.2,D.3,D.4. These are clustered to pixels, i.e small surface elements on which flow direction and velocity is synchronized. The clustering is illustrated Figure D.5. Multiple pixels (typically eight) are controlled by single adjacent control units, compare Figure D.6. Many of these control units with the respective pixels form the chip/pixel surface (compare figures 1.7,D.7). On this surface, probes can be transported on programmed paths. In fact, two of these chip surfaces are arranged on top and at the bottom of the fluid layer (sandwich arrangement).

The transported probes are diffuse and embedded into a carrier fluid as patented by M. Bazant and Prakash (2013). Continuous sample transport on the surface is possible (no pulsing). This allows performance of charge spectrometry on the chip surface and makes shorter transport or mixing times possible. Mixing can be performed by controlled desynchronizing of the top and bottom electrodes. The main function however is the quick transport of probes between in- and outlets, storage elements that we denote as fluid random access memory (compare Figure 6.1), and the addon elements. In order to do that, fluid flow is not only enforced at the loction of the sample. Instead, at each point of time a closed path of fluid is enforced to flow with the same velocity. Thus, mass continuity is always sustained and eddies avoided. At the boundaries of the chip, L-channels (compare figures 6.1, D.8) are used to separate sample and carrier fluid. Both substances can then exit or enter the chip area into two different channels. The carrier fluid is always transported from or into the carrier fluid channel which is arranged around the pixel area. At the same time, probes are transported into the desired channels to e.g. memory elements or add-ons. This procedure is illustrated by the sketch D.9.

6.2 Technical limitations

Miniaturization A possibility to overcome the architectural limitations of many LOC systems that we discussed in the introduction to this chapter is miniaturization. Smaller geometrical units that can be independently controlled have several advantages. The controllable length scales can be chosen to be of the size of DNA, viruses, or protein. Thus, these investigation objects can be handled individually, and the necessary amount of sample volume is reduced. The smaller length scales also make faster sample transport possible by high fluid transport speeds and short transport lengths. Chemical algorithms that require actions at high frequencies, e.g., quick interruption of the reaction, become possible.

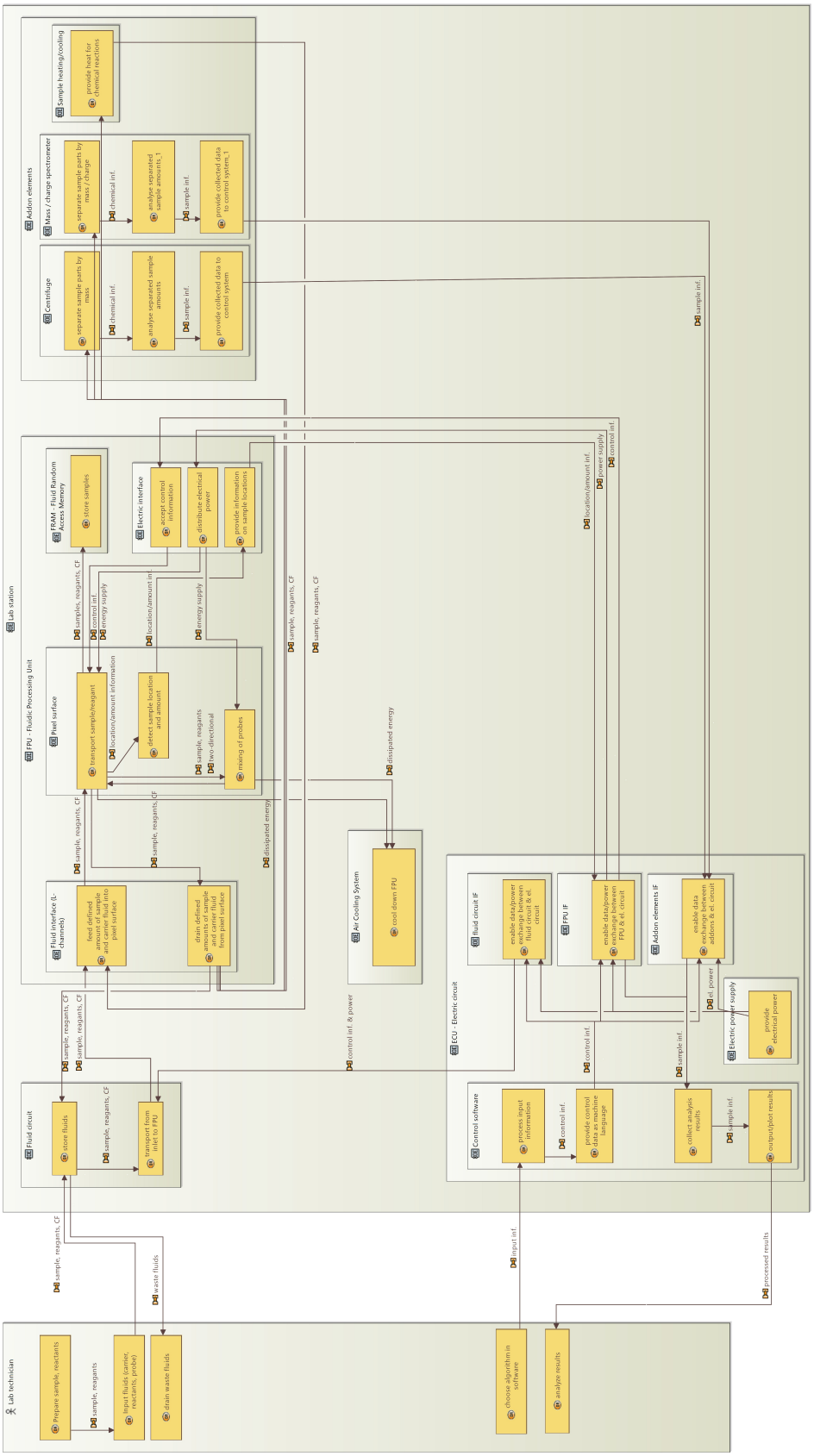

Figure 6.3: Overview of the functional structure of the lab system. The diagram was created using the open-source MBSE software Capella.

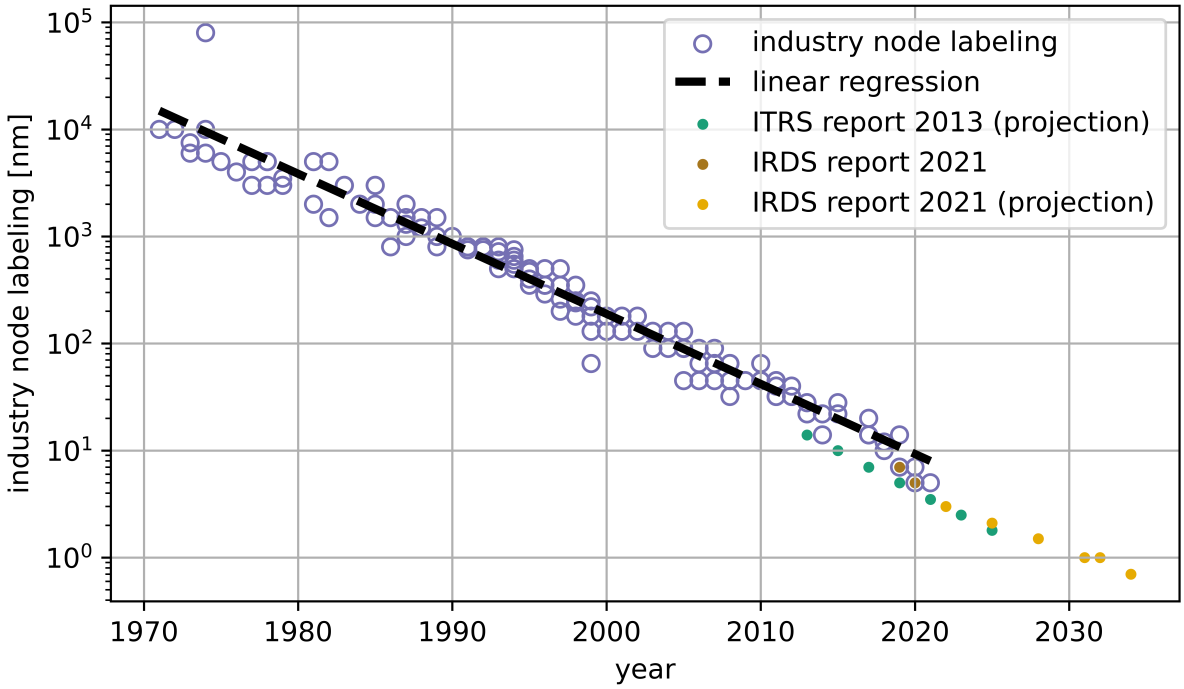

Figure 6.4: Historical overview of industry node labeling. The purple markers represent data from the Wikipedia article "Microprocessor chronology" (Wikipedia, 2022). Additionally, data from the 2013 ITRS report (Cogez et al., 2013) and the 2021 IRDS report (Balestra et al., 2021) is used.

The main problem of miniaturization are the manufacturing possibilities and their related cost. As a reference value for the smallest distance between two individually controllable electrodes, we use the node labeling as used in the semiconductor industry. We note that these names are in general marketing-driven and thus do not necessarily represent the real electrode distances on a chip. Although these absolute values should be used with care, their relative magnitude is correct. In Figure 6.4, a historical overview on node labeling is given together with projections by the International Technology Roadmap for Semiconductors (ITRS) (Cogez et al., 2013) and after 2013 by the International Roadmap for Devices and Systems (IRDS) (Balestra et al., 2021). The projections show that Moore's law is expected to be valid through to the year 2030. We note that just in the last few years, device fabrication with electrode distances at nanoscale have become an option in product design.

Prototyping cost Yet, in addition to manufacturing feasibility, an equally important aspect is the prototyping cost. The dependency between prototyping cost per area of a manufactured chip and node labeling is illustrated by Figure 6.5. We here refer to data published by Europractice, a consortium of five European research organizations that offer prototyping services for application-specific integrated circuits (ASIC) to academia and industry (Europractice, 2020, 2022). Four of the companies that offer ASIC man-

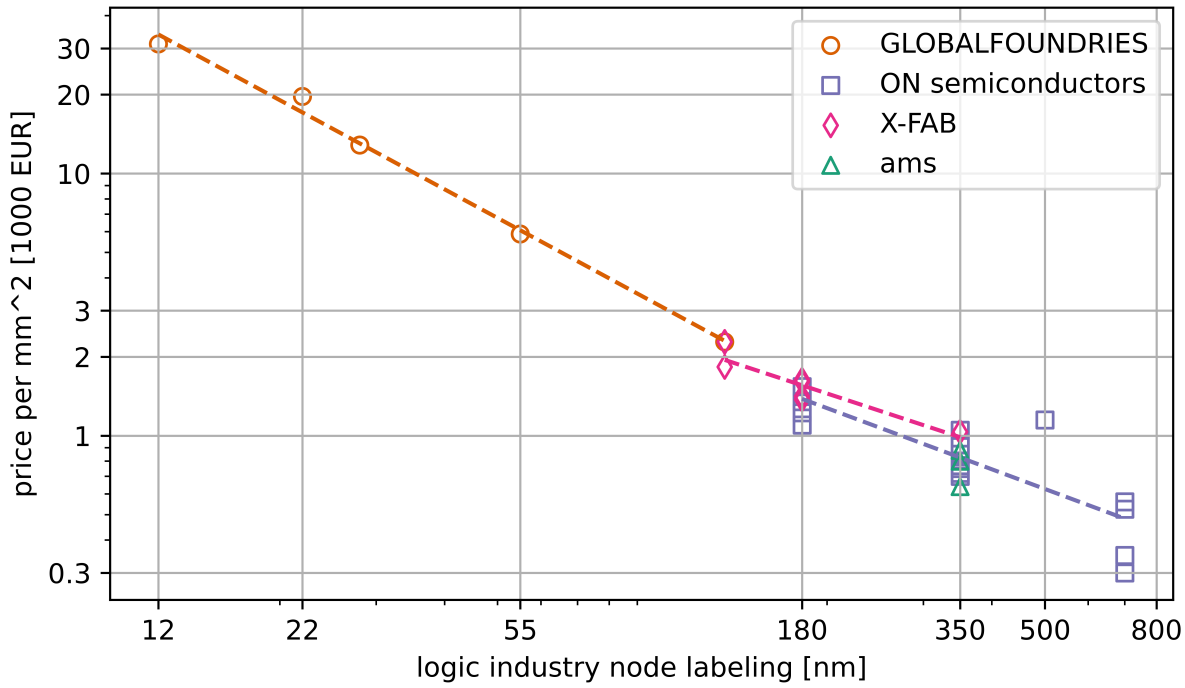

Figure 6.5: Cost per area of the chip as demanded by the ASIC service providers in the Europractice consortium (Europractice, 2020, 2022) over industry node labeling. On average, a double-logarithmic relation is observed.

ufacturing via Europractice are compared in Figure 6.5. We note that there exists a double-logarithmic relationship between cost and node distance. For instance, choosing a 55 nm technology instead of the state-of-the-art 12 nm nodes can save about 83 % of the expected cost.

Electric voltages Organic substances can change their properties under strong electric fields. Particularly, the membrane of cells breaks open permanently (cell lysis) or reversibly (electroporation) under strong voltage differences between the outer and inner phase. In some cases, this behavior is desired (release of DNA/RNA). However, this process is to be performed with care. Controlled membrane disruption needs to be performed without damaging other parts, e.g. organelles (Ledeboer, 2009). It is also important to clearly separate this function from the sample transport and thus to avoid unwanted sample damage. For that reason, the transport should be possible using relatively small voltages.

Excitation frequency During the last century, the excitation frequency in the semiconductor industry seemed to have a reached a natural boundary. A historical overview on clock frequencies in the processor industry is displayed in Figure 6.6. The latest IRDS report (Balestra et al., 2021) predicts an increase in the clock frequency in the next decades. Yet, for microfluidic actuators, higher frequencies might not be necessary as a heuristic reflection can illustrate. Relatively high flow velocities in such systems are of the order

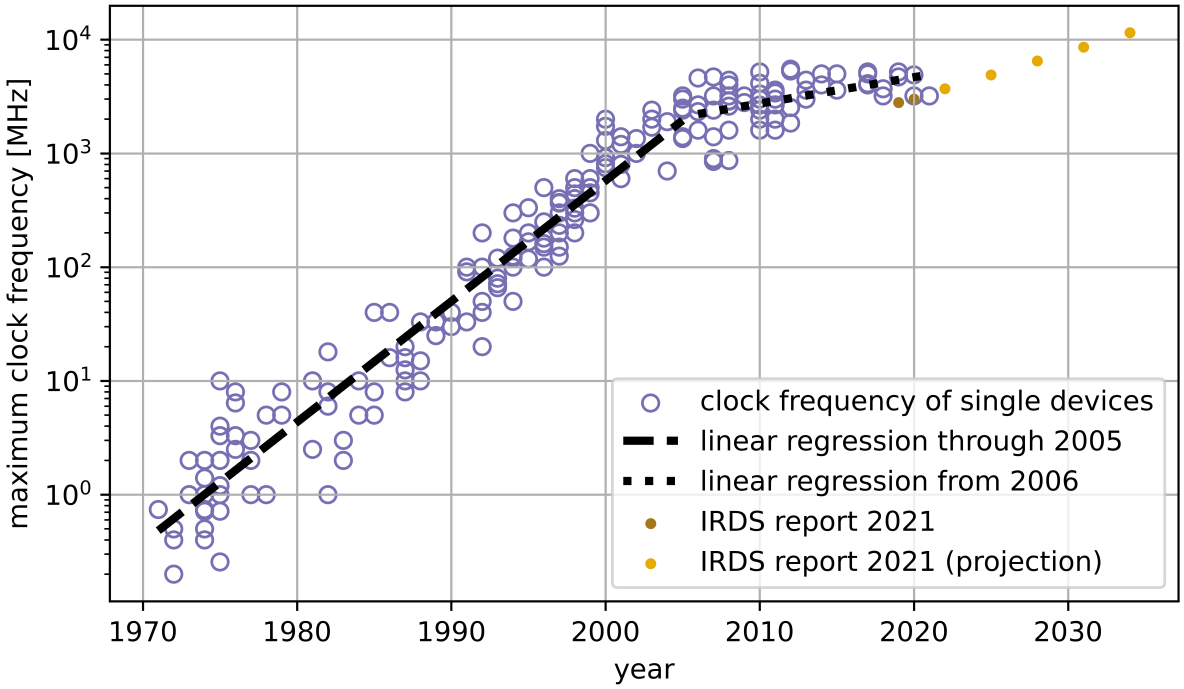

Figure 6.6: Historical overview of clock frequencies in the chip industry. The purple markers represent data from the Wikipedia article "Microprocessor chronology" (Wikipedia, 2022). Additionally, data from the 2013 ITRS report (Cogez et al., 2013) and the 2021 IRDS report (Balestra et al., 2021) is used.

of $v^* = 10\,\mathrm{mms}^{-1}$. For (quite small) electrode distances of $l^*_{\mathrm{ref}} = 10\,\mathrm{nm}$, the respective frequency is $\nu* = \frac{v^*}{l^*_{\mathrm{ref}}} = 1\,\mathrm{MHz}$. These are frequencies that have been reached in the 1970s already.

Heat dissipation One large challenge of miniaturization is the increasing heat production of conducting elements. This is true for semiconductors, as well as electrolytic systems. One important limitation is the air cooling limit, i.e. the amount of dissipated heat that can still be transported away from the heat source with a fan and is given by

$$\bar{\varepsilon}^{n,*}_{\mathrm{tot}} \leq \bar{\varepsilon}^*_{\mathrm{aircooling}} = 1.5\,\mathrm{W\,m}^{-2}, \tag{6.1}$$

where $\bar{\varepsilon}^{n,*}_{\mathrm{tot}}$ is the relative heat dissipation rate as defined in section 5.4.2. The index "tot" (for total) indicates that this dissipation rate is the sum of mechanical and electric dissipation.

However, under normal operating conditions, only a small part of the surface area of the chip is active. We can compute the maximum dissipation that is possible locally, by using the active area and a safety factor with the formula

$$\bar{\varepsilon}^{n,*}_{\mathrm{tot,local}} \leq \bar{\varepsilon}^*_{\mathrm{aircooling}} \frac{A_{\mathrm{total}}}{A_{\mathrm{active}}} \frac{1}{\mathrm{safety}}. \tag{6.2}$$

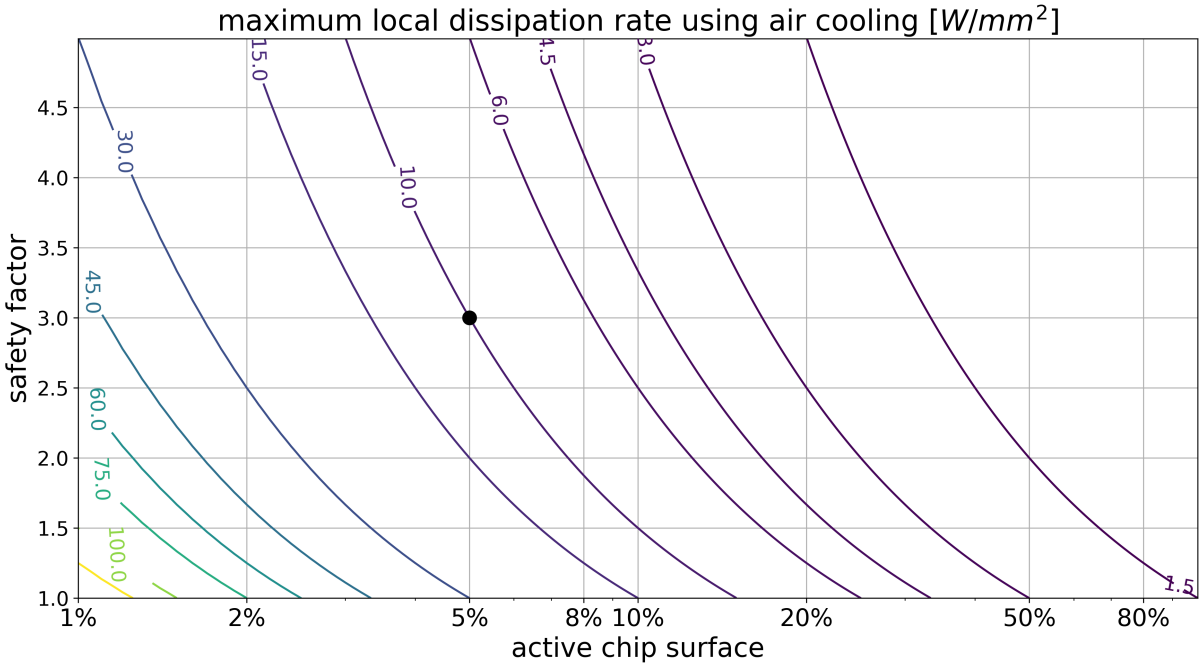

Figure 6.7: Maximum local dissipation rate over active chip surface and safety factor. The black marker represents the example calculation which is discussed in the text.

This relation is illustrated by Figure 6.7, giving an overview of the maximum allowed local dissipation with respect to the active chip area and the used safety factor. As an example, with a safety factor of 3 and an active area of $A_{\text{active}} = 5\,\%$, the maximum local dissipation rate is $\bar{\varepsilon}^{n,*}_{\text{tot,local}} = 10\,\text{W m}^{-2}$.

6.3 Optimization

Within the limitations discussed above, the actuator can be optimized. For that purpose, we assume that one actuator setting is defined by five independent variables. These include the electrical parameters, i.e. excitation frequency ν^* and amplitude ζ^*_{amp}, the geometrical parameters, i.e. electrode distance l^*_{ref} and channel height h^*, and the equilibrium ion concentration of the carrier fluid c^*_{equ}. Large velocities $\hat{v}^*_{x,h}$ are desirable in the center of the channel with small dissipation rates and thus, high efficiencies. Table 6.1 gives an overview on some dependencies that could be identified by a limited number of numerical experiments. These trends are to be handled with care as they are possibly not globally valid.

The actuator settings can be strategically optimized utilizing a differential algorithm, such as the "differential_evolution" routine in the scipy library. Giving an initial variable setting as candidate solution and variable constraints, the algorithm improves the candidate iteratively within the limitations. In our setting, an optimization with four variables takes about a week of computation time on a 8-core, 2.4 GHz machine. An example simulation is presented in table 6.2. In that case, the efficiency was optimized as function of

optimization parameter	$\nu^* \uparrow$	$\zeta^*_{\text{amp}} \uparrow$	$l^*_{\text{ref}} \uparrow$	$h^* \uparrow$	$c^*_{\text{equ}} \uparrow$
mid-channel velocity $\hat{v}^*_{x,h}$	opt.	$\uparrow$	opt.	$\rightarrow$	opt.
dissipation rate $\bar{\varepsilon}^{n,*}_{\text{tot,local}}$	$\uparrow$	$\uparrow$	$\uparrow$	$\rightarrow$	opt.
efficiency $e^{n,*}$	$\downarrow$	$\downarrow$	$\downarrow$	$\rightarrow$	opt.

Table 6.1: Relationship between actuator

optimization parameter	ν^*	$\zeta^*_{\text{amp}} \uparrow$	l^*_{ref}	h^*	c^*_{equ}
lower constraint	10 kHz	25 mV	100 nm	50 nm	0.01 mmol
upper constraint	100 kHz	25 mV	350 nm	500 nm	0.5 mmol
optimization	10 kHz	25 mV	95 nm	285 nm	0.12 mmol
mid-channel velocity $\hat{v}^*_{x,h}$	$0.1\,\text{mm}\,\text{s}^{-2}$				
dissipation rate $\bar{\varepsilon}^{n,*}_{\text{tot,local}}$	$0.04\,\text{W}\,\text{mm}^{-2}$				
efficiency $e^{n,*}$	$2.48\,\text{mm}^3\,\text{W}^{-1}\,\text{s}^{-1}$				

Table 6.2: Result of a differential evolution simulation with constraints.

four parameters $e^{n,*}\left(\nu^*, l^*_{\text{ref}}, h^*, c^*_{\text{equ}}\right)$. In that case, optimum values for $l^*_{\text{ref}}, h^*, c^*_{\text{equ}}$ were identified while the frequency variable hit the constraint. It is probable that the result could be improved using higher frequencies.

6.4 Final remarks

It must be clear, that different use cases require individual actuator setups. This work lays the foundation to build a prototype using the presented code, together with an optimization algorithm. A suggestion for a first design is made in the previous section. The optimization algorithm, in combination with the structural description of the system, sets the basis for further developments and their numerical verification. However there are a number of questions, one has to answer before beginning with the optimization:

- What chip size is needed?
- What is the budget for the prototype?
- Are biological samples to be handled?
- What is the maximum electric field, the samples can be exposed to?
- What is the maximum temperature, the samples can be exposed to?
- Which safety factor is appropriate?
- What is more important: high efficiency or high flow velocities?

This list is certainly not complete. The limitations discussed in this chapter before are not included and assumed to be preconditions.

For the product and prototyping design of the actuator, fabrication and operating limitations are to be considered, together with the constraints of the individual use case. Knowing the sample and budget, optimization can be significant and with the given code.

Speeding up the actuator simulation would allow for more setups to be explored and evaluated. Further work is required to identify a more adequate formulation of the efficiency. The parameter as defined above, tends to low dissipation rather than high velocities. Weight factors accounting for this imbalance can make the result more meaningful.

CHAPTER 7

Conclusion

7.1 Generalizing remarks on the electrokinetic transport phenomena in an LOC system

Two nonlinear electrokinetic transport phenomena, electromigration of a drop and wall-induced traveling-wave electrokinetic flow, were investigated in this study. Droplets, not necessarily carrying an effective surface charge, show electromigration. We note that this phenomenon is independent of the strength of the respective electrolytes. In fact, differences in the migration velocity for small Galvani potentials reduce to lower order. Modeling differences, such as the modeling of the surface geometry in an asymptotic setting, have a major impact on the outcome.

The carrier fluid in the actuator can be pumped by traveling wave electroosmosis. Charge clouds accumulate near the electrode wall and travel simultaneously with the excitation potential. The resulting net charge is negligibly small.

Both studies can provide evidence for a principle presented by Purcell (1977). He investigated the swimming motion of micro-organisms and defined the underlying principal.

> "One special kind of swimming motion is what I call a reciprocal motion. That is to say, I change my body into a certain shape and then I go back to the original shape by going through the sequence in reverse. At low Reynolds number, everything reverses just fine. Time, in fact, makes no difference – only configuration. [...] So, if the animal tries to swim by reciprocal motion, it *can't go anywhere.*"
> **Purcell (1977)**

His conclusion is that reciprocal motion alone is not sufficient for the swimmer to move at low Reynolds number. Yet, a second degree of freedom enabling asymmetric reciprocal

motion does allow micro-swimmer motility.

The same is true for electrokinetic transport. Earlier EHD models by Melcher and Taylor (1969); Saville (1997) for drops or vesicles did not include a Debye-layer analysis and could not observe migration as a result. In settings where no surface charge is present, the Galvani potential is an effect of a asymmetry of charge at the fluid-fluid interface. This asymmetry, together with the superposed electric field, is enough to induce motion of the particle.

In the case of the actuator, earlier versions of the design suggested AC-potentials at the electrodes (Barz & Class, 2007). At low Reynolds number, this excitation induces vortices in the flow field. But pumping along the wall is not possible.

Beyond these examples, Squires and Bazant (2006) presented other ideas of AC-electroosmotic pumping by breaking symmetries and delivering further proof to Purcell's hypothesis.

7.2 Development status of the Active-surface LOC and outlook

The present study is concluded by summarizing its logical continuations. These cover the modeling of electrokinetic problems, as well extensions and imrpovements of the numerical prediction method.

7.2.1 Electrohydrodynamic models

Electrohydrodynamic models with effective boundary conditions representing the Debye-layer physics have been derived for a number of different experimental settings. However, our work, as well as studies by Mori and Young (2018) and Ma et al. (2022), can only be derived assuming a relatively high surface tension. A study investigating under which conditions the drop is stable is still missing.

It remains unclear if the interface is permeable to ions. Models featuring impermeable membranes (Mori & Young, 2018; Schnitzer & Yariv, 2015), including our study[1], predict electromigration. In contrast to that, the model by Ma et al. (2022) includes an impermeable interface. They conclude the existence of surface charge convection and an electrodeformation deviating from the classical result by Taylor (1966). An interrelationship between interface permeability and electromigration is still to be investigated.

We have focused in our work on the effects on the droplet induced by an outer electric field. Significantly different results are likely to be obtained with an outer concentration

[1]Note that this work is based on the original publication by Mori and Young (2018) and that critics discussed in this work led to the corrigendum (Marthaler et al., 2023).

gradient. With the effective boundary conditions presented here, the effects of electrochemical gradients can be investigated.

The presented model is only valid for drops. Vesicles, that are commonly used as models for cells, feature more complex surface properties, like an interface capacitance or porosity (Ma et al., 2022; Mori, Liu, & Eisenberg, 2011). A model extension would allow for predictions on biochemical samples in the LOC system.

While this work explored the limits of strong and weak electrolytic solutions, a unified model also covering moderately dissociated electrolytic solutions has, to the authors' knowledge, not been derived. However, it is unclear if an analytical derivation is feasible.

7.2.2 Actuator and LOC simulation

The main deficiency of the developed code for the actuator simulation is its efficiency. As a first study, a highly accurate solution ensures that all physical effects are captured. Yet, the results show a relatively laminar flow field. For that reason, a faster solver, using a Galerkin-finite-difference method is under development and part of a later publication.

Predictions of a two-dimensional simulation are always limited to the assumption that gradients in third spatial direction vanish. However, this is not true for the presented chip design. The carrier fluid is transported in circular patterns (cp. Figure D.9). This method of transport can lead to eddies parallel to the chip surface complicating flow control and deminishing the performance. A three-dimensional analysis is indispansible in order to get a quantitative estimate of these effects and to explore solution strategies. Possible ideas are the testing of different electrolyte materials, or active flow adaption by involving more electrodes surrounding the streamchannels.

Arguably, the numerical simulation of two-phase flow in the actuator would allow for predicting the behavior of an immiscible fluid sample which is pumped together with the carrier fluid. The time-varying electric fields in the fluid domain are expected to affect transport, deformation, and rotation of the immiscible sample. Vice versa, samples which are of the size of the electrode distance affect the flow field, and indirectly also the charge distribution and the electric field. The study of this complex interaction is a logical next step of the presented work.

This study focused on the architecture and operational methods of the chip. However, microfluidic sytsems necessitate the integration analysis methods allowing for identification of sample parts. One analytical method to be performed on the chip is charge spectrometry, i.e. the separation of sample components by their electric mobility. We know that the diffusion coefficient and electric mobility of particles, and thus also the respective Péclet number are linearly dependent. These inertia differences thus lead to a distinct phase shift between different charges. In a numerical simulation, this phase shift can be observed as stripes reaching from the charge cloud near the wall into the fluid. In the LOC system, electric currents measured in the electrodes allow conclusions on the

mentioned phase shift and the respective particles.

The effective mixing of samples is another process to be validated using a numerical simulation. For that purpose, optimal phase shift between the top and bottom electrodes is to be identified. We assume that a standing wave with a 180° phase shift would produce eddies that can effectively mix two probes. This remains to be validated.

7.2.3 Product design

In the design of the LOC system, one essential piece missing is the control software. Setting up a prototype would require the development of a code, which could control electrode voltages. If the the actuator simulation could reach high enough efficiency to predict the flow behavior simultaneously, flow control can become more reliable. Additionally, a wider range of analyses on the chip surface become feasible.

Process monitoring in microfluidics is often performed with optical methods measuring the intensity of fluorescence from dye molecules. Our design makes optical access difficult. Charge spectrometry, as discussed in the section above, can be an alternative. Ion-sensitive field effect transistors (ISFETs) serve a similar purpose and are e.g. already utilized in systems with limited optical accessibility. By measuring the pH inside the fluid probes, chemical processes, such as a polymerase chain reaction (PCR) can be monitored. Incorporating this technique into the chip surface is quite promising. Thus, the related design capabilities are to be explored.

The system needs to be adapted to the samples investigated. While a large number of different processes is possible, design limitations lie in the size, electric charge, and vulnerability of the research objects. Measurements, carrier fluid, and electric excitation have to be adapted to these conditions, ensuring precise control and non-destructive analyses.

One major source of contamination, and thus technical problems in microfluidic systems, are the fluid interfaces. The presented design does neither include mechanisms to reduce contamination, nor can be estimated to which extent this affects the functional behavior.

An overall recommendation is the collaboration with possible users, in order to set optimization constraints and to streamline development goals. Possibly, a simple setup could be designed with quite large (and cheap) dimensions to transport only carrier fluid. In further steps, solid, fluid, and biochemical samples can be added.

7.3 Final remarks

Clearly, those questions in fundamental research and product design set the roadmap for future investigations. Yet, the goals defined in the introduction have been met in this study.

Analyzing existing EHD droplet models allowed us to investigate an electromigration problem with strong electrolytes. The influence of electrolyte strength was confirmed to be small, in the framework of droplet electromigration and -deformation. To the author's knowledge, this is the first systematic study investigating the influence of electrolyte strength on electrohydrodynamic problems in the tradition of the TM model. The results indicate that, no matter what electrolyte strength is used for deriving the model, the results remain valid – confirming an assumption which is widely used in the field. Experiments showing electromigration of (uncharged) droplets in the electric field could be confirmed. However, we note that it remains unclear what the correct interface properties in such a setting are. Future investigations shall give insights into the relationship between interface properties and electromigration.

The pre-study of the electrokinetic actuator verified its functional principle and highlighted the importance of heat dissipation in strong-electrolyte microfluidic systems. This effect is very similar to computer chips, especially for applications where miniaturization plays an important role. Relatively homogeneous flow fields keep probes compact while being transported. The relatively high pumping velocities predicted in this study are to be handled with care. In a three-dimensional case, viscous effects in the third direction are assumed to have a major impact. However, even a small precentage of the predicted velocity seems sufficient to transport samples efficiently. Design limitations were defined for the development and optimization of a first prototype. A systematic description of the system achitecture was developed. As a result, the basis for reciprocal system improvement and design verification are established with the presented work.

List of symbols

$\square$	here used as symbol for a general parameter	-
$\square^*$	parameter with unit	-
$\square^\star$	parameter appears with unit and dimensionless	-
$\square_\pm$	positive/negative ions in a binary electrolyte	-
$\square_\perp$	normal (to the surface)	-
$\square_\parallel$	parallel (to the surface)	-
$\square_{\mathrm{equ}}$	reaction equilibrium	-
$\square_{\mathrm{ref}}$	reference parameter	-
$\square_{\mathrm{ex}}$	external phase	-
$\square_{\mathrm{in}}$	internal phase	-
$[\![\square]\!]$	jump condition	-
$\bar{\square}$	internal phase (chapter 4)	-
$\square_\gamma$	applied boundary conditions (chapter 5)	-
$\vec{\square}$	vector	-
$\square^i$	vector (contravariant)	-
$\square_i$	vector (covariant)	-
$\otimes$	tensor product	-
$\odot$	elementwise matrix product	-
$*$	convolution operator	-
$\vec{\nabla}^\star$	nabla operator / spatial gradient	m^{-1}
$\vec{\nabla}\cdot$	divergence operator	m^{-1}
$\nabla^{\star 2}$	Laplacian	m^{-2}
$\nabla^{\star 4}$	biharmonic operator	m^{-4}
$\vec{\nabla\!\!/}$	spectral nabla operator / spatial gradient	-
$\vec{\nabla\!\!/}\cdot$	spectral divergence operator	-
$\nabla\!\!/^2$	spectral Laplacian	-
$\nabla\!\!/^4$	spectral biharmonic operator	-
α	electrolyte strength	-
$\mathrm{bc}_\pm$	spectral boundary condition operator	-
β	dimensionless electric field strength	-
$c^\star$	mean salt concentration	m^{-3}
$c_i^\star$	concentrations for each ion i	m^{-3}
$c_\pm^*$	ion concentrations in a binary electrolyte	m^{-3}

C	concentration in the Debye layer (chapter 4)		-
C	spectral concentration (chapter 5)		-
γ	apparent fluid-fluid interface		-
Γ	genuine fluid-fluid interface		-
Γ^i_{jk}	Christoffel symbols		-
$D^\star_\pm$	ion diffusivity		$\mathrm{m^2\,s^{-1}}$
$\vec{D}$	displacement field		$\mathrm{A\,s\,m^{-2}}$
Da	Damköhler number		-
$\mathcal{D}$	spectral differentiation operator		-
δ	dimensionless Debye length		-
$\delta(\vec{x}-\vec{x}_0)$	Dirac-delta sitribution		-
$\partial^\star$	partial derivative		$\mathrm{m^{-1}}$
e^*_0	elementary charge	$1.6\cdot10^{-19}$	$\mathrm{A\,s}$
$\vec{E}^\star$	electric field		$\mathrm{V\,m^{-1}}$
e^*	actuator efficiency		$\mathrm{m^3\,W^{-1}\,s^{-1}}$
ϵ^*_0	vacuum permittivity	$8.9\cdot10^{-12}$	
ϵ^*	relative permittivity		-
ε^*	dissipation rate		$\mathrm{W\,m^{-2}}$
ε^*_η	viscous dissipation rate		$\mathrm{W\,m^{-2}}$
ε^*_ς	Ohmic dissipation rate		$\mathrm{W\,m^{-2}}$
$\vec{f}$	(volume) force		-
Fa^*	Faraday constant	$9.6\cdot10^{4}$	$\mathrm{A\,s\,mol^{-1}}$
$\zeta^\star$	ζ-potential		V
$\vec{g}^*$	gravitational constant		$\mathrm{m^2\,s^{-1}}$
g_{ij}	metric tensor (covariant)		-
g^{ij}	metric tensor (contravariant)		-
$\sqrt{g}$	volume element		-
η^*	dynamic viscosity		$\mathrm{Pa\,s}$
η^*_{fric}	friction coefficient		$\mathrm{kg\,s^{-1}}]$
η^*_{mob}	mobility coefficient		$\mathrm{s\,kg^{-1}}$
$h^\star$	actuator height		m
Ha	Hartmann number		-
$\mathrm{Ha}_{\mathrm{el}}$	Hartmann number (Saville model)		-
$\mathcal{H}$	spectral Helmholtz operator		-
ϑ	polar coordinate		-
$\theta^\star$	Maxwell stress tensor		Pa
Θ	Maxwell stress tensor (Debye layer)		-
I	unity matrix		-
ß	imaginary unit		-
$\vec{j}^\star_\pm$	ion flux		$\mathrm{A\,m^{-2}}$
$\vec{j}^\star_{\mathrm{conv}}$	convective ion flux		$\mathrm{A\,m^{-2}}$
$\vec{j}^\star_{\mathrm{diff}}$	diffusive ion flux		$\mathrm{A\,m^{-2}}$
$\vec{j}^\star_{\mathrm{elph}}$	electrophoretic ion flux		$\mathrm{A\,m^{-2}}$
$\vec{j}$	ion flux (Debye layer)		-

κ	surface curvature (dimensionless)		-
$\varkappa$	adsorption coefficients		-
k_α^β	principal curvature at a surface point		-
k_B^*	Boltzmann constant	$1.4 \cdot 10^{-23}$	$\mathrm{kg\,m^2\,s^{-2}\,K^{-1}}$
$K_{d/a,equ}^*$	equilibrium constants		[various units]
$k_{d/a}^*$	reaction rates		[various units]
$k_{d/a,equ}^*$	reaction rates (equilibrium)		[various units]
λ	scalar parameter of the Helmholtz eq.		-
Λ_SA	dimensionless number (Saville model)		-
$l_\pm$	partition coefficients		-
M	viscosity ratio		
μ^*	ion mobility		$\mathrm{m^2\,V^{-1}\,s^{-1}}$
$\vec{n}$	surface normal vector		
n^*	molarity		$\mathrm{mol\,l^{-1}}$
ν^*	frequency		Hz
N	number of grid points		-
$\xi^\star$	Newton stress tensor		Pa
Ξ	Newton stress tensor (Debye layer)		-
$\mathcal{O}$	coordinate origin		-
$p^\star$	hydrostatic (and osmotic pressure)		Pa
P	pressure in the Debye layer (chapter 4)		-
P	spectral pressure (chapter 5)		-
$\vec{P}$	polarization density		$\mathrm{A\,s\,m^{-2}}$
$\mathcal{P}$	generic surface point		-
Pe	Péclet number		-
ϖ	numerical threshold values		-
ρ^*	fluid density		$\mathrm{kg\,m^{-3}}$
ϱ	characteristic constant of the C-BDF2 scheme		
$q^\star$	charge density		$\mathrm{A\,s\,m^{-3}}$
Q	charge density in the Debye layer (chapter 4)		-
Q	spectral charge density (chapter 5)		-
Re	Reynolds number		-
$\mathrm{Re_{el}}$	electric Reynolds number		-
R	conductivity ratio		-
$\mathcal{R}_\mathrm{c/s}^\star$	reaction term		$\mathrm{A\,m^{-3}}$
R^*	gas constant	8.31	$\mathrm{J\,K^{-1}\,mol^{-1}}$
S	permittivity ratio		
$\varsigma^\star$	conductivity		$\mathrm{S\,m^{-1}}$
$\sigma^\star$	total stress tensor		Pa
$\sigma_\Gamma^\star$	surface tension		$\mathrm{N\,m^{-1}}$
Σ	total stress tensor (Debye layer)		-
$t^\star$	time		s
t_C^*	charge relaxation time		s
t_D^*	diffusive time scale		s

t_{v}^{*}	convective time scale		s
t_{η}^{*}	viscous time scale		s
t_{Γ}^{*}	surface time scale		s
T_{a}^{*}	ambient temperature	298	K
T_n	Chebyshev polynomial of degree n		-
$\mathcal{T}$	spectral transformation operator		-
$\mathcal{T}_{\mathrm{F}}$	Fourier transformation operator		-
$\mathcal{T}_{\mathrm{C}}$	Chebyshev transformation operator		-
$u^{\star}$	surface velocity		$\mathrm{m\,s^{-1}}$
$v^{\star}$	flow velocity		$\mathrm{m\,s^{-1}}$
V	flow velocity in the Debye layer (chapter 4)		-
V	spectral flow velocity (chapter 5)		-
φ	azimuthal coordinate		-
$\phi^{\star}$	el. potential		V
$\phi_{\mathrm{G}}^{\star}$	Galvani potential		V
Φ	el. potential (Debye layer)		-
w^{*}	energy/weight function		J
$x_i^{\star}$	coordinates (covariant)		m
$x^{i\star}$	coordinates (contravariant)		m
X	Debye layer coordinate (normal)		-
$\psi^{\star}$	excess potential (chapter 2)		$\mathrm{m^2\,s^{-1}}$
$\psi^{\star}$	streamfunction (chapters 4 & 5)		V
Ψ	el. potential in the Debye layer (chapter 4)		-
Ψ	spectral el. potential (chapter 5)		-
$\mathcal{Z}$	valence		-
ω	bulk domain		-
Ω	Debye-layer domain		-

Abbreviations

ACEO	AC electroosmosis
ASIC	application-specific integrated circuit
BDF	backward differentiation formula
BDF2	backward differentiation formula of second order
BVP	boundary value problem
C-BDF2	composite backward differentiation formula of second order
DL	Debye layer
EDL	electric double layer
EHD	electrohydrodynamics
EK	electrokinetics
EML	electric mono layer
FPU	fluid processing unit
FRAM	fluid random access memory
IBVP	initial boundary value problem
IRDS	International Technology Roadmap for Devices and Systems
ITRS	International Technology Roadmap for Semiconductors
LFA	lateral flow assay
LOC	lab-on-chip
MBSE	model-based systems engineering
PDE	partial differential equation
PGD	product generation development
PNP	Poisson-Nernst-Planck
POC	point-of-care
TWEO	traveling-wave electroosmosis
WRM	weighted residuals methods

APPENDIX A

The Stokes equation in curvilinear coordinates

A.1 The Stokes equation in general curvilinear coordinates

The Stokes equation in general curvilinear coordinates reads

$$\sigma^{ij}_{,j} = 0. \tag{A.1}$$

The divergence of the total stress, i.e. the sum of Newton (hydrodynamic) stress ξ^{ij} and Maxwell (electrostatic) stress θ^{ij}, vanishes. Applying the covariant derivative $(..)_{,j}$ delivers

$$\partial_j \sigma^{ij} + \Gamma^j_{jk}\sigma^{ik} + \Gamma^i_{jk}\sigma^{jk} = 0. \tag{A.2}$$

With Aris (1989, p. 165), the second term symbol in the above relation can be replaced as

$$\Gamma^j_{jk}\sigma^{ik} = \left(\frac{1}{\sqrt{g}}\partial_k\sqrt{g}\right)\sigma^{ik} = \left(\frac{1}{\sqrt{g}}\partial_j\sqrt{g}\right)\sigma^{ij}. \tag{A.3}$$

Thus, eq. A.2 reads

$$\partial_j \sigma^{ij} + \left(\frac{1}{\sqrt{g}}\partial_j\sqrt{g}\right)\sigma^{ij} + \Gamma^i_{jk}\sigma^{jk} = 0. \tag{A.4}$$

We further assume that the total-stress tensor can be split up into an isotropic part (proportional to the metric g^{ij}) and a residual part as

$$\sigma^{ij} = g^{ij}\sigma^{\bullet} + \sigma^{\blacktriangleleft ij}. \tag{A.5}$$

We can rewrite the last term of eq. A.4 to find

$$\partial_j \sigma^{ij} + \left(\frac{1}{\sqrt{g}}\partial_j\sqrt{g}\right)\sigma^{ij} + \Gamma^i_{jk}g^{jk}\sigma^{\bullet} + \Gamma^i_{jk}\sigma^{\blacktriangleleft jk} = 0. \tag{A.6}$$

The forth term of this relation can be rewritten using Ricci's lemma (Aris, 1989, p. 165)

$$\Gamma^i_{jk}g^{jk} = \frac{-1}{\sqrt{g}}\partial_l\left(\sqrt{g}g^{il}\right) = \frac{-1}{\sqrt{g}}\partial_j\left(\sqrt{g}g^{ij}\right), \tag{A.7}$$

such that eq. A.6 reads

$$\partial_j \sigma^{ij} + \left(\frac{1}{\sqrt{g}} \partial_j \sqrt{g} \right) \sigma^{ij} - \frac{1}{\sqrt{g}} \partial_j \left(\sqrt{g} g^{ij} \right) \sigma^{\bullet} + \Gamma^i_{jk} \sigma^{\blacktriangleleft jk} = 0. \tag{A.8}$$

A.2 Normal and tangential directions

As discussed in chapter 4, we choose the metric g^{ij}, such that $g^{11} = 1$ and $g^{1\alpha} = 0$ where the Latin indices run through 1,2,3 and the Greek indices through 2,3. We use Ricci's lemma to find

$$\begin{aligned} 0 = g^{11}_{,j} = \partial_j g^{11} + 2\Gamma^1_{jl} g^{1l} = 2\Gamma^1_{1j} \quad &\Rightarrow \quad \Gamma^1_{1j} = 0, \\ 0 = g^{1\alpha}_{,1} = \partial_1 g^{1\alpha} + \Gamma^1_{1l} g^{\alpha l} + \Gamma^\alpha_{1l} g^{1l} = \Gamma^\alpha_{11} \quad &\Rightarrow \quad \Gamma^\alpha_{11} = 0. \end{aligned} \tag{A.9}$$

We also define the curvature for a surface defined by x_1 as

$$\kappa := \frac{1}{\sqrt{g}} \partial_1 \sqrt{g}. \tag{A.10}$$

The momentum equation A.8 can be rewritten to yield

$$\begin{aligned} \partial_1 \sigma^{i1} + \left(\frac{1}{\sqrt{g}} \partial_1 \sqrt{g} \right) \sigma^{i1} + \frac{1}{\sqrt{g}} \partial_\alpha \left(\sqrt{g} \sigma^{i\alpha} \right) - \frac{1}{\sqrt{g}} \partial_j \left(\sqrt{g} g^{ij} \right) \sigma^{\bullet} + \Gamma^i_{jk} \sigma^{\blacktriangleleft jk} = 0, \\ \partial_1 \sigma^{i1} + \kappa \sigma^{i1} + \frac{1}{\sqrt{g}} \partial_\alpha \left(\sqrt{g} \sigma^{i\alpha} \right) - \frac{1}{\sqrt{g}} \partial_j \left(\sqrt{g} g^{ij} \right) \sigma^{\bullet} + \Gamma^i_{jk} \sigma^{\blacktriangleleft jk} = 0. \end{aligned} \tag{A.11}$$

The normal direction of this equation is found by choosing $i = 1$. It yields

$$\partial_1 \sigma^{11} + \kappa \left(\sigma^{11} - \sigma^{\bullet} \right) + \frac{1}{\sqrt{g}} \partial_\alpha \left(\sqrt{g} \sigma^{1\alpha} \right) + \Gamma^1_{\alpha\beta} \sigma^{\blacktriangleleft \alpha\beta} = 0. \tag{A.12}$$

Equivalently, by choosing $i = \beta$, eq. A.11 yields

$$\partial_1 \sigma^{1\beta} + \kappa \sigma^{1\beta} + \frac{1}{\sqrt{g}} \partial_\alpha \left(\sqrt{g} \sigma^{\alpha\beta} \right) - \frac{1}{\sqrt{g}} \partial_\alpha \left(\sqrt{g} g^{\alpha\beta} \right) \sigma^{\bullet} + \Gamma^\beta_{jk} \sigma^{\blacktriangleleft jk} = 0. \tag{A.13}$$

Using the separation step A.5, the third term is modified and eq. A.13 reads

$$\begin{aligned} \partial_1 \sigma^{1\beta} + \kappa \sigma^{1\beta} + \frac{1}{\sqrt{g}} \partial_\alpha \left(\sqrt{g} g^{\alpha\beta} \sigma^{\bullet} \right) + \frac{1}{\sqrt{g}} \partial_\alpha \left(\sqrt{g} \sigma^{\blacktriangleleft \alpha\beta} \right) - \frac{1}{\sqrt{g}} \partial_\alpha \left(\sqrt{g} g^{\alpha\beta} \right) \sigma^{\bullet} + \Gamma^\beta_{jk} \sigma^{\blacktriangleleft jk} = 0, \\ \partial_1 \sigma^{1\beta} + \kappa \sigma^{1\beta} + g^{\alpha\beta} \partial_\alpha \sigma^{\bullet} + \frac{1}{\sqrt{g}} \partial_\alpha \left(\sqrt{g} \sigma^{\blacktriangleleft \alpha\beta} \right) + \Gamma^\beta_{jk} \sigma^{\blacktriangleleft jk} = 0, \\ \partial_1 \sigma^{1\beta} + \kappa \sigma^{1\beta} + g^{\alpha\beta} \partial_\alpha \sigma^{\bullet} + \frac{1}{\sqrt{g}} \partial_\alpha \left(\sqrt{g} \sigma^{\blacktriangleleft \alpha\beta} \right) + 2\Gamma^\beta_{1\alpha} \sigma^{\blacktriangleleft 1\alpha} + \Gamma^\beta_{\alpha\gamma} \sigma^{\blacktriangleleft \alpha\gamma} = 0. \end{aligned} \tag{A.14}$$

With $g^{1\alpha} = 0$ and relation A.5, we know that $\sigma^{\blacktriangleleft 1\alpha} = \sigma^{1\alpha}$, and we find

$$\partial_1 \sigma^{1\beta} + \kappa \sigma^{1\beta} + g^{\alpha\beta} \partial_\alpha \sigma^{\bullet} + 2\Gamma^\beta_{1\alpha} \sigma^{1\alpha} + \frac{1}{\sqrt{g}} \partial_\alpha \left(\sqrt{g} \sigma^{\blacktriangleleft \alpha\beta} \right) + \Gamma^\beta_{\alpha\gamma} \sigma^{\blacktriangleleft \alpha\gamma} = 0. \tag{A.15}$$

Finally, switching the indices α and β delivers

$$\partial_1 \sigma^{1\alpha} + \kappa \sigma^{1\alpha} + g^{\alpha\beta} \partial_\beta \sigma^{\bullet} + 2\Gamma^\alpha_{1\beta} \sigma^{1\beta} + \frac{1}{\sqrt{g}} \partial_\beta \left(\sqrt{g} \sigma^{\blacktriangleleft \alpha\beta} \right) + \Gamma^\alpha_{\beta\gamma} \sigma^{\blacktriangleleft \beta\gamma} = 0. \tag{A.16}$$

A.3 Hydrodynamic and electric stress tensors

In this section, the elements of the hydrodynamic (Newton) stress tensor ξ^{ij} and the electric (Maxwell) stress tensor θ^{ij} are computed. We perform the analysis for the region Ω and summarize the results for both regions and all relevant orders at the end of this section. We start with the nondimensionalized Newton stress for an incompressible fluid

$$\xi^{ij} = -g^{ij}p + g^{ik}\partial_k v^j + g^{kj}\partial_k v^i - v^k \partial_k g^{ij}. \tag{A.17}$$

Due to the shape of the metric with $g^{11} = 1$ and $g^{1\alpha} = 0$, we compute three elements of the tensor separately and find

$$\begin{aligned}
\xi^{11} &= -p + 2\partial_1 v^1, \\
\xi^{1\alpha} &= \partial_1 v^\alpha + g^{\alpha\beta}\partial_\beta v^1, \\
\xi^{\alpha\beta} &= -g^{\alpha\beta}p + g^{\alpha\gamma}\partial_\gamma v^\beta + g^{\beta\gamma}\partial_\gamma v^\alpha - v^\gamma \partial_\gamma g^{\alpha\beta}, \\
\xi^{\bullet} &= -p, \\
\xi^{\blacktriangleleft\alpha\beta} &= g^{\alpha\gamma}\partial_\gamma v^\beta + g^{\beta\gamma}\partial_\gamma v^\alpha - v^\gamma \partial_\gamma g^{\alpha\beta}.
\end{aligned} \tag{A.18}$$

The Maxwell stress for an electrostatic problem reads

$$\theta^{ij} = -\frac{1}{2} g^{ij} g^{kl} \left(\partial_k \phi\right) \left(\partial_l \phi\right) + g^{ik} g^{jl} \left(\partial_k \phi\right) \left(\partial_l \phi\right). \tag{A.19}$$

The elements of this tensor are

$$\begin{aligned}
\theta^{11} &= \frac{1}{2}\left(\left(\partial_1 \phi\right)^2 - g^{\alpha\beta} \left(\partial_\alpha \phi\right) \left(\partial_\beta \phi\right) \right), \\
\theta^{1\alpha} &= g^{\alpha\beta} \left(\partial_1 \phi\right) \left(\partial_\beta \phi\right), \\
\theta^{\alpha\beta} &= -\frac{1}{2} g^{\alpha\beta} \left(\left(\partial_1 \phi\right)^2 + g^{\gamma\delta} \left(\partial_\gamma \phi\right) \left(\partial_\delta \phi\right) \right) + g^{\alpha\gamma} g^{\beta\delta} \left(\partial_\gamma \phi\right) \left(\partial_\delta \phi\right) \\
\theta^{\bullet} &= -\frac{1}{2}\left(\left(\partial_1 \phi\right)^2 + g^{\gamma\delta} \left(\partial_\gamma \phi\right) \left(\partial_\delta \phi\right) \right), \\
\theta^{\blacktriangleleft\alpha\beta} &= g^{\alpha\gamma} g^{\beta\delta} \left(\partial_\gamma \phi\right) \left(\partial_\delta \phi\right).
\end{aligned} \tag{A.20}$$

An overview of all relevant stresses in the inner region can be found in table A.1. We used the assumption that $V^1 \sim O(\delta^1)$, $\phi, \Phi, v^i, V^\alpha \sim O(1)$, $p \sim O(\delta^{-1})$, and $P \sim O(\delta^{-2})$. The coordinate stretch was also employed as $\partial_1 = \delta^{-1}\partial_X$. We note that

$$\begin{aligned}
\Sigma^{\alpha\beta}_{(n)} &= g^{\alpha\beta}\Sigma^{\bullet}_{(n)}, \qquad && n \in \{-2, -1\}, \\
\Sigma^{\blacktriangleleft\alpha\beta}_{(n)} &= 0, && n \in \{-2, -1\}.
\end{aligned} \tag{A.21}$$

Newton stresses

$$\begin{array}{lll} \Xi^{11}_{(-2)} = -P_{(-2)} = \Xi^{\bullet}_{(-2)} & \Xi^{1\alpha}_{(-2)} = 0 & \Xi^{\alpha\beta}_{(-2)} = -g^{\alpha\beta}_{(0)} P_{(-2)} \\ \Xi^{11}_{(-1)} = -P_{(-1)} = \Xi^{\bullet}_{(-1)} & \Xi^{1\alpha}_{(-1)} = V^{\alpha\,\prime}_{(0)} & \Xi^{\alpha\beta}_{(-1)} = -g^{\alpha\beta}_{(0)} P_{(-1)} - X g^{\alpha\beta}_{(1)} P_{(-2)} \end{array}$$

Maxwell stresses

$$\begin{array}{lll} \Theta^{11}_{(-2)} = \frac{1}{2}\Phi'^2_{(0)} = -\Theta^{\bullet}_{(-2)} & \Theta^{1\alpha}_{(-2)} = 0 & \Theta^{\alpha\beta}_{(-2)} = -\frac{1}{2} g^{\alpha\beta}_{(0)} \Phi'^2_{(0)} \\ \Theta^{11}_{(-1)} = \Phi'_{(0)}\Phi'_{(1)} = -\Theta^{\bullet}_{(-1)} & \Theta^{1\alpha}_{(-1)} = g^{\alpha\beta}_{(0)} \Phi'_{(0)} \partial_\beta \Phi_{(0)} & \Theta^{\alpha\beta}_{(-1)} = -g^{\alpha\beta}_{(0)} \Phi'_{(0)} \Phi'_{(1)} - \frac{1}{2} X g^{\alpha\beta}_{(1)} \Phi'^2_{(0)} \end{array}$$

Table A.1: Newton and Maxwell stresses in the inner region of the external phase Ω

A.4 Relevant orders of the momentum equation

The relevant orders of the normal momentum equation A.12 read

$$\begin{aligned} \delta^{-3}: &\quad 0 = {\Sigma^{11}_{(-2)}}', \\ \delta^{-2}: &\quad 0 = {\Sigma^{11}_{(-1)}}' + \kappa_{(0)} \left(\Sigma^{11}_{(-2)} - \Sigma^{\bullet}_{(-2)} \right), \\ \delta^{-1}: &\quad 0 = \Sigma^{11\,\prime}_{(0)} + \kappa_{(0)} \left(\Sigma^{11}_{(-1)} - \Sigma^{\bullet}_{(-1)} \right) + X \kappa_{(1)} \left(\Sigma^{11}_{(-2)} - \Sigma^{\bullet}_{(-2)} \right) + \frac{1}{\sqrt{g}_{(0)}} \partial_\alpha \left(\sqrt{g}_{(0)} \Sigma^{1\alpha}_{(-1)} \right). \end{aligned} \tag{A.22}$$

Equivalently, from eq. A.16, we find for the tangential direction

$$\begin{aligned} \delta^{-2}: &\quad 0 = {\Sigma^{1\alpha}_{(-1)}}' + g^{\alpha\beta}_{(0)} \partial_\beta \Sigma^{\bullet}_{(-2)}, \\ \delta^{-1}: &\quad 0 = \Sigma^{1\alpha\,\prime}_{(0)} + g^{\alpha\beta}_{(0)} \partial_\beta \Sigma^{\bullet}_{(-1)} + X g^{\alpha\beta}_{(1)} \partial_\beta \Sigma^{\bullet}_{(-2)} + \kappa_{(0)} \Sigma^{1\alpha}_{(-1)} + 2\Gamma^{\alpha}_{1\beta(0)} \Sigma^{1\beta}_{(-1)}. \end{aligned} \tag{A.23}$$

A.5 Equations for weakly non-orthogonal coordinates

A coordinate system where the angle between the base vectors tangential to the surface deviates from a right angle only by the order of the small parameter δ. This is a special

case of the coordinate system used so far. The properties of this system are

$$\begin{aligned}
\breve{g}^{1\alpha} &= 0 && \forall \alpha \in \{2,3\}\,,\\
\breve{g}^{11} &= 1, && \text{(equivalent to } g^{ij}\text{)},\\
\breve{g}^{\alpha\beta} &\sim O(\delta), && \forall \alpha \neq \beta,\\
\breve{\Gamma}^1_{1j} = \breve{\Gamma}^\alpha_{11} &= 0, && \text{(equivalent to } g^{ij}\text{)},\\
\breve{\Gamma}^i_{jk} &\sim O(\delta) && \forall\, i \neq j \neq k,\\
\breve{\Gamma}^\alpha_{1\alpha(0)} &= \kappa_{(0)}, && \text{(summation over } \alpha\text{)},\\
\breve{\Gamma}^\alpha_{1\alpha(0)} &= \frac{\partial_1 \breve{g}_{\alpha\alpha(0)}}{2\breve{g}_{\alpha\alpha(0)}} := \frac{1}{2}\breve{k}^\alpha_{\alpha(0)}, && \text{(principal curvature, } \underline{\text{no}} \text{ summation over } \alpha\text{)},\\
\kappa_{(1)} &= 0.
\end{aligned} \tag{A.24}$$

The system of differential equations A.22 and A.41 simplifies for this geometry to (we are here dropping the breve accents for the geometry parameters)

$$\begin{aligned}
\delta^{-3}: &\quad 0 = {\Sigma^{11}_{(-2)}}',\\
\delta^{-2}: &\quad 0 = {\Sigma^{11}_{(-1)}}' + \kappa_{(0)}\left(\Sigma^{11}_{(-2)} - \Sigma^{\bullet}_{(-2)}\right),\\
\delta^{-1}: &\quad 0 = {\Sigma^{11}_{(0)}}' + \kappa_{(0)}\left(\Sigma^{11}_{(-1)} - \Sigma^{\bullet}_{(-1)}\right) + \frac{1}{\sqrt{g}_{(0)}}\partial_\alpha\left(\sqrt{g}_{(0)}\Sigma^{1\alpha}_{(-1)}\right),
\end{aligned} \tag{A.25}$$

and for the tangential direction

$$\begin{aligned}
\delta^{-2}: &\quad 0 = {\Sigma^{1\alpha}_{(-1)}}' + g^{\alpha\alpha}_{(0)}\partial_\alpha\Sigma^{\bullet}_{(-2)},\\
\delta^{-1}: &\quad 0 = {\Sigma^{1\alpha}_{(0)}}' + g^{\alpha\alpha}_{(0)}\partial_\alpha\Sigma^{\bullet}_{(-1)} + X g^{\alpha\beta}_{(1)}\partial_\beta\Sigma^{\bullet}_{(-2)} + \left(\kappa_{(0)} + k^\alpha_{\alpha(0)}\right)\Sigma^{1\alpha}_{(-1)}.
\end{aligned} \tag{A.26}$$

A.6 Equations for spherical coordinates

These equations can further be simplified by introducing the spherical metric $\mathring{g}^{ij}$ which is a special case of the weakly non-orthogonal metric that we used so far. The following simplifications hold

$$\begin{aligned}
\mathring{g}^{ij} &= 0 && \forall i \neq j,\\
\mathring{g}^{11} &= 1, && \text{(equivalent to } g^{ij}\text{)},\\
\mathring{g}^{22} &= \mathrm{fun}(x^1),\\
\mathring{g}^{33} &= \mathrm{fun}(x^1, x^2),\\
\mathring{\Gamma}^1_{1j} = \mathring{\Gamma}^\alpha_{11} &= 0, && \text{(equivalent to } g^{ij}\text{)},\\
\mathring{\Gamma}^i_{jk} &= 0 && \forall\, i \neq j \neq k,\\
\mathring{\Gamma}^\alpha_{1\alpha(0)} &= \frac{\mathring{\kappa}_{(0)}}{2} = \frac{\mathring{\kappa}}{2}, && (\underline{\text{no}} \text{ summation over } \alpha),\\
\kappa_{(n)} &= 0, && \forall n \geq 1.
\end{aligned} \tag{A.27}$$

We note that for the spherical coordinates the two principal curvatures are equal and the same as the mean curvature. Again, dropping the ring accents, the equations in normal direction A.25 stay the same. For the tangential direction, the Christoffel symbol can be replaced by a curvature formulation. Equations A.26 simplify to

$$\begin{aligned}\delta^{-2}: &\quad 0 = {\Sigma^{1\alpha}_{(-1)}}' + g^{\alpha\alpha}_{(0)}\partial_\alpha \Sigma^{\bullet}_{(-2)},\\ \delta^{-1}: &\quad 0 = {\Sigma^{1\alpha}_{(0)}}' + g^{\alpha\alpha}_{(0)}\partial_\alpha \Sigma^{\bullet}_{(-1)} + X g^{\alpha\alpha}_{(1)}\partial_\alpha \Sigma^{\bullet}_{(-2)} + 2\kappa_{(0)}\Sigma^{1\alpha}_{(-1)}.\end{aligned} \tag{A.28}$$

A.7 Charge form

The stress form of the momentum equations A.22 and A.41 can be formulated with respect to the charge density Q using the Poisson equation for the electric potential

$$\delta^2 \frac{1}{\sqrt{g}}\partial_i\left(\sqrt{g}g^{ij}\partial_j\phi\right) + q = 0. \tag{A.29}$$

The two leading orders of this equation read

$$\begin{aligned}\Phi''_{(0)} + Q_{(0)} &= 0,\\ \Phi''_{(1)} + \kappa_{(0)}\Phi'_{(0)} + Q_{(1)} &= 0.\end{aligned} \tag{A.30}$$

As we are especially interested in the $O(\delta^{-1})$-equation in tangential direction, we formulate the stresses

$$\begin{aligned}\Xi^{1\alpha}_{(0)} &= {V^{\alpha}_{(1)}}',\\ \Theta^{1\alpha}_{(0)} &= g^{\alpha\alpha}_{(0)}\left(\Phi'_{(0)}\partial_\alpha\Phi_{(1)} + \Phi'_{(1)}\partial_\alpha\Phi_{(0)}\right) + X g^{\alpha\alpha}_{(1)}\Phi'_{(0)}\partial_\alpha\Phi_{(0)}.\end{aligned} \tag{A.31}$$

We need the three derivatives for the Newton stresses

$$\begin{aligned}{\Xi^{1\alpha}_{(0)}}' &= {V^{\alpha}_{(1)}}'',\\ \partial_\alpha\Xi^{\bullet}_{(-2)} &= -\partial_\alpha P_{(-2)},\\ \partial_\alpha\Xi^{\bullet}_{(-1)} &= -\partial_\alpha P_{(-1)},\end{aligned} \tag{A.32}$$

and for the Maxwell stresses

$$\begin{aligned}{\Theta^{1\alpha}_{(0)}}' &= g^{\alpha\alpha}_{(0)}\left(\Phi''_{(0)}\partial_\alpha\Phi_{(1)} + \Phi'_{(0)}\partial_\alpha\Phi'_{(1)} + \Phi''_{(1)}\partial_\alpha\Phi_{(0)} + \Phi'_{(1)}\partial_\alpha\Phi'_{(0)}\right)\\ &\quad + g^{\alpha\alpha}_{(1)}\Phi'_{(0)}\partial_\alpha\Phi_{(0)} + X g^{\alpha\alpha}_{(1)}\left(\Phi''_{(0)}\partial_\alpha\Phi_{(0)} + \Phi'_{(0)}\partial_\alpha\Phi'_{(0)}\right),\\ \partial_\alpha\Theta^{\bullet}_{(-1)} &= -\left(\Phi'_{(1)}\partial_\alpha\Phi'_{(0)} + \Phi'_{(0)}\partial_\alpha\Phi'_{(1)}\right),\\ \partial_\alpha\Theta^{\bullet}_{(-2)} &= -\Phi'_{(0)}\partial_\alpha\Phi'_{(0)}.\end{aligned} \tag{A.33}$$

Thus, we find for eq. A.28

$$
\begin{aligned}
0 &= \Xi^{1\alpha\,\prime}_{(0)} + 2\kappa_{(0)}\Xi^{1\alpha}_{(-1)} + g^{\alpha\alpha}_{(0)}\partial_\alpha\Xi^{\bullet}_{(-1)} + Xg^{\alpha\alpha}_{(1)}\partial_\alpha\Xi^{\bullet}_{(-2)} \\
&\quad + \Theta^{1\alpha\,\prime}_{(0)} + 2\kappa_{(0)}\Theta^{1\alpha}_{(-1)} + g^{\alpha\alpha}_{(0)}\partial_\alpha\Theta^{\bullet}_{(-1)} + Xg^{\alpha\alpha}_{(1)}\partial_\alpha\Theta^{\bullet}_{(-2)}, \\
0 &= V^{\alpha\,\prime\prime}_{(1)} + 2\kappa_{(0)}V^{\alpha\,\prime}_{(0)} - g^{\alpha\alpha}_{(0)}\partial_\alpha P_{(-1)} - Xg^{\alpha\alpha}_{(1)}\partial_\alpha P_{(-2)} \\
&\quad + g^{\alpha\alpha}_{(0)}\left(\Phi''_{(0)}\partial_\alpha\Phi_{(1)} + \cancelto{*}{\Phi'_{(0)}\partial_\alpha\Phi'_{(1)}} + \Phi''_{(1)}\partial_\alpha\Phi_{(0)} + \cancelto{**}{\Phi'_{(1)}\partial_\alpha\Phi'_{(0)}}\right) \\
&\quad + g^{\alpha\alpha}_{(1)}\Phi'_{(0)}\partial_\alpha\Phi_{(0)} + Xg^{\alpha\alpha}_{(1)}\left(\Phi''_{(0)}\partial_\alpha\Phi_{(0)} + \cancelto{***}{\Phi'_{(0)}\partial_\alpha\Phi'_{(0)}}\right) \\
&\quad + 2\kappa_{(0)}g^{\alpha\alpha}_{(0)}\Phi'_{(0)}\partial_\alpha\Phi_{(0)} - g^{\alpha\alpha}_{(0)}\left(\cancelto{**}{\Phi'_{(1)}\partial_\alpha\Phi'_{(0)}} + \cancelto{*}{\Phi'_{(0)}\partial_\alpha\Phi'_{(1)}}\right) - \cancelto{***}{Xg^{\alpha\alpha}_{(1)}\Phi'_{(0)}\partial_\alpha\Phi'_{(0)}}, \\
0 &= V^{\alpha\,\prime\prime}_{(1)} + 2\kappa_{(0)}V^{\alpha\,\prime}_{(0)} - g^{\alpha\alpha}_{(0)}\partial_\alpha P_{(-1)} - Xg^{\alpha\alpha}_{(1)}\partial_\alpha P_{(-2)} \\
&\quad + g^{\alpha\alpha}_{(0)}\left(\Phi''_{(0)}\partial_\alpha\Phi_{(1)} + \Phi''_{(1)}\partial_\alpha\Phi_{(0)}\right) + g^{\alpha\alpha}_{(1)}\Phi'_{(0)}\partial_\alpha\Phi_{(0)} + Xg^{\alpha\alpha}_{(1)}\Phi''_{(0)}\partial_\alpha\Phi_{(0)} + 2\kappa_{(0)}g^{\alpha\alpha}_{(0)}\Phi'_{(0)}\partial_\alpha\Phi_{(0)}.
\end{aligned}
\tag{A.34}
$$

We plug in the Poisson equation A.30 and find

$$
\begin{aligned}
0 &= V^{\alpha\,\prime\prime}_{(1)} + 2\kappa_{(0)}V^{\alpha\,\prime}_{(0)} - g^{\alpha\alpha}_{(0)}\partial_\alpha P_{(-1)} - Xg^{\alpha\alpha}_{(1)}\partial_\alpha P_{(-2)} \\
&\quad - g^{\alpha\alpha}_{(0)}\left(Q_{(0)}\partial_\alpha\Phi_{(1)} + Q_{(1)}\partial_\alpha\Phi_{(0)}\right) + g^{\alpha\alpha}_{(1)}\Phi'_{(0)}\partial_\alpha\Phi_{(0)} - Xg^{\alpha\alpha}_{(1)}Q_{(0)}\partial_\alpha\Phi_{(0)} + \kappa_{(0)}g^{\alpha\alpha}_{(0)}\Phi'_{(0)}\partial_\alpha\Phi_{(0)}.
\end{aligned}
\tag{A.35}
$$

For a sphere, we find that

$$
\partial_1 g^{\alpha\alpha} = -\kappa g^{\alpha\alpha} \tag{A.36}
$$

which reads at leading order

$$
g^{\alpha\alpha}_{(1)} = -\kappa_{(0)}g^{\alpha\alpha}_{(0)}. \tag{A.37}
$$

Thus, equation A.35 reads

$$
\begin{aligned}
0 &= V^{\alpha\,\prime\prime}_{(1)} + 2\kappa_{(0)}V^{\alpha\,\prime}_{(0)} - g^{\alpha\alpha}_{(0)}\partial_\alpha P_{(-1)} - Xg^{\alpha\alpha}_{(1)}\partial_\alpha P_{(-2)} \\
&\quad - g^{\alpha\alpha}_{(0)}\left(Q_{(0)}\partial_\alpha\Phi_{(1)} + Q_{(1)}\partial_\alpha\Phi_{(0)}\right) - Xg^{\alpha\alpha}_{(1)}Q_{(0)}\partial_\alpha\Phi_{(0)}.
\end{aligned}
\tag{A.38}
$$

A.8 Integration of the Maxwell shear stress at $O(1)$

We integrate the Maxwell shear stress

$$
\begin{aligned}
&\int_{-\infty}^{\infty}\Theta^{1\alpha\,\prime}_{(0)}\mathrm{d}X \\
&= \left[g^{\alpha\alpha}_{(0)}\left(\cancel{\Phi'_{(0)}\partial_\alpha\Phi_{(1)}} + \Phi'_{(1)}\partial_\alpha\Phi_{(0)}\right) + \cancel{Xg^{\alpha\alpha}_{(1)}\Phi'_{(0)}\partial_\alpha\Phi_{(0)}}\right]^{\infty}_{-\infty}.
\end{aligned}
\tag{A.39}
$$

The remaining term is equivalent to the J_0-proportional term in equation 5.95 by Mori and Young (2018).
We now integrate the term which is neglected in the momentum balance by Mori and

Young (2018), equation 5.87

$$\begin{aligned}
&\int_{-\infty}^{\infty} -X g_{(1)}^{\alpha\alpha} Q_{(0)} \partial_\alpha \Phi_{(0)} \mathrm{d}X \\
=&g_{(1)}^{\alpha\alpha} \partial_\alpha \Phi_{(0)} \int_{-\infty}^{\infty} X \Psi'' \mathrm{d}X \\
=&g_{(1)}^{\alpha\alpha} \partial_\alpha \Phi_{(0)} \left(\left[X \Psi' \right]_{-\infty}^{\infty} - \int_{-\infty}^{\infty} \Psi' \mathrm{d}X \right) \\
=&-\kappa_{(0)} g_{(0)}^{\alpha\alpha} \partial_\alpha \Phi_{(0)} \left[\cancel{X\Psi'} - \Psi \right]_{-\infty}^{\infty} \\
=&\kappa_{(0)} g_{(0)}^{\alpha\alpha} \partial_\alpha \Phi_{(0)} \left[\Psi \right]_{-\infty}^{\infty}.
\end{aligned} \tag{A.40}$$

This term cancels out with the term proportional to κ_0 in equation 5.95 by Mori and Young (2018). Note that the term $-X g_{(1)}^{\alpha\alpha} \partial_\alpha P_{(-2)}$ vanishes as $\partial_\alpha P_{(-2)} = 0$.

A.9 Charge form before the asymptotic expansion

We start with equation A.16 and plug in the stresses from relations A.18 and A.20. After that, we use the Poisson equation A.29 to find the charge form. Splitting up the total stress into Newton and Maxwell stresses in A.16 delivers

$$\begin{aligned}
&\partial_1 \xi^{1\alpha} + \kappa \xi^{1\alpha} + g^{\alpha\beta} \partial_\beta \xi^{\bullet} + 2\Gamma_{1\beta}^{\alpha} \xi^{1\beta} + \frac{1}{\sqrt{g}} \partial_\beta \left(\sqrt{g} \xi^{\blacktriangleleft \alpha\beta} \right) + \Gamma_{\beta\gamma}^{\alpha} \sigma^{\blacktriangleleft \beta\gamma} \\
+&\partial_1 \theta^{1\alpha} + \kappa \theta^{1\alpha} + g^{\alpha\beta} \partial_\beta \theta^{\bullet} + 2\Gamma_{1\beta}^{\alpha} \theta^{1\beta} + \frac{1}{\sqrt{g}} \partial_\beta \left(\sqrt{g} \theta^{\blacktriangleleft \alpha\beta} \right) + \Gamma_{\beta\gamma}^{\alpha} \theta^{\blacktriangleleft \beta\gamma} = 0.
\end{aligned} \tag{A.41}$$

We know that the $\blacktriangleleft$-terms do not contribute to the equations of $O(\delta^{-2})$ and $O(\delta^{-1})$ after the expansion. Thus, we need the stresses

$$\begin{aligned}
\xi^{1\alpha} &= \partial_1 v^\alpha + g^{\alpha\beta} \partial_\beta v^1, \\
\xi^{\bullet} &= -p, \\
\theta^{1\alpha} &= g^{\alpha\beta} \left(\partial_1 \phi \right) \left(\partial_\beta \phi \right), \\
\theta^{\bullet} &= -\frac{1}{2} \left(\left(\partial_1 \phi \right)^2 + g^{\gamma\delta} \left(\partial_\gamma \phi \right) \left(\partial_\delta \phi \right) \right).
\end{aligned} \tag{A.42}$$

The first four terms of the hydrodynamic part read

$$\begin{aligned}
&\partial_1 \xi^{1\alpha} + \kappa \xi^{1\alpha} + g^{\alpha\beta} \partial_\beta \xi^{\bullet} + 2\Gamma_{1\beta}^{\alpha} \xi^{1\beta} \\
=&\partial_{11} v^\alpha + \partial_1 \left(g^{\alpha\beta} \partial_\beta v^1 \right) + \kappa \left(\partial_1 v^\alpha + g^{\alpha\beta} \partial_\beta v^1 \right) - g^{\alpha\beta} \partial_\beta p + 2\Gamma_{1\beta}^{\alpha} \left(\partial_1 v^\beta + g^{\beta\gamma} \partial_\gamma v^1 \right).
\end{aligned} \tag{A.43}$$

For a spherical particle, this formulation simplifies to

$$\begin{aligned}
&\partial_{11} v^\alpha + \partial_1 \left(g^{\alpha\alpha} \partial_\alpha v^1 \right) + \kappa \left(\partial_1 v^\alpha + g^{\alpha\alpha} \partial_\alpha v^1 \right) - g^{\alpha\alpha} \partial_\alpha p + 2\Gamma_{1\alpha}^{\alpha} \left(\partial_1 v^\alpha + g^{\alpha\alpha} \partial_\alpha v^1 \right) \\
=&\partial_{11} v^\alpha + \partial_1 \left(g^{\alpha\alpha} \partial_\alpha v^1 \right) + \kappa \left(\partial_1 v^\alpha + g^{\alpha\alpha} \partial_\alpha v^1 \right) - g^{\alpha\alpha} \partial_\alpha p + \kappa \left(\partial_1 v^\alpha + g^{\alpha\alpha} \partial_\alpha v^1 \right) \\
=&\partial_{11} v^\alpha + \partial_1 \left(g^{\alpha\alpha} \partial_\alpha v^1 \right) + 2\kappa \left(\partial_1 v^\alpha + g^{\alpha\alpha} \partial_\alpha v^1 \right) - g^{\alpha\alpha} \partial_\alpha p.
\end{aligned} \tag{A.44}$$

Equivalently, the first four terms of the electric part read

$$\begin{aligned}
&\partial_1\theta^{1\alpha} + \kappa\theta^{1\alpha} + g^{\alpha\beta}\partial_\beta\theta^\bullet + 2\Gamma^\alpha_{1\beta}\theta^{1\beta} \\
=&\partial_1\left(g^{\alpha\beta}\left(\partial_1\phi\right)\left(\partial_\beta\phi\right)\right) + \kappa g^{\alpha\beta}\left(\partial_1\phi\right)\left(\partial_\beta\phi\right) - \frac{1}{2}g^{\alpha\beta}\partial_\beta\left(\left(\partial_1\phi\right)^2 + g^{\gamma\delta}\left(\partial_\gamma\phi\right)\left(\partial_\delta\phi\right)\right) \\
&+ 2\Gamma^\alpha_{1\beta}g^{\beta\gamma}\left(\partial_1\phi\right)\left(\partial_\gamma\phi\right).
\end{aligned} \tag{A.45}$$

For a spherical particle, this formulation simplifies to

$$\begin{aligned}
&\partial_1\left(g^{\alpha\alpha}\left(\partial_1\phi\right)\left(\partial_\alpha\phi\right)\right) + \kappa g^{\alpha\alpha}\left(\partial_1\phi\right)\left(\partial_\alpha\phi\right) - \frac{1}{2}g^{\alpha\alpha}\partial_\alpha\left(\left(\partial_1\phi\right)^2 + g^{\beta\beta}\left(\partial_\beta\phi\right)\left(\partial_\beta\phi\right)\right) \\
&+ 2\Gamma^\alpha_{1\alpha}g^{\alpha\alpha}\left(\partial_1\phi\right)\left(\partial_\alpha\phi\right) \\
=&\partial_1\left(g^{\alpha\alpha}\left(\partial_1\phi\right)\left(\partial_\alpha\phi\right)\right) + 2\kappa g^{\alpha\alpha}\left(\partial_1\phi\right)\left(\partial_\alpha\phi\right) - \frac{1}{2}g^{\alpha\alpha}\partial_\alpha\left(\left(\partial_1\phi\right)^2 + g^{\beta\beta}\left(\partial_\beta\phi\right)\left(\partial_\beta\phi\right)\right) \\
=&\left(\partial_{11}\phi\right)\left(g^{\alpha\alpha}\partial_\alpha\phi\right) + \partial_1\left(g^{\alpha\alpha}\partial_\alpha\phi\right)\left(\partial_1\phi\right) + 2\kappa g^{\alpha\alpha}\left(\partial_1\phi\right)\left(\partial_\alpha\phi\right) - \frac{1}{2}g^{\alpha\alpha}\partial_\alpha\left(\left(\partial_1\phi\right)^2 + g^{\beta\beta}\left(\partial_\beta\phi\right)\left(\partial_\beta\phi\right)\right).
\end{aligned} \tag{A.46}$$

The Poisson equation A.29 can be rewritten as

$$\delta^2\partial_{11}\phi + \kappa\partial_1\phi + \delta^2\frac{1}{\sqrt{g}}\partial_\alpha\left(\sqrt{g}g^{\alpha\beta}\partial_\beta\phi\right) + q, \tag{A.47}$$

or for a sphere as

$$\partial_{11}\phi = -\delta^{-2}q - \delta^{-1}\kappa\partial_1\phi - \frac{1}{\sqrt{g}}\partial_\alpha\left(\sqrt{g}g^{\alpha\alpha}\partial_\alpha\phi\right). \tag{A.48}$$

We can now replace the second x_1-derivative in the first term of A.46 to find

$$\begin{aligned}
&\left(-\delta^{-2}q - \kappa\partial_1\phi - \frac{1}{\sqrt{g}}\partial_\alpha\left(\sqrt{g}g^{\alpha\alpha}\partial_\alpha\phi\right)\right)\left(g^{\alpha\alpha}\partial_\alpha\phi\right) + \partial_1\left(g^{\alpha\alpha}\partial_\alpha\phi\right)\left(\partial_1\phi\right) \\
&+ 2\kappa g^{\alpha\alpha}\left(\partial_1\phi\right)\left(\partial_\alpha\phi\right) - \frac{1}{2}g^{\alpha\alpha}\partial_\alpha\left(\left(\partial_1\phi\right)^2 + g^{\beta\beta}\left(\partial_\beta\phi\right)\left(\partial_\beta\phi\right)\right) \\
=&-\delta^{-2}qg^{\alpha\alpha}\partial_\alpha\phi + \partial_1\left(g^{\alpha\alpha}\partial_\alpha\phi\right)\left(\partial_1\phi\right) - \frac{1}{2}g^{\alpha\alpha}\partial_\alpha\left(\partial_1\phi\right)^2 \\
&+ \kappa g^{\alpha\alpha}\left(\partial_1\phi\right)\left(\partial_\alpha\phi\right) \\
&- \frac{1}{\sqrt{g}}\partial_\alpha\left(\sqrt{g}g^{\alpha\alpha}\partial_\alpha\phi\right)\left(g^{\alpha\alpha}\partial_\alpha\phi\right) - \frac{1}{2}g^{\alpha\alpha}\partial_\alpha\left(g^{\beta\beta}\left(\partial_\beta\phi\right)\left(\partial_\beta\phi\right)\right).
\end{aligned} \tag{A.49}$$

After the expansion of the parameters discussed above, the terms

$$-\delta^{-2}qg^{\alpha\alpha}\partial_\alpha\phi + \partial_1\left(g^{\alpha\alpha}\partial_\alpha\phi\right)\left(\partial_1\phi\right) - \frac{1}{2}g^{\alpha\alpha}\partial_\alpha\left(\partial_1\phi\right)^2 \tag{A.50}$$

will appear at order $O(\delta^{-2})$, the term

$$\kappa g^{\alpha\alpha}\left(\partial_1\phi\right)\left(\partial_\alpha\phi\right) \tag{A.51}$$

will appear at order $O(\delta^{-1})$, and the terms

$$-\frac{1}{\sqrt{g}}\partial_\alpha\left(\sqrt{g}g^{\alpha\alpha}\partial_\alpha\phi\right)\left(g^{\alpha\alpha}\partial_\alpha\phi\right) - \frac{1}{2}g^{\alpha\alpha}\partial_\alpha\left(g^{\beta\beta}\left(\partial_\beta\phi\right)\left(\partial_\beta\phi\right)\right) \tag{A.52}$$

will appear at order $O(1)$.

A.10 Equivalence of stress and charge form

We define the Maxwell stress using the electric field $\vec{E}$ with

$$E_i = \partial_i \phi \qquad \text{and} \qquad E^i = g^{ij}\partial_j \phi \tag{A.53}$$

as

$$\theta^{ij} = E^i E^j - \frac{1}{2} g^{ij} E^k E_k. \tag{A.54}$$

The divergence reads

$$\theta^{ij}_{,j} = E^i_{,j} E^j + E^i E^j_{,j} - \frac{1}{2} g^{ij}_{,j} E^k E_k - \frac{1}{2} g^{ij} E^k_{,j} E_k - \frac{1}{2} g^{ij} E^k E_{k,j}. \tag{A.55}$$

We know that derivatives of the metric vanish

$$g^{ij}_{,j} = g_{ij,j} = 0. \tag{A.56}$$

Furthermore, the electric field is irrotational, i.e.

$$\begin{aligned} E_{k,j} &= \partial_j E_k + \Gamma^l_{kj} E_l = \partial_{jk}\phi + \Gamma^l_{kj} E_l = E_{j,k}, \\ E^k_{,j} &= \left(g^{kl} E_l\right)_{,j} = g^{kl} E_{l,j} = g^{kl} E_{j,l}. \end{aligned} \tag{A.57}$$

Now, we can rewrite equation A.55 and find

$$\begin{aligned} \theta^{ij}_{,j} &= E^i_{,j} E^j + E^i E^j_{,j} - \frac{1}{2} g^{ij} g^{kl} E_{j,l} E_k - \frac{1}{2} g^{ij} E^k E_{j,k} \\ &= E^i_{,j} E^j + E^i E^j_{,j} - \frac{1}{2} \left(g^{ij} E_j\right)_{,l} \left(g^{kl} E_k\right) - \frac{1}{2} E^k \left(g^{ij} E_j\right)_{,k} \\ &= E^i_{,j} E^j + E^i E^j_{,j} - \frac{1}{2} E^i_{,l} E^l - \frac{1}{2} E^k E^i_{,k} \\ &= \cancel{E^i_{,j} E^j} + E^i E^j_{,j} \cancel{- \frac{1}{2} E^i_{,j} E^j - \frac{1}{2} E^j E^i_{,j}} \\ &= E^i E^j_{,j} = -\delta^{-2} q E^i \end{aligned} \tag{A.58}$$

We compare this to equation A.2 by plugging in the electric field

$$\begin{aligned} &\theta^{ij}_{,j} \\ =&\partial_j \theta^{ij} + \Gamma^j_{jk}\theta^{ik} + \Gamma^i_{jk}\theta^{jk} \\ =&\partial_j \left(E^i E^j - \frac{1}{2} g^{ij} E^k E_k\right) + \Gamma^j_{jk}\left(E^i E^k - \frac{1}{2} g^{ik} E^l E_l\right) + \Gamma^i_{jk}\left(E^j E^k - \frac{1}{2} g^{jk} E^l E_l\right) \\ =&\partial_j E^i E^j + E^i \partial_j E^j - \frac{1}{2}\partial_j g^{ij} E^k E_k - \frac{1}{2} g^{ij}\partial_j E^k E_k - \frac{1}{2} g^{ij} E^k \partial_j E_k \\ &+ \Gamma^j_{jk}\left(E^i E^k - \frac{1}{2} g^{ik} E^l E_l\right) + \Gamma^i_{jk}\left(E^j E^k - \frac{1}{2} g^{jk} E^l E_l\right). \end{aligned} \tag{A.59}$$

We summarize the derivatives

$$\begin{aligned}
\partial_j E^i &= E^i_{,j} - \Gamma^i_{jk} E^k, \\
\partial_j E^j &= E^j_{,j} - \Gamma^j_{jk} E^k, \\
\partial_j E^k &= E^j_{,k} - \Gamma^k_{jl} E^l, \\
\partial_j E_k &= E_{j,k} + \Gamma^l_{jk} E_l, \\
\partial_j g^{ij} &= g^{ij}_{,j} - \Gamma^j_{jk} g^{ik} - \Gamma^i_{jk} g^{jk},
\end{aligned} \tag{A.60}$$

and find

$$\begin{aligned}
=& E^i_{,j} E^j + E^i E^j_{,j} - \frac{1}{2} g^{ij}_{,j} E^k E_k - \frac{1}{2} g^{ij} E^k_{,j} E_k - \frac{1}{2} g^{ij} E^k E_{k,j} \\
& - \Gamma^i_{jk} E^k E^j - \Gamma^j_{jk} E^k E^i + \left(-\Gamma^j_{jk} g^{ik} - \Gamma^i_{jk} g^{jk}\right) \left(-\frac{1}{2} E^l E_l\right) + \frac{1}{2} g^{ij} \Gamma^k_{jl} E^l E_k - \frac{1}{2} g^{ij} \Gamma^l_{jk} E_l E^k \\
& + \Gamma^j_{jk} \left(E^i E^k - \frac{1}{2} g^{ik} E^l E_l\right) + \Gamma^i_{jk} \left(E^j E^k - \frac{1}{2} g^{jk} E^l E_l\right) \\
=& E^i_{,j} E^j + E^i E^j_{,j} - \frac{1}{2} g^{ij} E^k_{,j} E_k - \frac{1}{2} g^{ij} E^k E_{k,j} \\
& \cancel{-\Gamma^i_{jk} E^k E^j}^{*} - \cancel{\Gamma^j_{jk} E^k E^i}^{**} + \cancel{\frac{1}{2} \Gamma^j_{jk} g^{ik} E^l E_l}^{***} + \cancel{\frac{1}{2} \Gamma^i_{jk} g^{jk} E^l E_l}^{(4*)} \\
& + \cancel{\frac{1}{2} g^{ij} \Gamma^k_{jl} E^l E_k}^{(5*)} \cancel{-\frac{1}{2} g^{ij} \Gamma^l_{jk} E_l E^k}^{(5*)} \\
& + \cancel{\Gamma^j_{jk} E^i E^k}^{**} \cancel{-\frac{1}{2} \Gamma^j_{jk} g^{ik} E^l E_l}^{***} + \cancel{\Gamma^i_{jk} E^j E^k}^{*} \cancel{-\frac{1}{2} \Gamma^i_{jk} g^{jk} E^l E_l}^{(4*)} \\
=& E^i_{,j} E^j + E^i E^j_{,j} - \frac{1}{2} g^{ij} E^k_{,j} E_k - \frac{1}{2} g^{ij} E^k E_{k,j}.
\end{aligned} \tag{A.61}$$

APPENDIX B

The strong vs. weak electrolyte limit for moderate Péclet numbers

In the field of electrohydrodynamics, the explicit treatment of the reaction terms

$$\begin{aligned} \mathcal{R}_{\pm} &= \frac{\mathrm{Da}}{\alpha}\left(k_{\mathrm{d}} s - k_{\mathrm{a}} c_{+} c_{-}\right), \\ \mathcal{R}_{s} &= -\mathrm{Da}\left(k_{\mathrm{d}} s - k_{\mathrm{a}} c_{+} c_{-}\right) \end{aligned} \tag{B.1}$$

in the charge and salt transport equations is avoided. The set of nondimensional equations (cp. equations 4.10)

$$\begin{aligned} \mathrm{Pe}_{\pm}\left(\partial_t c_{\pm} + \left(\vec{\nabla}\cdot\vec{v}\right) c_{\pm}\right) + \vec{\nabla}\cdot\vec{j}_{\pm} &= \frac{\mathrm{Da}}{\alpha}\left(k_{\mathrm{d}} s - k_{\mathrm{a}} c_{+} c_{-}\right), \\ \mathrm{Pe}\left(\partial_t s + \left(\vec{\nabla}\cdot\vec{v}\right) s\right) &= -\mathrm{Da}\left(k_{\mathrm{d}} s - k_{\mathrm{a}} c_{+} c_{-}\right), \\ -\delta^2\nabla^2\phi &= q. \\ \vec{\nabla}\cdot\sigma &= \vec{0}, \\ \vec{\nabla}\cdot\vec{v} &= 0, \end{aligned} \tag{B.2}$$

can be simplified with two fundamentally strategies, i.e. assuming weak or strong electrolytic solutions. For weak electrolytes, the ratio of ion and salt concentrations is assumed to be small $\alpha \ll 1$, and for strong electrolytes we assume $\alpha \gg 1$.

In this appendix, we compare these two approaches. For that purpose, we first take one of the two above limits and use the assumption of small Debye layers $\delta \ll 1$ thereafter. The Péclet number is in both cases assumed to be of order unity $\mathrm{Pe} \sim O(1)$. The difference of the charge transport equations delivers on both cases an equation for the charge density q that is independent of the reaction term and reads (compare equation B.3)

$$\mathrm{Pe}\left(\partial_t q + \left(\vec{\nabla}\cdot\vec{v}\right) q\right) + \vec{\nabla}\cdot\vec{j}_q = 0. \tag{B.3}$$

We will also need the charge fluxes as derived in equations 4.12

$$\begin{aligned}\vec{j}_{\pm} &= D_{\pm}\left(-\vec{\nabla}c_{\pm} \mp c_{\pm}\vec{\nabla}\phi\right),\\ \vec{j}_{q} &= -\vec{\nabla}\left(D_{+}c_{+} - D_{-}c_{-}\right) - \left(D_{+}c_{+} + D_{-}c_{-}\right)\vec{\nabla}\phi.\end{aligned} \tag{B.4}$$

Finally, we only consider one phase with the reaction equilibrium constant $K = 1$. However, the following discussion can be easily copied for a two-phase problem. We also focus on the equations governing the charge and distributions and the electric potential, as the other equations transform equivalently.

The weak electrolyte limit $\alpha \ll 1$
The assumption on α delivers for the charge transport in B.2 that

$$k_{\mathrm{d}}s - k_{\mathrm{a}}c_{+}c_{-} = 0, \tag{B.5}$$

which is equivalent to

$$Ks - c_{+}c_{-} = 0. \tag{B.6}$$

The salt transport then reads

$$\partial_t s + \left(\vec{\nabla}\cdot\vec{v}\right)s = 0. \tag{B.7}$$

Together with the assumption on uniform salt distribution far away from the surface, we find that $s = 1$. Thus, the algebraic equation B.6 simplifies to

$$c_{+}c_{-} = 1. \tag{B.8}$$

The second equation for the charges is the transport relation for the charge density B.3.

The strong electrolyte limit $\alpha \gg 1$
The assumption that α is large delivers from B.2

$$\mathrm{Pe}_{\pm}\left(\partial_t c_{\pm} + \left(\vec{\nabla}\cdot\vec{v}\right)c_{\pm}\right) + \vec{\nabla}\cdot\vec{j}_{\pm} = 0. \tag{B.9}$$

We note that transport relation for the charge density B.3 also holds in this case.

The thin-Debye-layer limit $\delta \ll 1$
With the assumption of a thin small Debye layer, the Poisson equation delivers in the outer region $q_{(0)} = q_{(1)} = 0$. Thus, the ion distributions are equal at the two leading orders $c_{+(0,1)} = c_{-(0,1)} =: c_{(0,1)}$. Equation B.3 reads

$$\begin{aligned}\vec{\nabla}\cdot\vec{j}_{q(0,1)} &= \vec{\nabla}\cdot\left(-\vec{\nabla}\left(D_{+}c_{+(0,1)} - D_{-}c_{-(0,1)}\right) - \left(D_{+}c_{+(0,1)} + D_{-}c_{-(0,1)}\right)\vec{\nabla}\phi\right)\\ &= \vec{\nabla}\cdot\left(-D_{\Delta}\vec{\nabla}c_{(0,1)} - c_{(0,1)}\vec{\nabla}\phi\right).\end{aligned} \tag{B.10}$$

In the absence of charge sources / sinks and outer charge gradients, this transport equation delivers $c_{(0,1)} = c_{\pm(0,1)} = 1$ for both weak, and strong electrolytes. In the next step, we

consider the equations inside the Debye layer with the rescaled coordinate $x^1 = \delta X$. The equivalent of relation B.3 still holds for both electrolyte strengths and reads

$$\mathrm{Pe}_{(0)} \left(\partial_t Q + \left(\vec{\nabla} \cdot \vec{V} \right) Q \right) + \vec{\nabla} \cdot \vec{J}_Q = 0, \tag{B.11}$$

with

$$\begin{aligned} Q &\sim Q_{(0)} + \delta Q_{(1)} + \dots, \\ C_\pm &\sim C_{\pm(0)} + \delta C_{\pm(1)} + \dots, \\ V &\sim V_{(0)} + \delta V_{(1)} + \dots, \\ \vec{J}_Q &\sim \vec{J}_{Q(-1)} + \delta \vec{J}_{Q(0)} + \dots. \end{aligned} \tag{B.12}$$

Thus, the two leading orders of this equation read

$$\begin{aligned} \partial_X \vec{J}_{Q(-1)} &= 0, \\ \partial_X \vec{J}_{Q(0)} &= 0. \end{aligned} \tag{B.13}$$

The second equation for the charges is discussed separately

The weak electrolyte limit $\alpha \ll 1$
We find from equation B.8 that for the leading two orders the relation

$$C_+ C_- = 1 \tag{B.14}$$

holds, which can be expanded in the orders

$$\begin{aligned} C_{+(0)} C_{-(0)} &= 1, \\ C_{+(1)} C_{-(0)} + C_{+(0)} C_{-(1)} &= 0. \end{aligned} \tag{B.15}$$

The strong electrolyte limit $\alpha \gg 1$
We find from equation B.9 that for the leading two orders the relation

$$\partial_X J^1_\pm = 0 \tag{B.16}$$

holds. An integration with respect to X and the boundary condition $\lim_{X \to \infty} J^1_\pm = j^1_\gamma$ delivers

$$\begin{aligned} j^1_\gamma &= J^1_\pm, \\ j^1_\gamma &= -\partial_X C_\pm \mp C_\pm \partial_X \Phi. \end{aligned} \tag{B.17}$$

The solutions to the two leading orders of this equation are discussed in sections 4.2.1 and 4.2.2. They read

$$\begin{aligned} C_{\pm(0)} &= e^{\mp \Psi}, \\ C_{\pm(1)} &= \mp \left(\Phi_{(1)} \pm j^1_{\gamma(0)} E_\pm \right) e^{\mp \Psi}. \end{aligned} \tag{B.18}$$

We note that the solutions B.18 fulfill the leading order of B.15. However, when plugging them into the next order, we find an estimate of the difference between both descriptions

$$\begin{aligned} \text{residual} &= C_{+(1)} C_{-(0)} + C_{+(0)} C_{-(1)} \\ &= -\left(\Phi_{(1)} + j^1_{\gamma(0)} E_+ \right) + \left(\Phi_{(1)} - j^1_{\gamma(0)} E_- \right) \\ &= -j^1_{\gamma(0)} \left(E_+ + E_- \right). \end{aligned} \tag{B.19}$$

As a result, the solutions for the electric charges $C_{\pm(1)}$ and the potential $\Phi_{(1)}$ of $O(\delta)$ differ between the two models. The effective jump conditions of normal and shear stress are also different.

APPENDIX C

UML diagram of the spectral solver

The algorithm illustrated in the diagram 5.2 is implemented in Python as displayed in the UML diagram C.1. As discussed in section 5.3 in detail, it is split up in pre-processing, the solution, and a post-processing step.

The pre-processing is performed in the "actuator" class. Parameter assignment, meshing, and inversion of time-independent system matrices are contained here.

The time integration is performed by the class "solution_methods" which is split up in sub-classes for the solution of the electric PNP problem (Gummel's iteration and influence matrix method as discussed in sections 5.3.5 and 5.3.4) and the flow problem for the stream function (cp. sections 5.3.6). In another sub-class the nonlinear Coulomb-force terms of the charge balances are computed.

The "analysis"-class contains all post-processing steps (cp. section 5.4), such as the computation of dissipation and efficiency. Additionally, the termination mechanism is contained in this class.

Figure C.1: UML diagram of the solver displaying selected classes and sub-classes.

APPENDIX D

Patent graphics

This chapter delivers a collection of graphics that were already published in the patent applications Marthaler and Class (2022a, 2022b). Those illustrate the physical and functional structures of the lab system. They are sorted by their structural level (compare Figure 6.2).

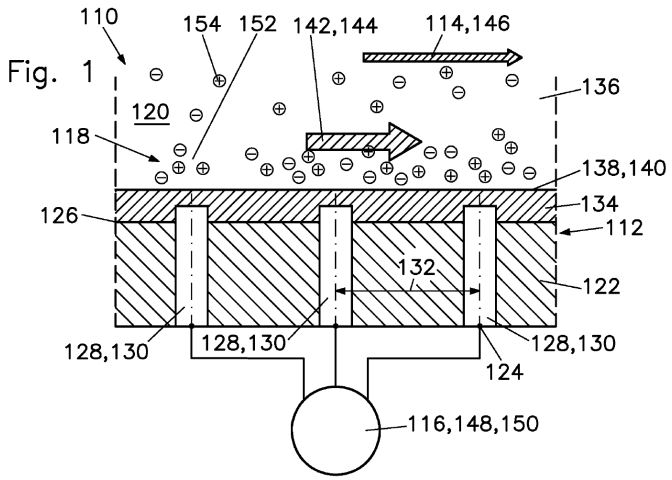

Figure D.1: Working principle of the actuator (Marthaler & Class, 2022b).

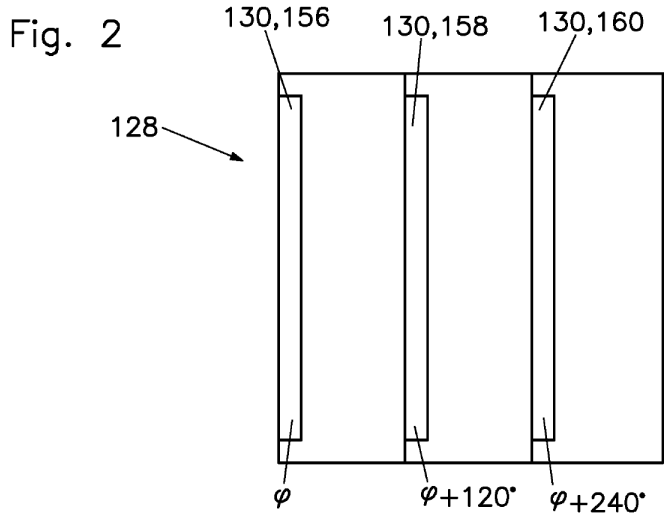

Figure D.2: One-dimensional actuator of three electrodes with a 120° phase shift (Marthaler & Class, 2022b).

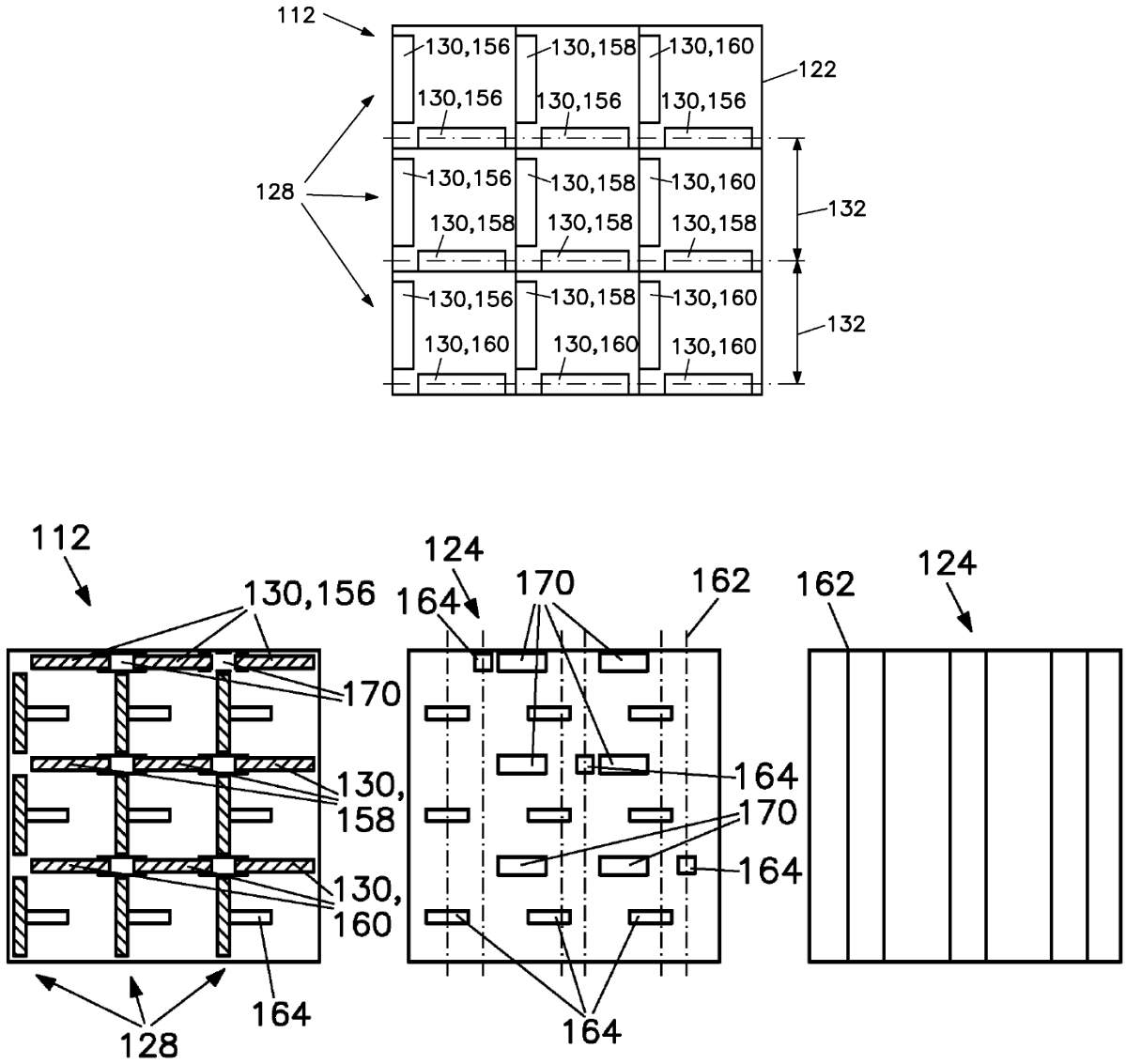

Figure D.3: Two-dimensional actuator consisting of 18 electrodes in the top level which is in contact with the fluid. The bottom graphics illustrate the wiring of the electrodes in the three sublevels (from sublevel 1 on the left to sublevel 3 on the right). At the third sublevel, three different wires with separate voltages are connected. In sublevel 1 and 2, these three phases are connected to six electrodes each (Marthaler & Class, 2022b).

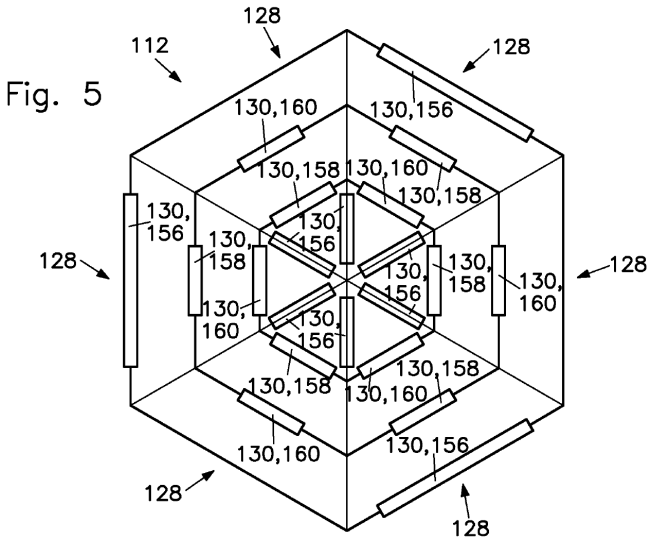

Figure D.4: Hexagonal actuator that allows three independent flow directions as an alternative to the one way actuator in figures D.2 and D.3 (Marthaler & Class, 2022b).

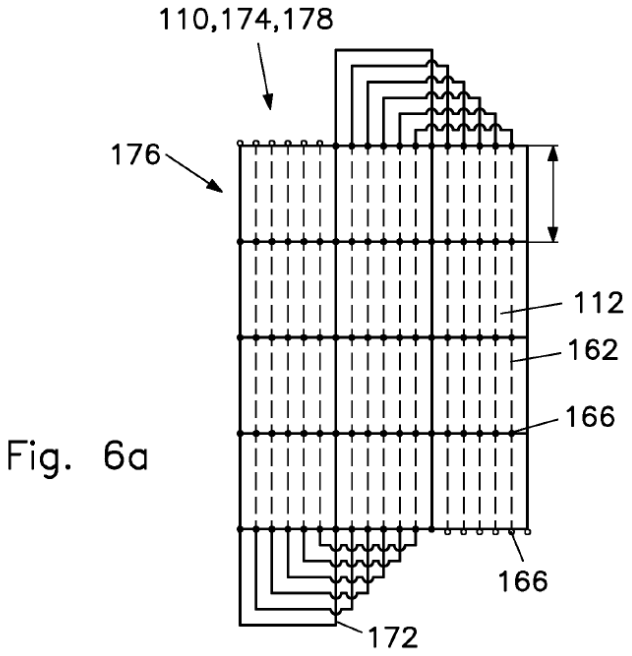

Figure D.5: Clustering of single actuators to synchronized pixels. These pixels consist of actuators that cannot be controlled individually but as a set. The wires at sublevel 3 (compare Figure D.3) form a serpentine pattern connecting all actuators in the pixel (Marthaler & Class, 2022b).

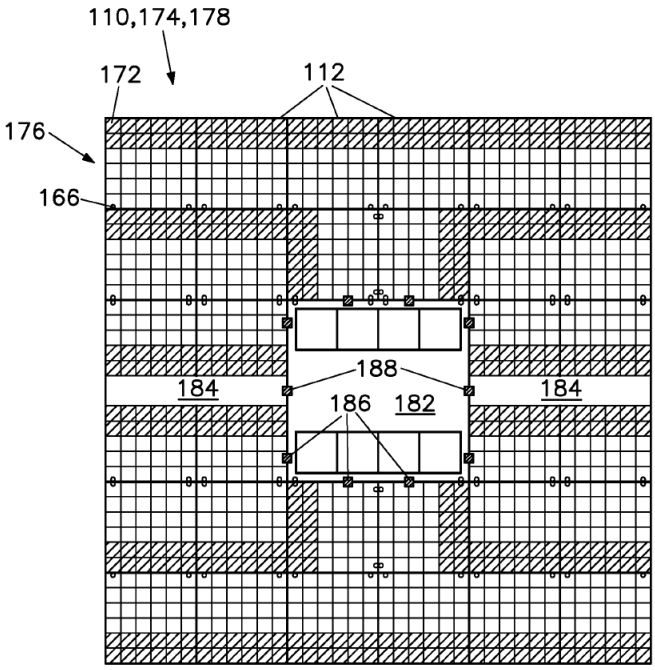

Figure D.6: Control unit for several pixels (synchronized actuators). Between the flow areas, control units are arranged distributing the control information to the single pixels. One control control unit is typically connected to 8 pixels. The input information to the control unit is provided by a data BUS (Marthaler & Class, 2022b).

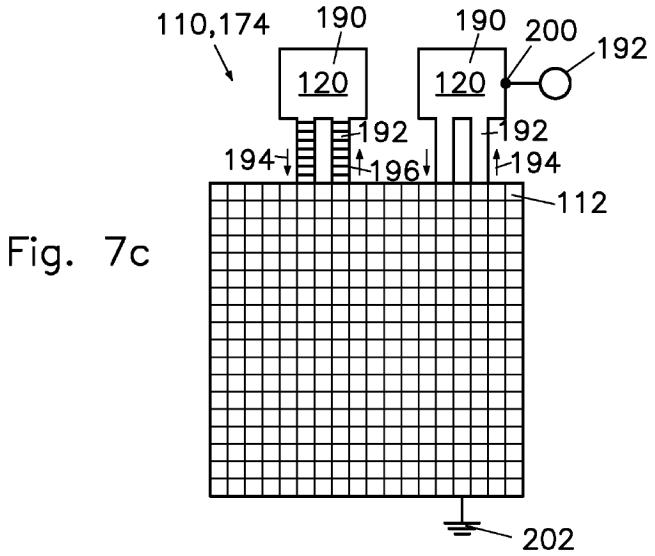

Fig. 7c

Figure D.7: Chip structure consisting of several pixels arranged in a matrix array. Each square box presents one element as displayed in Figure D.6, consisting of a control unit and eight pixels. Attached to the chip are several reservoirs. Liquids can be exchanged via channels between the reservoirs and the chip (Marthaler & Class, 2022b).

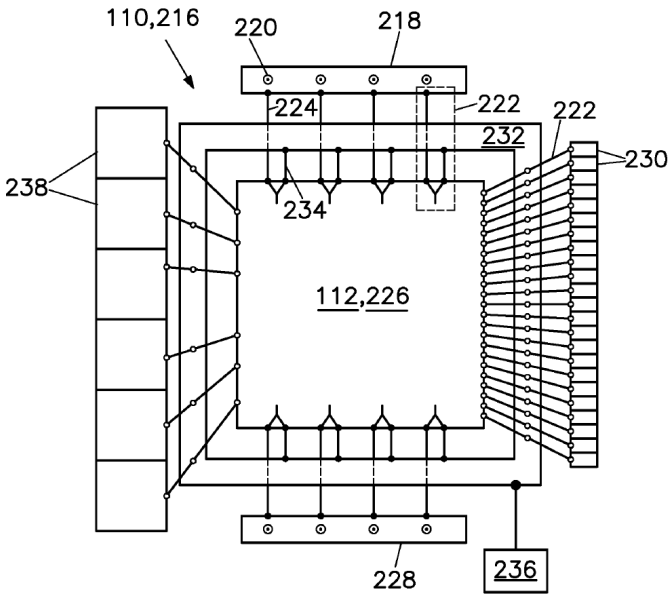

Figure D.8: Lab with the chip surface in the center. A liquid channel en-circulating the chip surface provides continuous availability of carrier fluid. The memory elements on the right are used to store probes. the in- and outlets at the top and the bottom allow for exchange of probes or waste fluids. On the right, add-on elements, such as centrifuges, heaters etc. can be attached (Marthaler & Class, 2022b).

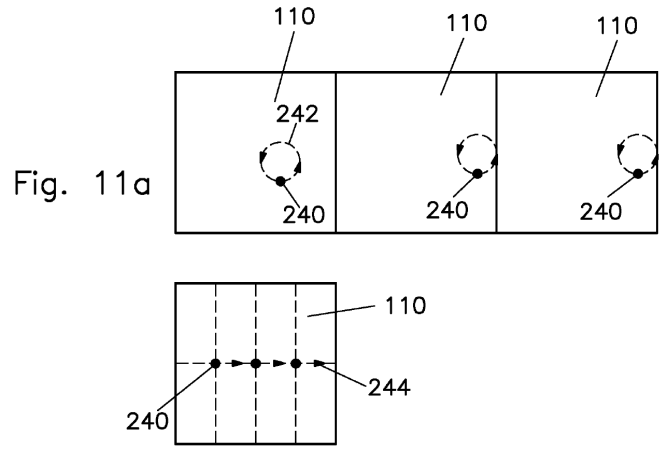

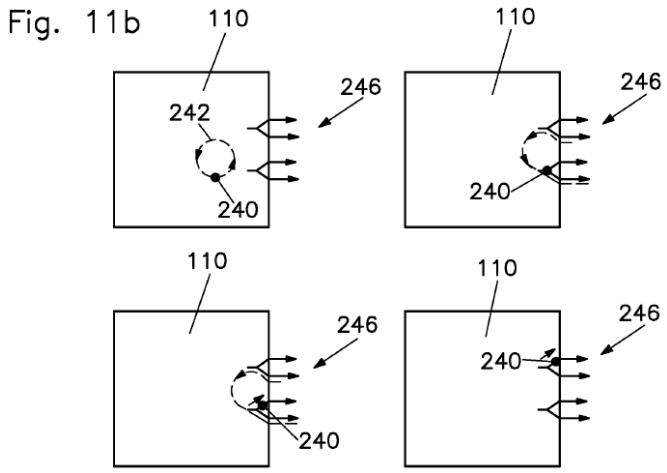

Figure D.9: Sample transport on the chip surface. In order to avoid unwanted recirculation zones on the chip surface, circular elements of carrier fluid are moved with constant speed. Thus, mass continuity is fulfilled. The top row of three images shows the sample (black dot) and the respective fluid flow along the dashed line. The image below shows the respective path of the sample. The bottom four pictures illustrate the sample transport near the boundary. The Y-form allows separate transport of sample and carrier fluid into two channels (Marthaler & Class, 2022b).

Graphics legend

110 system

112 arrangement for generating liquid flows

114 liquid flow

116 system providing electric voltages

118 electrically charged particles

120 liquid

122 substrate

124 controllable elements

126 substrate surface

128 electrode triplets

130 electrode

132 distance between electrodes

134 isolating layer

136 flow domain

138 flat surface (at level height)

140 plane surface (smooth)

142 component of the electric field

144 force

146 direction

148 electric power source for multi-phase currents

150 generator for multi-phase currents

152 region with charge unbalances

154 neutral region

156 first electrode

158 second electrode

160 third electrode

162 electric wire

164 electric connection for an electrode

166 electrical connection for the driving element

168 boundary

170 additional electrical connection

172 electrical connector

174 matrix array

176 row

178 column

180 electrical wire

182 control unit

184 data BUS

186 connector to the arrangement

188 connector to the data BUS

190 liquid reservoir

192 connecting channel

194 flow direction

196 multiple electrodes

198 voltage source

200 connector

202 grounding

204 active control unit

206 micro processor

208 storage element

210 analog switch

212 register level

214 input signal

216 liquid machine

218 inlet

220 pipet inlet

222 add-on element

224 liquid channel

226 liquid process unit

228 outlet

230 storage element

232 storage element

234 inner liquid reservoir

236 outer liquid reservoir

238 add-on element

240 diffuse sample

242 streaming pipe

244 west-east direction

246 outlet

248 method for manufacturing a system

250 fabrication of the arrangement

252 providing the substrate

254 providing control elements

256 providing electrode triplets

258 treatment of the substrate surface

260 integration of the system providing electric voltages

Publications

Articles

Marthaler, P. G., Class, A. G., Mori, Y., Young, Y. (2023). From electrodiffusion theory to the electrohydrodynamics of leaky dielectrics through the weak electrolyte limit – CORRIGENDUM. *J. Fluid Mech. 962*, E1. doi: 10.1017/jfm.2023.306

Liu, D., **Marthaler, P. G.**, Class, A. G., Long, G. (2023). Simulation of Stratification Phenomena with a Spectral Fourier-Chebyshev Method on the Background of a Lead-Cooled Fast Reactor. *Ann. Nucl. Energy, 192*, 109931. doi: 10.1016/j.anucene.2023.109931

Marthaler, P. G., & Class, A. G. (2022). Weak curvature asymptotics for Debye layers as electrohydrodynamic discontinuities. *Phys. Rev. E, 105(3).* 035106. doi: 10.1103/PhysRevE.105.035106

Marthaler, P. G., & Class, A. G. (2021). Integral effects of the Debye layer on a sedimenting particle with zeta-potential variations. *PAMM 21*(1), e202100209. doi: 10.1002/pamm.202100209

Marthaler, P. G., & Class, A. G. (2021): Integral jump conditions for singular problems–applied to Debye-layer phenomena. *PAMM 20*(1), e202000044. doi: 10.1002/ pamm.202000044

Albers, A., Marthaler, F., Orsolani Uhlig, E., **Marthaler, P. G.**, Kühfuss D., Strauch, M., Siebe A., & Bursac, N. (2019). Strategic potential identification for enabling an overarching generational product development: A qualitative study in the Live-Lab IP – Integrated product engineering. *SSP – Stuttgarter Symposium für Produktentwicklung SSP 2019*, 232–242

Conference Talks

Marthaler, P. G., & Class, A. G. (2022). *A Fourier-Chebyshev non-interpolating method for the direct numerical simulation of two-dimensional wall-induced electrokinetic flow.* Indianapolis, IN. (75th APS-DFD Meeting)

Marthaler, P. G., & Class, A. G. (2021). *An integral analysis in tensorial notation for streaming-potential phenomena.* Phoenix, AZ/virtual. (74th APS-DFD Meeting)

Marthaler, P. G., & Class, A. G. (2021). *Integral effects of the Debye layer on a sedimenting particle with zeta-potential variations.* Kassel/virtual. (GAMM, 91st Annual Meeting)

Marthaler, P. G., & Class, A. G. (2020). *Integral jump conditions for time-dependent Debye layer phenomena.* Chicago, IL/virtual. (73rd APS-DFD Meeting)

Patent Publications (Pending and Awarded Patents)

Marthaler, P. G., & Class, A. G. (2022): *Arrangement, system and method for generating liquid flows* (WO 2022/112474 A1, pending, submitted Nov 27, 2020). World Intellectual Property Organization

Marthaler, P. G., & Class, A. G. (2022): *Anordnung und System zur Erzeugung von Flüssigkeitsströmen* (DE 10 2020 214 957 A1, pending, submitted Nov 27, 2020). Deutsches Patent- und Markenamt

Marthaler, P. G., Boeck, A., Faltlhauser, V., Gallenschütz, K., Neuhorst, P., Steimer, S. (2020): *Fahrzeugtür und Fahrzeug mit zumindest einer Fahrzeugtür* (DE 10 2018 211 963 A1), Deutsches Patent- und Markenamt

Marthaler, P. G., Cocoma, A., Faltlhauser, V., Gallenschütz, K., Neuhorst, P., Steimer, S. (2019): *Fahrzeug mit einer Fahrzeugkarosserie und zumindest einer Fahrzeugtür* (DE 10 2018 202 386 A1), Deutsches Patent- und Markenamt

Bibliography

Albala, J. S. (2001). Array-based proteomics: the latest chip challenge. *Expert Review of Molecular Diagnostics*, *1*(2), 145–152. doi: 10.1586/14737159.1.2.145

Albers, A., Braun, A., Sadowski, E., Wynn, D. C., Wyatt, D. F., & John Clarkson, P. (2011). System Architecture Modeling in a Software Tool Based on the Contact and Channel Approach (C&C-A). *Journal of Mechanical Design*, *133*(10). doi: 10.1115/1.4004971

Albers, A., Bursac, N., & Wintergerst, E. (2015a). Product Generation Development – Importance and Challenges from a Design Research Perspective. In *Proceedings of the International Conference on Theoretical Mechanics and Applied Mechanics* (Vol. 13, pp. 16–21). Vienna.

Albers, A., Bursac, N., & Wintergerst, E. (2015b). Produktgenerationsentwicklung – Bedeutung und Herausforderungen aus einer entwicklungsmethodischen Perspektive. In *Stuttgarter Symposium für Produktentwicklung* (pp. 1–10). Stuttgart: Fraunhofer Verlag.

Albers, A., Dumitrescu, R., Marthaler, F., Strauch, M., Kuehfuss, D., Siebe, D., & Bursac, N. (2018). PGE-Product Generation Engineering and Foresight: A systematic consideration to determine the interrelationships. In *14. Symposium für Vorausschau und Technologieplanung.* Berlin.

Albers, A., Rapp, S., Birk, C., & Bursac, N. (2017). Die Frühe Phase der PGE – Produktgenerationsentwicklung. In *4. Stuttgarter Symposium für Produktentwicklung 2017 (SSP).* Stuttgart: Fraunhofer Verlag.

Albers, A., Rapp, S., Spadinger, M., Richter, T., Birk, C., Marthaler, F., ... Wessels, H. (2019). The Reference System in the Model of PGE: Proposing a Generalized Description of Reference Products and their Interrelations. *Proceedings of the Design Society: International Conference on Engineering Design*, *1*(1), 1693–1702. doi: 10.1017/dsi.2019.175

Albers, A., & Wintergerst, E. (2014). The Contact and Channel Approach (C&C2-A): Relating a System's Physical Structure to Its Functionality. In A. Chakrabarti & L. T. M. Blessing (Eds.), *An Anthology of Theories and Models of Design: Philosophy, Approaches and Empirical Explorations* (pp. 151–171). London: Springer. doi: 10.1007/978-1-4471-6338-1_8

Albers, A., & Zingel, C. (2013). Challenges of Model-Based Systems Engineering: A Study towards Unified Term Understanding and the State of Usage of SysML. In M. Abramovici & R. Stark (Eds.), *Smart Product Engineering* (pp. 83–92). Berlin:

Springer. doi: 10.1007/978-3-642-30817-8_9

Ananthanarayanan, V., & Thies, W. (2009). *Towards a High-Level Programming Language for Standardizing and Automating Biology Protocols.* San Francisco. (First International Workshop on Bio-Design Automation)

Aris, R. (1989). *Vectors, tensors, and the basic equations of fluid mechanics / Rutherford Aris.* New York, NY: Dover Publ.

Azizipour, N., Avazpour, R., Rosenzweig, D. H., Sawan, M., & Ajji, A. (2020). Evolution of Biochip Technology: A Review from Lab-on-a-Chip to Organ-on-a-Chip. *Micromachines*, *11*(6), 599. doi: 10.3390/mi11060599

Bahnemann, J., & Grünberger, A. (Eds.). (2022). *Microfluidics in Biotechnology* (1st ed., Vol. 179). Cham: Springer.

Balestra, F., Graef, M., Hayashi, Y., Ishiuchi, H., Conte, T., & Gargini, P. (2021). *International Roadmap for Devices and Systems, 2021 Update, Executive Summary* (Tech. Rep.). Retrieved 2022-07-22, from `https://irds.ieee.org/images/files/pdf/2021/2021IRDS_ES.pdf`

Balu, B., & Khair, A. S. (2020). Dynamic double layer force between charged surfaces. *Physical Review Research*, *2*(1), 013138. doi: 10.1103/PhysRevResearch.2.013138

Barz, D., & Class, A. (2007, August). *Vorrichtung zur Erzeugung von Flüssigkeitsströmungen, Verfahren zu ihrer Herstellung und zu ihrem Betrieb sowie ihre Verwendung* (No. DE 10 2006 004 887 A1). Deutsches Patent- und Markenamt.

Batchelor, G. K. (2010). *An Introduction to fluid dynamics* (14th ed.). Cambridge: Cambridge University Press.

Baygents, J. C., & Saville, D. A. (1990). The circulation produced in a drop by an electric field: A high field strength electrokinetic model. *AIP Conference Proceedings*, *197*(1), 7–17. doi: 10.1063/1.38956

Bazant, M., & Prakash, M. (2013, June). *Multiphase non-linear electrokinetic devices* (No. US 2013/0146459 A1). United States Patent Office.

Bazant, M. Z., Ben, Y., Levitan, J., & Urbanski, J.-P. (2010, May). *Induced-charge electro-osmotic microfluidic devices* (No. US 7 708 873 B2). United States Patent Office.

Bazant, M. Z., & Squires, T. M. (2004). Induced-Charge Electrokinetic Phenomena: Theory and Microfluidic Applications. *Physical Review Letters*, *92*(6), 066101. doi: 10.1103/PhysRevLett.92.066101

Bazant, M. Z., Thornton, K., & Ajdari, A. (2004). Diffuse-charge dynamics in electrochemical systems. *Physical Review E*, *70*(2), 021506. doi: 10.1103/PhysRevE.70.021506

Bender, C. M., & Orszag, S. A. (1999). *Asymptotic methods and perturbation theory* (14th ed., Vol. 1). New York, NY: Springer.

Boyd, J. P. (2000). *Chebyshev and Fourier Spectral Methods* (2nd ed.). Mineola, NY: Dover Publ.

Bég, O. A., Hameed, M., & Bég, T. A. (2013). Chebyshev Spectral Collocation Simulation of Nonlinear Boundary Value Problems in Electrohydrodynamics. *International Journal for Computational Methods in Engineering Science and Mechanics*, *14*(2), 104–115. doi: 10.1080/15502287.2012.698707

Canuto, C. (Ed.). (1988). *Spectral methods in fluid dynamics* (14th ed.). New York, NY:

Springer.

Canuto, C. (Ed.). (2006). *Spectral methods: fundamentals in single domains* (22nd ed.). Berlin: Springer.

Canuto, C. (Ed.). (2007). *Spectral methods: evolution to complex geometries and applications to fluid dynamics* (30th ed.). Berlin: Springer.

Castellanos, A. (Ed.). (1998). *Electrohydrodynamics*. Vienna: Springer.

Center for Systems Science and Engineering (CSSE) at Johns Hopkins University (JHU), n. (2022). *COVID-19 Dashboard*. Retrieved 2022-08-23, from `https://coronavirus.jhu.edu/map.html`

Chapman, D. L. (1913). LI. A contribution to the theory of electrocapillarity. *The London, Edinburgh, and Dublin Philosophical Magazine and Journal of Science*, *25*(148), 475–481. doi: 10.1080/14786440408634187

Checa, M., Millan-Solsona, R., & Gomila, G. (2019). Frequency-dependent force between ac-voltage-biased plates in electrolyte solutions. *Physical Review E*, *100*(2), 022604. doi: 10.1103/PhysRevE.100.022604

Chen, W., Yao, Y., Chen, T., Shen, W., Tang, S., & Lee, H. K. (2021). Application of smartphone-based spectroscopy to biosample analysis: A review. *Biosensors and Bioelectronics*, *172*, 112788. doi: 10.1016/j.bios.2020.112788

Class, A. G., Matkowsky, B. J., & Klimenko, A. Y. (2003). A unified model of flames as gasdynamic discontinuities. *Journal of Fluid Mechanics*, *491*, 11–49. doi: 10.1017/S002211200300507X

Cogez, P., Graef, M., Huizing, B., Mahnkopf, R., Ishiuchi, H., Ikumi, N., ... Choi, J. H. (2013). *International Technology Roadmap for Semiconductors 2013 – Executive Summary* (Tech. Rep.). Retrieved 2022-07-22, from `https://www.dropbox.com/s/k8mllgrc4vzzpbf/2013ExecutiveSummary.pdf?dl=0`

Cox, R. G. (1997). Electroviscous forces on a charged particle suspended in a flowing liquid. *Journal of Fluid Mechanics*, *338*, 1–34. doi: 10.1017/S0022112097004862

Debye, P., & Falkenhagen, H. (1928). Dispersion von Leitfähigkeit und Dielektrizitätskonstante bei starken Elektrolyten. *Physikalische Zeitschrift*, *29*, 401.

Desai, A., Tai, Y.-C., & Lee, S. W. (2001). *Electrostatic Particle Transportation* (No. US 6 185 084 B1). United States Patent Office.

Dhar, B. C., & Lee, N. Y. (2018). Lab-on-a-Chip Technology for Environmental Monitoring of Microorganisms. *BioChip Journal*, *12*(3), 173–183. doi: 10.1007/s13206-018-2301-5

Dittrich, P. S., & Manz, A. (2006). Lab-on-a-chip: microfluidics in drug discovery. *Nature Reviews Drug Discovery*, *5*(3), 210–218. doi: 10.1038/nrd1985

Dori, D. (2016). *Model-Based Systems Engineering with OPM and SysML* (22nd ed., Vol. 1). New York, NY: Springer New York. doi: 10.1007/978-1-4939-3295-5

Dukhin, S. S., Derjaguin, B. V., & Matijevič, E. (1974). *Electrokinetic phenomena* (Vol. 7). New York, NY: Wiley-Interscience.

Duncan, W. J. (1937). *Galerkin's method in mechanics and differential equations* (Technical Report). H. M. Stationery Office. Retrieved 2022-06-21, from `https://reports.aerade.cranfield.ac.uk/handle/1826.2/1428`

Eclipse Foundation, I. (n.d.). *Capella MBSE Tool – Arcadia*. Retrieved 2022-07-25, from `https://www.eclipse.org/capella/arcadia.html`

Ehrlenspiel, K. (2009). *Integrierte Produktentwicklung: Denkabläufe, Methodeneinsatz, Zusammenarbeit* (4th ed.). Munich: Hanser.

Elvesys. (2021, February). *Introduction to lab-on-a-chip 2020: review, history and future.* Retrieved 2022-07-20, from `https://www.elveflow.com/microfluidic-reviews/general-microfluidics/introduction-to-lab-on-a-chip-review-history-and-future/`

Elvira, K. S., i Solvas, X. C., Wootton, R. C. R., & de Mello, A. J. (2013). The past, present and potential for microfluidic reactor technology in chemical synthesis. *Nature Chemistry*, *5*(11), 905–915. doi: 10.1038/nchem.1753

Europractice. (2020). *General Eurpractice MPW Run Schedule and Pricelist.* Retrieved 2020-04-20, from `https://europractice-ic.com/schedules-prices-2020/`

Europractice. (2022). *Europractice, Schedules 2022.* Retrieved 2022-08-08, from `https://europractice-ic.com/schedules-prices-2022/`

Faigle, C. (2020, January). *Vorrichtung und Verfahren zur dielektrischen Trennung von Partikeln* (No. DE 10 2018 210 693 A1). Deutsches Patent- und Markenamt.

Farzanehnia, A., & Taheri, A. (2019). Optimization and parametric study of AC electroosmotic micropumping by response surface method. *Springer Nature Applied Sciences*, 1556.

Fatanat Didar, T., & Tabrizian, M. (2010). Adhesion based detection, sorting and enrichment of cells in microfluidic Lab-on-Chip devices. *Lab on a Chip*, *10*(22), 3043–3053. doi: 10.1039/C0LC00130A

Feldhusen, J. (Ed.). (2013). *Pahl/Beitz Konstruktionslehre: Methoden und Anwendung erfolgreicher Produktentwicklung* (8th ed.). Berlin: Springer. doi: 10.1007/978-3-642-29569-0

Finlayson, B. A. (2013). *The Method of Weighted Residuals and Variational Principles.* Society for Industrial and Applied Mathematics. doi: 10.1137/1.9781611973242

Francesko, A., Cardoso, V. F., & Lanceros-Méndez, S. (2019). Chapter 1 – Lab-on-a-chip technology and microfluidics. In H. A. Santos, D. Liu, & H. Zhang (Eds.), *Microfluidics for Pharmaceutical Applications* (pp. 3–36). William Andrew Publishing.

Gouy, M. (1911). Sur la tension de vapeur d'un liquide électrisé. *Journal de Physique Théorique et Appliquée*, *1*(1), 85–88. doi: 10.1051/jphystap:019110010208500

Gschwend, G. C., Olaya, A., Peljo, P., & Girault, H. H. (2020). Structure and reactivity of the polarised liquid-liquid interface: what we know and what we do not. *Current Opinion in Electrochemistry*, *19*, 137–143. doi: 10.1016/j.coelec.2019.12.002

Gummel, H. (1964). A self-consistent iterative scheme for one-dimensional steady state transistor calculations. *IEEE Transactions on Electron Devices*, *11*(10), 455–465. doi: 10.1109/T-ED.1964.15364

Gupta, K., Kim, D.-H., Ellison, D., Smith, C., Kundu, A., Tuan, J., ... Levchenko, A. (2010). Lab-on-a-chip devices as an emerging platform for stem cell biology. *Lab on a Chip*, *10*(16), 2019–2031. doi: 10.1039/c004689b

Haji Mohammadi, M., Mulder, S., Khashayar, P., Kalbasi, A., Azimzadeh, M., & Aref, A. R. (2021). Saliva Lab-on-a-chip biosensors: Recent novel ideas and applications in disease detection. *Microchemical Journal*, *168*, 106506. doi: 10.1016/j.microc.2021.106506

Happel, J., & Brenner, H. (1983). *Low Reynolds number hydrodynamics: with special*

applications to particulate media (1st ed.). The Hague: Nijhoff.

Henderson, R. M., & Clark, K. B. (1990). Architectural Innovation: The Reconfiguration of Existing Product Technologies and the Failure of Established Firms. *Administrative Science Quarterly*, *35*(1), 9–30. doi: 10.2307/2393549

Hermsen, S. A. B., Roszek, B., van Drongelen, A. W., & Geertsma, R. E. (2013). *Lab-on-a-chip devices for clinical diagnostics* (Tech. Rep. No. 080116001/2013). The Hague: National Institute for Public Health and the Environment.

Hernández-Neuta, I., Neumann, F., Brightmeyer, J., Ba Tis, T., Madaboosi, N., Wei, Q., ... Nilsson, M. (2019). Smartphone-based clinical diagnostics: towards democratization of evidence-based health care. *Journal of Internal Medicine*, *285*(1), 19–39. doi: 10.1111/joim.12820

Hinch, E. J. (1991). *Perturbation methods* (11th ed.). Cambridge: Cambridge University Press.

Holmes, M. H. (2013). *Introduction to Perturbation Methods* (2nd ed., Vol. 20). New York, NY: Springer.

Hooke, R., Allestry, J., & Martyn, J. (1665). *Micrographia: or, some physiological descriptions of minute bodies made by magnifying glasses. With observations and inquiries thereupon.* London: Printed by Jo. Martyn and Ja. Allestry, printers to the Royal Society.

Huang, K.-R., Hong, Z.-H., & Chang, J.-S. (2014). Microfluidic mixing on application of traveling wave electroosmosis. *European Journal of Mechanics - B/Fluids*, *48*, 153–164. doi: 10.1016/j.euromechflu.2014.05.010

Huang, W., Stan, M. R., Gurumurthi, S., Ribando, R. J., & Skadron, K. (2010, February). Interaction of scaling trends in processor architecture and cooling. In *2010 26th Annual IEEE Semiconductor Thermal Measurement and Management Symposium (SEMI-THERM)* (pp. 198–204). Santa Clara, CA: IEEE. doi: 10.1109/STHERM.2010.5444290

Jinek, M., Chylinski, K., Fonfara, I., Hauer, M., Doudna, J. A., & Charpentier, E. (2012). A programmable dual RNA-guided DNA endonuclease in adaptive bacterial immunity. *Science*, *337*(6096), 816–821. doi: 10.1126/science.1225829

Kano, N., Seraku, N., Takahashi, F., & Tsuji, S.-i. (1984). Attractive Quality and Must-Be Quality. *Journal of The Japanese Society for Quality Control*, *14*(2), 147–156. (Publisher: The Japanese Society for Quality Control) doi: 10.20684/quality.14.2_147

Kapoor, A., Balasubramanian, S., Muthamilselvi, P., Vaishampayan, V., & Prabhakar, S. (2020). Lab-on-a-Chip Devices for Water Quality Monitoring. In Inamuddin & A. M. Asiri (Eds.), *Nanosensor Technologies for Environmental Monitoring* (pp. 455–469). Cham: Springer.

Keeble, L., Moser, N., Rodriguez-Manzano, J., & Georgiou, P. (2020). ISFET-Based Sensing and Electric Field Actuation of DNA for On-Chip Detection: A Review. *IEEE Sensors Journal*, *20*(19), 11044–11065. doi: 10.1109/JSEN.2020.2998168

Kinahan, D., Mager, D., Vereshchagina, E., & Miyazaki, C. (2021). *Advances in Microfluidics Technology for Diagnostics and Detection.* Basel: MDPI – Multidisciplinary Digital Publishing Institute.

Kovarik, M. L., Gach, P. C., Ornoff, D. M., Wang, Y., Balowski, J., Farrag, L., & Allbrit-

ton, N. L. (2012). Micro Total Analysis Systems for Cell Biology and Biochemical Assays. *Analytical Chemistry*, *84*(2), 516–540. doi: 10.1021/ac202611x

Krebs, H. A., & Johnson, W. A. (1937). Metabolism of ketonic acids in animal tissues. *Biochemical Journal*, *31*(4), 645–660. doi: 10.1042/bj0310645

Lamb, H. (1975). *Hydrodynamics* (Unabridged and unaltered republ. of the 6. ed. ed.). New York: Dover Publ.

Lanczos, C. (1964). *Applied Analysis* (3rd ed.). Englewood Cliffs, N.J.: Prentice Hall.

Lazar, I. M., Gulakowski, N. S., & Lazar, A. C. (2020). Protein and Proteome Measurements with Microfluidic Chips. *Analytical Chemistry*, *92*(1), 169–182. doi: 10.1021/acs.analchem.9b04711

Leal, L. G. (2007). *Advanced transport phenomena: fluid mechanics and convective transport processes* (19th ed.). Cambridge: Cambridge University Pres.

Ledeboer, J. A. (2009, March). *Dielectrophoretic device for manipulation of particles* (No. EP 2 039 433 A1). European Patent Office.

Lee, J. M. (2018). *Introduction to Riemannian manifolds* (2nd ed., Vol. 176). Cham: Springer.

LeVeque, R. J. (2007). *Finite difference methods for ordinary and partial differential equations: steady-state and time-dependent problems* (No. 98). Philadelphia, PA: Society for Industrial and Applied Mathematics.

Li, D. (Ed.). (2023). *Electrokinetic Microfluidics and Nanofluidics* (13th ed., Vol. 133). Cham: Springer.

Liao, Z., Wang, J., Zhang, P., Zhang, Y., Miao, Y., Gao, S., ... Geng, L. (2018). Recent advances in microfluidic chip integrated electronic biosensors for multiplexed detection. *Biosensors and Bioelectronics*, *121*, 272–280. doi: 10.1016/j.bios.2018.08.061

Lim, Y. C., Kouzani, A. Z., & Duan, W. (2010). Lab-on-a-chip: a component view. *Microsystem Technologies*, *16*(12), 1995–2015. doi: 10.1007/s00542-010-1141-6

Lin, C.-C., Tseng, C.-C., Chuang, T.-K., Lee, D.-S., & Lee, G.-B. (2011). Urine analysis in microfluidic devices. *Analyst*, *136*(13), 2669–2688. doi: 10.1039/C1AN15029D

Lipmann, F. (1941). Metabolic Generation and Utilization of Phosphate Bond Energy. *Advances in Enzymology and Related Subjects of Biochemistry*, *1*.

Liu, D., Marthaler, P. G., Class, A. G., & Gu, L. (2023). Simulation of stratification phenomena with a spectral Fourier–Chebyshev method on the background of a lead-cooled fast reactor. *Annals of Nuclear Energy*, *192*, 109931.

Loucaides, N., Ramos, A., & Georghiou, G. E. (2007). Novel systems for configurable AC electroosmotic pumping. *Microfluidics and Nanofluidics*, *3*(6), 709–714. doi: 10.1007/s10404-007-0168-1

Lyklema, J. (1991). *Fundamentals of interface and colloid science* (Vol. 1: Fundamentals). London: Academic Press.

Ma, M., Booty, M. R., & Siegel, M. (2022). A model for the electric field-driven flow and deformation of a drop or vesicle in strong electrolyte solutions. *Journal of Fluid Mechanics*, *943*. doi: 10.1017/jfm.2022.469

Manz, A., Graber, N., & Widmer, H. M. (1990). Miniaturized total chemical analysis systems: A novel concept for chemical sensing. *Sensors and Actuators B: Chemical*, *1*(1), 244–248. doi: 10.1016/0925-4005(90)80209-I

Mareček, V., & Samec, Z. (2017). Ion transfer kinetics at the interface between two immiscible electrolyte solutions supported on a thick-wall micro-capillary. A mini review. *Current Opinion in Electrochemistry*, *1*(1), 133–139. doi: 10.1016/j.coelec.2016.11.004

Mark, D., Haeberle, S., Roth, G., von Stetten, F., & Zengerle, R. (2010). Microfluidic lab-on-a-chip platforms: requirements, characteristics and applications. *Chemical Society Reviews*, *39*(3), 1153–1182. doi: 10.1039/B820557B

Marthaler, P. G., & Class, A. (2022a, June). *Anordnung und System zur Erzeugung von Flüssigkeitsströmen* (No. DE 10 2020 214 957 A1). Deutsches Patent- und Markenamt.

Marthaler, P. G., & Class, A. (2022b, June). *Arrangement, system and method for generating liquid flows* (No. WO 2022/112474 A1). World Intellectual Property Organization.

Marthaler, P. G., Class, A., Mori, Y., & Young, Y.-N. (2023). From electrodiffusion theory to the electrohydrodynamics of leaky dielectrics through the weak electrolyte limit – CORRIGENDUM. *Journal of Fluid Mechanics*, *962*, E1.

Marthaler, P. G., & Class, A. G. (2021a). Integral effects of the Debye layer on a sedimenting particle with zeta-potential variations. *Proceedings in Applied Mathematics and Mechanics*, *21*(1), e202100209. doi: 10.1002/pamm.202100209

Marthaler, P. G., & Class, A. G. (2021b). Integral jump conditions for singular problems – applied to Debye-layer phenomena. *Proceedings in Applied Mathematics and Mechanics*, *20*(1), e202000044. doi: 10.1002/pamm.202000044

Marthaler, P. G., & Class, A. G. (2022c). Weak curvature asymptotics for Debye layers as electrohydrodynamic discontinuities. *Physical Review E*, *105*(3), 035106. doi: 10.1103/PhysRevE.105.035106

Medoro, G., Di Reno, C., & Manaresi, N. (2014, May). *Method and apparatus for the manipulation and/or the detection of particles* (No. US 2014/0131207 A1). United States Patent Office.

Melcher, J. R., & Taylor, G. I. (1969). Electrohydrodynamics: A Review of the Role of Interfacial Shear Stresses. *Annual Review of Fluid Mechanics*, *1*(1), 111–146. doi: 10.1146/annurev.fl.01.010169.000551

Mendel, G. (1865). Experiments in plant hybridization. *Verhandlungen des naturforschenden Vereines in Brünn*, *4*, 3–47.

Mori, Y., Liu, C., & Eisenberg, R. S. (2011). A Model of Electrodiffusion and Osmotic Water Flow and its Energetic Structure. *Biophysical Journal*, *100*(3), 86a–87a. doi: 10.1016/j.bpj.2010.12.678

Mori, Y., & Young, Y.-N. (2018). From electrodiffusion theory to the electrohydrodynamics of leaky dielectrics through the weak electrolyte limit. *Journal of Fluid Mechanics*, *855*, 67–130. doi: 10.1017/jfm.2018.567

Mouradian, S. (2002). Lab-on-a-chip: applications in proteomics. *Current Opinion in Chemical Biology*, *6*(1), 51–56. doi: 10.1016/S1367-5931(01)00280-0

Mullis, K., Faloona, F., Scharf, S., Saiki, R., Horn, G., & Erlich, H. (1986). Specific enzymatic amplification of DNA in vitro: the polymerase chain reaction. *Cold Spring Harbor Symposia on Quantitative Biology*, *51*, 263–273. doi: 10.1101/SQB.1986.051.01.032

Nguyen, T., Zoëga Andreasen, S., Wolff, A., & Duong Bang, D. (2018). From Lab on a Chip to Point of Care Devices: The Role of Open Source Microcontrollers. *Micromachines*, *9*(8), 403. doi: 10.3390/mi9080403

Noh, J. H., Noh, J., Kreit, E., Heikenfeld, J., & Rack, P. D. (2012). Toward active-matrix lab-on-a-chip: programmable electrofluidic control enabled by arrayed oxide thin film transistors. *Lab Chip*, *12*(2), 353–360. doi: 10.1039/C1LC20851A

Palmieri, M., & Brianza, A. (2005). *Microfluidic device and method for transporting electrically charged substances through a microchannel of a microfluidic device* (No. US 2005/0161327 A1). United States Patent Office.

Pascall, A. J., & Squires, T. M. (2011). Electrokinetics at liquid/liquid interfaces. *Journal of Fluid Mechanics*, *684*, 163–191. doi: 10.1017/jfm.2011.288

Peyret, R. (2002). *Spectral methods for incompressible viscous flow* (11th ed.) (No. 148). New York, NY: Springer.

Prandtl, L. (1904). Über Flüssigkeitsbewegungen bei sehr kleiner Reibung. *Verhandlungen des 3. internationalen Mathematiker-Kongresses*, 484–491.

Prandtl, L. (1938). Zur Berechnung der Grenzschichten. *Zeitschrift für augewandte Mathematik und Mechanik*, *18*, 77–82. doi: 10.1002/zamm.19380180111

Purcell, E. M. (1977). Life at low Reynolds number. *American Journal of Physics*, *45*(1), 3–11. (Publisher: American Association of Physics Teachers) doi: 10.1119/1.10903

Ramos, A., Morgan, H., Green, N. G., & Castellanos, A. (1999). AC Electric-Field-Induced Fluid Flow in Microelectrodes. *Journal of Colloid and Interface Science*, *217*, 420–422. doi: 10.1006/jcis.1999.6346

Ramos, A., Morgan, H., Green, N. G., González, A., & Castellanos, A. (2005, April). Pumping of liquids with traveling-wave electroosmosis. *Journal of Applied Physics*, *97*(8), 084906. doi: 10.1063/1.1873034

Russel, W. B., Russel, W. B., Saville, D. A., & Schowalter, W. R. (1991). *Colloidal dispersions*. Cambridge: Cambridge University Press.

Sachdeva, S., Davis, R. W., & Saha, A. K. (2021). Microfluidic Point-of-Care Testing: Commercial Landscape and Future Directions. *Frontiers in Bioengineering and Biotechnology*, *8*. doi: 10.3389/fbioe.2020.602659

Sanger, F., Nicklen, S., & Coulson, A. R. (1977). DNA sequencing with chain-terminating inhibitors. *Proceedings of the National Academy of Sciences of the United States of America*, *74*(12), 5463–5467. doi: 10.1073/pnas.74.12.5463

Saville, D. A. (1977). Electrokinetic Effects with Small Particles. *Annual Review of Fluid Mechanics*, *9*(1), 321–337. doi: 10.1146/annurev.fl.09.010177.001541

Saville, D. A. (1997). Electrohydrodynamics: The Taylor-Melcher Leaky Dielectric Model. *Annual Review of Fluid Mechanics*, *29*(1), 27–64. doi: 10.1146/annurev.fluid.29.1.27

Schlautmann, S., Gardeniers, J. G. E., & Van den Berg, A. (2003, November). *Method of fabrication of a microfluidic device* (No. EP 1 362 827 Al). European Patent Office.

Schnitzer, O., Frankel, I., & Yariv, E. (2012). Streaming-potential phenomena in the thin-Debye-layer limit. Part 2. Moderate Péclet numbers. *Journal of Fluid Mechanics*, *704*, 109–136. doi: 10.1017/jfm.2012.221

Schnitzer, O., & Yariv, E. (2015). The Taylor-Melcher leaky dielectric model as a macroscale electrokinetic description. *Journal of Fluid Mechanics*, *773*, 1–33. doi:

10.1017/jfm.2015.242

Schnitzer, O., & Yariv, E. (2016). Streaming-potential phenomena in the thin-Debye-layer limit. Part 3. Shear-induced electroviscous repulsion. *Journal of Fluid Mechanics*, *786*, 84–109. doi: 10.1017/jfm.2015.647

Schumpeter, J. (1913). Theorie der wirtschaftlichen Entwicklung. *Jahrbücher für Nationalökonomie und Statistik*, *101*(1), 84–91. doi: 10.1515/jbnst-1913-0108

Schwalbe, J. T., Vlahovska, P. M., & Miksis, M. J. (2011). Vesicle electrohydrodynamics. *Physical Review E*, *83*(4), 046309. doi: 10.1103/PhysRevE.83.046309

Sohel Murshed, S. M. (Ed.). (2021). *Advances in Microfluidics and Nanofluids* (1st ed.). Rijeka: IntechOpen.

Sohn, D.-k. (2006, March). *Fluid rotating apparatus using EHD technology* (No. US 2006/0054227 A1). United States Patent Office.

Squires, T. M., & Bazant, M. Z. (2006). Breaking symmetries in induced-charge electro-osmosis and electrophoresis. *Journal of Fluid Mechanics*, *560*, 65–101. doi: 10.1017/S0022112006000371

Srinivas, K., & Fletcher, C. A. J. (1992). *Computational techniques for fluid dynamics: a solutions manual*. Berlin: Springer.

Staicu, C. E., Jipa, F., Axente, E., Radu, M., Radu, B. M., & Sima, F. (2021). Lab-on-a-Chip Platforms as Tools for Drug Screening in Neuropathologies Associated with Blood–Brain Barrier Alterations. *Biomolecules*, *11*(6), 916. doi: 10.3390/biom11060916

Stokes, G. G. (1850). On the effect of the internal friction of fluids on the motion of pendulums. *Transactions of the Cambridge Philosophical Society*, *9*, 8–94.

Struik, D. J. (1961). *Lectures on Classical Differential Geometry* (2nd ed., Vol. 59). New York, NY: Dover Publ.

Stuetzer, O. M. (1962). Magnetohydrodynamics and Electrohydrodynamics. *Physics of Fluids*, *5*(5), 534.

Suryawanshi, P. L., Gumfekar, S. P., Bhanvase, B. A., Sonawane, S. H., & Pimplapure, M. S. (2018). A review on microreactors: Reactor fabrication, design, and cutting-edge applications. *Chemical Engineering Science*, *189*, 431–448. doi: 10.1016/j.ces.2018.03.026

Taylor, G. (1966). Studies in electrohydrodynamics. I. The circulation produced in a drop by an electric field. *Proceedings of the Royal Society of London. Series A. Mathematical and Physical Sciences*, *291*(1425), 159–166. doi: 10.1098/rspa.1966.0086

Terry, S., Jerman, J., & Angell, J. (1979). A gas chromatographic air analyzer fabricated on a silicon wafer. *IEEE Transactions on Electron Devices*, *26*(12), 1880–1886. doi: 10.1109/T-ED.1979.19791

Thirumalai, S., & Seshadri, R. (2019). Spectral solutions of fractional differential equation modelling electrohydrodynamics flow in a cylindrical conduit. *Communications in Nonlinear Science and Numerical Simulation*, *79*, 104931. doi: 10.1016/j.cnsns.2019.104931

Torza, S., Cox, R. G., Mason, S. G., & Taylor, G. I. (1971). Electrohydrodynamic deformation and bursts of liquid drops. *Philosophical Transactions of the Royal Society of London. Series A, Mathematical and Physical Sciences*, *269*(1198), 295–

319.

Tsuyoshi, H., Tsuyoshi, R., & Suguyama, S. (2009, December). *Fluid actuator, and heat generating device and analysis device using the same* (No. US 200910314462 Al). United States Patent Office.

Tucker, S. (2021). *The Meaning in the Making.* Rocky Nook, Inc.

Tymm, C., Zhou, J., Tadimety, A., Burklund, A., & Zhang, J. X. J. (2020). Scalable COVID-19 Detection Enabled by Lab-on-Chip Biosensors. *Cellular and Molecular Bioengineering*, *13*(4), 313–329. doi: 10.1007/s12195-020-00642-z

Van Dyke, M. (1964). *Perturbation methods in fluid mechanics* (10th ed., Vol. 8). New York, NY: Academic Press.

Venter, J. C., Adams, M. D., Myers, E. W., Li, P. W., Mural, R. J., Sutton, G. G., ... Zhu, X. (2001). The Sequence of the Human Genome. *Science*, *291*(5507), 1304–1351. (Publisher: American Association for the Advancement of Science) doi: 10.1126/science.1058040

Vidic, J., Vizzini, P., Manzano, M., Kavanaugh, D., Ramarao, N., Zivkovic, M., ... Gadjanski, I. (2019). Point-of-Need DNA Testing for Detection of Foodborne Pathogenic Bacteria. *Sensors*, *19*(5), 1100. doi: 10.3390/s19051100

Vizika, O., & Saville, D. A. (1992). The electrohydrodynamic deformation of drops suspended in liquids in steady and oscillatory electric fields. *Journal of Fluid Mechanics*, *239*, 1. doi: 10.1017/S0022112092004294

Vlahovska, P. M. (2019). Electrohydrodynamics of Drops and Vesicles. *Annual Review of Fluid Mechanics*, *51*(1), 305–330. doi: 10.1146/annurev-fluid-122316-050120

Watson, J. D., & Crick, F. H. C. (1953). Molecular Structure of Nucleic Acids: A Structure for Deoxyribose Nucleic Acid. *Nature*, *171*(4356), 737–738. doi: 10.1038/171737a0

Werner, W. (2019). *Vektoren und Tensoren als universelle Sprache in Physik und Technik 1: Tensoralgebra und Tensoranalysis.* Wiesbaden: Springer Vieweg.

Wesner, E. (1977). *Die Planung von Marketing-Strategien auf der Grundlage des Modells des Produktlebenszyklus* (Unpublished doctoral dissertation). Freie Universität, Berlin.

Wikipedia. (2022, July). *Microprocessor chronology.* Retrieved 2022-07-22, from `https://en.wikipedia.org/w/index.php?title=Microprocessor_chronology&oldid=1096926605` (Page Version ID: 1096926605)

Wilson, S., Steele, S., & Adeli, K. (2022). Innovative technological advancements in laboratory medicine: Predicting the lab of the future. *Biotechnology & Biotechnological Equipment*, *36*(1), S9–S21. doi: 10.1080/13102818.2021.2011413

Wood, C. S., Thomas, M. R., Budd, J., Mashamba-Thompson, T. P., Herbst, K., Pillay, D., ... Stevens, M. M. (2019). Taking connected mobile-health diagnostics of infectious diseases to the field. *Nature*, *566*(7745), 467–474. doi: 10.1038/s41586-019-0956-2

Wöhler, F. (1828). Ueber kuenstliche Bildung des Harnstoffs. *Annalen der Physik und Chemie*, *12, Folge 2*. doi: 10.5962/bhl.title.62545

Yariv, E., Schnitzer, O., & Frankel, I. (2011). Streaming-potential phenomena in the thin-Debye-layer limit. Part 1. General theory. *Journal of Fluid Mechanics*, *685*, 306–334.

Ying, W. (2005). *A multilevel adaptive approach for computational cardiology* (Unpub-

lished doctoral dissertation). Duke University, Durham, NC.

Ying, W., Rose, D. J., & Henriquez, C. S. (2008). Efficient fully implicit time integration methods for modeling cardiac dynamics. *IEEE Transactions on Biomedical Engineering*, *55*(12), 2701–2711. doi: 10.1109/TBME.2008.925673

Zenobi, R. (2013). Single-Cell Metabolomics: Analytical and Biological Perspectives. *Science*, *342*(6163), 1243259. doi: 10.1126/science.1243259

Zhai, J., Li, H., Wong, A. H.-H., Dong, C., Yi, S., Jia, Y., ... Martins, R. P. (2020). A digital microfluidic system with 3D microstructures for single-cell culture. *Microsystems & Nanoengineering*, *6*(1), 1–10. Retrieved 2023-02-13, from `https://www.nature.com/articles/s41378-019-0109-7#citeas` doi: 10.1038/s41378-019-0109-7

Zhu, H., Sencan, I., Wong, J., Dimitrov, S., Tseng, D., Nagashima, K., & Ozcan, A. (2013). Cost-effective and rapid blood analysis on a cell-phone. *Lab on a Chip*, *13*(7), 1282–1288. doi: 10.1039/C3LC41408F